University of Southampton

Faculty of Engineering and Physical Sciences

Engineering Materials, Mechanical Engineering

Influence of build orientation on high temperature fatigue crack propagation mechanisms in Inconel 718 fabricated by laser powder bed fusion

by

Diego Martínez de Luca

Thesis for the degree of Doctor of Philosophy

December 2022

UNIVERSITY OF SOUTHAMPTON

Abstract

Faculty of Engineering and Physical Sciences

Engineering Materials

Doctor of Philosophy

Influence of build orientation on high temperature fatigue crack propagation mechanisms in Inconel 718 fabricated by laser powder bed fusion

by Diego Martínez de Luca

Additively manufactured (AM) Inconel 718 (IN718) was characterised in terms of microstructure, effect of post heat treatment and hence dependence of fatigue crack growth on build orientation, even after heat treatment. The AM specimens were manufactured in two orientations so that cracks would propagate either parallel (horizontal samples) or perpendicular (vertical samples) to the build direction. In addition, cast and wrought IN718 specimens were studied to benchmark AM against established processing techniques. The AM as-built microstructure exhibited a columnar, dendritic structure parallel to the build direction. No differences were found between specimen orientations in terms of Laves phase, and MC type carbides precipitating in inter-dendritic regions. There were however differences in average grain size, with vertical specimens having a coarser grain structure. Post processing heat treatments recrystallised the structure eliminating the columnar grain morphology, although some columnar-type grain shape was retained. In addition, a high percentage of twin grain boundaries were formed during the heat treatment process for both orientations, and vertical specimens again had a larger average grain size than horizontal. Laves phase were dissolved, and precipitation of common IN718 strengthening precipitates (δ-phase, γ', and γ'') occurred, with no difference between sample orientations. The cast and wrought material used for comparison had a finer, equiaxed microstructure with a lower area fraction of twin grain boundaries compared to heat treated L-PBF.

Long crack fatigue tests were conducted on single edge notched samples at 350 and 650 ºC in air at a load ratio 0.1, under 1-X-1-1 trapezoidal loading waveforms with dwell times, X, of 1s and 90s at maximum load. At 350 ºC no apparent difference in crack growth rates was found, with transgranular fracture modes found at all ΔK levels for all tested specimens. Intergranular fracture modes became evident when testing at higher

temperatures, with the vertical samples showing greater crack growth resistance at both frequencies. Horizontal specimens had on average a higher degree of intergranular failure. Their smaller grain size, and lower area fraction of twins resulted in a higher number of grains susceptible to high-temperature embrittlement. With longer dwell times, vertical samples again showed greater crack growth resistance, with crack arrest occurring at low ΔK values due to observed crack deflection reducing the effective stress intensity at the crack tip. For all testing at 650 ºC cast and wrought specimens displayed higher fatigue crack growth rates, and significant differences in grain boundary failure mechanisms. The equiaxed grain structure in cast and wrought specimens was not as effective deflecting cracks, plus the smaller grain size and lower area fraction of twins resulted in a much larger number of grains susceptible to high-temperature embrittlement.

The extent of oxidation related damage formed ahead of the crack tip during dwell-fatigue was further studied by performing tests alternating between high (5 Hz) and low frequency (1-90-1-1) regimes at 650 ºC. Crack arrest occurred again for vertical specimens and subjected to 90 s dwells with no apparent oxidation embrittlement formed ahead of the crack tip. In contrast, horizontal and cast and wrought specimens both exhibited the formation of a large oxidation related damaged zone ahead of the crack tip during dwell fatigue promoted by dynamic embrittlement. This was linked to a large surge in crack propagation rates when switching to higher frequency (5 Hz) as the crack propagated through embrittled grain boundaries. In order to further study the effect of dwell time on damage ahead of the crack tip and understand the large differences between sample orientations, pre-cracked specimens were held under a sustained load at 650 ºC for 16 hours. The resultant crack tip and oxides formed were studied using scanning electron microscopy, electron backscatter diffraction and energy dispersive spectroscopy. No differences were found in the composition of oxides. However, the location of the oxide layer with respect to the crack tip was different for horizontal (ahead of the crack), and vertical (filling the crack) specimens. This resulted in a more conventional grain boundary failure process by dynamic embrittlement for horizontal specimens, comparable to that in the literature for cast and wrought IN718. The microstructure of vertical specimens, however, promoted a very tortuous crack path compromising oxygen delivery to the crack tip. In addition, the reduction in effective ΔK associated with crack deflection will have lowered the local stresses at the crack tip. Thus, at low ΔK levels the combination of limited available oxygen and low local stress at the crack tip was not sufficient to promote diffusion of oxygen ahead of the crack tip, with oxidation forming inside the crack and stopping fatigue crack propagation.

Table of contents

List of figures

List of tables

Research Thesis: Declaration of Authorship

Print name: Diego Martinez de Luca

Title of thesis: Influence of build orientation on high temperature fatigue crack propagation mechanisms in Inconel 718 fabricated by laser powder bed fusion.

I declare that this thesis and the work presented in it are my own and has been generated by me as the result of my own original research.

I confirm that:

1. This work was done wholly or mainly while in candidature for a research degree at this University;
2. Where any part of this thesis has previously been submitted for a degree or any other qualification at this University or any other institution, this has been clearly stated;
3. Where I have consulted the published work of others, this is always clearly attributed;
4. Where I have quoted from the work of others, the source is always given. With the exception of such quotations, this thesis is entirely my own work;
5. I have acknowledged all main sources of help;
6. Where the thesis is based on work done by myself jointly with others, I have made clear exactly what was done by others and what I have contributed myself;
7. Parts of this work have been published/presented as:
   - D. Martinez de Luca, A. R. Hamilton, P. A. S. Reed, Influence of build orientation on high temperature fatigue crack growth mechanisms in Inconel 718 fabricated by laser powder bed fusion: effects of temperature and hold time, *submitted to International Journal of Fatigue* (2022)

Signature:

Date:

Acknowledgements

There are a few people I would like to thank for their help and support both in my research and daily life over the past few years. It would have been quite tricky to get here without their kindness and support.

First, my supervisors Professor Philippa Reed, and Dr Andrew Hamilton. Thanks for all the patience, guidance, and support through every stage of my research career. I would also like to thank Dr Nong Gao, and Professor Ian Sinclair for their feedback from my 9-month, and confirmation progression reviews. For all their assistance, I wish to thank the technical and support staff, Aga, Dr Geoff Howell and Dr Andy Robinson. Thanks, as well to Dr Shuncai Wang for all the help with the SEM, and TEM.

I would also like to thank Dr Donghyuk Kim with whom I have spent a lot of time trying to get the infamous Instron 1 to work, and basically taught me everything I needed to know for my PhD. I am also greatly indebted to past and present members of the research group for the valuable discussions, and friendship. In no particular order I would like to thank Anqi, Ara, Alvaro, Ben, Corentin, Deepak, Ellis, Joe, Kieran, Maruti, Mike, Mostafa, Somsubhro, Yeajin, and Yuanguo (thanks for helping me get my head round oxidation, and deflected cracks). I would also like to thank the formula student team at university and their members for keeping me entertained with all their weird problems, and random ideas.

Finally, to my parents and sister ¡Muchas gracias por todo!

Abbreviations

3D	3 Dimensional
AM	Additive Manufacturing
APB	Antiphase boundary
BD	Build direction
BEI	Backscatter electron imaging
BCT	Body-centred cubic
CAD	Computer aided design
CSL	Coincident site lattice
CT	Computed tomography
CW	Cast and wrought
DCPD	Direct current potential drop
DED	Direct energy deposition
EBM	Electron beam melting
EBSD	Electron backscattered diffraction
EDM	Electric discharge machining
EDX	Energy dispersive X-ray
ESR	Electro-slag remelting
FCC	Face centred cubic
FCG	Fatigue crack growth
FEG	Field emission gun
GA	Gas atomisation
HCF	High cycle fatigue
HCP	Hexagonal closed packed

HIP	Hot isostatic pressing
IN718	Inconel 718
KW	Kear Wilsdorf
L-PBF	Laser-Powder Bed Fusion
LCF	Low cycle fatigue
LEFM	Linear elastic mechanics
LOF	Lack of fusion
NDT	Non-destructive testing
OM	Optical microscopy
PD	Potential drop
PMZ	Partially melted zone
PREP	Plasma rotating electrode process
PSB	Persistent slip bands
RA	Rotary atomisation
SAGBO	Stress assisted grain boundary oxidation
SEI	Secondary electron imaging
SEM	Scanning electron microscope
SENB	Single edge notch bend
SFE	Stacking fault energy
TA	Tensile axis
TEM	Transmission electron microscope
UAM	Ultrasonic additive manufacturing
VAR	Vacuum arc remelting
VIM	Vacuum induction melting
WA	Water atomisation
WD	Working distance

1 Introduction

1.1 Background

Nickel-based superalloys are materials extensively used in the aerospace industry due to their excellent mechanical properties and corrosion resistance at elevated temperatures [1], [2]. Polycrystalline superalloys are usually produced via the cast and wrought (CW) route, and the performance of these components is often limited by the mechanical properties of the parts and/or design/geometry constraints introduced in the manufacturing process [3]. Additive manufacturing (AM) offers a relatively new route for processing superalloys and has attracted significant attention from the aerospace industry in recent years for the production of superalloys [4]. AM is the general term used to describe specific manufacturing techniques that enable the production of complex 3-dimensional components by adding material where needed rather than subtracting it, in a layer-by-layer fashion [5], [6]. It does not require the need for dedicated tooling, and it is highly flexible with shorter lead times compared to traditional manufacturing techniques. However, as with any new manufacturing method, its application for safety critical components must be carefully reviewed.

Commercially, the advantages of using AM in aerospace components can be primarily related to reduced lead times (and associated costs) and with the ability to produce novel and complex geometries that were previously impossible to manufacture [7], [8]. By utilising the design freedom of AM, it is also possible to combine components reducing the need for fastening and adhesion in complex assemblies, and thus avoid potential failures across joints. Furthermore, AM provides a nearer net shape manufacturing solution, hence the amount of scrap material will be reduced per component improving buy-to-fly ratios [7], [9]. Along with all the benefits of AM, there are some challenges for the adoption of this technology in the aerospace industry. It is a complex process with a large number of processing variables that can have an effect on the quality of the final parts. Although significant research has been done to optimise/control the process, these parameters affect the thermal history, and thus the quality and mechanical properties of the fabricated parts in ways that are still not entirely understood. Some of these are manifested as surface roughness, porosity, residual stresses, unique microstructures as

well as anisotropy in the mechanical properties. Further challenges include limited data (knowledge of material properties), or standardised certifications for AM processes [9]. Since, all aerospace manufacturing is subject to strict certifications and quality controls, it will be necessary to develop standard procedures, and to improve knowledge of process-microstructure-property relationships for the successful implementation of AM.

AM research of nickel superalloys has mainly concentrated on Inconel 718 (IN718) due to its excellent weldability allowing the production of near fully dense components [10]. IN718 is a γ'' (Ni_3Nb) precipitation strengthened nickel-based superalloy that has been extensively used in the aerospace industry for turbine disks operating up to temperatures of 650 ºC [11]. Most of this AM research has focussed on microstructure, process parameter optimisation and monotonic mechanical properties (tensile testing, and hardness) [12]–[19]. However, knowledge of cyclic loading performance, i.e. fatigue strength or fatigue lives (main failure mechanism for nickel-based superalloys), under service relevant conditions is still very limited. Fatigue studies have mainly focussed on room temperature high cycle fatigue (HCF) lifetime analysis where AM parts have commonly shown inferior fatigue endurance compared to CW components [3], [12], [20], [21]. Furthermore, the main parameters of interest in these prior fatigue studies are loading orientation (relative to building orientation), surface quality, process induced defects and effect of heat treatment. In general, when heat treated, AM specimens show comparable lifetimes to cast and wrought IN718, due to the precipitation of IN718 strengthening precipitates γ″ and γ′. However, as-built components exhibit reduced performance mainly related to the presence of process induced pores, lack of appropriate bonding between layers and the high content of Laves phase in the as-built microstructure.

In service, AM components will be subjected to fatigue loading conditions with varying temperatures and frequencies [1]. Fatigue crack growth (FCG) behaviour is known to be affected by the material microstructure, environment, temperature, loading conditions and the interaction between them [22]. Generally, high frequency testing at low/intermediate temperatures shows cycle dependent crack growth, with transgranular fracture modes. Conversely, by decreasing loading frequency or introducing dwell periods at maximum load in oxidising environments, time dependent crack propagation mechanisms and oxidation-enhanced intergranular fracture modes become apparent, significantly accelerating crack growth rates [23]. Such detrimental temperature and dwell effects are widely recognised and studied for CW IN718 [24]–[30]. The typical AM microstructure is, however, very different from that of CW IN718 (in terms of grain boundary character, precipitate distribution, grain shape anisotropy, etc.), potentially

leading to different FCG behaviour at high temperature. Understanding the effect of these microstructural differences on high temperature fatigue is needed for the optimisation of AM structures and has therefore motivated this study where the effect of frequency, temperature, and oxidation on FCG mechanisms will be assessed for AM IN718.

1.2 Aim and objectives

The following objectives were set to improve the understanding of the fatigue crack propagation mechanisms of additively manufactured Inconel 718. This aims to contribute to improved fatigue performance and to inform printing strategies to improve structural integrity of AM components. To achieve this, the following broad objectives have been set:

1. Characterise the role of AM processing and post heat treatments on material response, defect formation/distribution and microstructure.
2. Assess high temperature fatigue crack propagation mechanisms in AM IN718 and benchmark the material response to comparable cast and wrought IN718.
3. Explain synergies between microstructure, temperature, loading conditions, and oxidation on fatigue crack propagation at high temperatures, and the corresponding implications for AM processing and part design.

2 Literature review

2.1 Additive manufacturing

Additive manufacturing (AM) is defined in the American Society for Testing and Material (ASTM) standard F2792 as "the process of joining materials to make objects from 3-D model data, usually layer upon layer, as opposed to subtractive manufacturing technologies" [31]. This feature allows production of complex parts directly from design reducing the need for complex tooling, dies or casting moulds and reducing the number of processing steps [5]. Complex parts can be produced with fewer limitations compared to conventional methods (e.g., straight cuts, round holes) or standard shapes (e.g., tubes, sheet). Another advantage is the reduction of material usage, and the possibility of recycling un-melted/sintered feedstock materials [6]. For these reasons, AM is being considered more and more for the production of high performance components for aerospace, automotive, and energy applications [5], [6], [32]. There are, however, some metallurgical aspects specific to AM (i.e., mechanical anisotropy, porosity, different phase distribution and residual stresses) that need to be further understood to improve/optimise AM components. This section will focus on AM of IN718, particularly on the manufacturing processes and the resultant microstructure.

2.1.1 Process

AM processes for metals can be divided into different categories depending on the feedstock materials, or energy source used. However, for this study only laser-powder bed fusion (L-PBF) will be discussed. L-PBF uses a high energy density laser to selectively melt and fuse regions of powder, layer by layer according to computer aided design (CAD) data [33]. It consists of a series of steps from CAD data preparation to part removal from the building platform. Figure 2.1 shows the building process which includes:

1. Digital model data is converted into machine instructions to generate support structures for any overhanging features, and slices for scanning of the individual layers.

2. A substrate (to support the part) is fixed to the build platform and levelled for process control.
3. Protective inert gas (e.g., argon, or nitrogen) is fed into the chamber containing the build platform. It helps protect the hot metallic parts from oxidation.
4. A powder roller spreads a thin (thickness < 100 μm) layer of loose powder, evenly distributing the powder across the entire substrate width.
5. The laser beam scans the powder bed, to melt and fuse selected areas according to the digital data. Once the scanning of a specific layer is completed, the build platform steps down, a new layer of powder is spread on top of the substrate and the laser scans a new layer. The process is then repeated for successive layers, until the components are built.
6. Process parameters such as laser power, scanning speed, hatch spacing, and layer thickness (Figure 2.2) are adjusted for each build, such that melt pools completely fuse with the neighbouring melt pool and the preceding layer. This remelting process of the previous layer helps to fully consolidate the component.
7. Once the process is completed, loose powder is removed, and the component can be detached from the substrate either manually or by electric discharge machining (EDM)

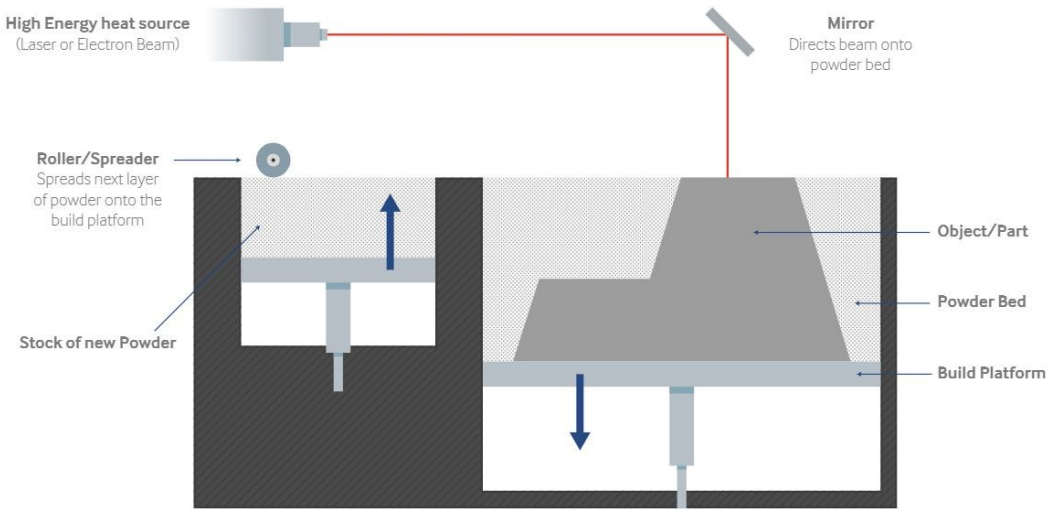

Figure 2.1 L-PBF process schematic [9]

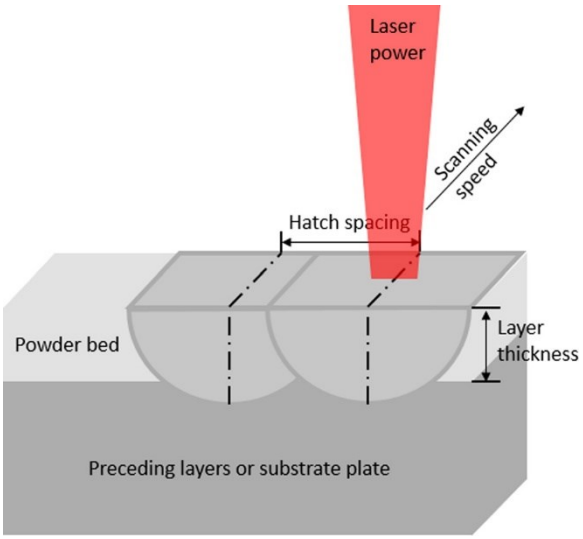

Figure 2.2 Schematic of L-PBF process parameters [33].

During the L-PBF process many parameters will affect the quality of the final component. The main parameters include: laser type, wavelength, beam diameter (or spot size), laser power, scanning speed, hatch spacing, scanning strategy, and layer thickness [5], [33]–[35]. Some parameters will be fixed by the selection of hardware, whereas others are adjusted for different build jobs and different powder materials. Materials can only absorb light energy for certain wavelengths. Therefore, CO_2 lasers ($\lambda \approx 10.6$ μm) are used for ceramics or polymers, because of their higher optical absorptivity and fibre lasers (e.g. Nd:YAG, Yb:YAG with $\lambda \approx 1.06$ μm) are used for metals [5]. The beam diameter or spot size (around tens of micrometers in diameter) determines the spatial resolution of the machine. Finally, continuous wave lasers are commonly used, however, pulsed lasers can also be applied [36]. This introduces more parameters: pulse duration, frequency, shape, etc. which have proven to affect surface quality.

Figure 2.2 shows a representation of the process parameters that can be changed to optimise processing and material properties. The laser power and the speed of the moving laser spot should be adjusted to provide enough heat to melt the powders. The hatch spacing is the distance between two neighbouring scan lines, which usually is smaller than the laser spot size (to achieve fusion of two adjacent layers). Finally, the layer thickness is the thickness of the powder before being scanned. These parameters together with the energy absorption of the powders affect the volumetric energy density applied to melt the powders [5], [37]. The resultant volumetric energy density is given by equation 2.1, where: P is the laser power (W), v is the scanning speed (mm/s), h is the hatch spacing (mm) and t is the layer thickness (mm). Insufficient energy densities (low laser power, high scanning speed or large layer thickness) may lead to a phenomenon known as balling, where spherical beads are formed due to insufficient surface tension

and wetting of the preceding layer molten pool [6]. On the other hand, high power and low scanning speeds can lead to excessive material evaporation and the keyhole effect, which could cause porosity due to excessive penetration of the molten pool [6], [38]. Furthermore, poor selection of hatch spacing might lead to porosity as adjacent lines do not fully fuse together. Hence, a suitable combination of these parameters is necessary to successfully build near fully-dense parts. The effect of different parameter combinations will be commented upon later on the report.

$$E = \frac{P}{v\,h\,t} \qquad (2\text{-}1)$$

The path that the laser follows during the process is known as the scanning strategy. Various strategies have been developed, and Figure 2.3 shows some conventional strategies. Uni-directional and bi-directional are strategies where the laser sequentially scans the part dimension in the scanning direction across each layer. The island strategy (Figure 2.3-c) has been used to reduce residual stresses [6], [39]. For island scanning, the part is segmented and scanned in parts of N x N areas, where N is the length of the segmented area. The unidirectional fills in island scanning are alternated, which results in a decrease in the temperature gradients in the scan plane by better distributing the heat through the process. Linear contour scanning is also possible with L-PBF, where the contour of the scan pattern follows the edge of the part, and multiple passes are done to improve the surface finish of the process [5]. Moreover, the scan patterns are usually rotated by a given angle for every layer. Finally, the scan strategy will have an impact on the other process parameters. Thus, laser power and scanning speed need to be optimised for a given scanning strategy to eliminate porosity and improve the mechanical performance of the parts.

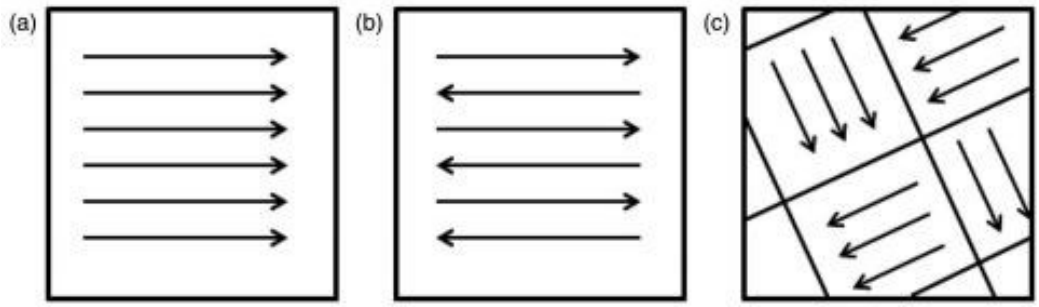

Figure 2.3 Scan strategies used to determine laser path in L-PBF: a) uni-directinal, b) bi-directional, c) island scan strategy [6]

2.1.1.1 Feedstock materials

Alloy powders are used in L-PBF due to ease of feeding and controlled melting [6]. Mixtures of powders in pre-set ratios can also be fed to produce controlled composition/property gradients [5]. Powders will have a large influence on the properties of the final component; therefore, high quality powders should be used. However, manufacturing of high quality powder is a complex process, considering the high surface area and the susceptibility to oxidation.

Powders are characterised by shape, size distribution, surface morphology and flowability [33]. Typical particle sizes for L-PBF range between 10 to 60 μm, and their size distribution is usually controlled by sieving methods [5]. Shape and surface morphology are usually characterised using scanning electron microscopes (SEM), and the flowability is measured by the Hall flow test. Finally, for L-PBF processes, another parameter to consider is the powder packing structure. It is dependent on all of the characteristics previously mentioned, and it will determine the local configuration of individual particles on the powder bed, highly influencing the final component structure and properties. These characteristics will depend on the manufacturing process. Four powder manufacturing techniques are [5]:

- Gas atomization (GA) process. The molten alloy is atomized using high pressure flow of argon or nitrogen. Once solidified the droplets can be collected as powder.
- Rotary atomization (RA) process. The molten alloy is deposited on a rotary disk. Upon contact with the disk, fine droplets of metal are thrown away, and when solidified they are collected as powder.
- Plasma rotating electrode process (PREP). The end of a rotating metal bar is melted using an electric arc or plasma. The resulting molten metal is centrifugally ejected as fine droplets, and when solidified, collected as powder.
- Water atomization (WA) process. The molten metal is atomized using a high pressure water jet. Once solidified the droplets are collected as powder.

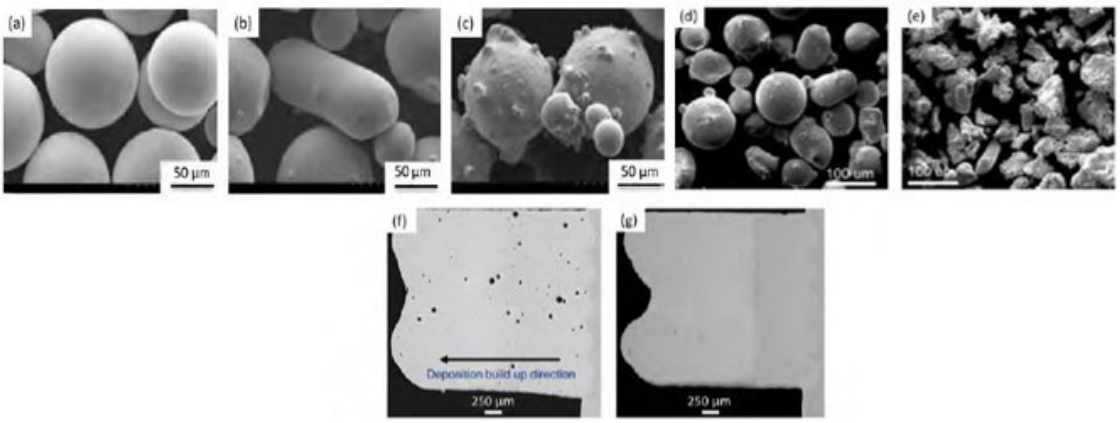

Figure 2.4 SEM image of alloy powders manufactured by a) PREP, b) RA, c) GA [34]. Comparison of shape between d) GA and e) WA [40]. IN718 component porosity when produced with f) GA powder, and g) PREP [41].

Figure 2.4 shows SEM images of powders produced by the above mentioned processes [34]. PREP gives the best results, with particles that are spherical with relatively smooth surfaces. Particles produced by RA exhibit random shapes with a smooth surface. The GA process forms powders with relatively spherical morphology and dimpled surfaces [34]. Furthermore, there are smaller particles attached to the surface that increase the surface roughness. Finally, the powders from the WA process are characterised by irregular shapes and a coarse surface roughness [40]. Powders with uniform size distribution and smooth surface texture will arrange and pack more efficiently. In addition, they will enhance powder flowability and the ability to spread a uniform powder bed density, promoting homogeneous melting and inter-layer bonding, which results in improved mechanical properties and surface finish [34]. As a result, PREP will usually yield the better results. The coarse surface of the powders processed via GA and WA will lead to higher surface roughness [40]. Moreover, components processed via GA, WA or RA where the size distribution variation is high, will have higher porosity due to entrapped gas bubbles [41]. Figure 2.4-f, g shows the difference in porosity between components produced using PREP and GA under the same processing conditions.

2.1.2 Defects

As mentioned previously, many parameters are involved in a L-PBF process. Optimised parameters can result in high density levels (> 99 %), however, if any of the parameters are improperly chosen higher proportion of defects will occur [38]. The common AM defects can be divided into two categories: porosity and cracks. Understanding these defects and their formation is important as it will improve the process reliability and the quality of the parts produced.

2.1.2.1 Defect types

Porosity is a common defect in AM, and it needs to be minimised due to the detrimental effects it can have on the material mechanical properties. Porosity in AM can be classified as powder induced or process induced.

Powder-induced porosity is typically small in size (<50 μm) and it has a spherical shape (shown in Figure 2.5-c) [42]. There are two main mechanisms by which this type of porosity might emerge. First, gas pores between the metal powder might form and dissolve in the molten pool. Due to the high cooling rates of the L-PBF process the dissolved gas cannot escape before solidification occurs, forming a pore [38]. Second, gas can be entrapped in the powders during the manufacturing process, especially for GA powders. These entrapped gas particles will result in micro spherical pores, smaller than pores caused by low packing density of the metal powders [5], [38].

Process-induced porosity, referred to as lack-of-fusion (LOF), is caused by inadequate overlap of the molten pool from a new layer on the previously deposited layer [34]. Furthermore, LOF defects can be classified into two types: (i) un-melted powders, and (ii) poor bonding between layers. If the energy input is low, the melt pool width will not be enough to ensure sufficient overlap between scan tracks, resulting in un-melted powder between the tracks [43]. Moreover, if the energy input is even lower, the melt pool depth will be insufficient to achieve appropriate interlayer bonding, leading to the formation of pores because of poor bonding between layers. Finally, LOF defects are much larger than powder-induced pores and have an irregular shape with sharp edges, as shown in Figure 2.5-a, b [44].

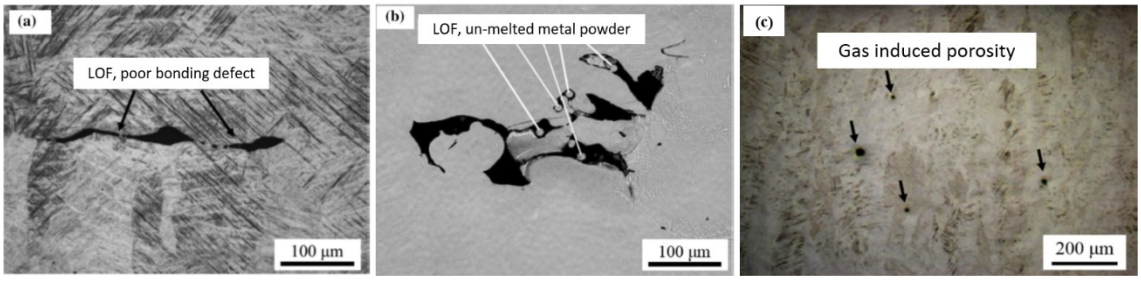

Figure 2.5 Optical images of porosity defects in L-PBF; a) LOF poor bonding, b) LOF un-melted powder, c) gas porosity [44], [45].

Cracking or delamination might occur in AM components due to the rapid melting and solidification processes that take place [35]. Cracks can be very long, spreading over several layers, or as short as the layer thickness [38]. Two main types of cracks can occur in a L-PBF process [5], [38]:

1. Solidification cracking along grain boundaries, or between two consecutive layers. As the newly deposited layer solidifies, it will tend to contract due to solidification shrinkage and thermal contraction. The substrate or previous layer, will, however, be at a lower temperature. As a consequence, there is a difference in contraction between the two layers. This results in a tensile stress at the solidifying layer, and if its magnitude is large enough cracking will occur.

2. Liquation cracking in the partially melted zone (PMZ) of the build. In the PMZ, rapid melting below the alloy liquidus temperature might cause melting of phases such as carbides. Due to the solidification shrinkage that occurs under cooling, a tensile force is exerted into the liquid films around the carbides, that may act as cracking initiation sites.

2.1.2.2 Effect of process parameters in defect formation

The applied energy density will control the dimensions of the molten pool which, as explained above, has a significant impact on the type and size of potential defects. Figure 2.6, shows a scatter plot for void fraction and crack density against volumetric energy density for the Ni-superalloy CMSX486. As shown, with increasing energy density, the penetration depth of the melt pool is larger, and thus void fraction decreases [46]. However, cracking content increases as the thermal stresses are larger. Furthermore, if the energy density is too high then keyholing may occur [5]. If the keyhole becomes unstable, it can collapse and form voids in the form of entrapped gas [35]. Lower energy densities (rapid scanning or low power) reduce crack formation, however, LOF pores increase due to the smaller size of the molten pool.

The scanning strategy will not only affect the melting and solidification process, but it will also have an influence on the location and distribution of the defects [38]. Uni and bi-directional scan strategies can suffer from scanning speed variations across a scanning track (if producing a large component), which will result in a local increase in laser energy, and a possibility for defect formation [47]. Furthermore, impurities might be pushed to the edges, resulting in a cluster of defects at the perimeter of the component. Rotating the strategy from one layer to the other can prevent defect clustering by balancing the energy input across all layers [38]. Furthermore, the island scan strategy can be used to balance the overall residual stresses and reduce the formation of cracks. However, porosity and LOF are generally formed at the border of the different scan islands. Finally, post-processing treatments such as hot isostatic pressing (HIP), can be

used to reduce porosity and crack content. However, due to the nature of HIP process it will not be able to close surface intersecting pores [48].

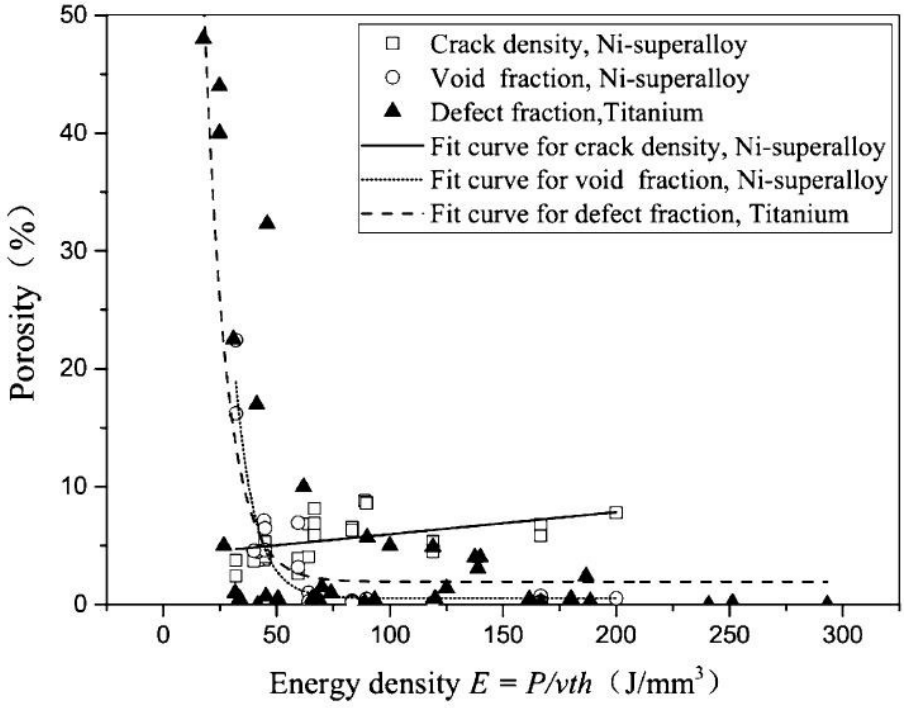

Figure 2.6 Scatter plot of void fraction and crack density in L-PBF against energy density [38].

2.1.3 Structure of AM materials

During AM, a selected volume of material is subjected to a complex thermal cycle. This cycle involves rapid heating of the powder above its melting temperature, rapid solidification once the heat source moves on, and numerous re-heating and re-cooling cycles as the following layers are scanned [35], [49]. The resultant spatially variable thermal cycle yields meta-stable microstructures and non-equilibrium compositions of the resultant phases that may vary from layer to layer [5]. Furthermore, the resultant microstructures, irrespective of the material, are usually fine-grained in comparison to e.g., casting, which can be explained by the rapid solidification [6], [49].

The temperature profiles, and thus final microstructure, will depend on the melting and solidification of the melt pool. Additionally, the thermal gradients will be affected by the surrounding powder, due to the different heat conduction between the solidified material and powder. Generally, as heat conduction in the build direction is higher than in any other directions, solidification occurs from the previously deposited layer, which results in elongated columnar grains in the build direction that can exceed the layer thickness [49]. These columnar grains can lead to anisotropic properties. The G/R ratio is commonly used to predict the growth of columnar or equiaxed dendrites and can be

applied for AM processes, where G represents the thermal gradient, and R the cooling rate of the melt pool [6], [49]. Columnar dendrites are favoured under higher thermal gradients and lower cooling rates, whereas equiaxed dendrites are the opposite. Therefore, the process parameters can be tailored to control the thermal conditions and crystallographic orientation, depending on the location of the part, and reduce the anisotropy of the microstructure.

In optical microscope images the features of L-PBF processing can be clearly seen, as shown in Figure 2.7. The x-y direction (cross-section) shows regular laser tracks, which correspond to the laser scanning strategy. The laminar structure can be seen in the vertical sections (x-z, y-z), as well as characteristics of the build strategy such as: scanning pattern, hatch spacing, layer thickness and melt pool. At higher magnifications, the columnar dendritic microstructure can be observed. More on the specific microstructure of L-PBF IN718 will be explained in section 2.2.3.

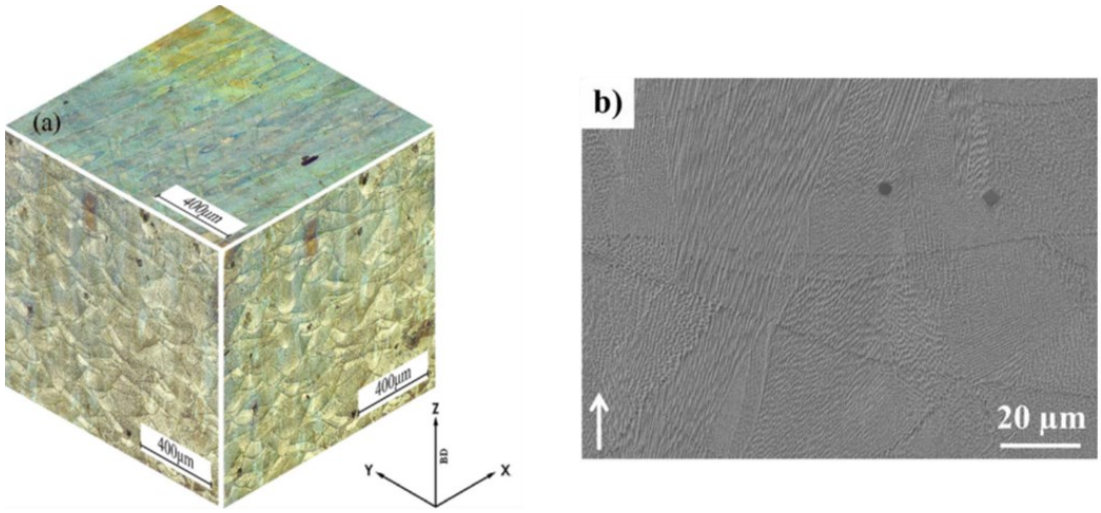

Figure 2.7 Microstructure of IN718 in as-built condition a) in three mutually perpendicular planes [50]*, b) at higher magnifications showing the dendritic structure* [51].

2.2 IN718 and its fatigue behaviour

This section will give a description of the composition, physical metallurgy, and microstructure (cast and wrought, and L-PBF) of IN718, with reference to their influence on fatigue performance. The published literature is reviewed, concentrating on the effects of high temperature environments on crack initiation and growth, as well as the effects of L-PBF processing on fatigue performance.

2.2.1 Composition and physical metallurgy

Table 2-1 AMS5662 Inconel 718 composition in wt-percentage.

C	**Si**	**Mn**	**P**	**S**	**Cr**	**Mo**	**Ni**	**Cu**	**Co**
0.025	0.07	0.07	0.011	0.0003	17.86	2.97	53.7	0.05	0.026
Ti	**Al**	**Nb**	**B**	**Fe**	**N**	**Pb**	**Ta**	**O**	**Bi**
0.92	0.54	5.33	0.0029	18.12	0.005	<0.0003	<0.02	<0.0003	<0.00003
Ca	**Mg**	**Sn**	**Se**	**Ag**					
<0.0003	0.0012	<0.001	<0.0003	<0.0001					

The chemical composition of IN718 can be found in Table 2-1. The strength of IN718 is due to a combination of solid solution strengthening and precipitation hardening of the face-centred cubic (FCC) nickel rich matrix (γ phase) [52]. However, precipitation hardening is the main strengthening mechanism. Solid solution strengthening is enabled by elements such as Fe, Cr, Al, Ti, Mo and Co and it remains effective up to temperatures of 60 % the melting temperature [52]. Mo and Co improve the creep properties by lowering the stacking fault energy and impeding dislocation slip [53]. The main precipitate forming elements are Nb, Ti and Al. Nb favours the formation of the main strengthening phase, the γ'' phase, whereas Al and Ti favour the formation of the γ' phase [54]. Furthermore, Nb provides the added benefit of stabilising primary MC type carbides. Cr enhances oxidation and corrosion resistance by forming a stable, non-porous Cr_2O_3 surface oxide layer. The presence of carbon improves the melt processing of the alloy, as it reduces the solidus temperature of nickel enabling better control of the liquid metal properties [55]. However, the remaining carbon can affect the material properties through the formation of a variety of carbide phases. These carbides are important precipitates to consider given their effect on the mechanical properties and fatigue resistance of IN718.

2.2.2 Microstructure (cast and wrought)

Table 2-2 Main strengthening precipitates of IN718 [56]

Phase	Composition	Crystal Structure	Orientation wrt to gamma matrix	Precipitate Morphology	Theoretical max. amount (vol %)	Temp. range (°C)
γ'	$Ni_3(Ti, Al)$	FCC	$(001)_{\gamma'}$ // $(001)_{\gamma}$ $[100]_{\gamma'}$ // $<100>_{\gamma}$	Spherical / cuboid <<1 μm	8	650 - 850
γ''	Ni_3Nb	BCT	$(001)_{\gamma''}$ // $(001)_{\gamma}$ $[100]_{\gamma''}$ // $<100>_{\gamma}$	Discs: 20-60 nm diameter 5-9 nm thickness	13	620 - 900
δ	Ni_3Nb	orthorhombic	$(010)_{\delta}$ // $(001)_{\gamma}$ $[100]_{\delta}$ // $<110>_{\gamma}$	Long thing plates	13	750 to 1020

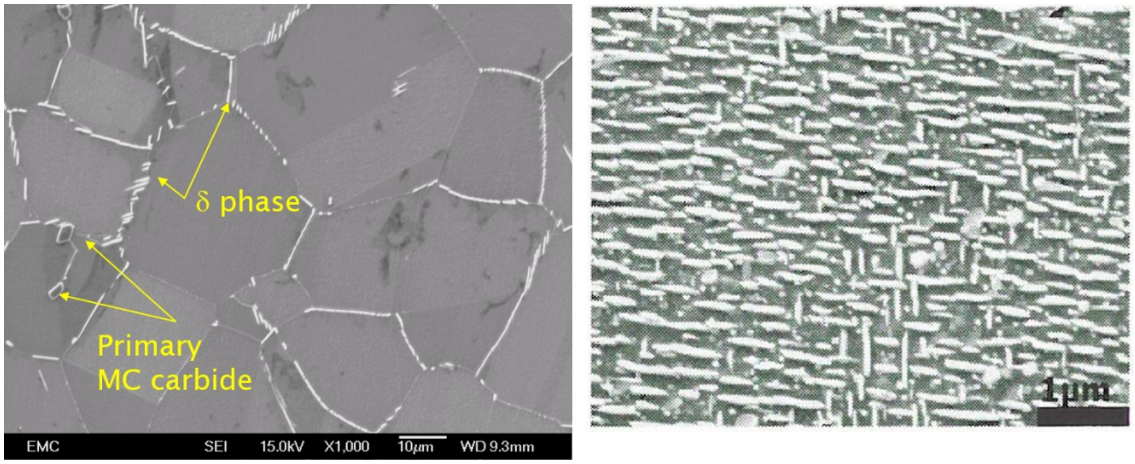

Figure 2.8 SEM Micrographs showing left) typical cast and wrought microstructure and the precipitation of δ-phase and MC carbides, right) precipitation of γ' and γ'' in cast and wrought IN718 [56].

The crystallographic characterisation of the main strengthening phases (γ'', γ', and δ) are shown in Table 2-2. Furthermore, images of the microstructure of the material and precipitates are provided in Figure 2.8. In IN718, γ'' is a Ni_3Nb metastable phase with a body-centred tetragonal (BCT) crystal structure [57]. It forms during the ageing treatment as coherent disk shape particles on the {100} planes of the FCC structure [54]. Typical particle sizes are 20-60 nm diameter and thickness 5-9 nm [53]. Additional contributions to strength come from the $Ni_3(Al, Ti)$ γ' phase, which has a FCC structure [54]. The role of γ'' as the main strengthening precipitate differentiates IN718 from other Ni-based superalloys, in which γ' is the principal strengthening phase. Both phases precipitate homogeneously as fine particles distributed uniformly across the microstructure [58]. The precipitation of both phases is very sensitive to the ratio (Ti + Al)/Nb (in atomic %) [54].

For standard IN718, this ratio is ≈ 0.7, which results in a higher volume of γ'' (≈ 13 %) compared to γ' (≈ 8%) [56]. Another factor that makes γ'' the main strengthening factor is its higher lattice mismatch, which induces more coherency strain strengthening [53], [59].

Phase stability is relatively poor in IN718 at temperatures above 650 ºC caused by the transformation of γ'' into the more stable δ-phase, which provides lower strengthening [59]. At temperatures above 800 ºC this process can take place in 100 hours. A second factor limiting phase stability at temperatures above 700 ºC is the significant coarsening of γ'' (more rapid than the coarsening of γ') [56]. Some studies have shown that a compact morphology precipitation of γ'' and γ' can improve the thermal stability and mechanical properties of IN718 at temperatures above 650 ºC [54], [60], [61]. This morphology can be obtained by increasing the ratio of (Ti + Al)/Nb, while at the same time increasing the total content of Nb, Ti and Al above standard IN718 [59]. In this case, precipitation of γ' would occur first. It will then be surrounded by a shell of γ'' plates after ageing at 650-800 ºC for 4 hours. Extended ageing shows that the compact morphology can have greater resistance to coarsening than standard precipitates morphologies, indicating a possible way of enhancing the stability of the alloys at higher temperatures.

The δ-phase is a stable form of Ni_3Nb and has an orthorhombic structure [62], [63]. Precipitation of the δ phase can occur at grain boundaries at low aging temperatures (below 900 ºC), and inside grains at higher temperatures. Periods of long thermal exposure can also lead to precipitation of the δ phase [53]. Below 900 ºC, precipitation of δ will be preceded by γ' and γ'', while at higher temperatures it can precipitate directly from the γ matrix [57]. It generally precipitates with an acicular morphology although in wrought IN718 globular shaped precipitates can also be found. The globular morphology is associated with plastic deformation leading to fragmentation of the phase plates [56]. The δ-phase has generally been considered as detrimental, as it forms instead of the strengthening γ''. However, under certain circumstances it may have beneficial effects. When it precipitates at grain boundaries a surrounding Nb depleted region will form, which can lead to zones of increased plasticity improving the notched stress rupture properties of the material [53], [57]. Furthermore, it has been found to have a pinning effect on the grain boundaries, enabling control of grain size at high temperatures [62], [63].

Carbides and nitrides can also be found in the microstructure of IN718. Primary carbides are of the form MC, where M is Ti, Nb, Ta, Hf, Th or Zr. Nitrides take the form MN, where M is Ti, Nb or Zr. For IN718 the main nitride and carbide forming elements are Ti and Nb

[55]. Furthermore, they are generally globular with an irregular shape. MC and MN form early in the solidification process, nitrides form first in the melt and act as nucleation sites for primary carbides [64]. Furthermore, not all the carbon present forms carbides during solidification, some remains in solid solution. As a result, during heat treatments or service, primary carbides that are not completely stable might react with the γ matrix to form lower carbides [53]. The lower carbides that can form in IN718 are $M_{23}C_6$, and M_6C. These can either precipitate at grain boundaries ($M_{23}C_6$) or be randomly distributed across the matrix (M_6C).

The Laves phase is a brittle, intermetallic phase and is a product resulting from the terminal eutectic reaction (liquid → γ + Laves) in the solidification of IN718 [64]. Laves phases have a hexagonal close packed (HCP) crystal structure, and their chemical composition is (Nb, Mo, Ti)$(Ni, Fe, Cr)_2$ [64]. The formation of Laves phases occurs at temperatures higher than 982 ºC and it is typically avoided, if possible, as it has a detrimental effect on the mechanical properties of IN718 [52]. It can be found in as-cast ingots or welds; however, it is usually eliminated by a homogenisation treatment [65]. Thus, it is rare to find Laves phases in wrought IN718. Finally, other minor phases can be found in IN718, such as: borides, sulphides, and phosphides [53]. These phases, however, do form during welding or in AM where non-equilibrium cooling conditions exist.

2.2.2.1 Processing and heat treatments

The manufacturing process for Nickel superalloys will depend on the alloy system, shape and form of the end product, and the service conditions and properties needed for the specific application [1]. In general, superalloys can be processed by: (i) casting, (ii) wrought processes through ingot metallurgy and forging, and (iii) powder metallurgy (PM) if the material is very heavily alloyed. IN718 has been primarily produced by cast and wrought methods, and therefore, will be the only processing route explained. The cast and wrought process is described in Figure 2.9.

Vacuum induction melting (VIM) is used as the standard melting procedure for the preparation of superalloys [1], [66]. For VIM, raw alloying elements are melted under high vacuum, then the fluid is decanted from the crucible into a mould where casting will occur under pressure in an argon atmosphere [1]. However, the VIM-cast material is not suitable for immediate use. First, the level of segregation is too high. Second, it may contain solidification cracks, porosity and refractory particles may be present [67]. For these reasons, conventional cast-and-wrought processing uses secondary melting processes such as vacuum arc remelting (VAR) and possibly electro-slag remelting

(ESR). The additional steps are used to further increase the quality of the final product, and to improve the yield and forgeability of the ingots.

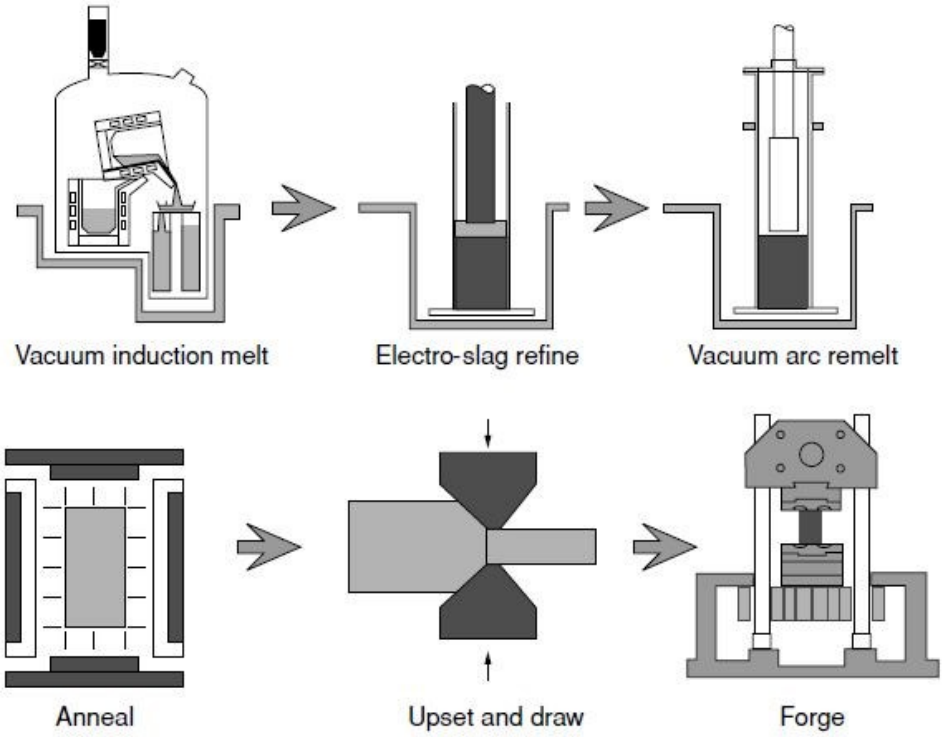

Figure 2.9 Sequence of processes used for the production of turbine disc alloys by ingot metallurgy [66].

VAR involves the melting under vacuum of a consumable electrode into a copper-cooled crucible (see Figure 2.10-b) [1]. The electrode is the casting that has been previously produced by VIM. A high current is passed through the electrode and the baseplate of the copper crucible. This creates a direct current (DC) arc which melts the surface of the electrode and forms a new ingot as the material cools down at the bottom of the crucible [1], [67]. The resulting ingot has a structure and chemistry far superior to the electrode (VIM part) that is being melted.

ESR is an alternative method of secondary melting. Similar to VAR a consumable electrode is remelted, however, in this case a molten slag pool sits between the electrode and the solidifying ingot (see Figure 2.10-a) [1], [67]. An alternating current (AC) is then applied between the electrode and the forming ingot through the resistive slag [1], [67]. Hence, solidification occurs in the slag skin and not the crucible baseplate [66]. Both methods can be independently used to meet the alloy requirements. However, more recently triple melting is being used to exploit their combined advantages. Triple melting will start with VIM followed by ESR, which produces a higher integrity ingot, but it may contain microstructural defects due to segregation [1]. Then, the ESR ingot is remelted

using the VAR method. Finally, after the remelting processes have finished the ingot is annealed to remove or reduce elemental segregation.

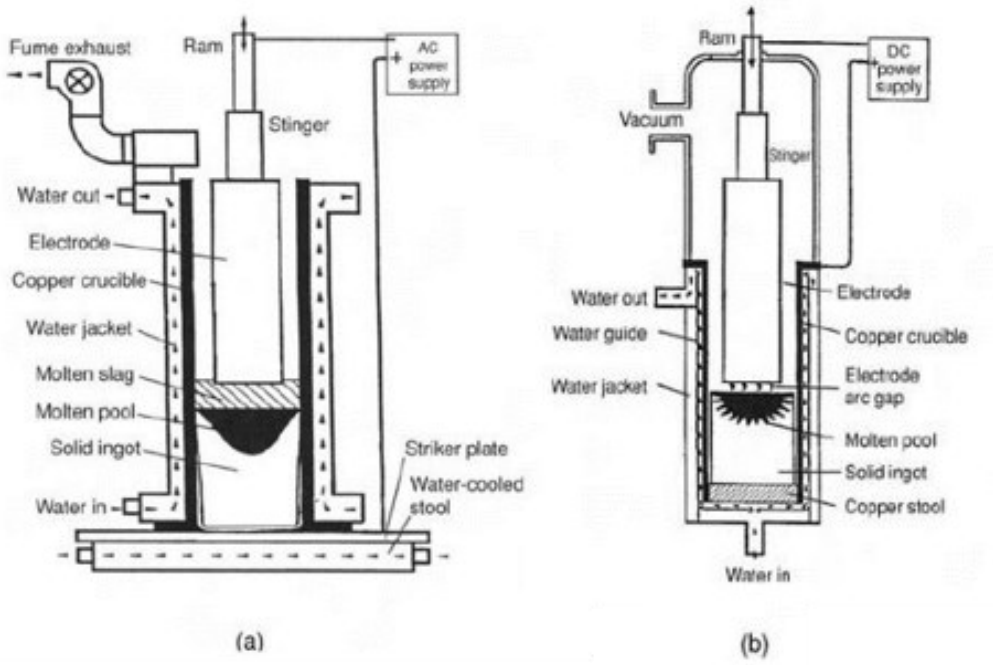

Figure 2.10 a) Schematic representation of the ESR process, b) Schematic representation of the VAR process [1].

The ingots produced by the remelting processes are unsuitable for direct mechanical applications [66]. Therefore, they undergo thermal-mechanical work to break down the as-cast structure and reduce the grain size. The first step is to anneal the material to remove or reduce elemental segregation. Next, a process known as ingot conversion takes place (usually achieved by cogging), during which the diameter of the bar is reduced [1]. The ingot is placed in a furnace and heated until it reaches an appropriate temperature for forging. Then, it is manipulated between two horizontal dies causing it to deform in and out of plane. The process is then repeated as the ingot rotates, resulting in an octagonal cross-section, see Figure 2.11 for a representation of the process. At the end of this procedure the ingot is returned to the furnace and the process is repeated until the desired reduction is achieved. For the later stages the temperature is reduced below the relevant solvus temperature to inhibit grain growth after deformation [1], [53]. This deformation causes substantial recrystallization to a finer microstructure [1]. Finally, a rounding operation is performed prior to slicing the billet for forging. The resultant cylinder is then forged into a shape close to the final product shape. After forging, a heat treatment is usually applied to manipulate the final microstructure of the superalloy and make them suitable to specific applications. Typically, forging of IN718 takes place at 900-1120 ºC, starting at the top of the temperature range, and progressively reducing

the temperature to finish around 900-950 ºC [4]. At this temperature, precipitation of the δ phase occurs, providing some grain size control by pinning the grain boundaries. If finer grain sizes are required, the δ phase can be precipitated before forging, which is then performed below the solvus temperature of δ [53].

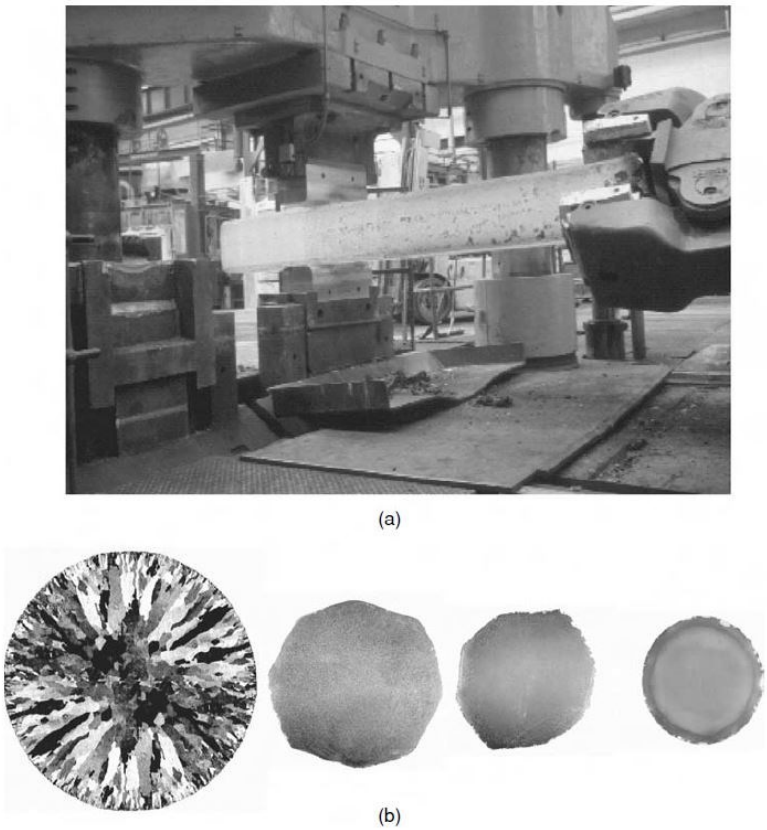

Figure 2.11 a) Cogging operation for the thermal-mechanical working of a superalloy billet, b) cross-sections of the worked billet after various stages of working, with the un-worked billet at the left [1].

The precipitation kinetics for IN718 have been reported in the form of Transformation-Time-Temperature diagrams, an example is given in Figure 2.12. These diagrams provide a summary of the approximate precipitation and solutioning ranges that are commonly used in standard IN718 heat treatments. These are:

- 1010-1050 ºC for 1 hour followed by water quench. This will dissolve all intermetallic precipitates (δ, γ', and γ'').
- 900-980 ºC for 1-5 hours will precipitate δ phase.
- 620-850 ºC precipitate γ', and γ'.

A common heat treatment for IN718 would consist of 1-2 hours of solution treatment (925-1010 ºC), followed by a duplex age treatment at 720 ºC and 620 ºC. The solution treatment dissolves γ' and γ'', while at the same time precipitates some δ phase and

retains any that precipitated during the forging process. The δ phase will inhibit grain growth by pinning the grain boundaries during the solution treatment, thus preserving the grain size obtained post forging. The wide solution temperature is due to the large variation of Nb accepted in IN718 (4.75-5.3 wt.%) [56]. The next step in the heat treatment would be ageing at 720 ºC for 8 hours, furnace cool to 620 ºC, and then hold at 620 ºC for 10 hours followed by air cooling. This duplex age treatment will lead to γ'/γ'' precipitation giving optimum strengthening properties. Direct ageing processes have been developed for turbine discs showing improved high temperature fatigue strength, however, there is some reduction in stress rupture life for low stress / high temperature regimes [68]. The direct ageing process intends to produce fine grained components with a very low quantity of δ phase. For this process, forging will start at temperatures of 1025 ºC, with a final upset at 980 ºC followed by water quenching. After forging, the standard duplex ageing treatment is applied to precipitate γ'/γ'', without any solution treatments.

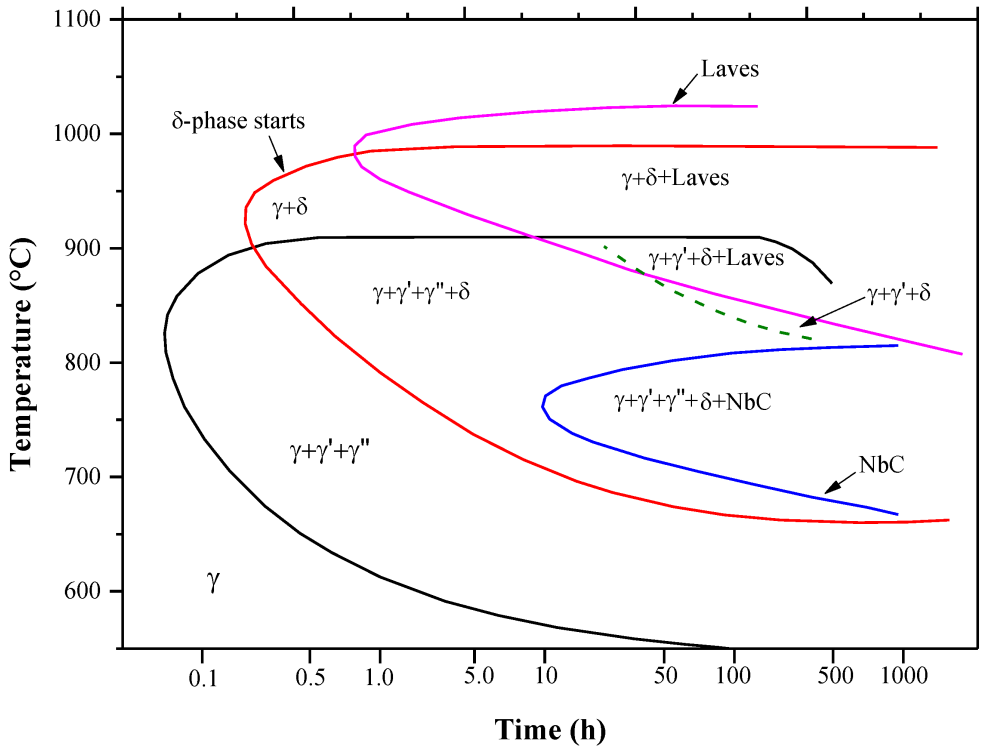

Figure 2.12 Transformation-time-temperature diagram for IN718 [69].

2.2.2.2 Slip behaviour of cast and wrought IN718

Plastic deformation in metals is mainly related to the movement of dislocations. A characteristic of plastic deformation in IN718 is that slip generally occurs heterogeneously. Hence, dislocation motion is concentrated in planar bands (slip bands) rather than occurring homogeneously throughout the material. The FCC matrix of IN718 has a low stacking fault energy, which leads to a large degree of dislocation dissociation

into partials with a stacking fault between them. This will help strengthen the material by inhibiting dislocation cross slip (main deformation mechanism at high temperatures) and favouring the movement of dislocations across specific slip bands.

As previously mentioned, γ' and γ'' are the main strengthening precipitates of IN718. These are coherent with the matrix, and their most significant contribution is that they constrain the movement of dislocations [70]. Coherency strains between the matrix and precipitates caused by differences in their lattice parameters, is the first way in which the particles restrict dislocation motion. Furthermore, the thermal expansion coefficient of the matrix is higher than the precipitates. This results in an increase of the lattice mismatch with temperature, improving the creep response of the material. If the stresses are high enough, however, the dislocations can pass through the precipitates by shearing them. This shearing process provides another strengthening mechanism, due to the energy necessary to create additional precipitate/matrix interfaces. The γ' and γ'' are also ordered phases. Shearing of the particles disrupts the ordered atomic structure in its slip plane, leaving behind a distorted plane known as anti-phase boundary (APB). In order to remove the APB, dislocations need to move through the precipitates in pairs. The leading dislocation will cause the APB, and the trailing dislocation will then interact with the distorted particle reordering the structure. The resultant breaking and re-arrangement of chemical bonds leads to strengthening of the material. This again favours the formation of slip bands (heterogeneous slip) instead of cross-slip [70].

Another characteristic of IN718 is marked cyclic softening during low cycle fatigue, at both room and high temperatures [71], [72]. The repeated shearing of precipitates by dislocations that occurs during cyclic loading, leads to the formation of preferential paths for dislocations to travel across the microstructure. This constant movement of dislocations through the precipitates will lower their strengthening effectiveness, leading to cyclic softening. This is supported by TEM studies performed by Fournier et al. [71], showing how the repeated cutting of γ'' reduces the size of the particle to an extent that they offer reduced resistance to dislocation motion. Since cross-slip of coupled dislocations is more complicated, slip will continue to occur in the same slip plane during deformation, forming planar slip bands in the cyclically loaded IN718 specimen. As a result, cyclic softening will occur, and almost precipitate-free planar slip bands will form.

2.2.3 Microstructure (AM)

In general, L-PBF IN718 exhibits a columnar dendritic structure (see Figure 2.13 for differences observed in the cross-section and longitudinal-section) [48], [50], [73]. The microstructures are finer than those produced by the cast and wrought route [73]. In

addition to the grain structure generated by L-PBF, the phase composition has been found to be different to conventional cast and wrought IN718. Several authors have reported the difficulty of precipitating the γ', γ'' phases due to the high cooling rates [17], [35], [51]. However, other studies argue the presence of γ'' [50], [74]. Amato *et al*. [74] found ellipsoidal γ'' precipitates perpendicular and parallel to the build direction. Furthermore, they found the presence of γ'' to be related to the scan strategy and size of the melt pool. The γ'' precipitates, appeared at the interaction point between adjacent melt pools, possibly because of their short interaction time and high thermal gradient. Moreover, Ni *et al*. [50] showed the anisotropy of their distribution, with a higher content of precipitates in the vertical cross-section (shown in Figure 2.14). A more common feature is the presence of Laves and MC-type carbides at interdendritic regions or grain boundaries, because of micro-segregation of these elements during the AM process [36]. This is largely due to the rapid cooling and localised melt pool, resulting in non-equilibrium conditions during solidification. Under the rapid solidification conditions there is insufficient time for elements such as Nb or C to diffuse back into the solid. As the concentration of these particles increases in the remaining liquid, formation of precipitates such as NbC and Laves occurs [36]. Furthermore, the different thermal cycles across the height of the component can lead to the formation of location dependent precipitates. Thus, the precipitates at the bottom of the sample, which are exposed to more thermal cycles, are usually larger than those found at the top [5]. This results in significant spatial heterogeneity for L-PBF components.

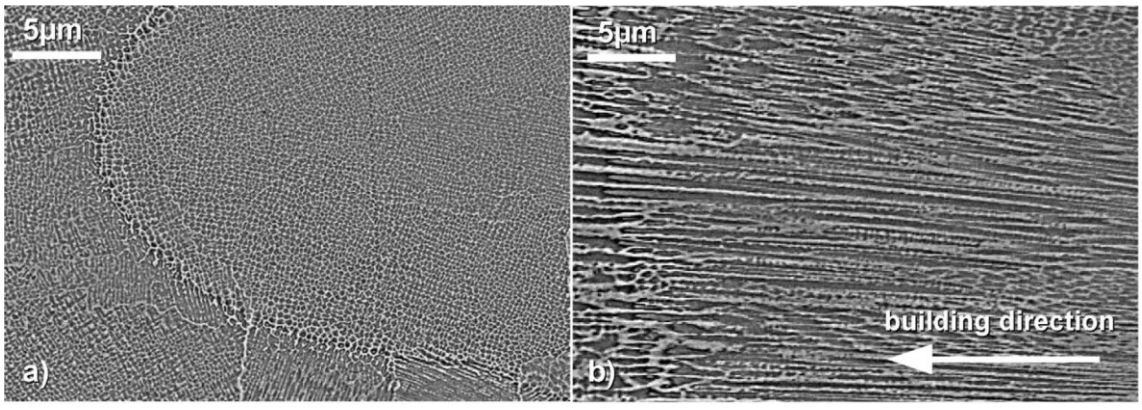

Figure 2.13 Differences in dendrite orientation between a) section perpendicular to BD, b) section parallel to BD [48].

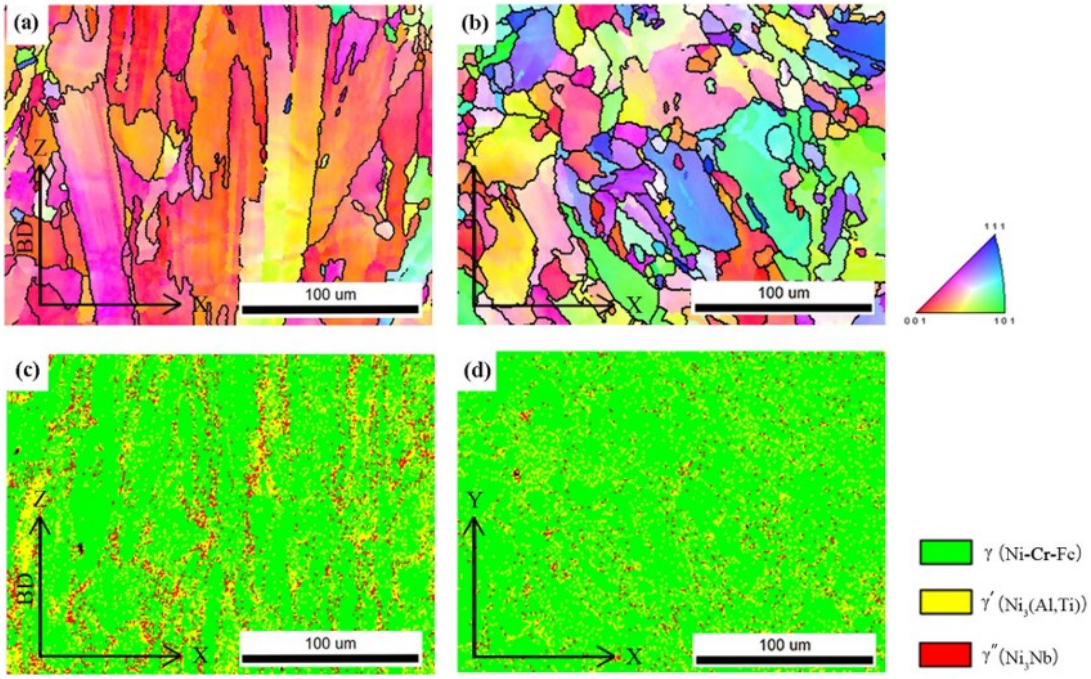

Figure 2.14 EBSD orientation maps showing grain morphology a) parallel to BD and b) perpendicular to BD. Distribution of different phases is shown in c) vertical section, and d) horizontal section [50].

2.2.3.1 Effect of process parameters on microstructure

In addition to achieving high relative density, the selection of process parameters has significant effects on microstructure, and phase composition. The shape of the melt pool, which determines the solidification process is a function of the laser power and scanning speed. High power and high speed will result in a comet-shaped melt pool (or keyhole if the power is too high), whereas low power and low speed will yield a spherical melt pool [49]. The comet-shaped melt pool will generate the linear columnar grains explained above. Spherical melt pools, on the other hand, generate curved columnar grains, as the thermal gradient is directed from the boundary to the liquid free surface [5]. Deviations from columnar grains can also be seen with increasing the scan velocity [75], [76]. As the velocity increases, the angle between the build direction axis and dendrites increases, as the angle between the thermal gradient and build direction starts to be affected by the high velocity. Furthermore, if the velocity is high enough, grains might suffer a zigzag effect, as the thermal gradient would significantly vary between layers [76] (see Figure 2.15). The formation of carbides can also be affected by scan velocity. As the velocity increases, solidification will occur before significant elemental diffusion takes place, preventing their precipitation [49].

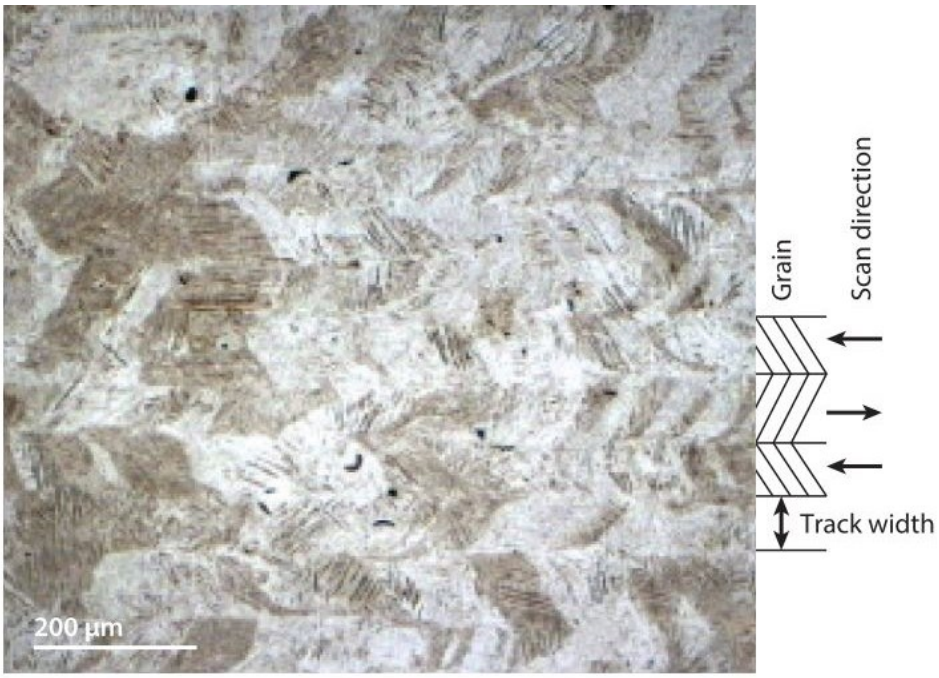

Figure 2.15 Observed zig-zag patterns caused by changes in scanning strategy [76].

As explained before, the G/R ratio can be used to determine the resultant dendrite structure. The ratio can be represented in a solidification map and Figure 2.16, shows the relationship for IN718. Using this principle, the processing parameters can be chosen to achieve a certain G/R ratio. Dehoff *et al*. [77] used the G/R ratio to achieve parts with controlled crystallographic orientations at specific locations within the component. The G/R ratio can also be used to predict the formation of Laves phases and avoid them. Low G/R promotes the formation of equiaxed dendrites, which can separate the liquid between them, avoiding the formation of inter-dendritic Laves phases [78]. There are, however, limitations on what G/R ratios can be achieved depending on the maximum power of the laser used.

Energy density, and laser power will also have an impact on microstructure and phase composition. Jia, *et al*. [79] studied the effect of increasing energy density, and found the resultant microstructures changed from coarse columnar dendrites to clustered dendrites, and finally slender, finer and ordered dendrites. Furthermore, as the energy density increases the grain size decreases. Popovich *et al*. [17] investigated the effect of varying L-PBF parameters within the same IN718 tensile sample. Two different parameters were chosen with the same energy density but different laser powers (950 W, and 250 W). The 250 W sections resulted in finer grains (5-100 µm) randomly oriented, and the 950 W sections showed long columnar grains (≈ 1000 µm) along the build direction. The change between parameters could be distinguished by sharp changes in texture, demonstrating the possibility of tailoring the structure and mechanical

properties throughout the part geometry, as shown in Figure 2.17. Furthermore, the 950 W section showed higher values of porosity and a higher content of Laves and carbide content.

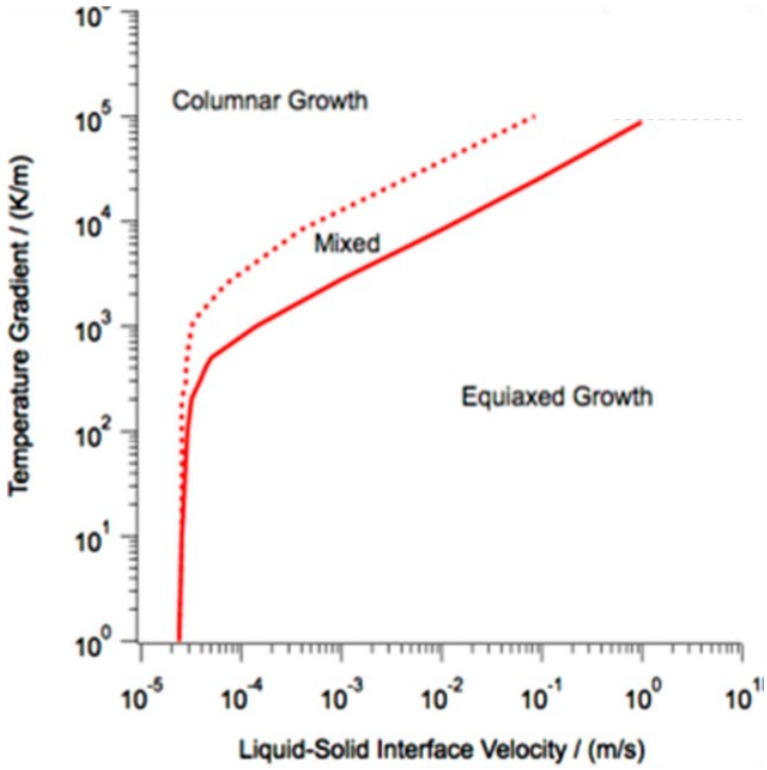

Figure 2.16 Solidification map for IN718 [6].

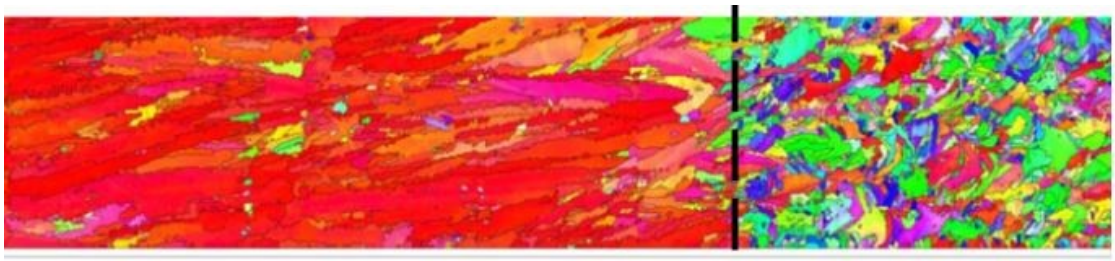

Figure 2.17 EBSD analysis of L-PBF IN718 featuring a coarse grain structure and fine grains in the same plane [17].

Scanning strategy will affect the microstructural texture and residual stresses. Nadamal *et al*. [15] studied the effect of the hatch length (laser scan vector length) on the microstructure. The reported structure showed coarser columnar grains for shorter scans, whereas longer scans lead to refined grains (Figure 2.18). Furthermore, they studied the resultant residual stresses, with the shorter scans causing high compressive stresses in the build direction, and the longer scans leading to an overall reduction of the residual stresses but with high stress gradients in the scan direction. Lu *et al*. [16] characterised changing scanning strategies, by varying the island size. The results showed a reduction in residual stresses, as the island size decreased. However, lower

island sizes promoted the formation of cracks, which limits its application. Arisoy *et al*. [80] studied the effect of changing the angle between layers (hatch angle), at 67º and 90º. The 67º rotation showed a finer microstructure, and furthermore, the angle of inclination of the columnar grains was less affected by laser power and scanning speed. Finally, Foster *et al*. [81] studied the effect of changing the interlayer dwell time (delay between layers). The specimens were produced with the same process parameters, only varying the waiting period between each layer by 0, 20 or 40 seconds. The results showed a reduction in the secondary dendrite arm spacing with increasing dwell time (3.7 µm for 0 s, and 3.2 µm for 40 s), caused by an increase of the thermal gradient.

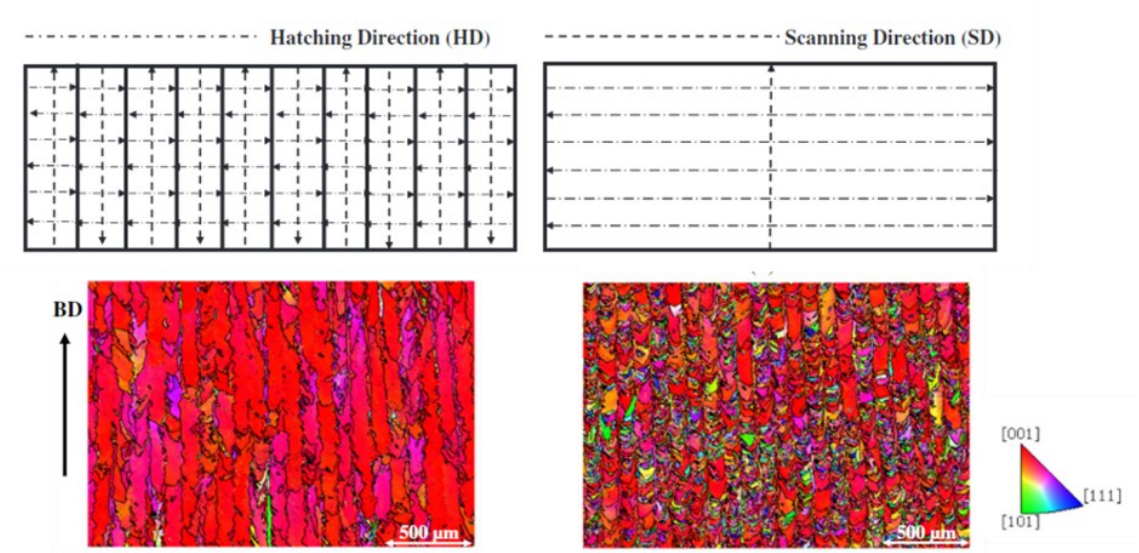

Figure 2.18 Grain structure for shorter (left) and longer (right) laser scan paths/hatching from EBSD [15].

2.2.3.2 Heat treatment of IN718 AM components

Thermal treatments for AM materials may be used to relieve residual stresses, close pores/cracks or improve the properties of the material. As explained previously, given the high cooling rates of the AM process, the starting as-built microstructure is different to that found in conventional cast or wrought IN718. Different heat treatments have been investigated for AM IN718, such as: stress relief, hot isostatic pressing (HIP), solution treatment and/or age treatment. Stress relief treatments may be performed to reduce the residual stresses formed during the AM process. HIP is used to reduce the internal porosity and cracks. Solution treatments homogenise the structure and reduce elemental segregation, and age treatments will induce the formation of the precipitating phases γ' and γ''. Standard heat treatments have been developed for cast and wrought IN718 (AMS 5662/3), however, there are no specific standards for thermal processing of AM IN718. ASTM F3055 (standard for AM IN718), sets recommendations for thermal treatments depending on the classification of the component: recommending stress

relieving, standard solution and age treatments, and HIP for higher strength components. Nonetheless, the parameters are not fully agreed, and these should be developed depending on the processing parameters used, as they can significantly vary the starting microstructure.

Some studies have considered the application of the standard IN718 heat treatment (solution + double step age treatment). The results show a partially recrystallised microstructure, where the Laves phases cannot fully dissolve into the matrix during the solution treatment. The γ' and γ'' phases, precipitated during the age treatment as usual. Chlebus *et al*. [82] investigated increasing the solutioning temperature from 980, 1040 to 1100 ºC to fully homogenise the γ phase. It was determined, that for 980 and 1040 ºC the structure maintained its columnar grain structure, but Laves phases are still present. At temperatures above 1100 ºC the γ phase was fully homogenised, and the structure was fully recrystallised. Liu *et al*. [83] considered direct double ageing, to compare with standard heat treatments. The structure maintained its columnar nature, and the strength significantly increased, due to the high precipitation of the strengthening γ'' and γ' phases. However, the ductility was lower compared to standard heat treatments, due to the presence of fine Laves particles in interdendritic areas. Finally, other studies have added a homogenisation step to the standard heat treatment to remove the Laves phases, however, it resulted in substantial grain growth [10], [69].

Mostafa *et al.* [69] studied the effect before and after HIP and homogenisation. The HT sequence consisted of homogenisation at 1100 ºC for 1 h, then HIP at 1160 C for 4 h under 100 MPa. Both heat treatments resulted in complete recrystallisation. The homogenisation treatment induced the precipitation of δ-phase at the grain boundaries, and HIP resulted in the formation of MC carbides. Aydinoz *et al*. [18] produced specimens that were HIPed and age treated. HIP caused a complete recrystallisation of the structure and subsequent ageing led to the evolution of γ'', and the formation of δ-phase at grain boundaries. Furthermore, the HIPed and aged specimens showed a decrease in strength, but higher ductility compared to AM specimens with the standard IN718 heat treatment. Tillmann et al. [48] studied the effect of HIP on porosity reduction, it was found that for IN718 processed with L-PBF the HIP temperature should not be higher than 1150 ºC, and above 100 MPa for a maximum of 4 hours. Relative density increased from 99.17 to 99.98 %, however, the AM as-built structure disappears, and grain size is larger.

Stress relief treatments have also been considered, however, the temperature required for this treatment is very high and can lead to microstructural changes, that may

compromise the material properties [39]. Deng et al. [10] studied the remaining residual stresses in AM IN718 after different heat treatments, using the Zener-Wert-Avrami function and parameters determined for laser shock-peened IN718. The remaining residual stresses (ratio between initial and post-treatment residual stresses) after different heat treatments were:

- Age treatment: 720 C/8 h and 620 C/8 h. Residual stress ratio - 0.985
- Solution treatment: 980 C/1 h. Residual stress ratio - 0.217
- Homogenisation: 1080 C/1 h. Residual stress ratio - 0

2.2.4 Fatigue characteristics of Ni-superalloys and cast and wrought IN718

For materials used in the energy and aerospace industry, a critical aspect of their performance is their resistance to fatigue crack initiation and propagation at elevated temperatures. Therefore, understanding these processes is of considerable interest to industry. This section will review the current fatigue related knowledge for cast and wrought IN718, which will be later compared to L-PBF IN718. Most of the work on cast and wrought material has focussed on long crack propagation studies at elevated temperatures. Crack growth behaviour will be affected by a combination of microstructure, temperature, oxidation and loading mode effects. The resultant fracture mode can be transgranular, intergranular or a mixture of both depending on the loading conditions. Furthermore, fatigue behaviour can be divided into two broad regimes:

- Cycle dependent behaviour, where crack growth is controlled by the loading cycle characteristics: stress intensity range, maximum stress intensity applied, and load ratio.
- Time dependent behaviour, where thermally activated processes influence crack propagation, resulting in time and temperature dependent crack growth.

Generally, low temperatures, high frequencies and inert atmospheres result in cycle dependent behaviour, whereas time dependent behaviour is favoured by low frequency, high temperature and aggressive environments.

2.2.4.1 Effect of microstructure

Microstructural features such as grain size, and the distribution of carbides or strengthening precipitates will have an influence on the crack propagation behaviour. Nickel superalloys can be processed with different grain sizes and precipitate distributions, and therefore some studies have been performed to assess their influence

on fatigue crack initiation and propagation by comparing coarse grained, and fine grained microstructures. Microstructural effects will be different if short or long fatigue crack growth is studied. Furthermore, the effect of microstructure will be different for cycle-dependent or time-dependent regimes.

Under cycle-dependent conditions, fine grained structures provide more resistance to crack initiation, and short crack growth [84]. The better short crack growth resistance can be attributed to the greater crack arrest and deflection at grain boundaries, since there are more of them. When considering long crack growth rates, however, coarser grained materials tend to perform better [85]. At low ΔK values, crack deviation induced by large grains can promote roughness-induced crack closure, improving the crack propagation resistance. Furthermore, large grains promote longer slip paths and enhanced slip reversibility, that can reduce fatigue damage accumulation. Under time-dependent conditions, larger grain sizes exhibit lower crack growth rates. This is because, materials with larger grains have less grain boundary area through which oxygen can diffuse, and therefore a higher resistance to oxidation assisted fatigue crack growth. Necklace microstructures, may force the crack to follow a more tortuous path, thus, improving the resistance to intergranular crack propagation.

Precipitate size can influence crack growth by affecting dislocation movement, which will lead to the activation of different slip behaviours. For instance, fine precipitates exhibit a heterogeneous slip behaviour that can decrease fatigue damage accumulation and improve the resistance to crack propagation under cycle dependent conditions [86]. Whereas, under time-dependent conditions coarse precipitates can reduce stress-assisted grain boundary oxidation by promoting more homogeneous slip, lowering the fatigue crack growth rate [87]. The presence of carbides along grain boundaries can also lead to changes in crack growth behaviour. The presence of discrete MC-type carbides at grain boundaries can prevent them from sliding and thus inhibit crack growth. On the other hand, continuous carbides at grain boundaries can reduce the binding force at grain boundaries, enhancing crack growth [86].

2.2.4.2 Effect of temperature

At elevated temperatures the fatigue crack growth rate increases due to a decrease in the material yield strength and enhanced dislocation mobility. Additionally, as temperature increases the diffusivity of aggressive species is higher, leading to degradation of grain boundaries and faster crack growth rates [88]. Time dependent behaviour, with thermally activated processes such as creep and stress relaxation, become more pronounced as temperature increases. Activation of creep can contribute

to lower crack growth resistance, and a transition from transgranular to intergranular fracture due to grain boundaries sliding, although this is not common for IN718 for normal operating temperatures. In contrast, elevated temperatures might activate stress relaxation and change the slip character (as discussed in relation to precipitate size) to more homogeneous slip, reducing local stress concentrations and reducing crack growth rate [86]. A comprehensive study of the effects of temperature on crack growth in IN718 is that of Weerasooriya [89]. Constant ΔK tests at R=0.1 were conducted at K_{max} of 40 MPa√m for frequencies ranging between 0.001-0.1 Hz. Results of these tests can be seen in Figure 2.19. For temperatures between room temperature and 650 ºC, the crack growth rates increase as temperature increases (the effects of frequency will be discussed in the following section). The rate of increase in the cycle dependent regime is limited, and the fracture mode is transgranular. At some transition temperature, dependent on frequency, the fracture mode will be mixed transgranular/intergranular. The temperature required for this transition to occur will be higher as frequency increases. Finally, at the highest temperatures, the behaviour of IN718 is purely intergranular, and characterised as time-dependent. The effects of temperature can also be observed when fatigue testing IN718 under vacuum. However, the increase in crack growth rate is lower when compared to air due to the lack of oxidation effects.

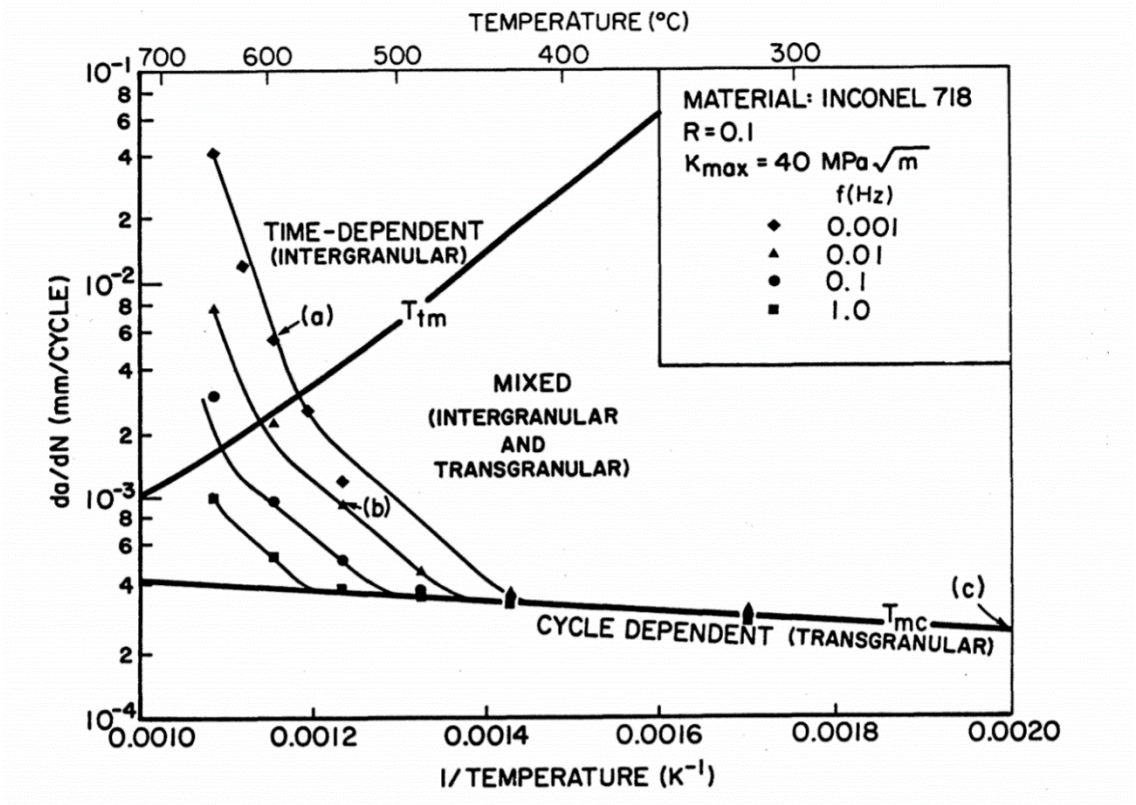

Figure 2.19 Crack growth rate as a function of temperature at Kmax of 40 MPa √a. Showing the change in micromechanisms of crack growth with changes in frequency and temperature [89].

2.2.4.3 Effect of cycle parameters

At high temperatures, where crack growth can be affected by oxidation, parameters such as: load ratio, frequency or loading waveform can influence the transition from cycle-dependent to time-dependent crack growth. The effect of these parameters on the transition and crack growth rate will be discussed below.

In terms of the effect of load ratio, it is reported that increasing the load ratio generally leads to an increase in crack growth rates [90], [91]. Higher load ratios lower the applied ΔK_{th}, and therefore crack closure effects are absent. Furthermore, it has been found that the load ratio effect is more pronounced for coarse grained structures [86]. Frequency effects on the fatigue performance of superalloys have been widely studied. This is because frequency plays an important role in determining whether fatigue occurs under cycle or time-dependent regimes. Furthermore, it is known that frequency has a significant effect on crack growth in air at high temperatures [90], [91]. Testing in alloy IN718 performed at 550 ºC by Clavel and Pineau [28], shows that for frequencies higher than 0.5 Hz, fatigue crack growth rates are mostly independent of testing frequency. However, for frequencies lower than 0.5 Hz, a decrease in frequency leads to an increase in fatigue crack growth rate. Floreen and Kane [92] reported similar variations in crack growth with respect to frequency at 650 ºC. At room temperature, and at a frequency of 10 Hz (under purely cyclic-dependent conditions), transgranular fracture modes can be observed with some accommodation of plastic strain ahead of the crack tip due to shearing of the γ'' precipitates [93]. For specimens at higher temperatures (550 ºC) but at frequencies higher than 0.5 Hz, propagation is still in a transgranular mode. Below 0.5Hz at 550 ºC, mixed transgranular/intergranular modes are observed, with the quantity of intergranular fracture increasing as the frequency is decreased. Furthermore, TEM studies performed show that slip became more heterogeneous as the frequency was lowered [28].

The shape of the loading waveform can also have an effect on crack growth rates. Generally, the addition of a dwell time at maximum load to a fatigue cycle will increase crack growth rate for IN718 [91]. Adding or increasing dwell time will significantly affect the introduction of time dependent processes such as oxidation. Under these time-dependent conditions, crack growth rate is inversely proportional to frequency, and thus sensitive to dwell times imposed at maximum load. There are some cases, however, where dwell time can retard crack growth. This can occur when dwell time occurs at other than the maximum load. In this case, significant creep can occur blunting the crack tip and reducing the crack growth rate [91].

2.2.4.4 Oxidation effects

The intergranular failure modes previously discussed in high temperature fatigue tests in air suggest that grain boundary oxidation is a major cause for accelerated fatigue crack growth rates for IN718. Some aspects of oxidation have been previously discussed in relation to frequency effects; this section will further discuss the effects of oxidation enhanced fatigue crack growth.

The underlying mechanism controlling the interaction between oxygen and the fatigue crack tip is still not fully understood, and it is still a reason for debate in the literature. There are two main theories: dynamic embrittlement, and stress assisted grain boundary oxidation (SAGBO) [26], [94]. The dynamic embrittlement process can be explained in three steps, and a schematic of the process is shown in Figure 2.20 [95]. First, oxygen will diffuse along the grain boundaries ahead of the crack tip over very short distances (nano-metre scale). This diffusion is promoted by the combination of both high temperatures and stress. The oxygen will embrittle the grain boundaries ahead of the crack tip reducing their cohesion strength. When stress is applied the grain boundaries will break leading to accelerated fatigue crack growth rates. For SAGBO, the diffusing oxygen reacts with an alloying element present at the grain boundaries (Nb in the case of IN718) forming a brittle oxide. This oxide cracks when stress is applied and is believed to be the reason for the intergranular failure and faster propagation rates. Studies have indicated that, for IN718, dynamic embrittlement is the main mechanism causing intergranular failure [29], [96]–[98]. The concept of a damaged zone ahead of the crack tip, caused by dynamic embrittlement, has also been proposed in the literature [25], [99]. The results show that an embrittled area forms ahead of the crack tip during dwell fatigue loading conditions, which has a lower resistance against crack propagation. The size of this damaged zone will increase with increasing temperature and dwell time.

The addition of hold times during the loading cycle can further increase the time available for grain boundary oxidation and thus increase crack growth rate. Numerous studies demonstrate that the addition of holding times at maximum and minimum load can increase the crack growth rate [85], [100], [101]. However, this effect might saturate for very long dwells. Pineau et al. [102] found that for hold times longer than 1000 seconds at minimum load, there was no additional increase in fatigue crack growth rate. This was attributed to the formation of a Cr_2O_3 oxide layer at the crack tip that prevented more oxygen from penetrating.

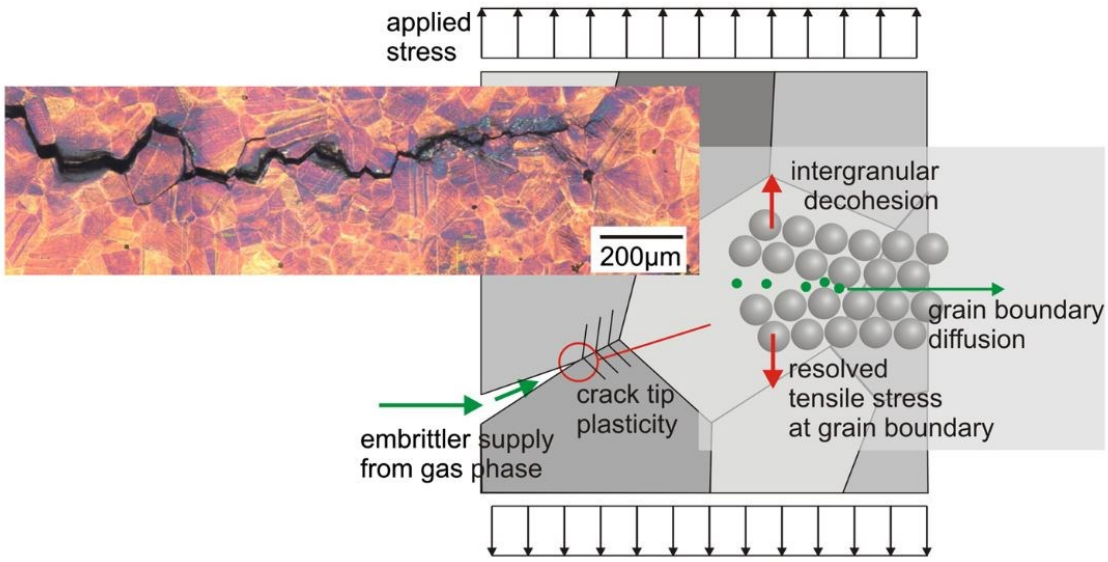

Figure 2.20 Schematic representation of dynamic embrittlement, representing the relationship between oxygen, microstructure, and applied stress [95].

The degree of oxidation ahead of the crack tip is usually dependent on the oxygen partial pressure, content of aggressive species and the applied load [27]. Work performed by Mollins *et al*. [103] showed that for IN718 there is a critical partial pressure (10^{-1} Pa) beyond which fatigue crack growth rate increases dramatically, due to oxidation assisted processes. Work performed by Andrieu *et al*. [100], further corroborates this idea; their study focussed on the effect of oxygen partial pressure on grain boundary oxidation and fracture mode. Spinel-type $Ni(Fe_2Cr)_2O_4$ oxides formed at high partial pressures, whereas Cr_2O_3 oxides formed at lower partial pressures (10^{-1} Pa). The change in oxide type led to a change in the fracture mode: intergranular for high partial pressures, and transgranular for lower pressures. This change in propagation mode is related to the ability of the formed oxide to limit further penetration of oxygen along grain boundaries. The spinel-type oxides are brittle and porous, whereas the Cr_2O_3 oxides can restrict oxygen penetration showing higher resistance to intergranular crack growth. So far oxidation has been related to detrimental effects on crack growth rates. However, the formation of a thick oxide layer in the crack path/tip can result in crack closure. Such oxide induced crack closure can improve the fatigue performance at low ΔK levels close to the threshold region. Higher thresholds linked to oxide-induced crack closure have been reported by Yuen *et al* [104], and Lynch *et al*. [79] for example.

Grain boundary character will also have a key influence on crack propagation by dynamic embrittlement. Oxygen diffusivity can vary depending on the type of grain boundary. There is some evidence in the literature that for special CSL (coincident site lattice) grain boundaries oxygen diffusion is slower [98], [105], [106]. Therefore, intergranular failure

will preferentially occur along random high angle grain boundaries, with materials containing a high number of CSL grain boundaries exhibiting improved resistance to cracking by dynamic embrittlement.

2.2.5 Fatigue characteristics of L-PBF materials

Fatigue knowledge of L-PBF IN718 is currently limited in the literature, with no special attention paid as yet to high temperature performance. These prior studies have been primarily focussed on S-N curve lifetime analysis where AM parts have commonly shown inferior fatigue endurance compared to cast and wrought components. As-built components exhibit reduced performance mainly related to the presence of process induced pores, lack of appropriate bonding between layers, and the high content of Laves phase in the microstructure [107]. Heat treated specimens sometimes show comparable lifetimes to cast and wrought IN718 due to the precipitation of the strengthening particles γ'' and γ' [12]. Furthermore, looking at the published L-PBF fatigue related literature, it is apparent that most of the work is focussed on improving the lifetime of L-PBF specimens, and thus to demonstrate that it can be comparable to wrought IN718. However, to improve the trustworthiness and performance of parts fabricated via AM, more focus is needed to understand the fatigue damage process, crack initiation and growth micro-mechanisms, and their specific relationship to the characteristic microstructures of AM specimens.

The wide range of processing variables found in L-PBF, and the effect they have on the microstructure and mechanical properties makes it difficult to predict and control the fatigue characteristics of the final product. Current studies have considered build orientation, surface quality, process induced defects and post heat treatment as the main parameters controlling the behaviour of L-PBF specimens [4], [108], [109]. In addition, other studies have considered the effect of varying process parameters, and temperature on the fatigue performance of IN718. The effect of these parameters will be discussed in more detail below. It should also be noted that due to the wide variety of L-PBF process parameters, feedstock material, post-manufacturing processes, specimen type, loading conditions, etc. it is difficult to make direct comparisons between different AM publications, and also appropriate comparator cast and wrought materials.

2.2.5.1 Effect of build orientation (room temperature)

Given the anisotropy of the microstructures, the direction of the applied stress with respect to the orientation of the deposited layers (build direction) can have an effect on

the lifetime of the components [110]. In this review, specimens where the build orientation is parallel to the loading direction will be considered as vertical, while specimens where the build direction is normal to the loading direction will be considered as horizontal, as shown in Figure 2.21.

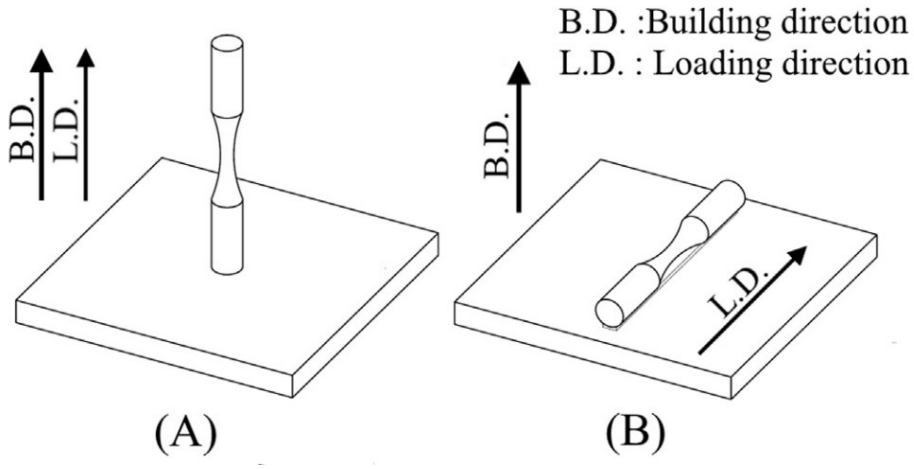

Figure 2.21 L-PBF fatigue specimens a) vertical test specimens, b) horizontal test specimens [110].

Multiple studies have shown that fatigue lifetime is generally longer for specimens manufactured in the horizontal direction [108], [110], [111]. Figure 2.22 shows an example from two publications on as-built microstructures where the fatigue life was lower for vertical specimens (other studies show comparable results). The difference in lifetime between the two publications in Figure 2.22, is due to some of the testing being done on notched samples [108]. Furthermore, regardless of their building direction, the majority of specimens in as-built condition showed inferior fatigue lifetimes compared to cast and wrought components.

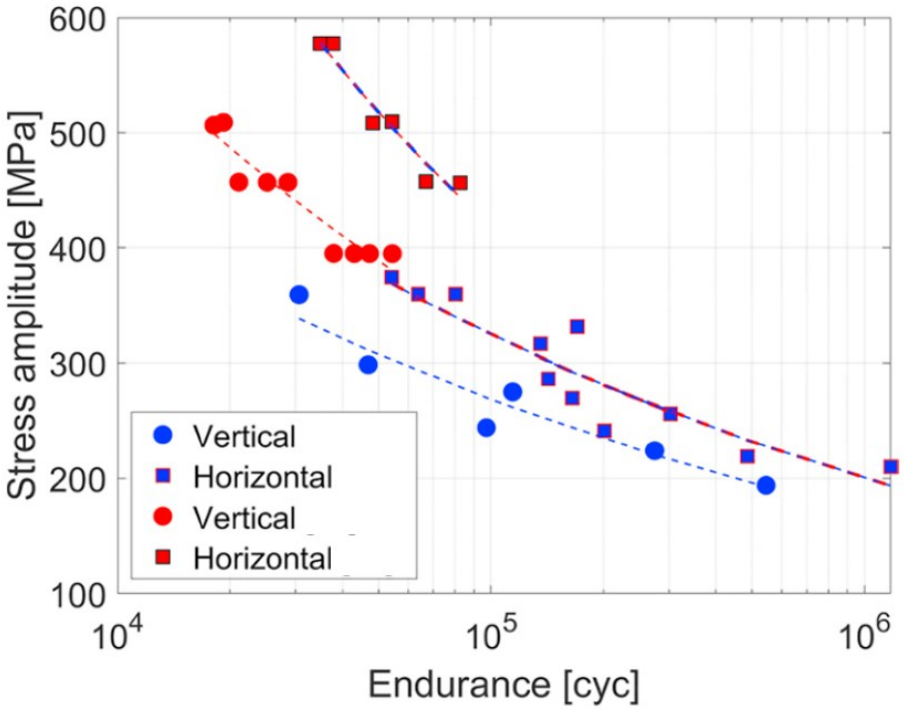

Figure 2.22 Fatigue life of L-PBF IN718 specimens with respect to build orientation [108], [111].

As-built specimens have an anisotropic microstructure due to the uneven thermal history and directional heat transfer that takes place during the L-PBF manufacturing process. This means that microstructural features, such as grain size, grain morphology and crystallographic orientation will be different for the horizontal and vertical specimens. Furthermore, build orientation will affect the heating and cooling cycles during the L-PBF process. Horizontally manufactured specimens usually have longer inter-layer time intervals, due to their larger footprint on the baseplate (it will also depend on the sample aspect ratio, see Figure 2.22 for reference), which in turn results in higher cooling rates [110]. The difference in thermal gradient leads to different as-built microstructures, which are usually finer for horizontally built specimens [5]. The finer microstructure can improve the resistance to crack initiation, and thus, improve the overall fatigue lifetime. Although the finer grain size, and anisotropy of the microstructure can have an influence on the fatigue lifetime, it has been reported that the biggest contributing factor to the difference in performance is the difference in distribution and orientation of process induced defects with respect to the loading direction [4], [110]. LOF defects tend to be large voids with high aspect ratios, and usually form between layers due to insufficient fusion. The orientation of these weak interlayer points with respect to the loading direction is regarded as the main source for the structural anisotropy. A schematic of the arrangement of these weak links between layers in the macrostructure with respect to the loading direction is shown in Figure 2.23. In vertical specimens, LOF defects are

normal to the loading direction. This arrangement creates a higher stress concentration around the void when compared to horizontal specimens and thus easier means for void growth and crack initiation [110].

The effect of grain boundary orientation on fatigue crack growth has not been as studied in the literature, with studies mostly limited to stainless steel 316L. It is reported that specimens where crack growth is parallel to the build direction (horizontal) have a lower threshold value, and also show slightly lower resistance to crack growth [112]. The presence of process induced defects doesn't play a major role in this case, and the differences are mostly attributed to easier propagation paths due to grain boundary alignment with the crack growth path. A schematic of the interaction between the microstructure and crack growth depending on build orientation, is shown in Figure 2.24, along with da/dN vs ΔK plot representing the difference in fatigue crack growth rate for two different build orientations. It can be seen how the microstructure in the vertical specimens offer a more tortuous path for cracks to propagate, hence, reducing the fatigue crack growth rate [112]. This effect, however, is somewhat limited at room temperature since propagation is mostly transgranular. At higher temperatures, and low frequencies where intergranular propagation is dominant build orientation could have a bigger influence on crack growth rate, and therefore needs to be further investigated.

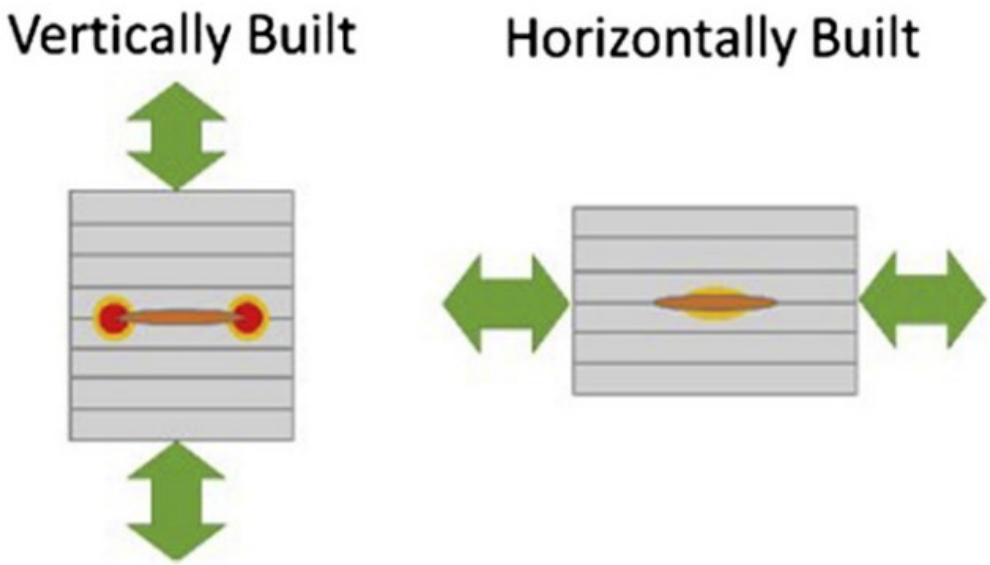

Figure 2.23 Schematic showing the orientation of lack of fusion defects for vertical and horizontal samples with respect to loading direction, and the resultant stress concentration [4].

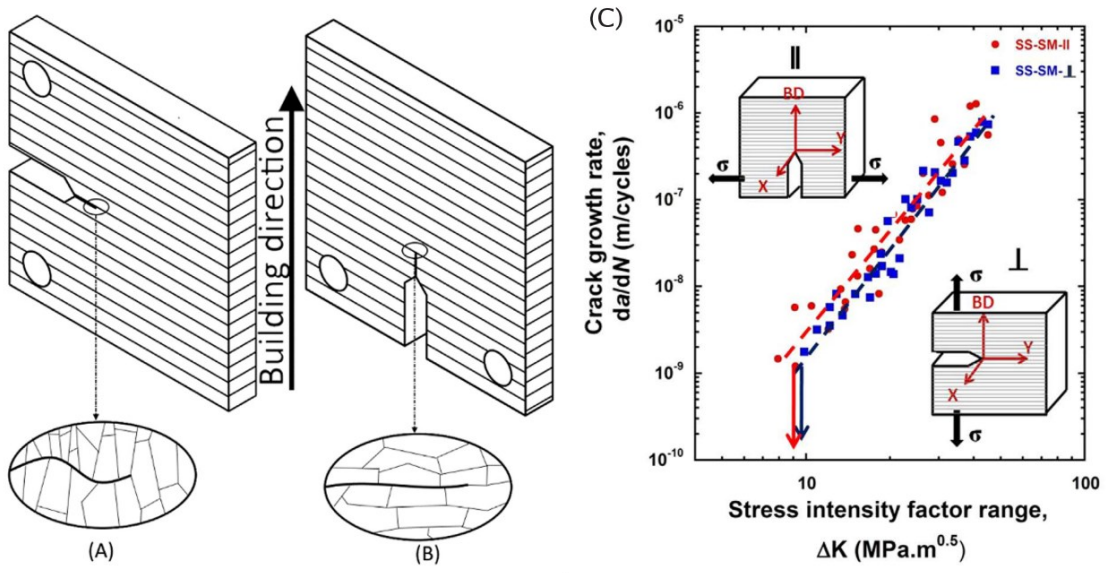

Figure 2.24 Interaction between the microstructure and crack growth for a) vertical and b) horizontal specimen [110]*, c) fatigue crack growth rate (da/dN) vs k for 316L stainless steel with respect to build orientation as shown in the inset images* [112].

2.2.5.2 Effect of heat treatment (room temperature)

Some studies have considered the use of post manufacture heat treatments to reduce the effect of build orientation, and to improve the fatigue lifetime by dissolving Laves-phase and precipitating IN718 common strengthening precipitates (delta-phase, γ', and γ'') [12]. It is expected that stress relief, solution annealing and ageing treatments will remove some of the microstructural directionality, and thus reduce differences in grain size and morphology between horizontal and vertical samples. However, although proper heat treatment may be able to alleviate microstructural heterogeneity, it might not be able to remove the effect of build orientation on fatigue performance due to the presence of defects in the specimens [4]. Hence, some studies have considered adding a HIP process to reduce the void content and directionality (e.g., reduce aspect ratio in shape of LOF defect), and therefore reduce the difference in fatigue lifetime between build orientations [12]. On the other hand, if appropriate process parameters are selected to avoid the formation of LOF defects, the need for a HIP stage might be avoided. Figure 2.25 shows testing performed by NASA on vertical and horizontal specimens with the same void content that had been stress relieved, HIPed, solution treated, and age treated (see Figure 2.25 caption for specific temperatures) [113]. It can be seen how there is no apparent effect of build orientation on the fatigue lifetimes, and that the L-PBF results are comparable to standard cast and wrought IN718. This increase in the fatigue lifetime compared to as-built specimens is mainly related to the dissolution of Laves-phase and

the precipitation of γ' and γ''. The difference in response at mid stress levels can be attributed to the larger grain size found in the L-PBF specimens, and the lower quantity of γ' and γ'' compared to the cast and wrought samples caused by the precipitation of δ-phase during the stress relief and HIP process [113].

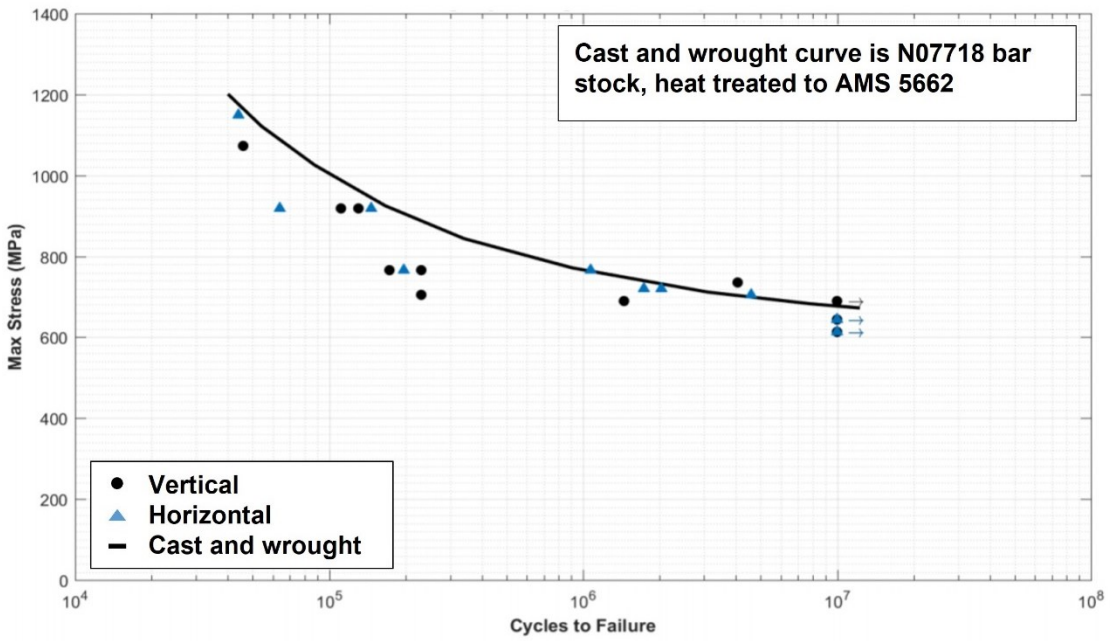

Figure 2.25 S-N curve of heat treated L-PBF IN718 built in two orientations vs standard cast and wrought IN718. Heat treatment for L-PBF specimens involved: stress relief (1065 C for 1.5 hours; furnace cool), HIP (1165 C, 100 MPa, 3-4 hours), Solution treat (1066 C for 1 hour; air cool), age treat (760 C for 10 hours; furnace cool to 650 C; hold for 20 hours at 650 C; air cool) [113].

The effect of post heat treatments is assessed in most reports by comparing the performance of as-built specimens with samples that have been heat treated using the standard IN718 heat treatment plus a HIPing stage (to reduce void content). However, less attention is being paid to developing specific heat treatments for L-PBF IN718 to optimise its fatigue properties, and either match or improve the fatigue performance of cast and wrought components. Some studies have considered multiple heat treatments, and compared the results, however, more work is needed to fully understand the micromechanisms of fatigue within heat treated specimens. Wan *et al*. [109], performed high cycle fatigue (HCF) tests on three different heat treatments, and compared the results with as-built L-PBF IN718. Figure 2.26 shows their results along with the specific heat treatments employed. It shows how the fatigue response of L-PBF IN718 can be enhanced after heat treatment. According to the authors, void content did not change, hence the differences in fatigue response may be attributed to the absence of brittle Laves phases in the heat treated samples and the precipitation of γ''. Additionally, the improved response of HA treated samples was related to smaller δ-phase compared to the other treatments, which induced a higher void damage tolerance at the same applied

stress. Aydinoz *et al*. [18] studied the effect of five different heat treatments (see Figure 2.27 for specific temperatures) on the cyclic stress behaviour of L-PBF IN718 at constant strain. They found that the performance after solution annealing was marginally better compared to the HIPed material. The closure or reduction in size of pores did not play a major role in the fatigue performance, and the difference was attributed to the microstructural changes that occurred during the HIP process. They argued that a complete recrystallisation of the sub-micron cell structures found in the as-built material during HIP was responsible for the inferior fatigue lifetime at room temperature. During solution annealing, these structures are maintained, and after ageing, precipitates form around them. These structures can then efficiently obstruct dislocation motion providing better performance than HIPed specimens.

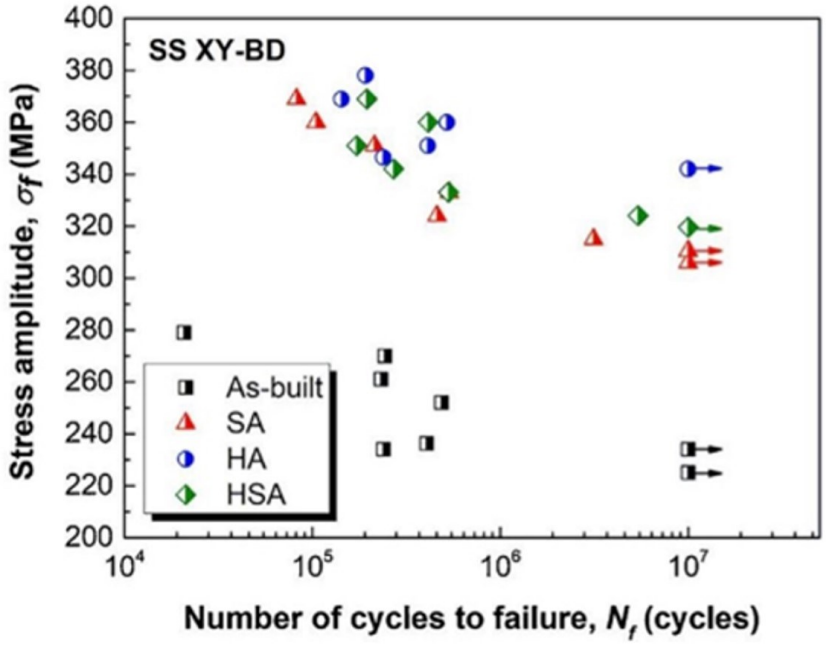

	Homogenization	Solution	Aging
	1065 °C, 1 h/AC	980 °C, 1 h/AC	760 °C, 10 h/FC at 55 °C h^{-1} to 650 °C, 8 h/AC
As-built	No	No	No
SA	No	Yes	Yes
HA	Yes	No	Yes
HSA	Yes	Yes	Yes

Figure 2.26 top) S-N curve of L-PBF fabricated IN718 and bottom) parameters used for the heat treatment [109].

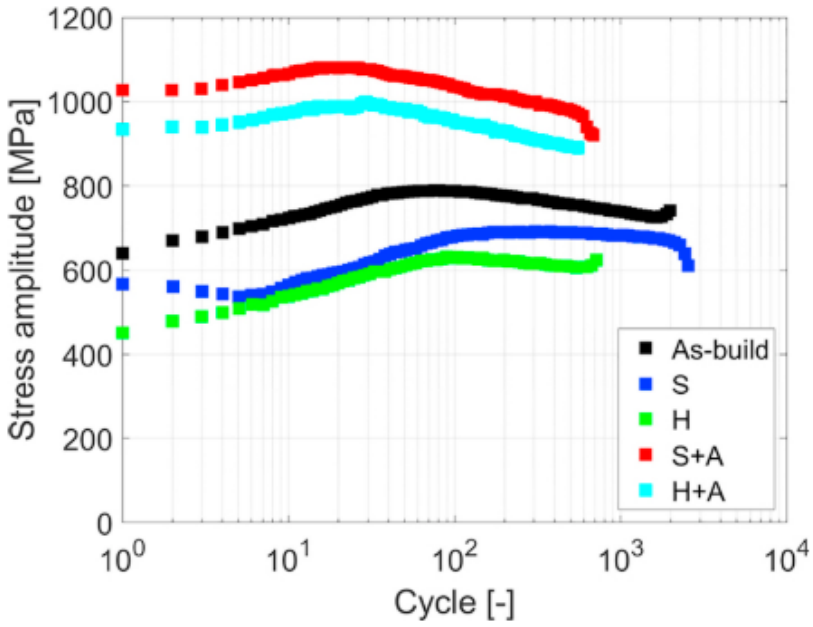

Figure 2.27 Cyclic stress response at room temperature and strain amplitude 0.5% for L-PBF IN718 under five different heat treatments. S: solution annealing (1000 C for 1 hour; air cooling), H:HIP (1150 C, 1000 bar, 4 hours; furnace cool), A:aged (720 C for 8 hours; furnace cool 50 C/hour to 621 C; hold at 621 C for 8 hours; air cool [18].

2.2.5.3 Effect of process induced defects

The surface roughness of AM parts in the as-built state is considerably higher than traditionally manufactured metallic parts [5]. This is mostly due to the presence of partially melted powder on the boundary of the parts, and the staircase effect on the surface resultant from building the parts layer-upon layer [114]. Surface roughness acts as a stress raiser and has a negative effect on the fatigue lifetime of the materials by accelerating crack initiation. Kelley *et al*. [111] reported a decrease in lifetime of 30-40 % for parts in the as-built condition (R_a = 6-16 µm) compared to cast and wrought (R_a = 1 µm). Similar results were provided by Balachandramurthi *et al*. [115], and Witkin *et al*. [116] for heat treated specimens. They found, however, a larger scatter in the data for machined specimens, related to the presence or absence of surface voids. Therefore, post processing surface treatments (grinding, electropolishing, surface milling, etc.) are usually applied to reduce the surface roughness of the fabricated parts and improve their fatigue lifetimes. It should, however, be noted that one of the advantages of AM is the ability to produce near-net shape complex parts reducing the need for any machining, and with complex internal features that might make surface roughness reductions impossible [114]. Hence, the impact of the as-built surface roughness on fatigue performance, and surface roughness control via changes in the process parameters (i.e., contour scanning, or re-scanning), should be studied more deeply for AM design purposes.

Yang *et al*. [117] studied multiple crack initiation sites caused by pores and their location with respect to the surface for as-built IN718 in HCF tests. Surface intersecting pores caused the largest reduction in fatigue lifetime, as shown in Figure 2.28. Internal pores (not intersecting with surface, see Figure 2.28 for schematic) with comparable or larger size to surface pores caused the initiation of primary cracks in some cases, however, the lifetime for those components was higher. The porosity distribution in the materials surface will therefore be a key parameter controlling fatigue lifetime. Interestingly, however, studies have focussed on quantifying the reduction in lifetime related to the presence of pores but almost no attention has been paid to the relationship between short crack growth and porosity distribution. There is well developed literature focussing on the relationship between crack initiation, short crack growth and porosity distribution for other processing routes (e.g., castings, welds). It is of interest to compare between processing techniques and understand if AM porosity effects are any different.

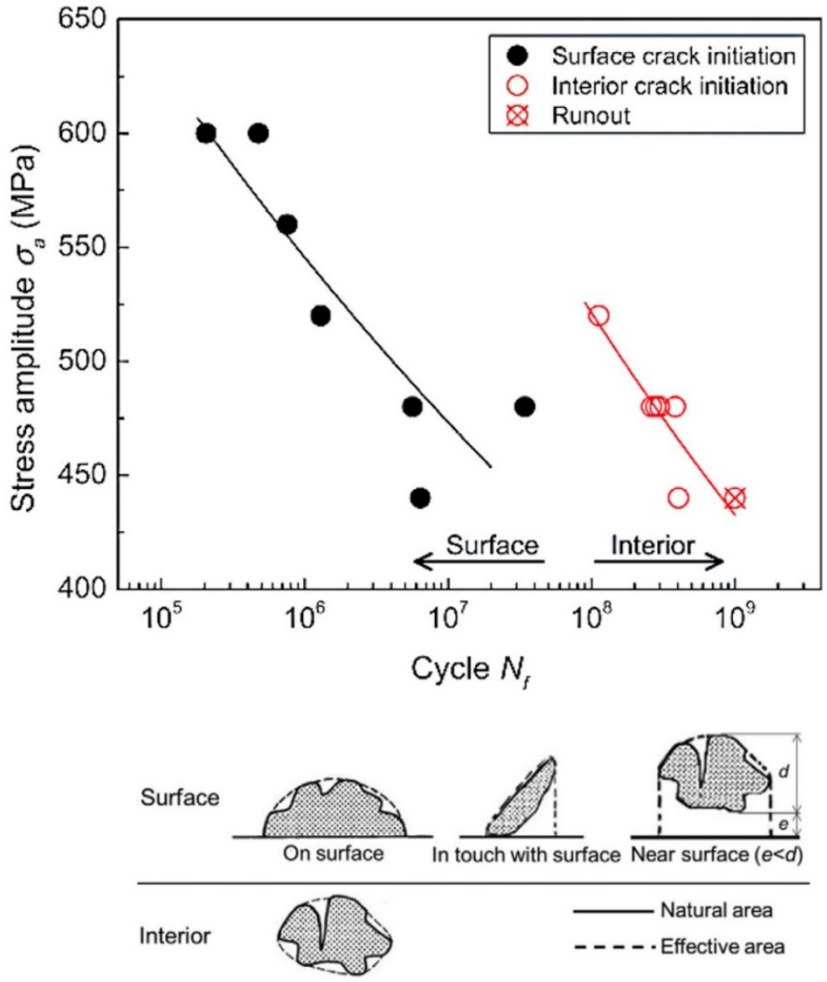

Figure 2.28 top) S-N data for as-built L-PBF IN718 at R=-1, room temperature, 20 kHz, and surface polished to 0.5 µm, bottom) summary of pores characterised for surface and interior crack initiation [117].

Watring *et al*. [118], and Kantzos *et al*. [119] have studied the effect of process parameter modifications for as-built and heat treated components respectively. In both cases they reported similar findings, where a combination of parameters would give the best performance, and outside this optimal range fatigue lifetime would considerable decrease due to the presence of process induced defects. Figure 2.29 shows HCF tests results performed by Watring *et al*. [118] using specimens manufactured with different process parameters by varying laser power, scan speed, and built orientation. The results show that two mechanisms governed the HCF response of L-PBF IN718. These are: (i) relationship between build orientation and surface roughness, and (ii) increase of defects due to sub-optimal laser-energy input. Horizontal specimens (0º build orientation) had the highest surface roughness compared to the other build directions, and therefore had the worst fatigue life. The difference between vertical and angled specimens (60º build direction) was also attributed to the difference in surface roughness. Tests were performed in dog bone specimens, and to manufacture the horizontal specimens support structures were needed. The addition of support structures increased the roughness substantially, and thus, decreased the fatigue lifetime. Therefore, support structures should be avoided were possible, as the associated increase in surface roughness can have a negative impact on fatigue performance. Furthermore, the effect of build orientation contradicts previous studies that reported better fatigue performance for machined/polished horizontal (0-degree) specimens. The contradiction may be explained by a dominant effect of surface roughness over build direction. The lifetimes as a function of energy density followed a bell shape within build orientation, with an optimal energy density of 60-70 J/mm^3. Outside this window, lifetimes were lower due to the presence of LOF defects at lower energy densities, or keyhole pores at higher energies. The presence of these pores and their negative impact on fatigue can be seen in the fracture surfaces presented in Figure 2.29. Furthermore, variations in the scanning strategy have been shown to impact the microstructure of L-PBF IN718, as explained in section 2.2.3.1. The effect of scanning strategy on microstructure and fatigue performance was studied by Wan *et al*. [120], by performing HCF tests on machined vertical samples with two different scan strategies in the as-built condition. They used bidirectional scanning, with and without a 90º rotation between layers. They found that not rotating the scan strategy between layers produced a finer microstructure (up to 2.3 times smaller), and led to a small increase of 9 % on fatigue lifetime. Although further tests would be necessary to assess the reproducibility of the results.

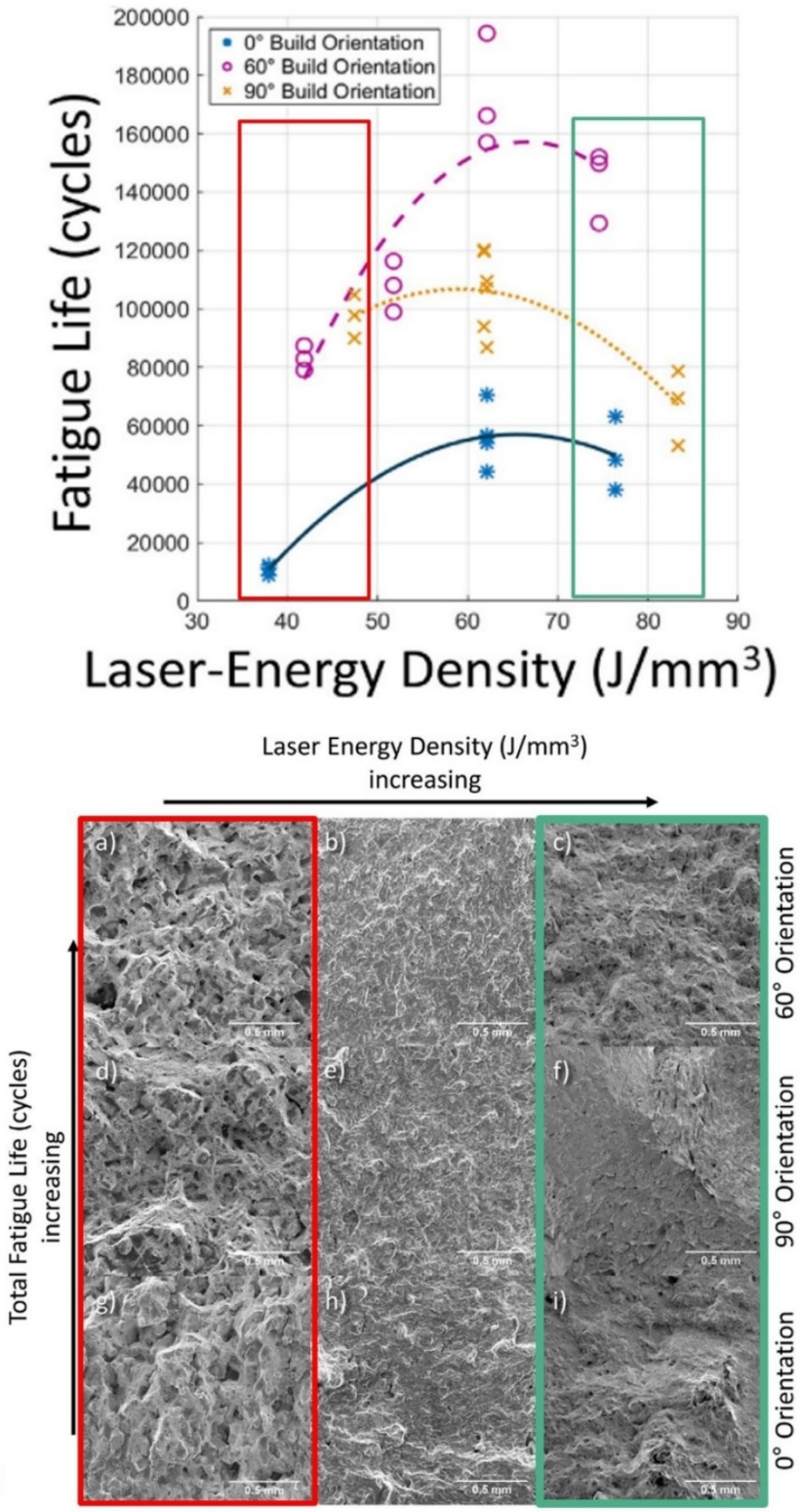

Figure 2.29 Fatigue tests on as-built IN718 components with no surface or heat treatments top) HCF life vs volumetric energy density for specimens built under different build orientations. Bottom) SEM images of fracture surfaces a, d, and g) 45 J/mm³; b, d, and h) 62 J/mm³ and c, f, and i) 77 J/mm³ [118].

2.2.5.4 High temperature fatigue

Most of the fatigue related work has focussed on room temperature performance, instead of high temperature, which is surprising given the likely served conditions for nickel-based superalloys. A limited number of studies have investigated the fatigue properties of AM IN718 at elevated temperatures. These studies have mostly focussed on lifetime analysis, and the main factors they have concentrated on are, effect of texture, build orientation, and heat treatment.

Gribbin *et al*. [121] have investigated high temperature (500 ºC) HCF behaviour of direct metal laser melted (DMLM), and cast and wrought IN718, at a test frequency of 50 Hz (Figure 2.30). Two types of heat treatments were considered (standard AMS5663, and standard AMS5663 + HIP at 1163 ºC for 4 hours at 100 MPa), and the specimens were built horizontally, and diagonally (45º with respect to build orientation). There were small differences in lifetime between orientations, however, differences between heat treatments had bigger effect. HIPed specimens had the lowest lifetime, which was related to a coarser grain structure promoted by the higher temperatures during the HIP treatment. Similar results for the influence of build orientation on fatigue lifetime at temperature by Ma *et al*. [122] for short crack tests at 650 ºC under vacuum. However, in both cases the temperature/frequency combination chosen did not promote intergranular failure modes. Hence, the effect of grain boundary orientation with respect to the direction of crack propagation is expected to be reduced.

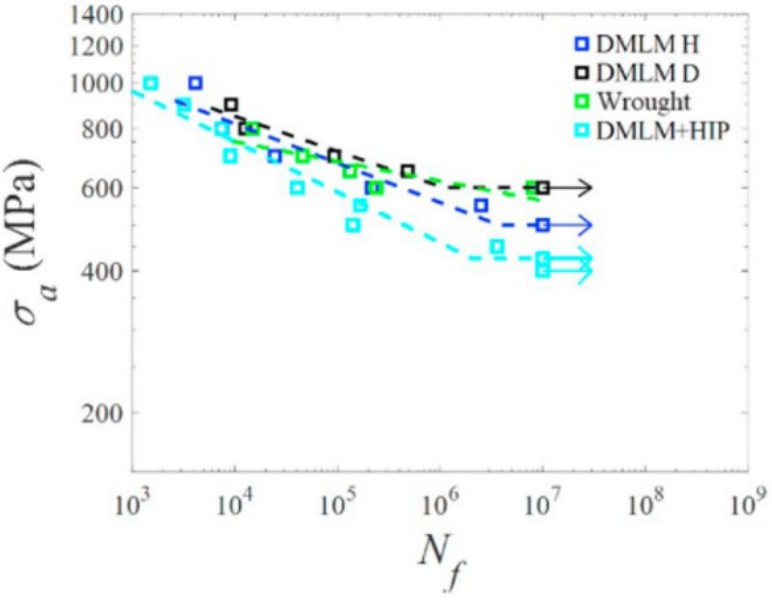

Figure 2.30 HCF data (testing at 50 Hz, and 500 ºC) for AM IN718. Samples heat treated as per AMS5663 (standard IN718 treatment: solution anneal + ageing). For DMLM + HIP, HIP stage (1163 C for 4 h, 100 MPa) added before AMS5663 treatment. DMLM H - Horizontal sample, DMLM D - Diagonal sample built at a 45º angle with respect to the build direction [121].

Kim *et al.* compared fatigue crack propagation rates between heat treated L-PBF and cast and wrought IN718 (see results in Figure 2.31) [123]. Testing was performed at room temperature, 650 ºC, and 10 Hz (cycle-dependent conditions) on heat treated (AMS5662) specimens built in the vertical direction (crack growth occurred perpendicular to build direction). Crack propagation rates increased as temperature increased for L-PBF specimens, as expected. At 650 ºC and high ΔK values fatigue crack growth rates were comparable for both L-PBF and CW specimens. However, at low/mid ΔK regions L-PBF specimens exhibited much higher crack propagation rates. Laves phase were not fully dissolved by the heat treatment, which promoted the difference between L-PBF and CW specimens at high temperatures.

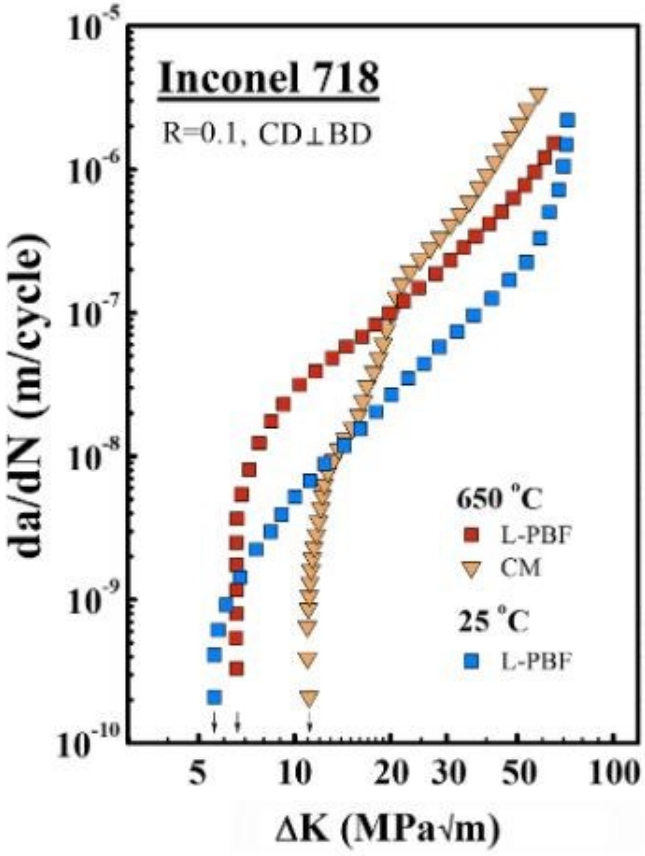

Figure 2.31 da/dN vs ΔK for L-PBF and CW IN718 at R=0.1, 10 Hz, and temperature 650 C, and 25 C [123].

A relatively detailed study on high temperature crack propagation of AM IN718 was recently published by Deng *et al.* [124] (see Figure 2.32). They studied dwell-fatigue crack propagation on heat treated samples (see Figure 2.32 for specific parameters) at 550 ºC, and a triangular loading waveform with 2160 seconds dwell at peak load with 10

seconds unloading-reloading segments. Intergranular failure modes were dominant and large differences in crack propagation rates between sample orientations were reported. The columnar grains characteristic of as-built components was not removed by the heat treatment, resulting in large crack deflection and lower effective stress intensity for vertical samples (n-type). Interestingly, differences in damage mechanisms were reported between L-PBF and traditional cast and wrought specimens, with creep being the main damage mechanism at 550 ºC with the nucleation and growth of cavities along grain boundaries, as opposed to dynamic embrittlement for cast and wrought. This was related to the dislocation sub-structure typically found in AM as-built specimens. The dislocation structure was not fully removed during either heat treatment (SA and HSA, see Figure 2.32 for reference), and was found to be similar to that found in the tertiary creep regime for IN718, promoting creep damage even at 550 ºC.

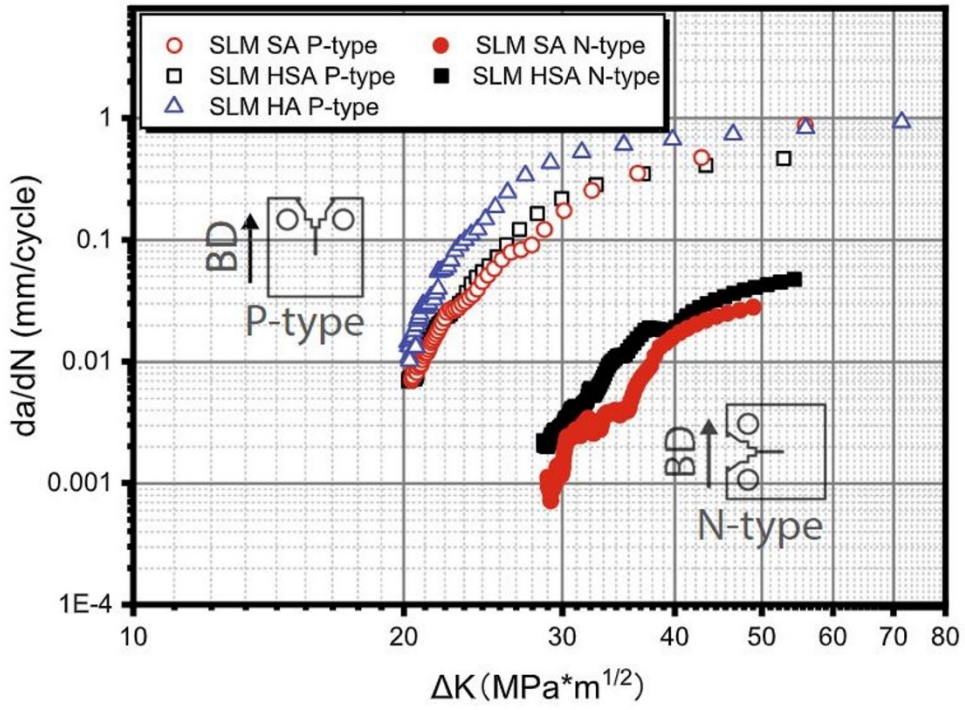

	Homogenization	Solution	Aging
SA	None	1253 K (980 °C)/1 h/WC	993 K (720 °C)/8 h
HA	1353 K (1080 °C)/1 h/WC	None	50 K/h FC to 893 K (620 °C)
HSA	1353 K (1080 °C)/1 h/WC	1253 K (980 °C)/1 h/WC	893 K (620 °C)/8 h/AC

FC, AC and WC denotes furnace cooling, air cooling and water cooling, respectively. SA is the standard heat treatment for wrought IN718 (AMS 5662). HSA is the standard heat treatment for cast IN718 (AMS 5383).

Figure 2.32 Crack propagation rates da/dN vs ΔK for L-PBF IN718 manufactured in two orientations, and subject to different heat treatments. Details on the specific heat treatments are provided in the table

2.3 Summary of literature review

- L-PBF offers a cost effective alternative to manufacture IN718 parts, however, there are still a variety of metallurgical factors specific to AM (anisotropy, porosity, phase distribution, heat treatment etc) that need to be further understood. During the manufacturing process, there are a large number of parameters that will affect the final component such as laser power, scanning speed, hatch spacing, scanning strategy, and layer thickness. The selection of these parameters will have a large influence on the thermal history of the material and will therefore control the final microstructure. Furthermore, if any of the parameters are improperly chosen, it will result in the formation of defects in the material compromising its mechanical properties. Although a significant effort has been done to understand their effects, there is a lack of research relating process parameters to defect formation and microstructure formations. Hence, further work needs to be performed to be able to systematically reveal the influence of these parameters on the final material.

- The microstructure of as-built AM IN718 is significantly different to that found in cast and wrought materials. It consists of a columnar and dendritic grain structure, generally oriented parallel to the build direction, which results in anisotropic properties. Furthermore, the fast cooling rates result in the formation of Laves phases, not commonly found in cast and wrought IN718. Multiple heat treatments have been studied to improve the mechanical properties of AM parts. However, these have been limited to slight variations of conventional heat treatments for IN718, which has ultimately resulted in only slight improvements, since the microstructure of AM parts is significantly different from cast and wrought components. Therefore, further refinement of these heat treatments is needed in order to optimise the mechanical properties of AM.

- Long crack growth behaviour of cast and wrought IN718 has been extensively studied in the literature. Complex interactions between microstructure, cycle parameters and environmental effects have been reported. Furthermore, considerable attention has been given to the interaction between cycle parameters (i.e frequency), temperature and environmental effects on FCG rates.

- There are few publications studying the fatigue properties of L-PBF IN718, especially for crack propagation, and elevated temperatures. Thus, the fatigue

behaviour of L-PBF specimens needs to be further studied to improve/optimise future AM structures. Current investigations show the importance and effect of build orientation, surface roughness, heat treatment and process parameters on the fatigue lifetime of L-PBF specimens. There are as yet many unknowns on the micromechanisms of fatigue crack initiation and growth that require further research. According to the reviewed studies, build orientation has a measurable impact on fatigue lifetime. Horizontally built specimens have shown better performance, mainly related to the orientation and location of large LOF defects with respect to the loading direction, and deposited layers. For crack propagation, however, the distribution of grains in horizontal specimens allows for an easier path for crack growth, and thus they show higher FCG rates. Effects of heat treatment on the microstructure have been shown to improve the fatigue lifetime of L-PBF specimens to comparable levels with cast and wrought samples. Decreasing the surface roughness through machining has significantly improved fatigue lifetimes for as-built IN718. However, AM parts have very complex geometries where surface roughness reductions might be impossible. Hence, the impact of the as-built surface roughness on fatigue performance, and surface roughness control via changes in the process parameters (i.e. contour scanning), should be studied more deeply for AM design purposes. Finally, very few studies have looked at high temperature fatigue performance, mostly focussing on lifetime analysis. Therefore, further work is required to understand the effect of cycle parameters and time-dependent mechanisms on crack propagation at high temperatures to improve L-PBF IN718 components for high temperature applications.

3 Materials and Methodology

3.1 Material

The material used for this study is IN718. Two material conditions will be discussed: L-PBF and cast and wrought. L-PBF specimens were manufactured in two different orientations, which will be referred to as horizontal and vertical (see Figure 3.1 for reference). The different orientations will be used to determine the effect of grain orientation and anisotropy in the fatigue performance of the material. Although only heat treated L-PBF specimens have been fatigue tested, the microstructure of both as-built, and heat treated specimens will be discussed. All heat treated L-PBF samples have undergone multiple thermal processing stages (stress relief + hot isostatic pressing + solution treatment + precipitation treatment). The AM specific steps are stress relief and HIP, whereas the solution and ageing treatments are comparable to cast and wrought IN718 and aim to precipitate IN718 common strengthening precipitates (γ', γ'' and δ-phase). Stress relief is performed before separating the samples from the baseplate, followed by HIP to reduce porosity and induce recrystallisation to mitigate anisotropic properties. The specific details of the printing process parameters, and heat treatment are commercially proprietary. Furthermore, all specimens were printed as larger rectangular blocks, from which smaller microscopy and fatigue test specimens were cut.

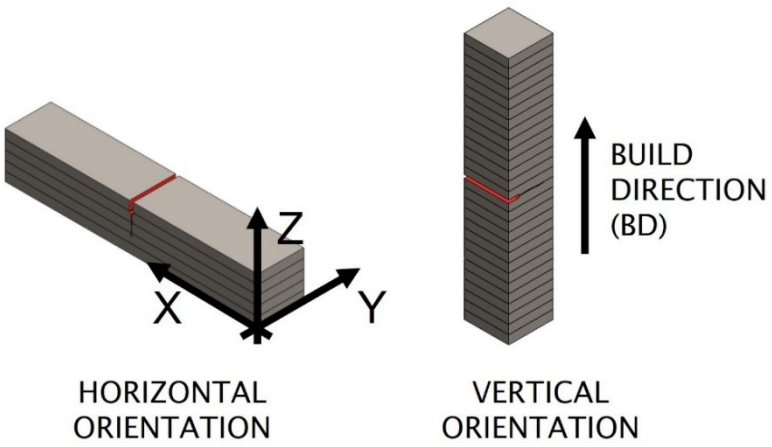

Figure 3.1 Building strategy for horizontal and vertical samples. Printing layers, and position of the notch (red) are presented for reference.

Cast and wrought IN718 was also analysed to compare the microstructure of L-PBF specimens to conventional IN718. The material was provided as a bar that had been cast and then rolled compliant with AMS5662 [125]. When manufacturing, the material was solution treated at 965 ºC for 1 hour followed by air cool. It was then aged at 720 ºC for 8 hours, furnace cooled at 50 ºC/h to 620 ºC, then aged at 620 ºC for a further 8 hours, finishing with air cooling.

3.2 Microstructural Characterisation

Metallographic samples for optical and SEM microscopy were prepared using standard techniques. Rectangular samples were cut from the various samples (in y-z, and x-y planes for AM materials, see Figure 3.1 for reference) using a Mechatome T210 linear precision saw, with an abrasive wheel. Specimens were then mounted in conducting phenolic resin (bakelite) for microscopy examination. The polishing route employed can be found in Table 3-1. In addition, specimens were thoroughly cleaned with distilled water and ethanol between each step.

Table 3-1 Polihing route for IN718 sections.

Paper / Cloth	Abrasive size	Wheel speed (rpm)	Time (min.)
SiC	120 grit	350	Until planar
SiC	800 grit	350	4
SiC	1200 grit	350	4
Struers DP-Mol	6 μm	150	4-6
Struers DP-Nap	1 μm	150	4-6

Etching was performed using Kalling's reagent 2 (100 ml Ethanol + 100 ml Hydrochloric acid + 5g Copper (II) Chloride). Following preparation, specimens were examined under an Olympus BH-2 optical microscope, a JSM 6500F field emission gun (FEG) scanning electron microscope (SEM), and a JSM 7200 FEG-SEM, using accelerating voltages of 10-15 kV at a working distance of 10 mm. The SEM was operated in secondary electron imaging (SEI), and backscatter electron imaging (BEI) modes. Element analysis was performed using an energy dispersive X-ray spectrometer (EDX) detector attached to the SEM.

TEM imaging was used to characterise the precipitation of both γ' and γ'' precipitates. Thin foils were prepared by mechanically thinning down discs to a thickness of ≈100 μm from which discs with a diameter of 3 mm were extracted. These discs were then electropolished using a dual jet electropolishing system Struers Tenupol 3, in a solution

of 10% perchloric acid and 90% ethanol at -25 ºC. Images were then recorded using a Jeol JEM3010 TEM operated in bright field mode.

Electron Backscatter Diffraction (EBSD) was used to investigate microstructural features in more detail. A final polishing stage using alumina suspension (OPA, 0.3 μm), and colloidal silica suspension (OPUS, 0.04 μm) was carried out for EBSD analysis. All EBSD data was processed in Matlab using the MTex Toolbox, and average grain size, grain size distribution, grain aspect ratio, and CSL boundaries were extracted from the EBSD maps. Furthermore, to determine microstructural effects on crack propagation. EBSD characterisation was conducted on fatigue samples that had been sectioned (more detail on the sectioning procedure will be given in section 3.4.1). Kernel average misorientation (KAM) maps were extracted from the tested samples to qualitatively analyse the extent of plastic deformation around the crack tip/path. KAM is a method that measure local grain misorientation between a point, and its neighbours and for this study, KAM was calculated considering only first order neighbouring points.

3.3 Characterisation of porosity

To measure the density and characterise the defect distribution of L-PBF specimens two methods were used. The Archimedes method (used to obtain information on overall porosity) and analysis of optical micrographs from cross sections (for local porosity information).

3.3.1 Archimedes method

For the Archimedes method a Mettler AE 240 balance was used with a measuring accuracy of ± 0.1 mg. In order to obtain the density, the specimen's mass was measured in lab air and submerged in a fluid, according to ASTM B962-17 [126]. The calculation of the part density, ρ follows:

$$\rho_p = (\rho_{fl} - \rho_{air})\frac{m_a}{m_a - m_{fl}} + \rho_{air} \quad (3\text{-}1)$$

Where ρ_{fl} is the fluid density, ρ_{air} is the air density, m_a is the mass of the part, and m_{fl} is the mass of the fluid. Each sample was measured independently five times for two days, allowing for the samples to fully dry between measurements. The measurements were conducted in acetone, and the temperature dependence of its density was taken into consideration. Once the samples were introduced in the fluid, a settling time of 30 seconds was allowed before taking any measurements. Furthermore, to consider

evaporation of the liquid during testing, the evaporation rates of acetone were calculated and the total mass lost due to evaporation over 30 seconds was added to the mass of the specimen in the fluid.

3.3.2 Microscopy

Each L-PBF specimen was cut in two perpendicular sections (y-z, and x-y planes) to prepare samples for local porosity assessment (the analysed samples were at least 9 x 9 mm). The specimens were then prepared for microscopy using the method explained in section 3.1. These were then observed under an Olympus BH-2 optical microscope without etching. For each cross section, the full area was imaged under x10, and x20 magnification. The process was repeated at different heights in the part with a distance of at least 0.5 mm between images. Overall, four sections of the entire surface area were taken per sample and orientation.

All micrographs were analysed using the Image Processing and Analysis in Java (ImageJ) software. To evaluate void content, size, and morphology the images were segmented using the thresholding technique to discriminate between solid material and pores. The critical threshold was determined as the point at which isolated bright pixels increased abruptly. Furthermore, to characterise the shape of pores their circularity was calculated This was defined as:

$$Circularity = \frac{4\pi A}{P^2} \qquad 3\text{-}2$$

Where A and P are the area and perimeter of the pore, respectively.

3.4 Fatigue crack propagation testing

Single edge notch bend (SENB) specimens with dimensions 55 x 10 x 10 mm were tested in a three point bend test configuration with a loading span of 40 mm. A notch was machined at the centre of the specimen by wire-EDM cutting, and the length of the notch was 2.5 mm (25 % of total cross section) to comply with BS ISO 12108:20188 [127]. To characterise the effect of build orientation, both AM specimen orientations were tested, and an EDM notch was introduced so that cracks would propagate either perpendicular or parallel to the build direction, as shown in Figure 3.2. All tested specimens were manufactured in the same build plate, although the specific location of each sample on the build plate is unknow. The sides of the sample were polished to a 1 μm finish to allow for post-test characterisation of oxidation processes at the side surface. The other faces were mechanically abraded (1200 grit) to improve contact when spot welding wires for the direct current potential drop (DCPD) method, as elaborated below.

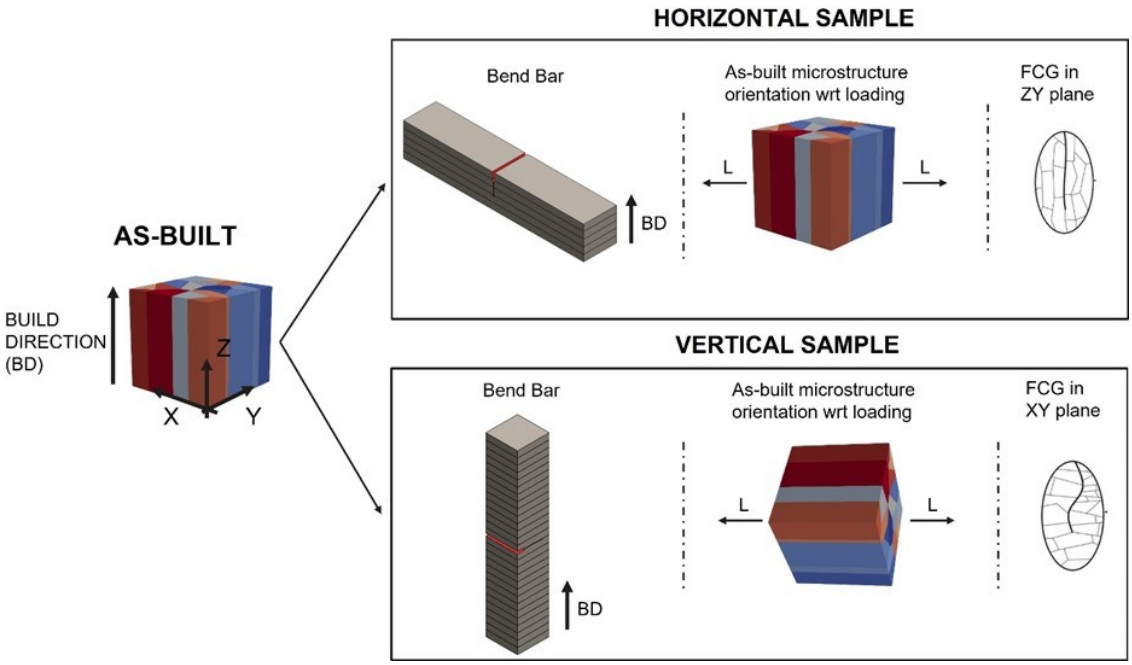

Figure 3.2 Schematic of expected microstructure orientation (columnar grains in as-built configuration) with respect to (wrt) loading direction.

Fatigue testing was conducted using a 50 kN (load cell) Instron 8501 servo-hydraulic test machine, with a high temperature vacuum chamber (though all tests were conducted under standard atmosphere and pressure) fitted with four quartz lamps to achieve high temperatures. Temperature was controlled with an R-type thermocouple spot welded to the side surface close to the crack, connected to a Eurotherm 815 controller (system error: ± 1 ºC). Cyclic loading was applied in load control mode with a load ratio of 0.1, and a trapezoidal waveform of the type: 1s-Xs-1s-1s, (see Figure 3.3-a for reference), where the 1s segments correspond to loading, reloading, and holding at minimum load, while dwell time at maximum load (X segment) is different depending on the test. Fatigue crack growth (FCG) was monitored using the direct current potential drop (DCPD) method. Current was provided by two wires at the end of the specimen, two PD wires were spot welded across the notch, and two more wires were placed away from the crack to normalise data against temperature and current variations (see Figure 3.3-b for reference). The FCG rate was then derived from the potential drop variation with time using the secant method. A post-test crack length calibration was performed by comparing the derived crack length (from the initial PD calibration) with beachmarks formed on the crack fracture surface at known parts of the testing cycle. Prior to testing, the specimens were pre-cracked using a load-shedding method, with a sine waveform, stress ratio of 0.1, frequency of 10 Hz and initial ΔK of 20 MPa$\sqrt{m}$. The ΔK was stepped down in 10 % intervals after the crack had grown through four monotonic plastic zones (calculated using Irwin's approach [128]), to ΔK levels of ≈ 12-15 MPa$\sqrt{m}$. The final

precrack length was ≈ 0.8–1 mm, which ensured that crack growth would occur from a sharp crack away from any effects caused in the machining of the notch. After pre-cracking, the specimen was heated and allowed to stabilise at the testing temperature for 10 minutes, the loading was changed to trapezoidal, and the test was started.

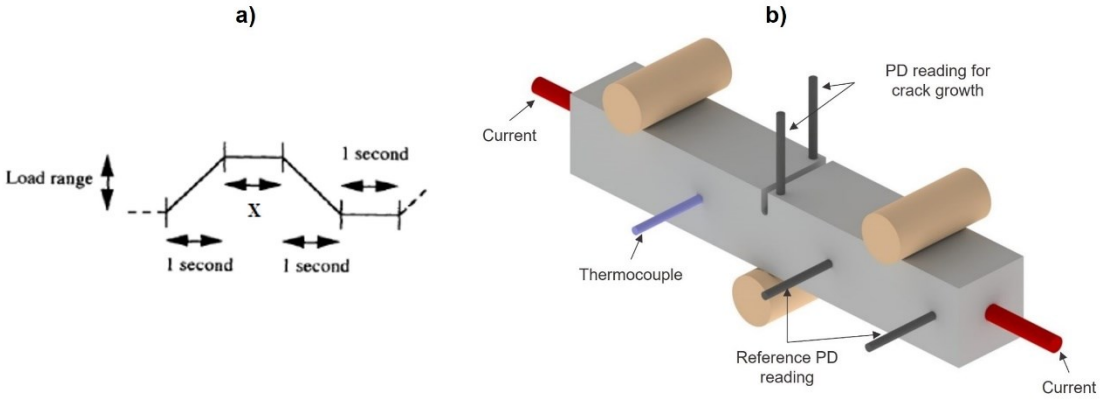

Figure 3.3 a) Schematic of a trapezoidal loading waveform, b) Schematic of long crack test setup with DCPD wires.

The experimental work included three different types of tests as summarised in Table 3-2, and are outlined below:

- **Fatigue crack propagation tests (constant load, increasing ΔK)** were run to failure and performed to obtain the characteristic da/dN vs. ΔK response for all material conditions, at different temperatures (350, and 650 ºC), and trapezoidal frequencies (1s dwells, or 90s dwells at maximum load). Tests with one second dwells at peak load were used as a baseline frequency to characterise the performance of the alloy, whereas tests under 90s dwells were used to assess more time-dependent fatigue crack growth mechanisms.
- **Interrupted tests** were employed to characterise oxidation ahead of the crack tip for testing with 90s dwells (time-dependent regime). Specimens were pre-cracked to a ΔK of 12 MPa√a, and then run for approximately 1500 cycles using a 1-90-1-1 waveform. The testing was then interrupted and held at maximum load for 16 hours, during which crack growth was monitored using DCPD.
- **Alternating dwell / Block tests** have been previously employed by *Gustafsson et al.* [99] to assess the extent of oxidation related damage ahead of the crack tip for IN718 at different ΔK levels. During these tests, loading is separated into two regimes: first low frequency (fully time-dependent), followed by loading at high frequency (fully cycle-dependent). This allows characterisation of the amount of oxidation related damage formed during dwell-fatigue by assessing relative crack

growth rates through any affected region during the transition to high frequency. These tests were run to failure (constant load, increasing ΔK), alternating between 5 Hz, and 1-90-1-1 blocks for crack increments of at least 0.5 mm. A schematic representation of the loading waveform can be found in Figure 3.4

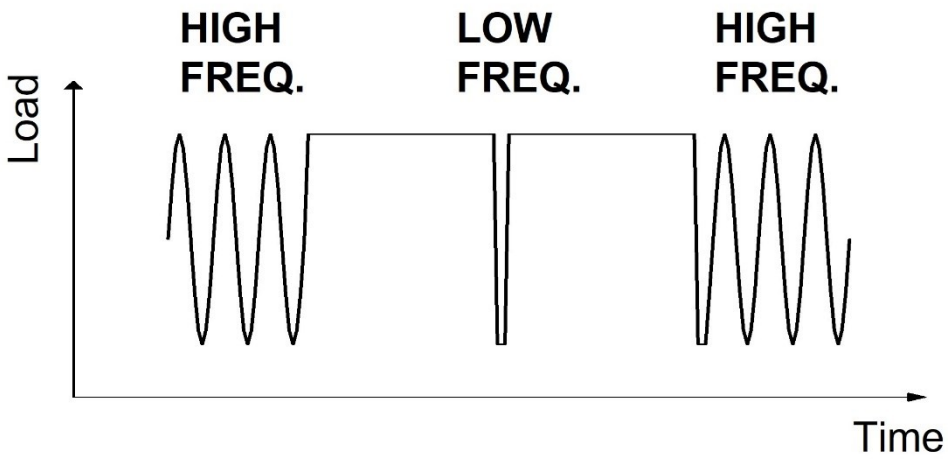

Figure 3.4 Schematic of the block tests loading waveforms.

Table 3-2 Test matrix for long crack testing.

	Temperature and sample condition					
	350 ºC			**650 ºC**		
Test type	**L-PBF Vertical**	**L-PBF Horizontal**	**C&W**	**L-PBF Vertical**	**L-PBF Horizontal**	**C&W**
1-1-1-1	√	√	√	√	√	√
1-90-1-1				√	√	√
Block test				√	√	√
Interrupted				√	√	

3.4.1 Fractography

Fracture surfaces obtained from fatigue testing were investigated at different ΔK levels to understand the underlying fracture mechanisms. A Wild M420 macroscope was used to obtain images of the entire fracture surface, whereas higher magnification images were taken at selected regions of interest with a JSM 6500F FEG-SEM, and JSM 7200 FEG-SEM at an accelerating voltage of 15 kV and working distance of 10 mm.

Some specimens were sectioned perpendicular to the fracture surface (see Figure 3.5 for schematic of the sectioning strategy) to inspect the microstructure around the cracked surface, and to examine the interaction between secondary cracks and precipitates or grain boundaries. To preserve the integrity of the fracture surface during the sectioning procedure, specimens were nickel plated using a Watt's solution (500 ml H_2O, 150 g $NiSO_46H_2O$, 20 g $NiCl_26H2O$, 20 g H_3BO_3) at a temperature range of 40-60 ºC, using a 99.9% pure Ni anode, and a current density of 40 mA/cm^2 for 60 minutes (see Figure 3.6 for an schematic of the setup). The nickel-plated specimens were mounted in Bakelite resin and ground, polished and etched as described in section 3.2. They were then observed under an optical microscope, FEG-SEM and EBSD.

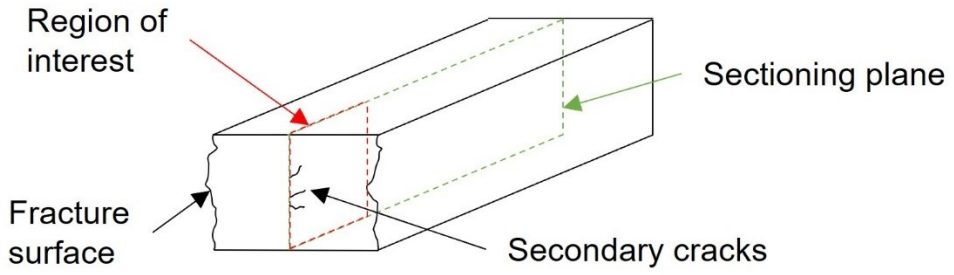

Figure 3.5 Schematic illustration of sectioning strategy for analysis of secondary cracks

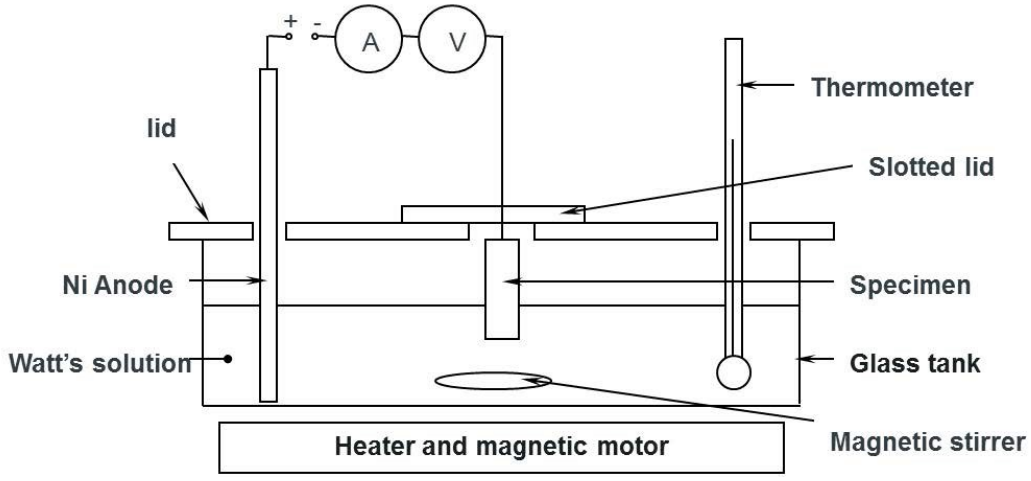

Figure 3.6 Schematic of Nickel plating setup [129].

Fracture surface roughness measurements were taken at different ΔK levels using an Alicona infinite focus microscope. The images were taken at x10 magnification at selected regions of interest, and the average surface roughness (Sa) was measured to characterise the surface roughness of the fracture surfaces. The filter cut-off (λc) values to obtain the average surface roughness were selected following the BS EN ISO 4288:1998 standard [130]. Given the high surface roughness of the fracture surfaces (Sa > 10 μm) the cut-off value was set to 8 mm for all specimens except 1-1-1-1 tests at 350 ºC on CW specimens where the recorded roughness was lower (2 < Sa < 10), thus the cut-off filter was set to 2.5 mm. Average surface roughness can be mathematically described as Equation (3-3), where Z(x,y) is the instantaneous local height measurement, and a is the area of the micrograph.

$$Sa = \frac{1}{A}\iint_A |Z(x,y)|dx\,dy \qquad (3\text{-}3)$$

4 Microstructure characterisation

4.1 Introduction

Materials microstructures are closely linked to mechanical properties and thus, characterisation of the microstructure of L-PBF IN718 is essential to fully understand its fatigue behaviour. In this chapter the microstructures of both L-PBF and comparable cast and wrought IN718 were investigated using the metallographic techniques described in chapter 3. In addition, although as-built specimens were not fatigue tested, their microstructure is presented in this chapter. This is because, to characterise differences caused by build orientation on heat treated components it is important to also understand the original as-built microstructure. Some aspects of the work detailed in this chapter have been published/presented in the following paper:

D. Martinez de Luca, A. R. Hamilton, P. A. S. Reed, Influence of build orientation on high temperature fatigue crack growth mechanisms in Inconel 718 fabricated by laser powder bed fusion: effects of temperature and hold time, submitted to International Journal of Fatigue (2022).

4.2 Results and discussion

4.2.1 As built L-PBF IN718 microstructure

Optical metallographic images of the macrostructure in as-built condition can be seen in Figure 4.1, in two perpendicular planes (y-z, and x-y planes). After etching the melt morphology and laminar material nature are visible. From the top view (x-y plane) the scanning strategy can be observed as straight lines that represent the laser scanning tracks. The scanning tracks between adjacent layers intersect with each other at approximately 67º, following the presumed interlayer rotation. From the front (y-z plane) view a fish-scale pattern of the melt pool boundaries can be distinguished. As expected, no apparent differences were measured in the melt pool shape/dimensions, since the process parameters were the same for both orientations.

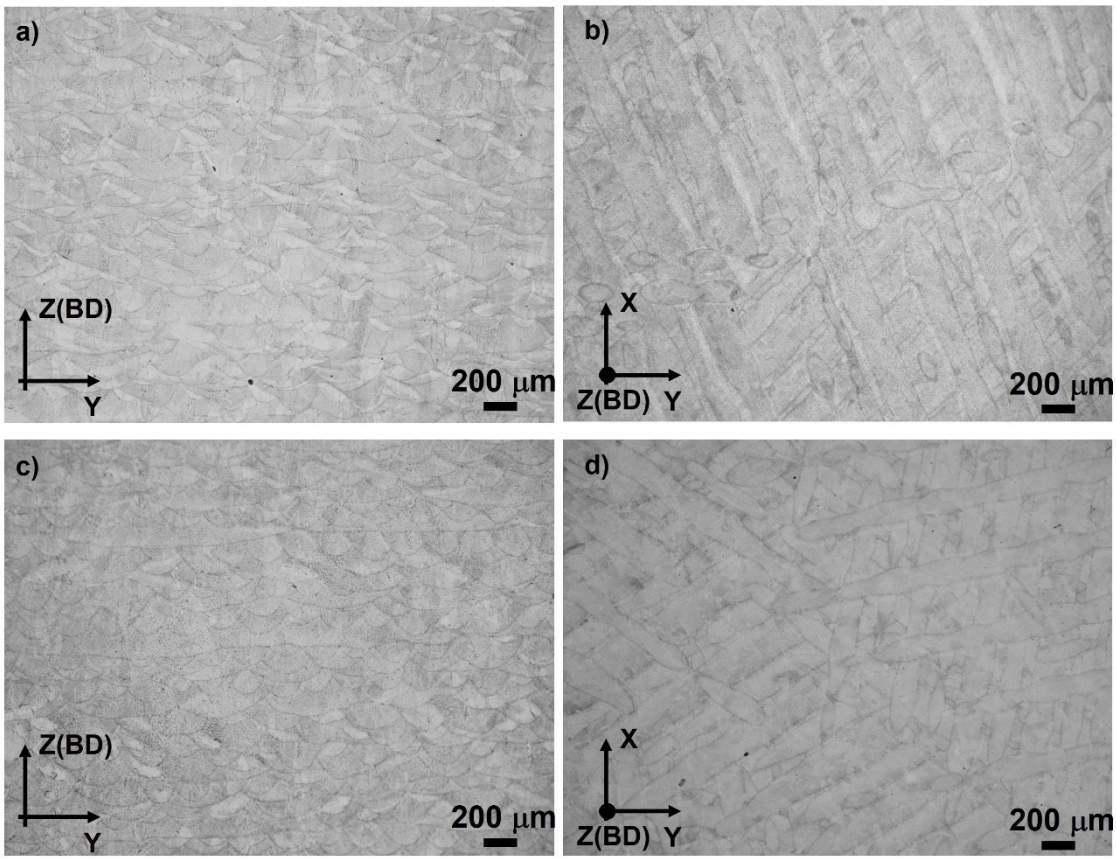

Figure 4.1 Optical micrographs of the as-built microstructure in two orthogonal planes (y-z, and x-y planes) for: a-b) vertical specimens, and c-d) horizontal specimens.

To obtain a better understanding of the microstructure, SEM micrographs of the as-built specimens were taken. Figure 4.2-a,c show the solidified structure of vertical specimens in the y-z plane, composed of an array of dendrites with similar orientations to the build direction. These can either go through several layers or be contained within the melt pool. Furthermore, it can be observed in Figure 4.2-c, that the growth direction in the newly-formed (e.g., upper) molten pools, either follows the dendrites outside the molten pool, or it is at an angle of ≈90º. Tao et al. [131], also reported a similar phenomenon and believed it to be related to the local relationship between partially re-melted dendrites and molten pools. Moreover, different dendrite morphologies can be seen in melt pool overlapping regions. The difference between these regions arises from the variation in cooling resulting from overlapping laser scans. Similar morphological differences were observed by Mostafa et al [69]. The influence of the thermal gradient on the microstructure in the x-y plane is shown in Figure 4.2-b, d. Since most of the dendrites are oriented along the build direction, the cross-sectional view (x-y plane) renders a honeycomb like structure: demonstrating the anisotropic nature of the structure. The SEM observations presented for vertical as-built specimens are representative of

horizontal specimens as well, since no differences in the structure could be discerned. The dark areas in the SEM images are the matrix (γ) phase, and Laves phases are present in the bright inter-dendritic regions. These particles form as products of eutectic reactions if the cooling rate is very fast and if the concentration of Nb, Mo, and C in the melt pools is sufficiently high [36], [69], [82]. These are brittle intermetallics and detrimental to the mechanical properties of the material. Fine MC-type carbides (mostly NbC) can also be present in the interdendritic regions [69]. IN718 common strengthening precipitates (δ-phase, γ', and γ'') are not present, due to the high cooling rates of the AM process. Finally, no observable differences in precipitation were found between sample orientations, with the micrographs presented in Figure 4.2 being representative of horizontal specimens.

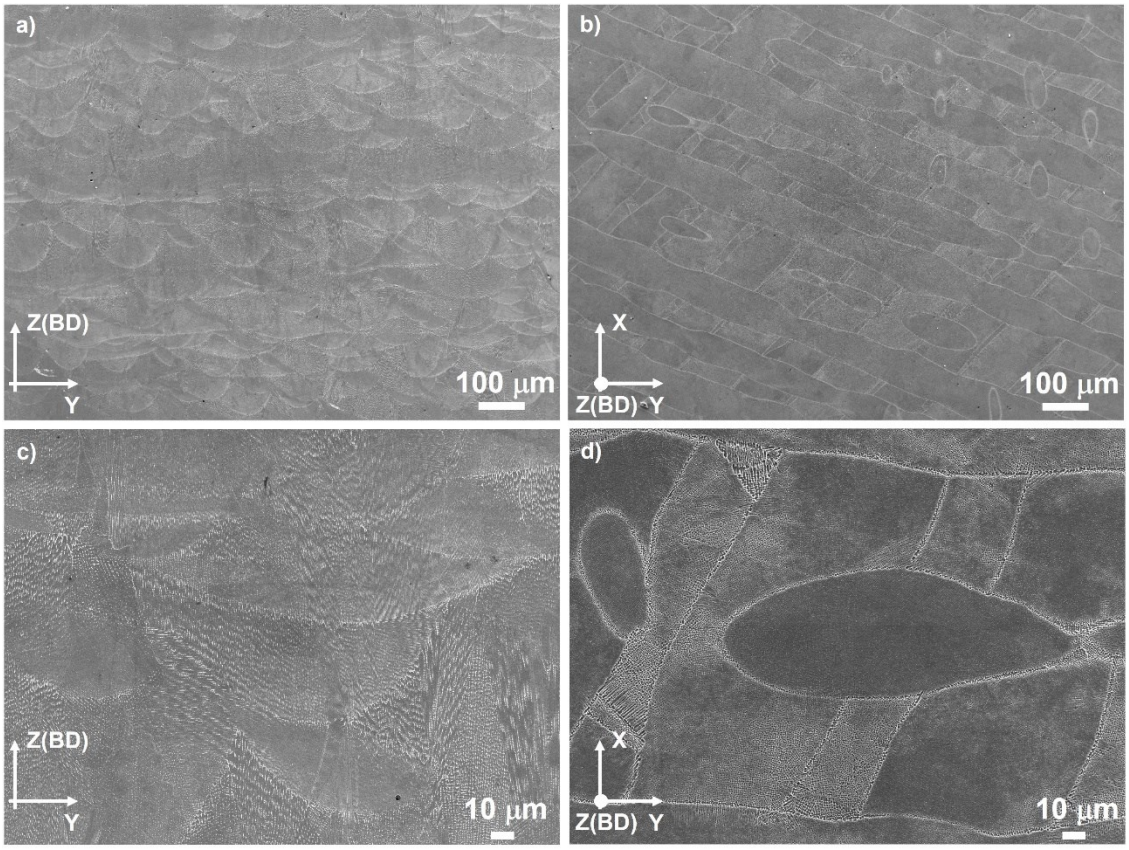

Figure 4.2 Low and high magnifications SEM micrographs of the as-built microstructure in two orthogonal planes (y-z, and x-y planes) vertical specimens. Micrographs are representative of horizontal specimens.

To further understand the as-built microstructure, EBSD scans were performed in two different planes (y-z, and x-y plane) for both L-PBF orientations, and the results are shown in Figure 4.3, and Figure 4.4. For both orientations the anisotropic grain structure is evident, with grains growing parallel to the build direction, and primarily textured in the <001> orientation. This results in long, elongated grains parallel to the build direction and

a finer grain size perpendicular to the build direction. For calculating the average grain size, micrographs from both orientations were considered given the anisotropic grain structure. The average grain length was calculated from micrographs parallel to the BD, and the average grain diameter from micrographs perpendicular to the BD. The calculated mean grain length was 43.85 ± 64.44 μm, and 35.91 ± 51.18 μm for vertical and horizontal specimens. Perpendicular to the build direction, however, the average grain size is much finer 12.61 ± 11.36 μm, and 10.95 ± 13.81 μm for vertical and horizontal specimens respectively. Resulting in overall longer grains for vertical specimens (parallel to build direction) compared to horizontal specimens, but with a similar diameter. The grain size distribution (both parallel and perpendicular to the build direction) for as-built specimens is shown in Figure 4.5 (based on grains shown in Figure 4.3, and Figure 4.4). In Figure 4.5-a, the grain lengths for both orientations mostly range from 10-50 μm (≈80 %), with approximately 15 % of larger grains at 50-250 μm. Furthermore, there are some larger columnar grains up to 500 μm long in both cases. Perpendicular to the build direction, grain size distribution is much finer, with grain size mostly ranging between 10-30 μm.

There is a large number of low angle grain boundaries for both material conditions, indicating a large number of sub-grains (see Figure 4.3-c, d, and Figure 4.4-c, d for reference). These sub-grain structures are characteristic of L-PBF as-built microstructures and are linked to the differences seen in dendrite orientations within the melt pools (see Figure 4.2-c) leading to a sub-grain structure [132]. Furthermore, the percentage of twin grain boundaries was below 0.5 % for both orientations, with a large spread in grain boundary misorientation angles as shown in Figure 4.6. Twins are not expected to form during the L-PBF process; however, they are commonly found in CW IN718, showing overall a very different starting microstructure prior to heat treatment compared to CW.

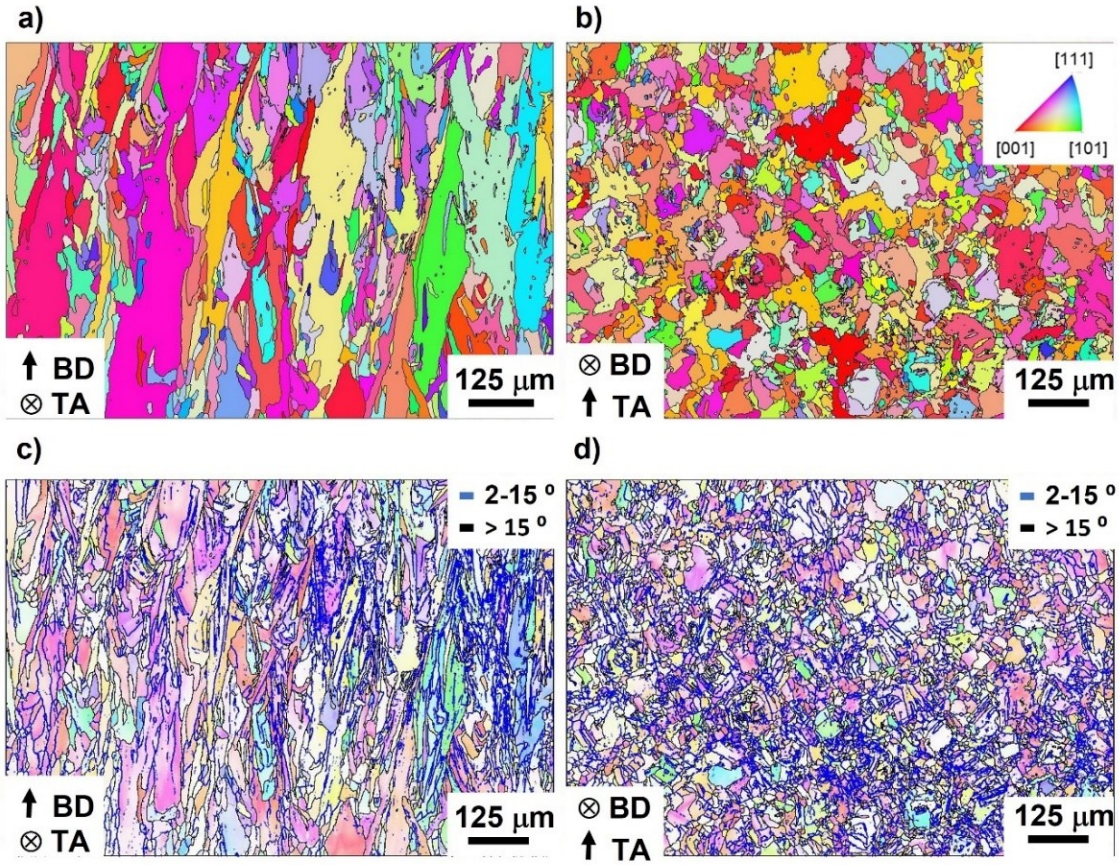

Figure 4.3 EBSD micrographs of as-built horizontal specimens: a) IPF map (z-orientation) on y-z plane, b) IPF map (z-orientation) on x-y plane, c) sub-grain structure on y-z plane, and d) sub-grain structure on x-y plane. The tensile axis (TA) from the fatigue tests is included for reference.

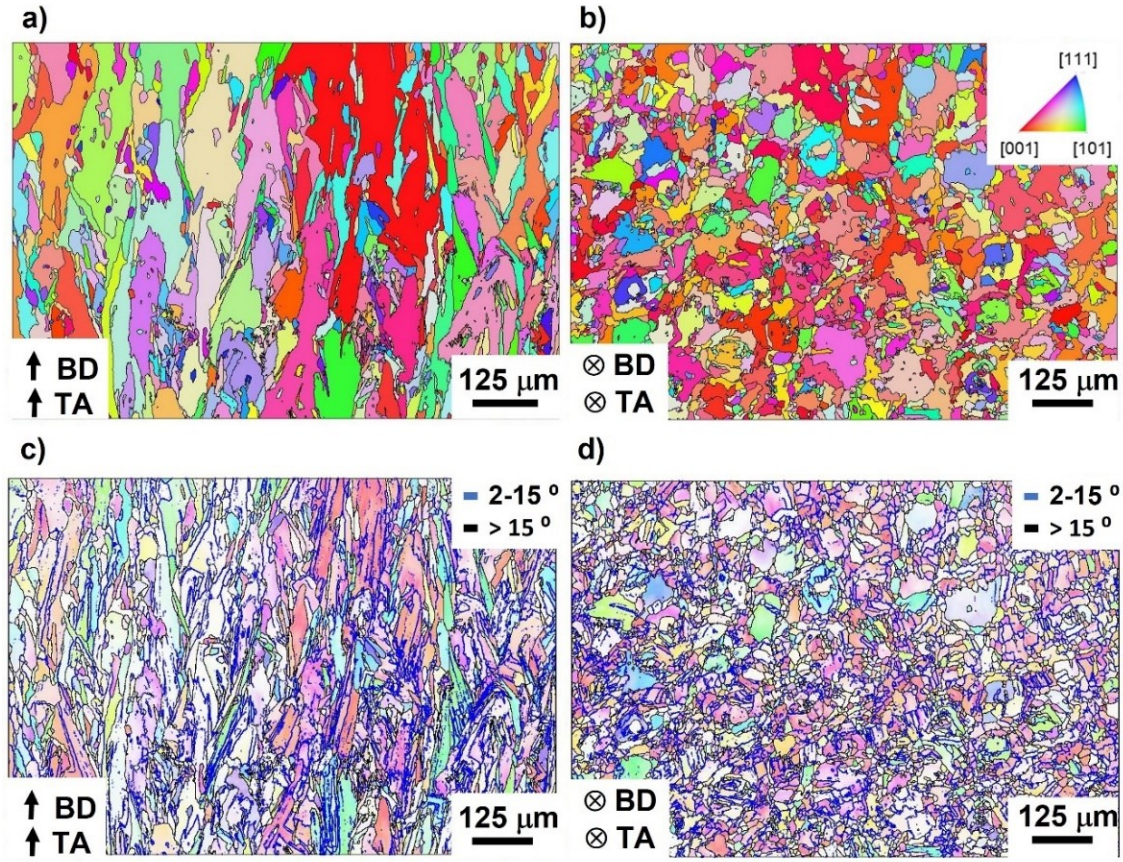

Figure 4.4 EBSD micrographs of as-built vertical specimens: a) IPF map (z-orientation) on y-z plane, b) IPF map (z-orientation) on x-y plane, c) sub-grain structure on y-z plane, and d) sub-grain structure on x-y plane. The tensile axis (TA) from the fatigue tests is included for reference.

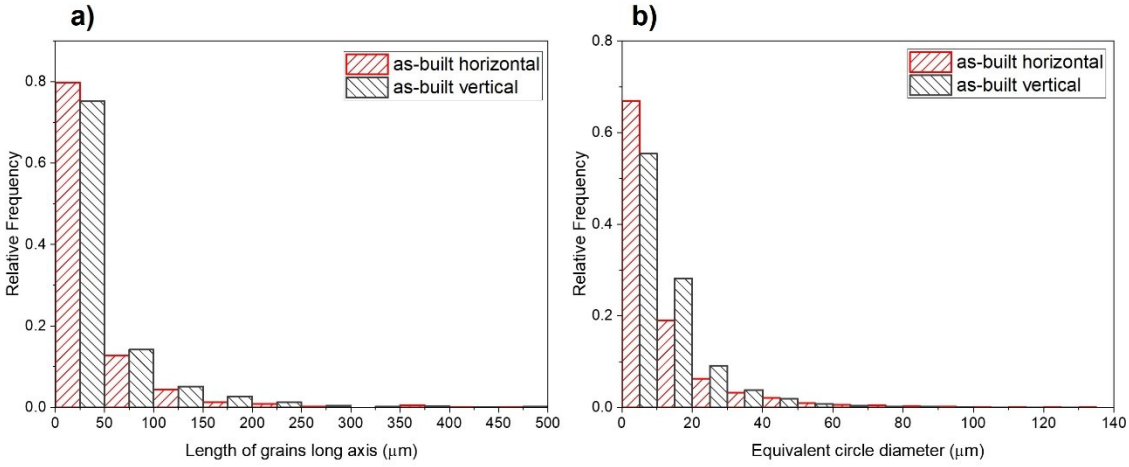

Figure 4.5 Grain size distribution for L-PBF as-built IN718, a) length of grains long axis measured parallel to the build direction, b) grain size measured perpendicular to build direction.

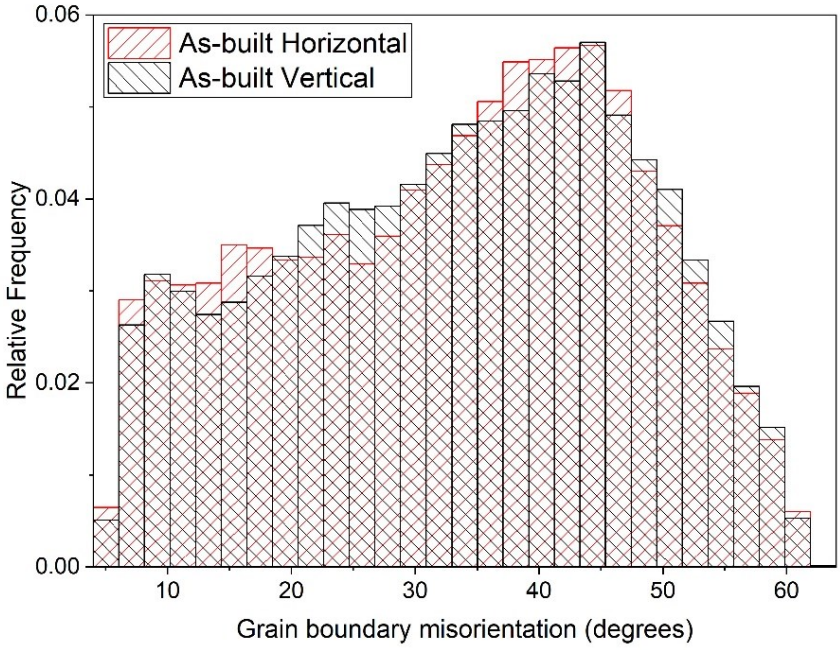

Figure 4.6 Grain boundary misorientation plots for as-built horizontal and vertical specimens.

4.2.2 Heat treated L-PBF IN718 microstructure

The EBSD micrographs presented in Figure 4.7, and Figure 4.8 depict the microstructure in two different planes (y-z, and x-y plane) for both L-PBF orientations after heat treatment. Recrystallisation occurred during HIP processing, with grain coarsening taking place, and grains losing their strictly columnar morphology. As can be seen, the strong texture commonly found in as-built specimens with a high fraction of <001> oriented grains has been removed, with a structure more similar to that commonly found in C&W IN718 being observed. Twin grain boundaries can be discerned in the microstructure (see Figure 4.7-c and Figure 4.8-c). These are believed to have occurred during the HIP treatment and the average area fraction occupied by twin subdomains is higher for the vertical samples, 56 % compared to 52 % for the horizontal samples. A histogram representing grain boundary misorientation angle is also included in both figures, showing a large frequency at a misorientation of 60º (twin grain boundary misorientation angle for a fcc crystal). It is important to note the change in grain boundary misorientation between as-built (see Figure 4.6 for reference) and heat treated components, with the heat treatment successfully removing the low angle grain boundaries (sub-grain structure present in as-built components).

The mean grain size for the horizontal and vertical samples was found to be 24.4 μm ± 27 μm, and 31.3 μm ± 31.1 μm respectively. The grain size distribution in the L-PBF

samples is shown in Figure 4.9. As shown in Figure 4.9-a, the grain size for both orientations mostly ranges from 10-70 μm (≈87 %), with approximately 10 % of larger grains at 70-250 μm. If the grain size distribution is expressed by area fraction, grains between 10-70 μm account for 37 %, and 49 % of the total area for vertical and horizontal samples respectively. It should also be noted that larger grains ranging between 70-250 μm occupy 32 %, and 46 % of the measured area for horizontal and vertical samples respectively, even though they only account for approximately 10 % of the grains counted. Both sample orientations were manufactured on the same build plate, using the same process parameters, and underwent the same heat treatment steps. The main difference being the orientation of the bars with respect to build direction, leading to different heating and cooling cycles during the manufacturing process. Horizontally manufactured specimens have a shorter conductive path length from the scanned layer to the build plate (heat sink) due to their smaller height (see Figure 3.1 for reference), which could have resulted in higher cooling rates, and finer microstructures.

The aspect ratio of the grains, and orientation of the long axis, which are indicators of shape characteristics of the microstructure, are plotted in Figure 4.10 (both micrographs show the fatigue crack growth plane of each sample orientation). It was found that there is some retained grain shape from the as-built material, with grains having large aspect ratios. It can be seen that the orientation of the grains' long axis is somewhat parallel to the crack propagation direction for horizontal specimens and somewhat perpendicular for vertical specimens.

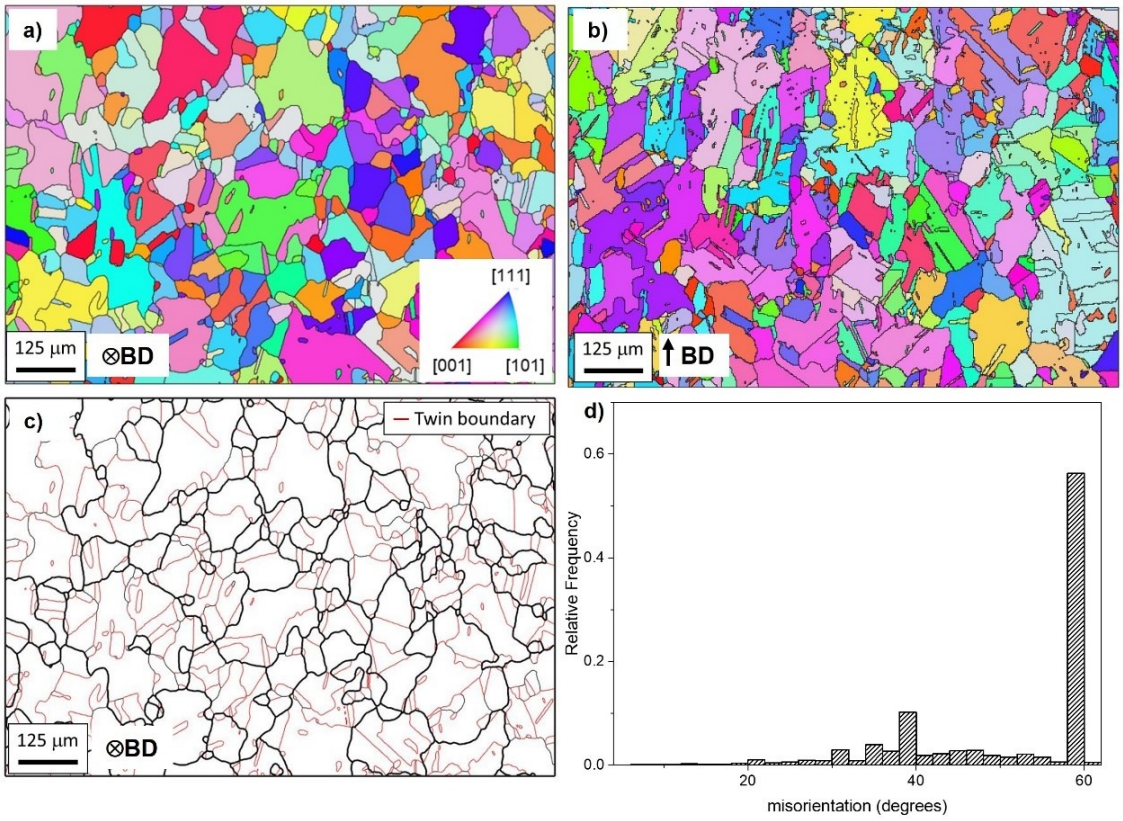

Figure 4.7 EBSD micrographs of heat treated vertical specimens: a) IPF maps (z-orientation) on x-y plane (fatigue crack growth plane), b) IPF map (z-orientation) on y-z plane, c) twin grain boundaries (x-y plane), and d) histogram representing grain boundary misorientation.

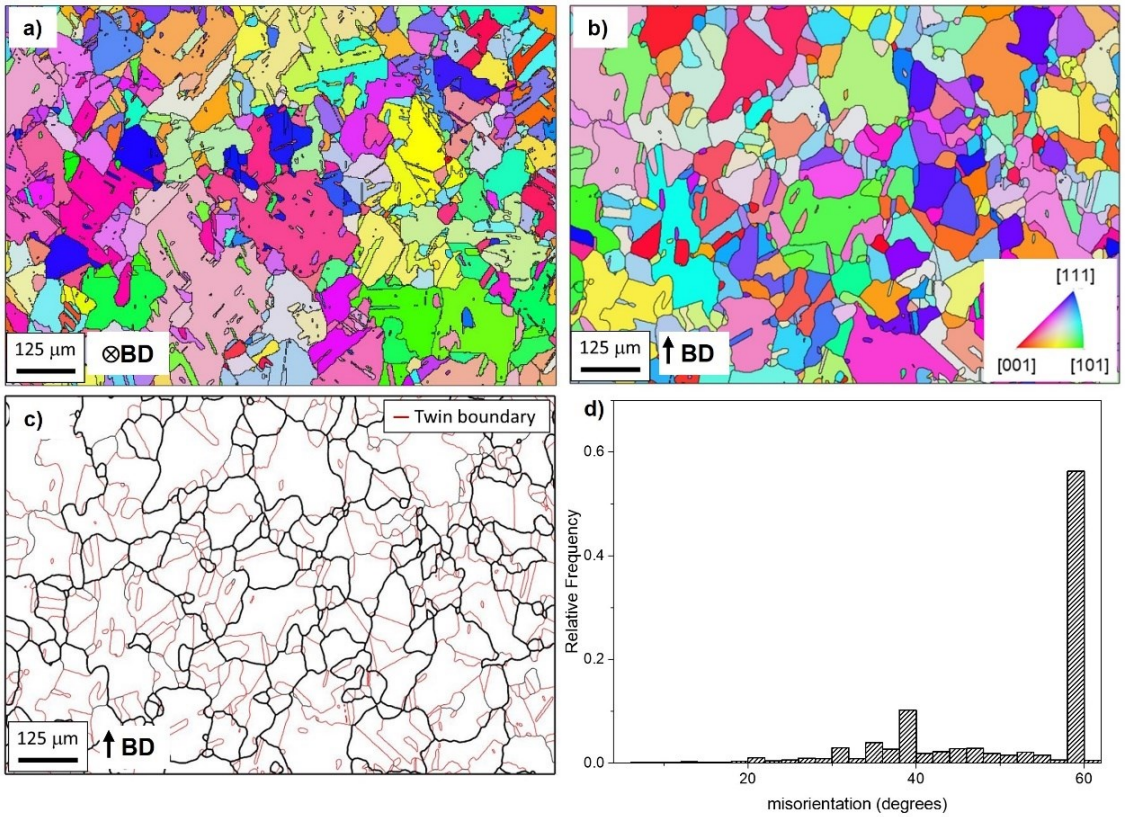

Figure 4.8 EBSD micrographs of heat treated horizontal specimens: a) IPF map (z-orientation) on x-y plane, b) IPF map (z-orientation) on y-z plane (fatigue crack growth plane), c) twin grain boundaries (y-z plane), and d) histogram representing grain boundary misorientation.

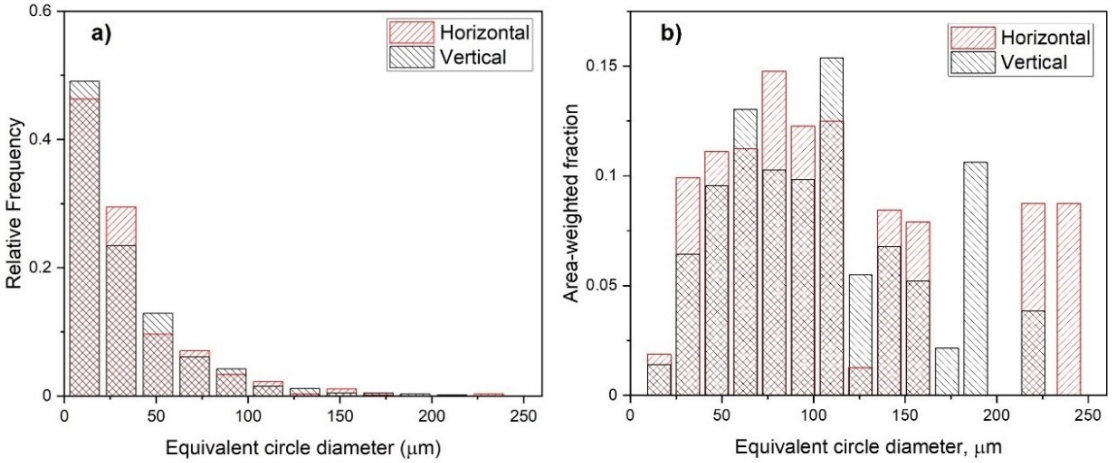

Figure 4.9 Grain size distribution for heat treated L-PBF IN718: a) Frequency, b) Area weighted fraction.

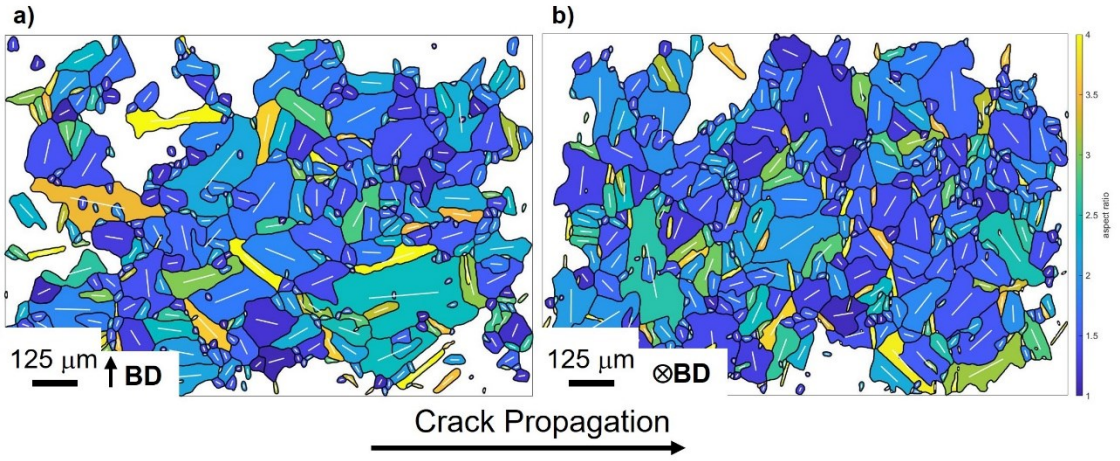

Figure 4.10 Grain aspect ratios, with orientation of grains' long axes superimposed in white for: a) Horizontal, b) vertical heat treated samples. Both micrographs are taken on the fatigue crack growth plane.

SEM and TEM micrographs showing the microstructure of the vertical heat-treated L-PBF specimens are presented in Figure 4.11. Observations from the vertical L-PBF sample in Figure 4.11 are representative of horizontal samples as no major differences in precipitation were found between sample orientations. Some of the characteristic microstructural features found in the as-built specimens (Laves phase, melt pool morphology, dendritic and sub-grain structure) have been effectively removed by the heat treatment. Grain boundaries are decorated with the precipitation of fine needle-like δ-phase, although it is more discontinuous when compared to typical cast and wrought material. Furthermore, δ-phase with globular morphology is present in the matrix (not commonly found in cast and wrought IN718), as shown in Figure 4.11-c. Intergranular δ-phase is longer (0.81 ± 0.4 μm), and the intragranular precipitates are more uniform (aspect ratio closer to 1) and smaller (0.19 ± 0.01 μm). The precipitation of needle-like δ-phase occurs at lower aging temperatures, whereas intragranular precipitation occurs at the higher temperatures associated with the HIPing process [27, 29]. Fine primary carbides appear at grain boundaries and are also finely dispersed across the microstructure for L-PBF specimens. The majority of the primary carbides were found to be rich in niobium, with some richer in titanium, and their diameter ranges between 0.4-1.5 μm. Finally, precipitation of γ', and γ'' occurred, as shown in Figure 4.11-d, finely distributed across the entire microstructure. The identification of the precipitates in the image was based on morphological differences between them, since γ'' precipitates as thin discs whereas γ' has a globular shape. Given the higher area fraction of γ'' in IN718 the majority of the precipitates are expected to be γ'' and some are labelled in Figure 4.11-d where the cross-section of the discs is apparent. Examples of possible γ'

precipitates are labelled in Figure 4.11-d. However, these could also be γ'' where the circumference of the precipitate is visible, thus further TEM characterisation would be required to fully characterise these precipitates. Furthermore, in some regions, clusters of precipitates can be seen, consistent with some heat treatment studies performed by Cozar and Pineau for cast and wrought IN718 [54].

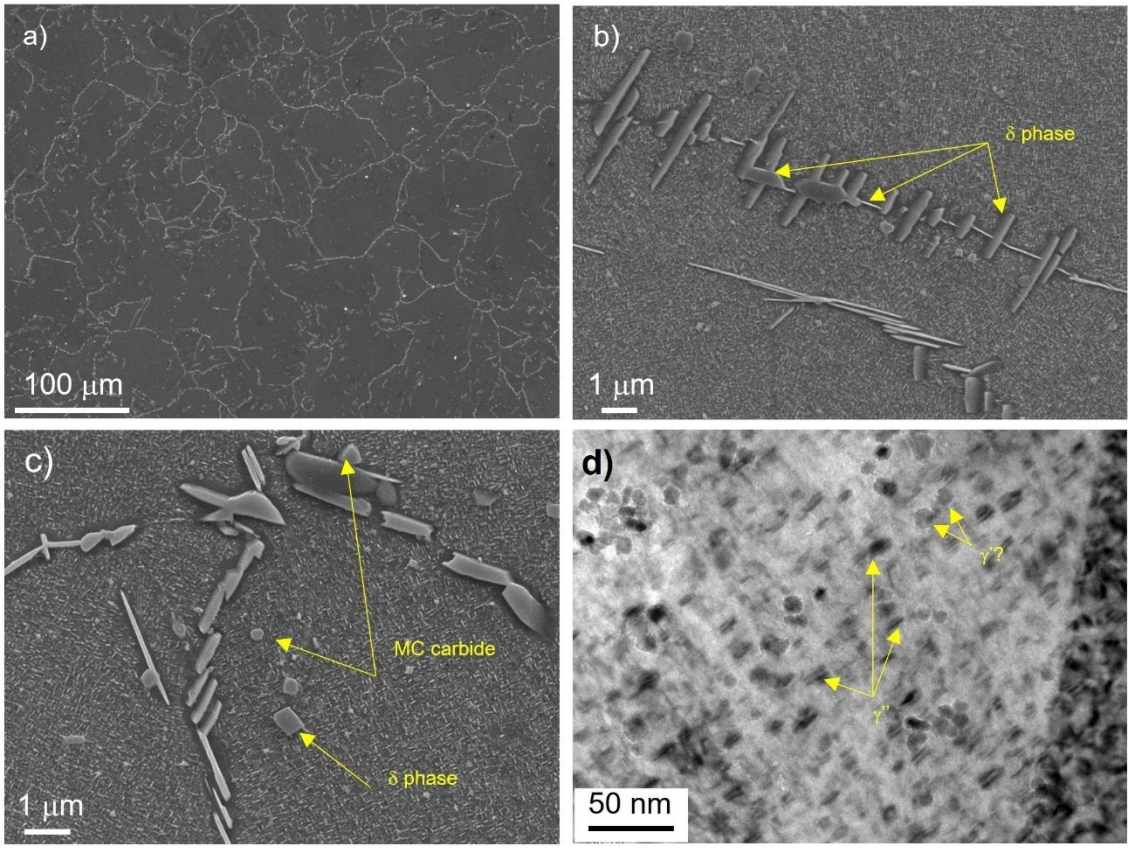

Figure 4.11 (a) SEM micrograph of the etched heat treated L-PBF microstructure (vertical sample), (b and c) are magnified images showing the precipitated δ-phase and primary carbides, (d) TEM bright field micrograph (vertical sample) showing the distribution of strengthening precipitates.

4.2.3 Density and defect distribution of L-PBF IN718

The results from density measurements using the Archimedes method for all material conditions can be found in Figure 4.12. It can be seen that the heat treated specimens have a higher relative density (99.7% and above) when compared to as-built samples. The HIPing stage was successful in increasing density by 1%. Furthermore, differences between orientations on overall density are minor in both as-built and heat treated conditions (<0.2%).

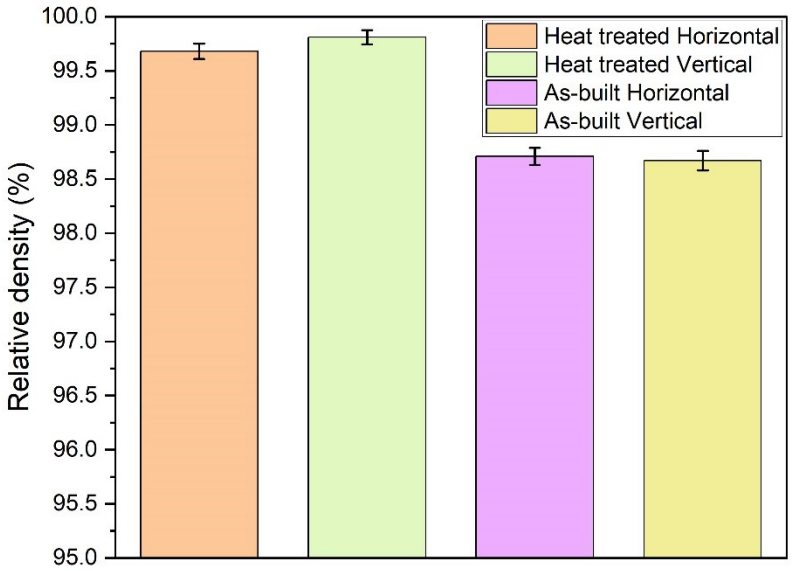

Figure 4.12 Relative density for all material conditions measured using the Archimedes method.

Representative micrographs used for analysing local defect distributions are shown in Figure 4.13. To understand the size distribution of the pores, a histogram is presented in Figure 4.14, representing all sample conditions. Pore diameter ranges primarily between 5-50 μm for all samples. Overall, smaller pores (5-10 μm) accounted for the majority of the observed defects (approximately 80%), and larger pores (>20 μm) accounted for less than 5%. Generally, smaller pores (<20 μm) are a result of entrapped gas in the powder during the manufacturing process, whereas larger pores can be caused by either entrapped gas during L-PBF or lack of fusion between layers [38]. Comparing the results between as-built and heat treated samples no big differences can be discerned in pore size distribution, showing that the print quality of the as-built samples was good and porosity already low before heat treating. Furthermore, the majority of the porosity in the heat treated specimens was attributed to small pores primarily located around the perimeter of the samples since surface pores cannot be closed by the HIP process [18]. Figure 4.15, presents a histogram of the circularity of the observed pores. Spherical pores will have circularity of 1 whereas more elongated pores have smaller values approaching 0. This can be used as an indicator of the smoothness of the pore contour, with powder production pores having values closer to one, when compared to process induced pores (lack of fusion, cracks…). The results show a skewed distribution tending towards higher values with a peak in the range 0.95-1. Furthermore, all observed specimens show similar results with no significant differences between heat treated, and as-built samples.

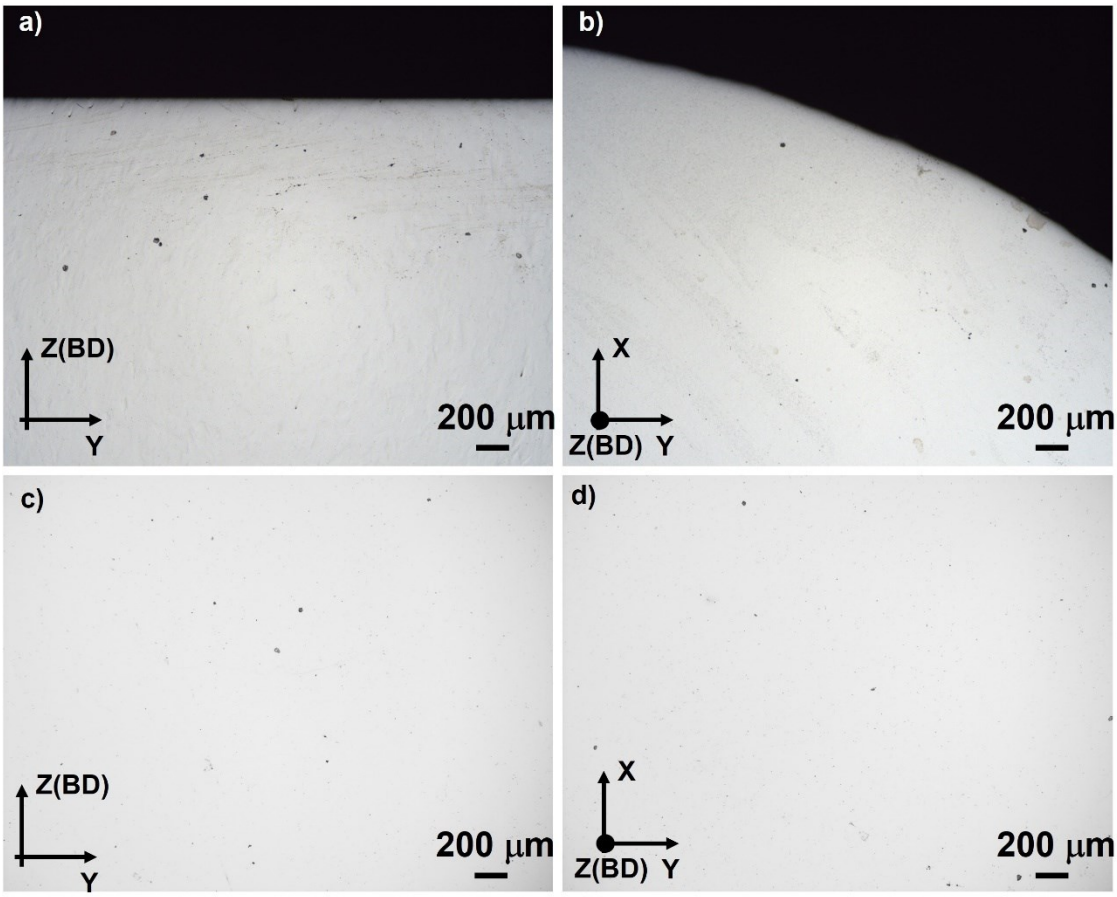

Figure 4.13 Examples of optical micrographs used for local porosity analysis via optical microscopy: a) heat treated horizontal sample, b) heat treated vertical sample, c) as-built horizontal sample, d) as-built vertical sample

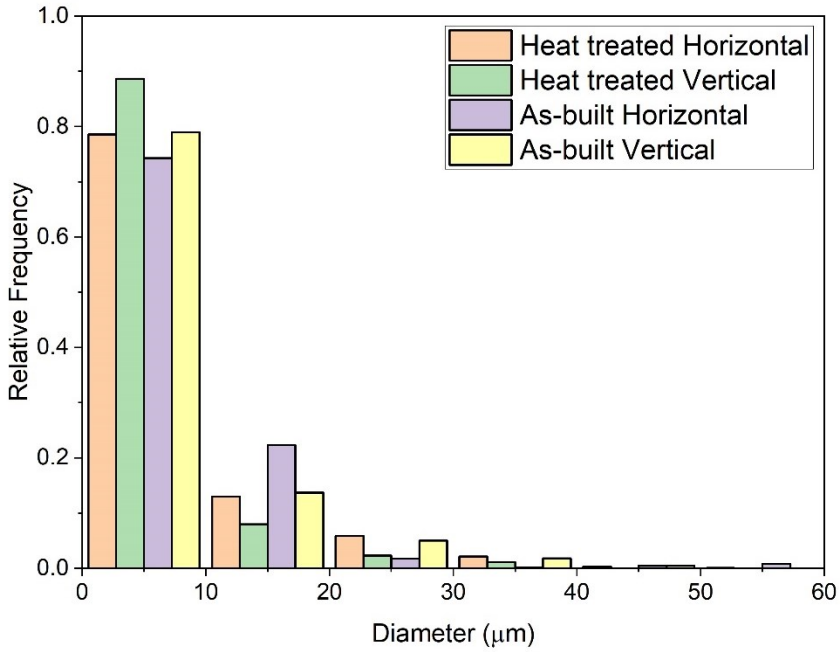

Figure 4.14 Pore size distribution for all material conditions, obtained using optical microscopy.

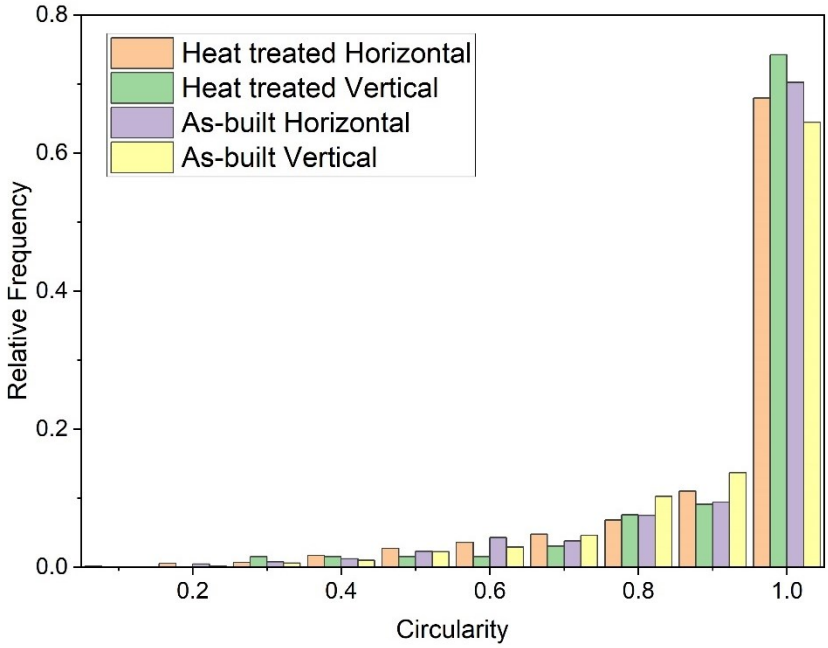

Figure 4.15 Pore circularity for all material conditions, obtained using optical microscopy.

4.2.4 Cast and wrought IN718

The EBSD micrographs presented in Figure 4.16 show the microstructure of cast and wrought IN718. The material presents an equiaxed grain structure, different to heat treated L-PBF specimens where some grain shape from the as-built microstructure is retained. Twin grain boundaries can be discerned in the microstructure (see Figure 4.16-b). However, the fraction occupied by twin grain boundaries in CW specimens is smaller, 24 %, when compared to both heat treated L-PBF orientations (56 %, and 52 % for vertical and horizontal respectively). A histogram representing grain boundary misorientation angle is included showing again a large frequency at a misorientation of 60º, as for heat treated L-PBF specimens. The mean grain size for CW specimens was found to be 16.8 ± 13.7 µm, and the grain size distribution is presented in Figure 4.17. As shown, the grain size mostly ranges from 5-40 µm (≈88 %), with some larger grains between 40-90 µm. Overall, the cast and wrought specimens show a finer grain size distribution when compared to heat treated L-PBF samples, where the high temperatures in the HIP process led to grain growth.

SEM micrographs of the cast and wrought microstructure are presented in Figure 4.18. Grain boundaries are highly decorated with δ phase with different morphologies, ranging from globular to nearly continuous films along the grain boundaries. Plus, there is very limited precipitation of δ-phase in intragranular regions, as opposed to the heat treated

L-PBF specimens. As explained previously, this is related to the high temperatures employed in the HIP process causing precipitation of δ-phase in intergranular regions. Furthermore, a small number of large primary carbides can be observed. The majority of carbides are rich in niobium and are bigger than those found in L-PBF specimens ranging between 5-12 μm (compared to 0.4-1.5 μm for heat treated L-PBF specimens). Furthermore, they mostly precipitated at grain boundaries, however, some smaller intergranular primary carbides can also be seen distributed through the material (not as much as was observed for L-PBF material).

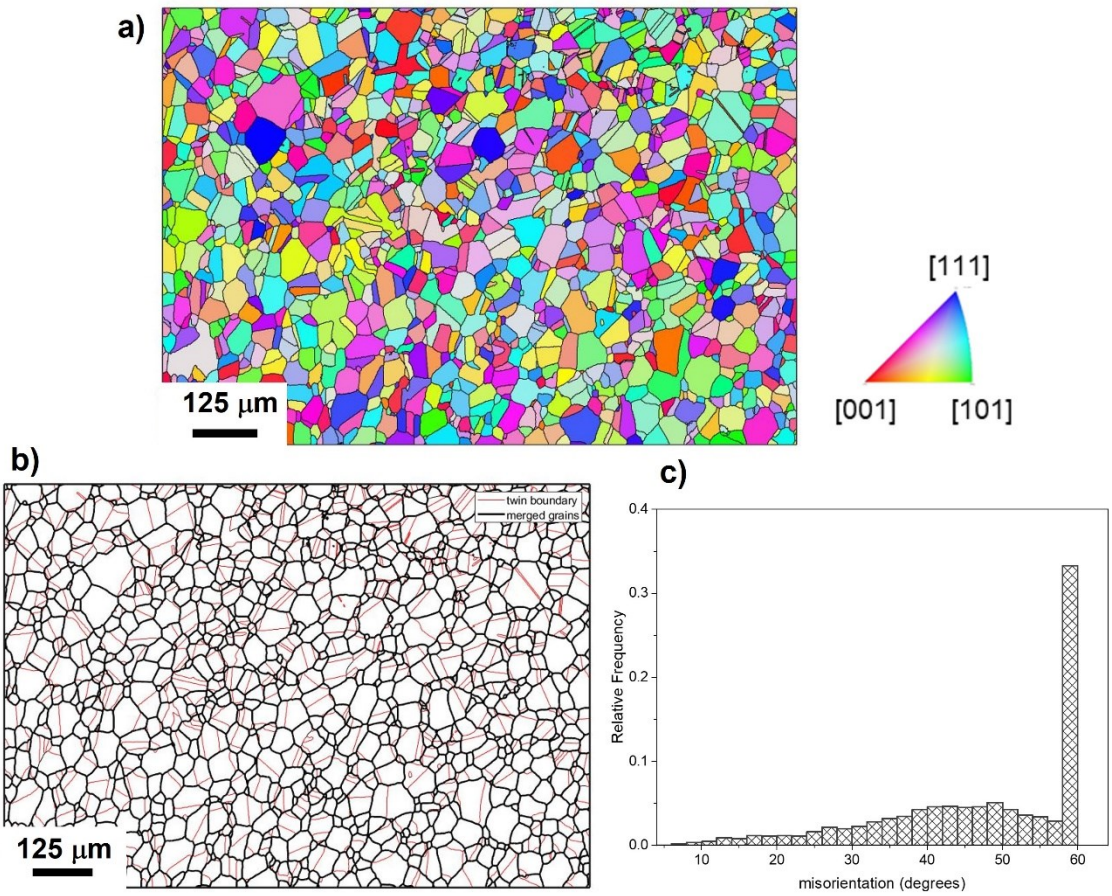

Figure 4.16 EBSD micrographs of CW specimens: a) IPF map (z-orientation), b) twin grain boundaries, and c) histogram representing grain boundary misorientation.

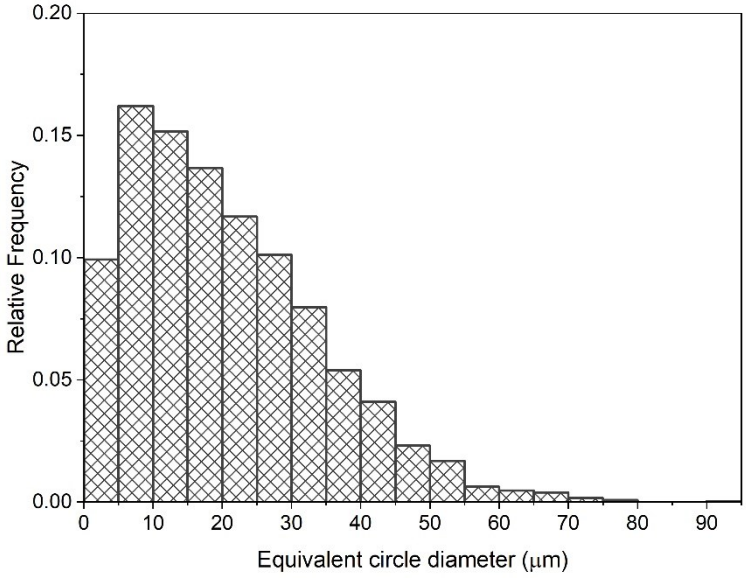

Figure 4.17 Grain size distribution for cast and wrought IN718.

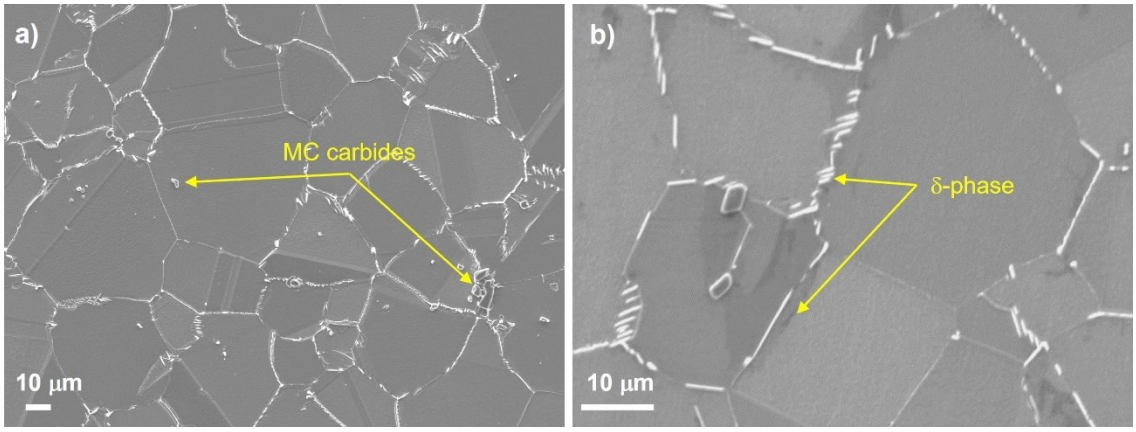

Figure 4.18 SEM micrographs showing the microstructure of cast and wrought IN718 at different magnifications

4.3 Summary and conclusions

Microstructural, and defect characterisations were carried out on CW and L-PBF IN718 in both heat treated and as-built conditions. The as-built microstructure exhibited a columnar dendritic structure, parallel to the build direction due to higher heat transfer in this direction. No major variations in melt pool dimensions were found between specimens; Laves phase and MC type primary carbides were found to precipitate in inter-dendritic regions. There were, however, differences in average grain size between as-built orientations, with vertical specimens having overall a coarser grain structure. Post-

processing heat treatments recrystallised the grain structure, eliminating the anisotropic texture and the columnar grains, although some elongated grain shape was retained with some grains having large aspect ratios. Furthermore, the high number of low angle grain boundaries (sub-grains) found in the as-built material were removed and formation of twin grain boundaries occurred after HIPing (4 % more twins for vertical specimens than horizontal). In addition, post heat treatment, vertical specimens had again a larger average grain size although the difference was reduced when compared to the as-built materials. Both specimens were manufactured using the same L-PBF parameters and underwent the same heat treatment steps, with the main difference between specimens being the orientation of the part with respect to the build direction. This has influenced the overall heating and cooling cycles rendering a finer microstructure for horizontal specimens. After the heat treatment, Laves phases were dissolved, and precipitation of IN718 common strengthening precipitates (δ-phase, γ', and γ'') occurred. Grain boundaries for heat treated L-PBF specimens were highly decorated with the δ-phase, plus there was a large amount of intergranular precipitation of δ-phase.

The cast and wrought material used for comparison had a finer, apparently equiaxed microstructure with a much lower area fraction of twin grain boundaries compared to heat treated L-PBF specimens. Precipitation of δ-phase occurred mainly as continuous films along the grain boundaries with very limited intergranular precipitation of δ-phase. Furthermore, there were significant differences in the size and precipitation of carbides between heat treated LPBF and CW specimens. Blocky carbides (5-12 μm) precipitated at grain boundaries for CW specimens, whereas smaller (0.4-1.5 μm) carbides were finely dispersed across the microstructure for L-PBF specimens as a result of their precipitation in interdendritic areas during L-PBF processing.

The overall density, and local defect distributions were characterised for all L-PBF specimens. Overall, all analysed specimens had a high relative density (higher than 98.5%) with the HIPing step successfully reducing porosity by 1% when compared to as-built specimens. The pore size and shape distributions revealed a dominant void type for all material conditions; globular with a small diameter (5-10 μm) with no major differences between as-built and heat treated specimens. The majority of the remaining pores post heat treatment were primarily located around the perimeter of the sample as surface pores cannot be closed by the HIP process. This shows that the production of near fully-dense materials is possible where porosity is not the main driving factor influencing mechanical performance, as will be shown in the next chapters.

5 Temperature and dwell effects on fatigue crack propagation

5.1 Introduction

In service, IN718 L-PBF components will be subjected to fatigue loading conditions at varying temperatures and frequencies [1]. The detrimental effects of temperature and frequency on fatigue are widely recognised and have been studied for CW specimens, however, for L-PBF specimens their influence is still relatively unknown. As presented in chapter 4, the typical L-PBF microstructure is very different from that of CW IN718 (in terms of grain boundary character, precipitate distribution, grain shape anisotropy, etc.) potentially leading to different FCG behaviour at high temperature. This has motivated the current chapter where the effect of frequency (increased dwell time at maximum load) and temperature on FCG will be assessed for CW, and L-PBF IN718 printed in two different orientations (loading parallel and perpendicular to building orientation) after a post processing heat treatment is applied to ensure the production of strengthening precipitates γ″ and γ′. Some aspects of the work detailed in this chapter have been published/presented in the following paper:

D. Martinez de Luca, A. R. Hamilton, P. A. S. Reed, Influence of build orientation on high temperature fatigue crack growth mechanisms in Inconel 718 fabricated by laser powder bed fusion: effects of temperature and hold time, submitted to International Journal of Fatigue (2022).

5.2 Results

5.2.1 Fatigue crack growth behaviour

Figure 5.1-a presents FCG rates for the tests at different temperatures (350 and 650 ºC) on CW, and both heat treated L-PBF orientations at a baseline frequency of 0.25 Hz (1-1-1-1 trapezoidal loading waveform). For testing at 350 ºC no difference in FCG rates can be found between both L-PBF sample orientations and the cast and wrought material. The response for the same loading frequency at 650 ºC was, however, very

different. It was found that the FCG rates varied by one or two orders of magnitude at a given ΔK level for the vertical and horizontal samples, respectively. At lower testing temperatures (350 ºC, expected to be cyclic-dependent for IN718) the heat treatment was successful in eliminating any effects from build orientation. However, at higher temperature (time-dependent conditions) fatigue cracks propagate at a higher rate in horizontal samples (crack growth parallel to build orientation). It is worth remembering that there is a grain size difference between these samples. Vertical samples have a coarser grain structure (25% larger grains), which will have a beneficial effect against crack propagation in time-dependent conditions. Furthermore, for L-PBF 1-1-1-1 tests at 650 ºC there is a marked change in FCG rates close to final failure where the slope of the curve deviates from the expected Paris-law behaviour, resulting in fairly flat crack growth rates. It is important to note that at these high ΔK values (30-50 MPa√m), crack growth rates are very fast, and this response is indicative of samples plastically collapsing towards the end of the test and not fully representative of fatigue mechanisms. Nevertheless, the entire dataset is plotted here for completeness. The cast and wrought material showed significantly higher crack propagation rates compared to both L-PBF orientations at 650 ºC under time-dependent crack propagation conditions. In addition, the cast and wrought material produced a fairly flat fatigue crack growth curve across the entire ΔK range, again indicative of samples plastically collapsing and not fully representative of fatigue mechanisms. The difference in grain size between material conditions is large as presented in chapter 4, and this can have a large influence on the measured FCG rates. As a consequence, FCG rates cannot be used accurately for comparison between L-PBF and CW specimens. Instead, only the fracture surfaces will be used to compare failure mechanisms between L-PBF and CW components.

The effect of introducing 90 s dwells at maximum load for both L-PBF sample orientations can be seen in Figure 5.1-b. Crack arrest occurred for vertical built samples at ΔK values ranging from 12-25 MPa√m. This is evidenced by the vertical blocks of data points shown in Figure 5.1-b, where the crack would start to grow at a given ΔK value, and after a short period of time it would decelerate and arrest. Loads were increased by 10% after each arrest to increase the applied ΔK and continue the test, but it arrested again a total of three times. No crack arrest was observed for horizontal samples tested at the same ΔK values. However, there was a shift in crack growth rates during the test, where FCG was relatively slow at low ΔK values and between ΔK = 20-22 Pa√m there was a marked increase. In addition, when testing with 90 s dwells, there is no significant difference in FCG rates at high ΔK values (30-50 MPa√m), with both orientations exhibiting very fast FCG rates. By combining the data for both testing frequencies at 650 ºC, in two separate

plots, we can assess the effect of dwell time on FCG rates for each sample orientation. As shown in Figure 5.2-b, FCG rates for the vertical sample are an order of magnitude higher (once away from the crack arresting periods) with 90 s dwells. This is expected, as with longer dwells there is more time for oxidation enhanced mechanisms to take place ahead of the crack tip, accelerating crack growth. For horizontal samples (Figure 5.2-a) however this difference is not as apparent. At low ΔK values, FCG rates are marginally higher with 90s dwells, this difference then slightly increases from ΔK = 25 Pa$\sqrt{m}$ until failure. This result might be linked to a saturation point for the horizontal samples under these testing conditions, where the crack growth increment per cycle outstrips any effect of longer diffusion time for oxidation to occur, usually associated with longer dwells. No data for cast and wrought material was included in Figure 5.2 as the 1-90-1-1 test only lasted a total of 7 cycles, hence, the transient crack growth rates are not very representative of true fatigue mechanisms, rather signalling progressive accumulation of significant overall plastic damage with each cycle.

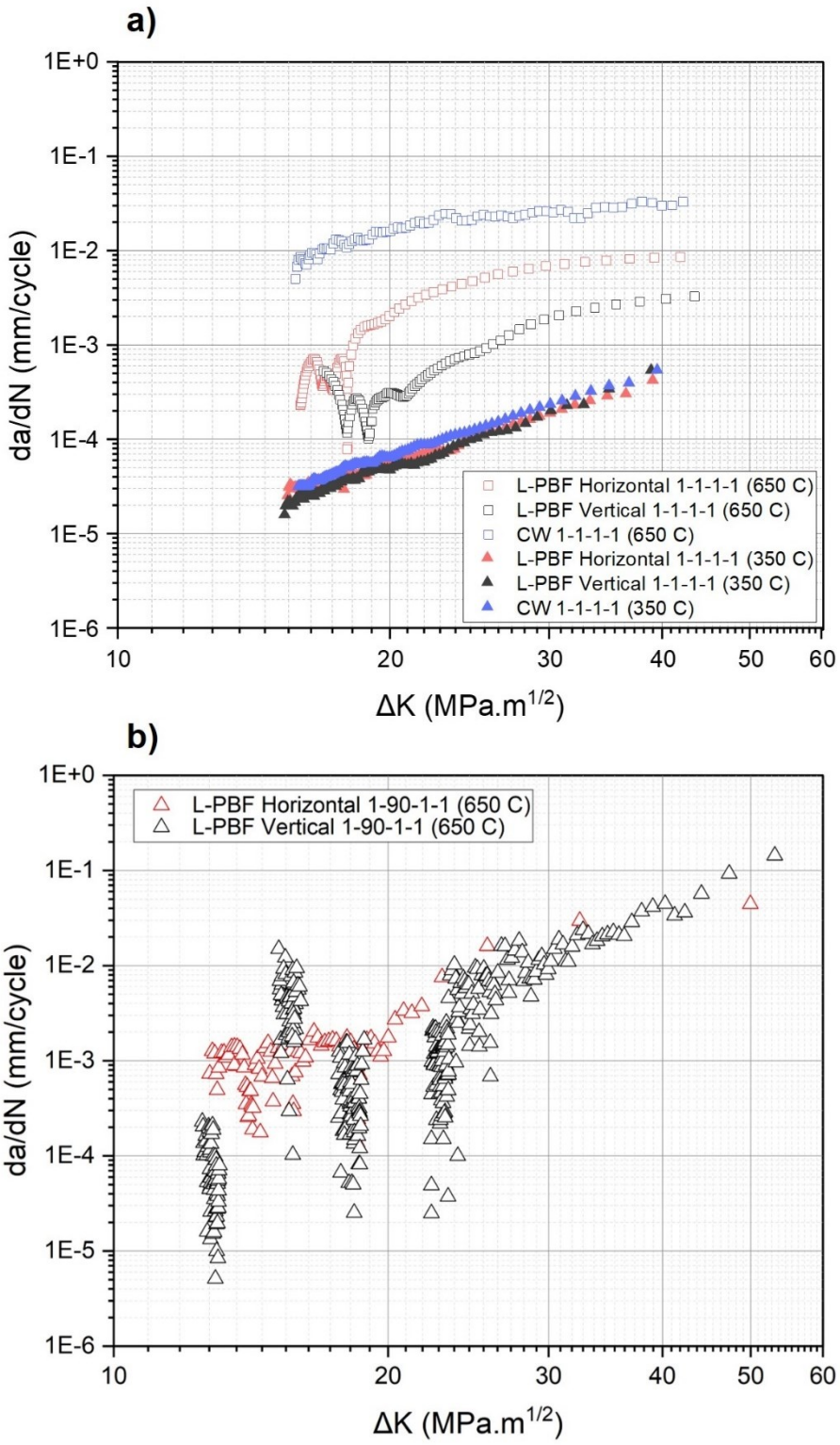

Figure 5.1 FCG rates (da/dN vs ΔK) for both heat treated L-PBF orientations, and cast and wrought at 650ºC and different loading frequencies: a) comparison between 1 s dwell tests, b) comparison between 90 s dwell tests.

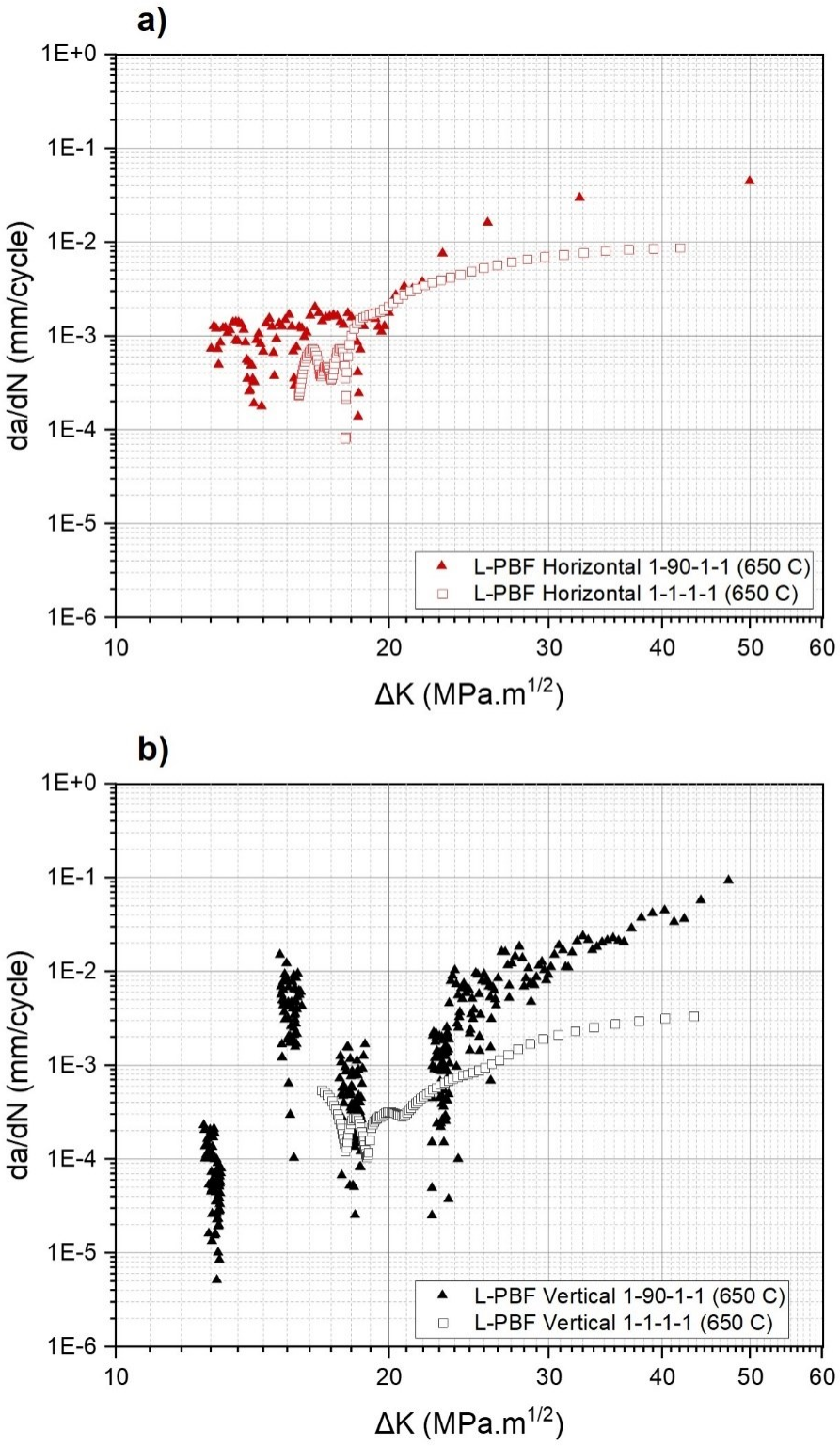

Figure 5.2 Comparison in FCG rates (da/dN vs ΔK) between 90 s dwells, and 1 s dwells at 650 ºC for: a) horizontal, and b) vertical heat treated specimens.

5.2.2 Fractography

Macroscopic overviews of the fracture surfaces from all tested specimens are presented in Figure 5.3. The EDM notch, pre-crack (at room temperature, and marked by beach marks), fatigue crack growth at high temperature and final failure can be easily distinguished and are indicated. All tests produced, in general, symmetric crack propagation and flat fracture surfaces within the FCG region. Differences in fracture surface roughness are apparent in the FCG area between L-PBF and cast and wrought specimens. These differences will be discussed in more detail later but can be mostly related to the large difference in grain size.

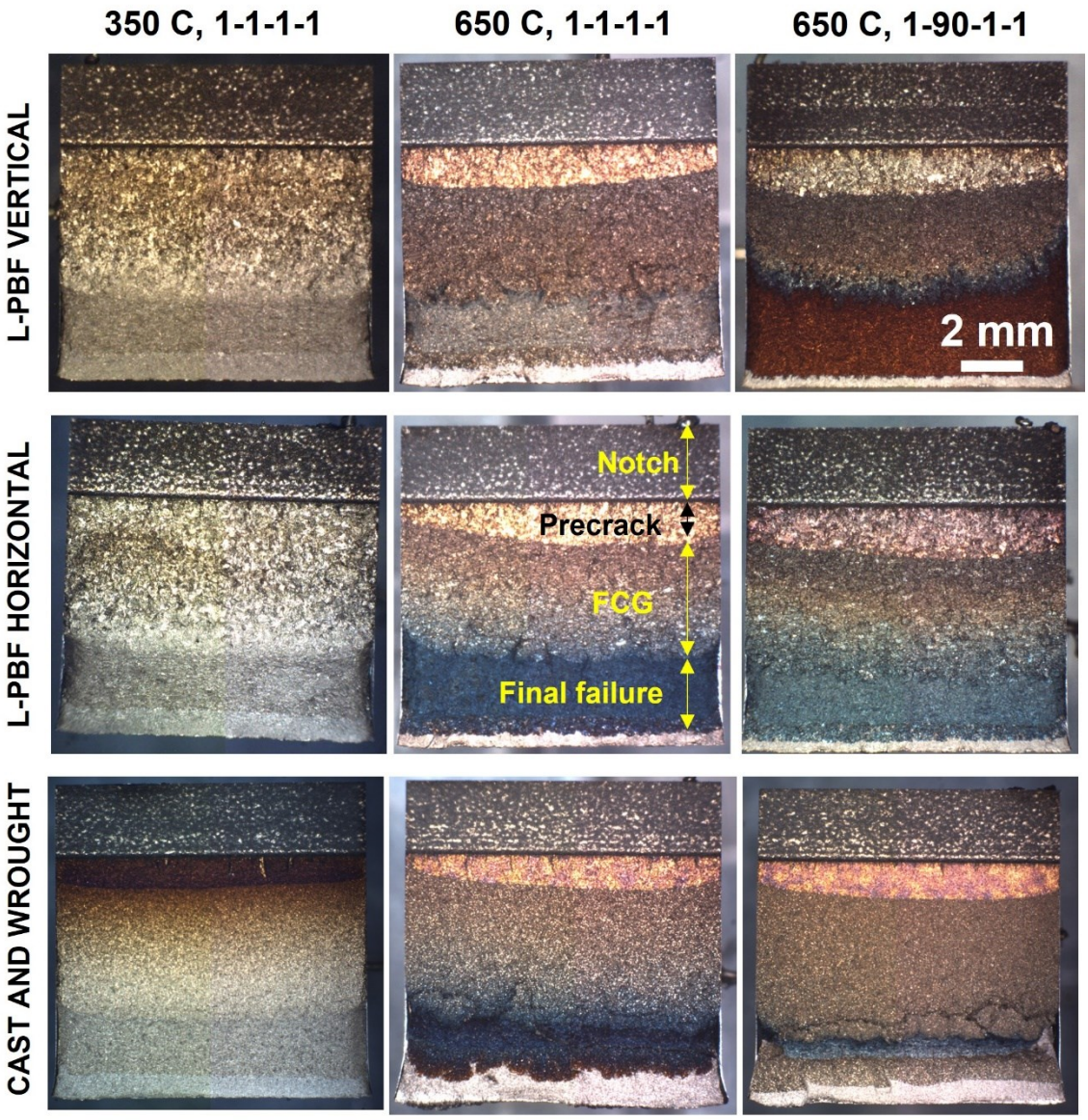

Figure 5.3 Overview of fracture surfaces for all tested specimens indicating different regions (notch, precrack, FCG, and final failure). Indicated scale applied to all images.

To further understand the mechanisms of FCG, the fracture surfaces were examined via SEM. A series of images were taken at different magnifications, and at various ΔK levels. The results from the SEM fractography investigations are shown in Figure 5.4 – 5.8. At 350 ºC and 1-1-1-1 testing frequency (see Figure 5.4), the fracture surfaces for all specimens are characterised by transgranular crack growth, across all ΔK levels. This is expected for IN718 at this temperature and frequency combination [134]. For all samples, a degree of faceting is seen, linked to slip band crack growth (indicative of stage I crack growth), these reduce as ΔK increases. This faceted fracture surface is similar for both L-PBF specimens, with build direction not having an apparent effect. CW specimens display flatter fracture surfaces, when compared to L-PBF mainly related to the differences in grain size resulting in smaller facets. Furthermore, ruptured blocky carbides could be seen in CW fracture surfaces, whereas no effect from carbides could be discerned from L-PBF specimens (note carbides are smaller when compared to CW). Secondary cracks are present for all specimens, and the quantity is consistent across all ΔK levels. These were mostly short, (size ranging between 5-10 μm), and were mostly present in intragranular areas with no apparent interaction with grain boundaries, which is expected for a material showing quasi-stage I /slip-band behaviour.

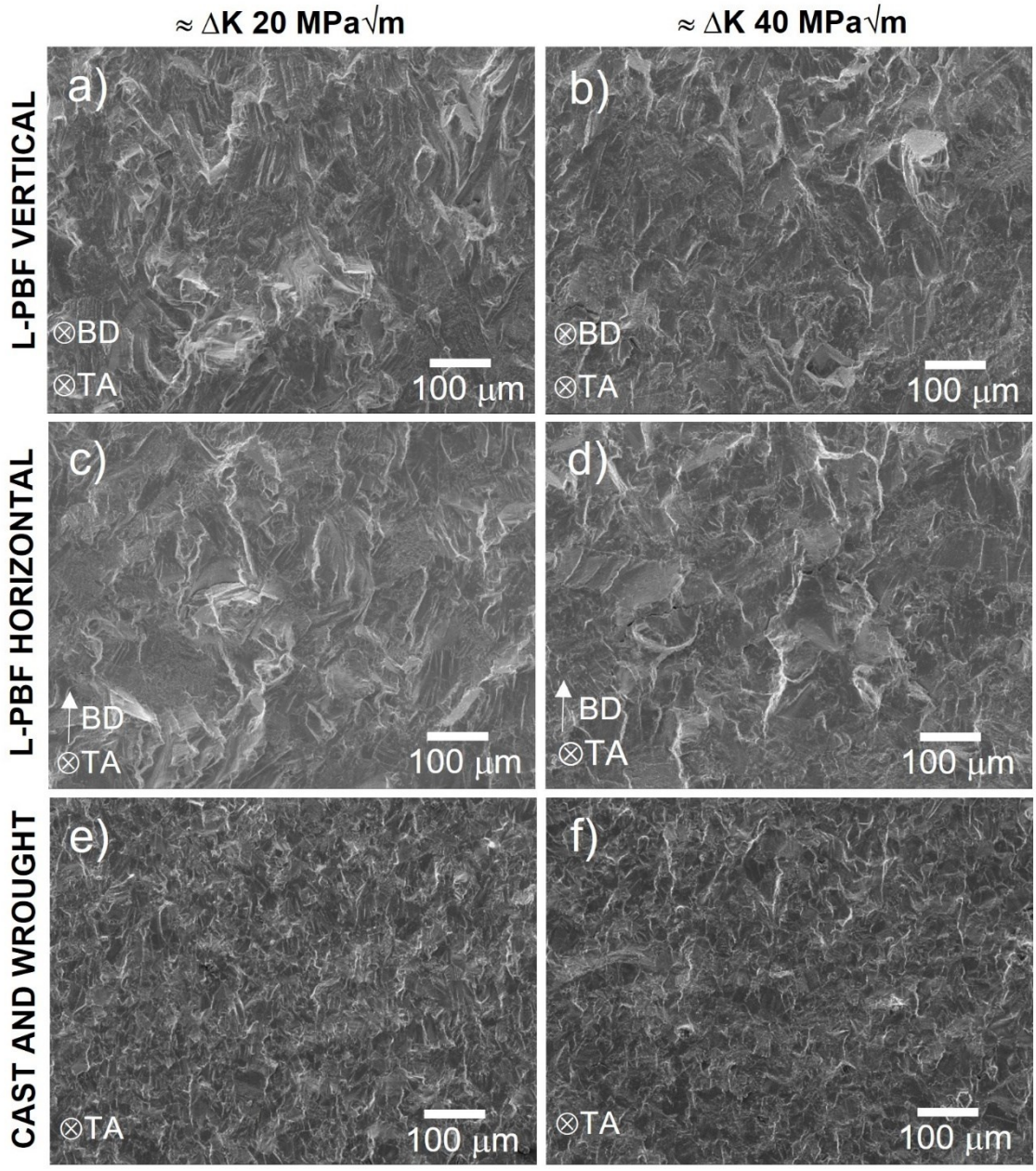

Figure 5.4 SEM micrographs at two different ΔK levels (20, and 40 MPa √m) for specimens tested at 350 ºC, and 1-1-1-1 testing frequency: vertical (a, b), horizontal (c, d), and cast and wrought (e,f).

When the testing temperature was increased to 650 ºC, while maintaining the same 1-1-1-1 testing frequency, the fracture surface for all specimens exhibits intergranular fracture modes with varying ΔK levels as shown in Figure 5.5, and Figure 5.6. This is ascribed to a greater degree of grain boundary oxidation with increased temperature, as expected in IN718, where the transition to intergranular failure at 650 ºC is reported to occur at frequencies around 0.5 Hz [135]. Even though intergranular failure is predominant in all cases, marked differences in failure mode between CW and L-PBF

specimens are apparent. CW specimens show brittle oxide cracking along grain boundaries, with the equiaxed shape of grains being clearly visible in the fracture surface. At higher magnifications (see Figure 5.6) clear intergranular fracture features are visible with detached grains and secondary cracking along grain boundaries. L-PBF vertical specimens exhibit a rougher and more tortuous fracture surface when compared to horizontal samples, mainly related to the difference in grain size (30 % larger grain size for vertical specimens). In addition, both L-PBF orientations have a considerably rougher looking fracture surface than CW. L-PBF specimens have a larger grain size with a less uniform shape, and a more discontinuous precipitation of δ-phase along grain boundaries, which can effectively pin cracks in between precipitates leading to a more tortuous crack path [136]. This rougher appearance is also linked to the presence of dimples/globular-like particles (primarily δ-phase) in the fracture surface, linked to the higher content of precipitation in intragranular areas for L-PBF compared to CW specimens.

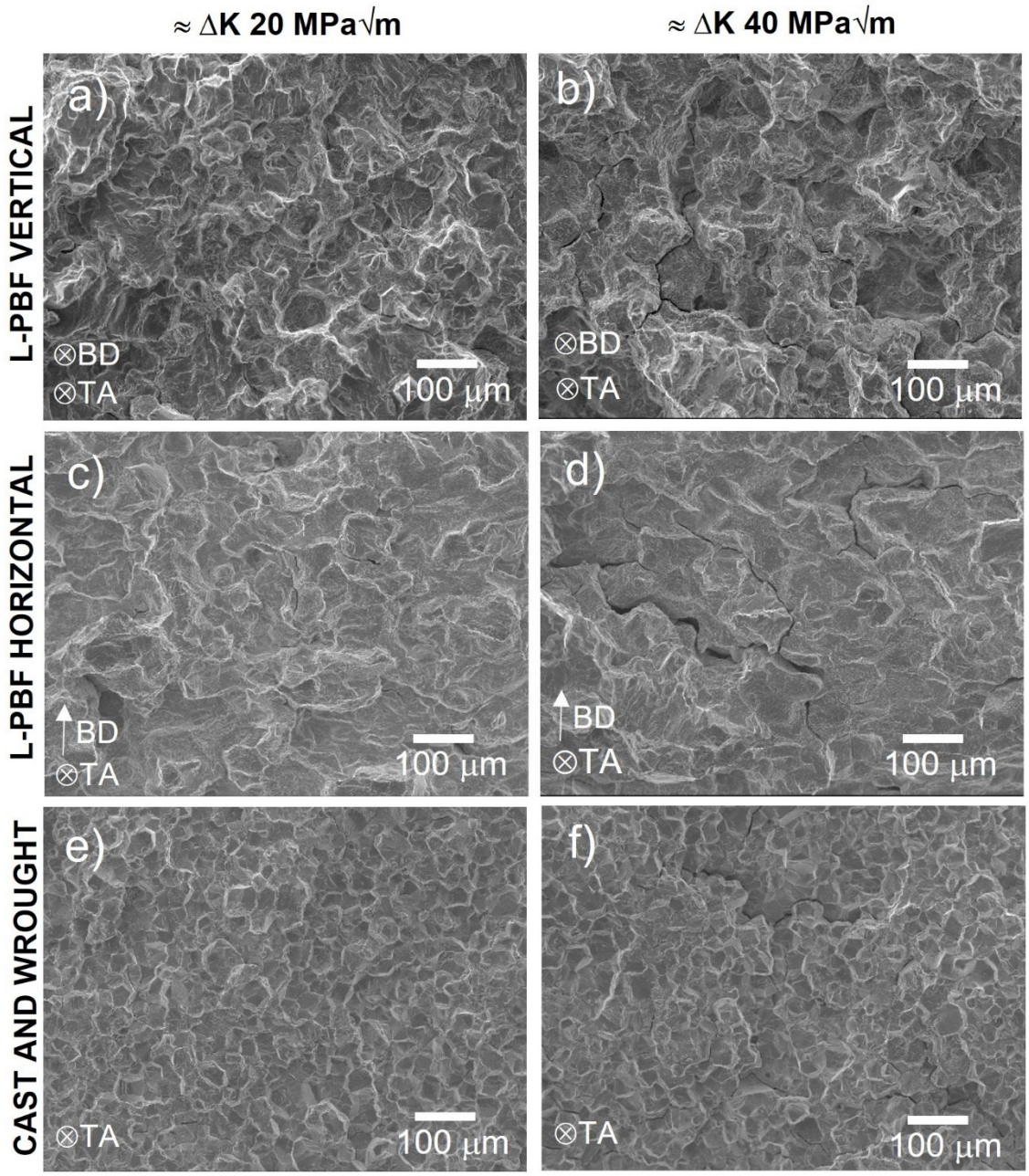

Figure 5.5 Low magnification SEM micrographs at two different ΔK levels (20, and 40 MPa √m) for specimens tested at 650 ºC, and 1-1-1-1 testing frequency: vertical (a, b), horizontal (c, d,) and cast and wrought (e, f).

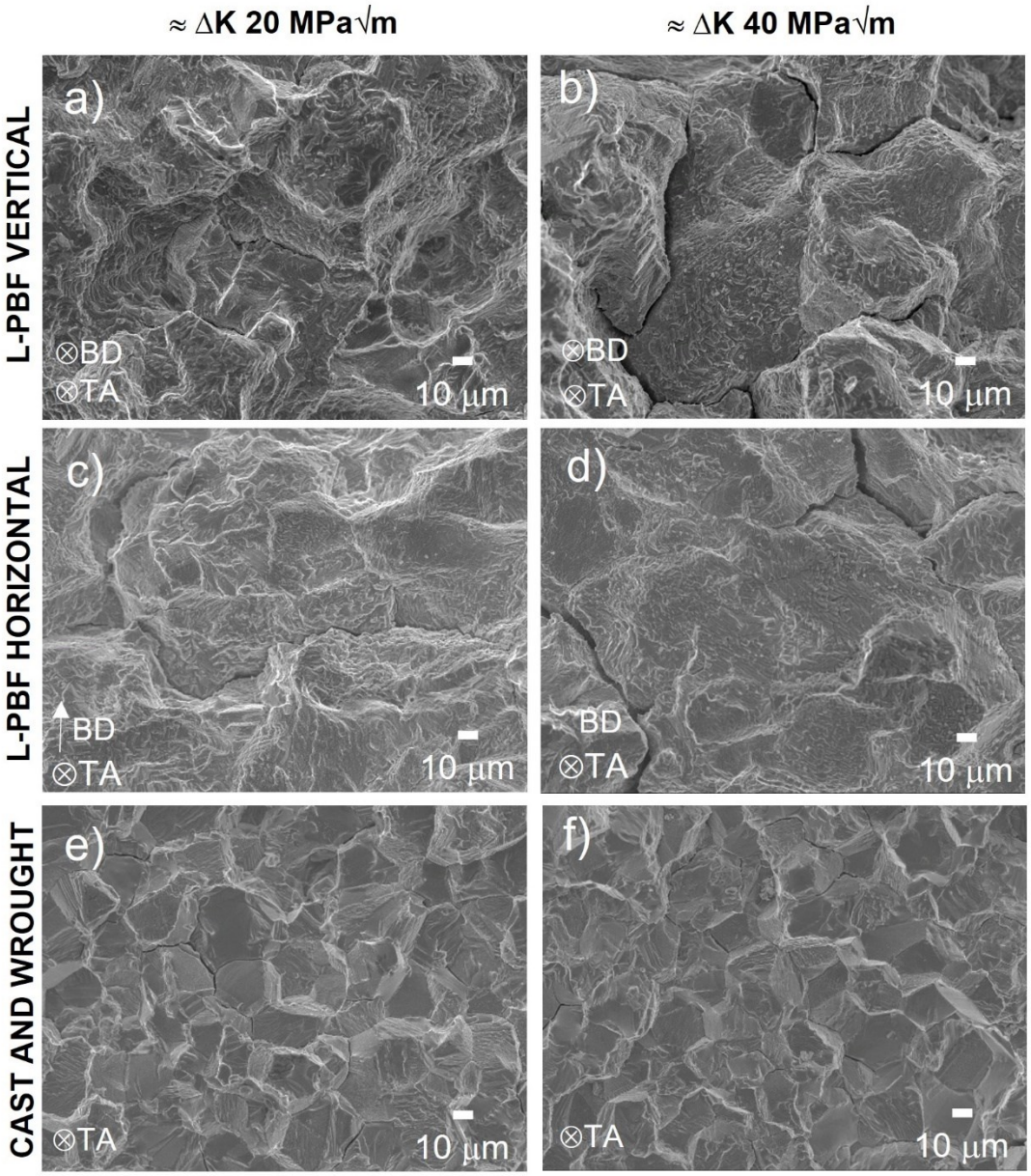

Figure 5.6 High magnification SEM micrographs at two different ΔK levels (20, and 40 MPa √m) for specimens tested at 650 ºC, and 1-1-1-1 testing frequency: vertical (a, b), horizontal (c, d,) and cast and wrought (e, f).

The fracture surfaces for tests with 90 s dwell at 650 ºC are shown in Figure 5.7, and Figure 5.8. The fracture surfaces show again clear intergranular failure modes, and the same difference in appearance between CW and L-PBF specimens is visible. Fracture surfaces display a rougher appearance when compared to those with 1 s dwells, plus vertical samples show again a more tortuous fracture surface, when compared to horizontal specimens. Long and continuous secondary cracks, and detachment of clusters of grains (see Figure 5.7) can be seen for all material conditions, especially at

higher ΔK values. Dimples/precipitates are once again visible along grain boundaries on the fracture surfaces of L-PBF specimens only (see Figure 5.8 a, b, c and d).

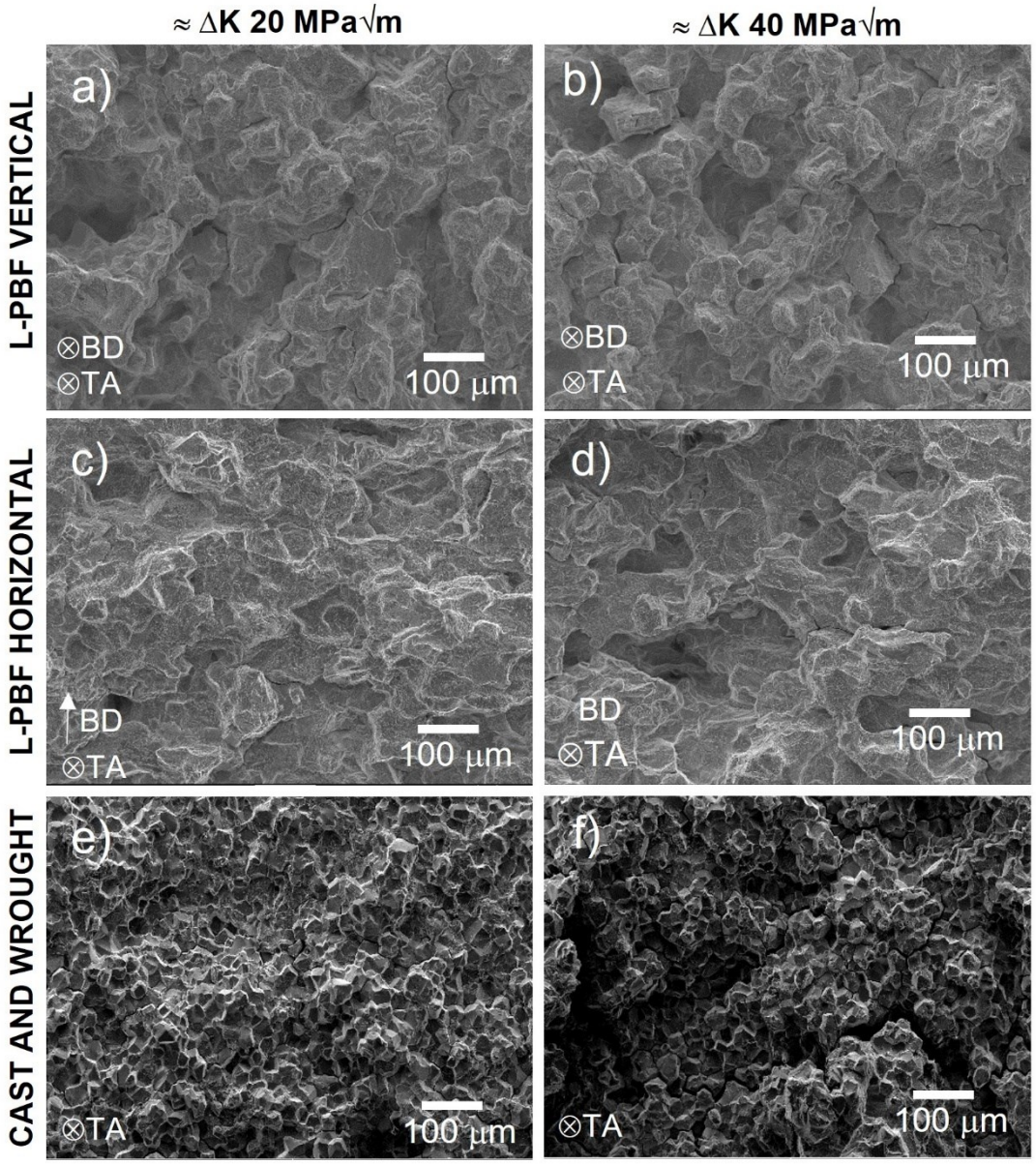

Figure 5.7 Low magnification SEM micrographs at two different ΔK levels (20, and 40 MPa √m) for specimens tested at 650 ºC, and 1-90-1-1 testing frequency: vertical (a, b), horizontal (c, d,) and cast and wrought (e, f).

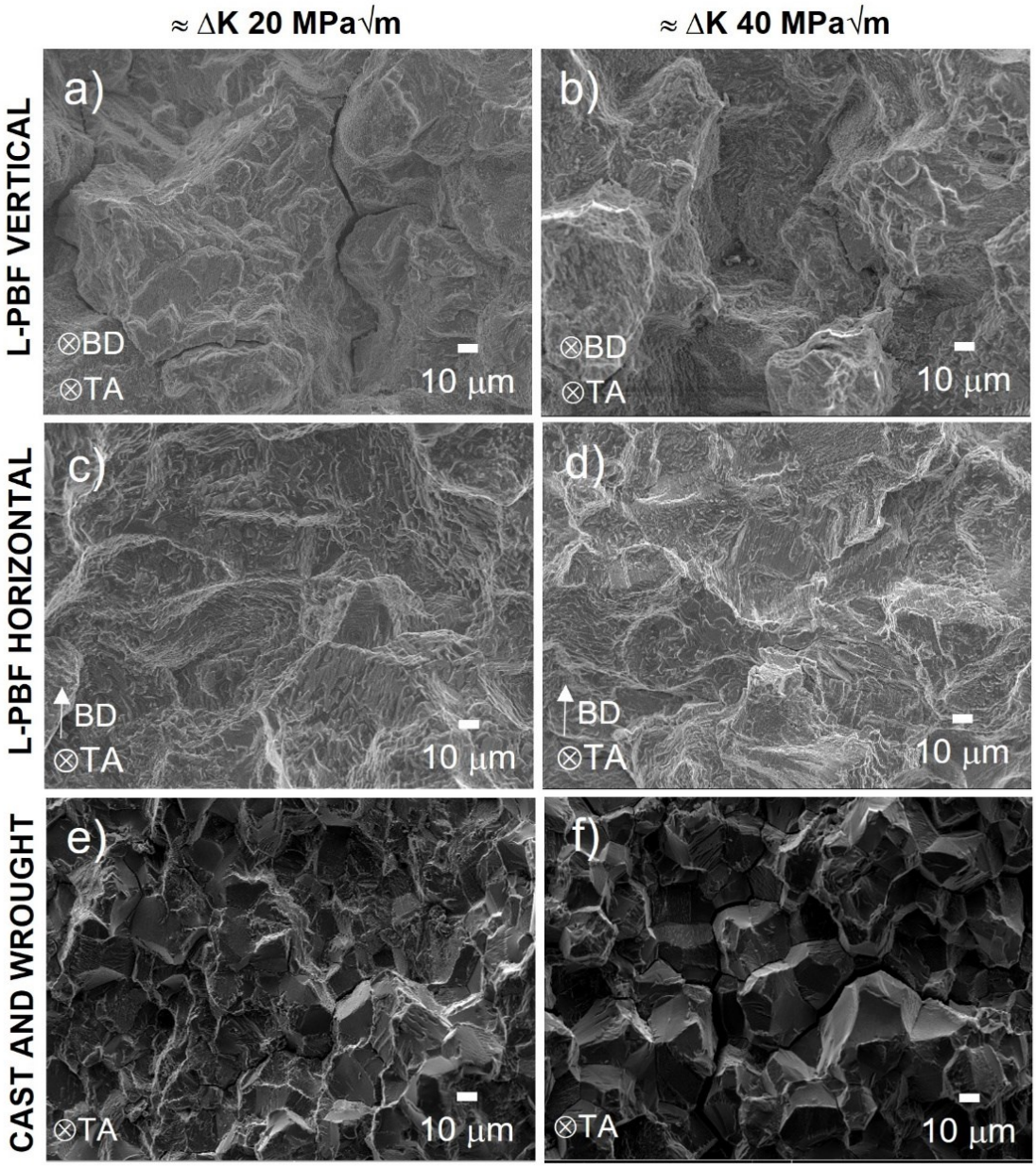

Figure 5.8 High magnification SEM micrographs at two different ΔK levels (20, and 40 MPa√m) for specimens tested at 650 ºC, and 1-90-1-1 testing frequency: vertical (a, b), horizontal (c, d,) and cast and wrought (e, f).

To further understand the difference in fracture mechanisms at different ΔK levels, surface area roughness measurements were taken using an Alicona infinite focus microscope, and the results are summarised in Figure 5.9-a. Generally, surface roughness increases (except for 1-90-1-1 tests on vertical samples) with increasing ΔK for all material conditions, and the results can be divided into two groups: transgranular FCG (lower roughness), and intergranular FCG (higher roughness). There are clear differences in fracture surface roughness between CW, and L-PBF specimens

(consistent with fractography), which is again primarily linked to the differences in grain size. Focussing on L-PBF specimens, at 350 ºC, both orientations exhibit a similar response with roughness varying between 15-30 µm approximately. By increasing the temperature and maintaining the same frequency (1 s dwells) the roughness increases significantly. Both L-PBF sample orientations show again a similar response with roughness varying between 40-75 μm, and roughness increasing as ΔK increases. Comparing the change in fracture surface roughness between 350 and 650 ºC, it is apparent that the effect of temperature is more significant than frequency, except for vertical specimens with 90s dwells. For horizontal samples however, at 650 ºC the surface roughness was comparable for tests with 1 s and 90 s dwells. Vertical samples show a very different response at low ΔK levels with the introduction of a 90 s dwell. Surface roughness values are significantly higher ranging between 70-85 μm over the ΔK range 15-25 MPa√m. This correlates with the data presented in Figure 5.1-b, where crack arrests were taking place over that ΔK range. The surface roughness then gradually decreases to similar values to horizontal specimens.

For intergranular fracture surfaces, the roughness will be related to the material grain size. To separate differences in grain size between L-PBF specimens, surface roughness values were normalised with grain size, shown in Figure 5.9-b. It can be seen that horizontal samples have a higher Sa/grain size value, which can be attributed to a higher degree of intergranular failure, explaining the higher FCG rates seen for this sample orientation. Interestingly, the normalised roughness values for vertical specimens with 90 s dwells is slightly higher than horizontal samples for low ΔK values (15-20 MPa√m). This is the same region where crack arrests took place showing a very tortuous crack path.

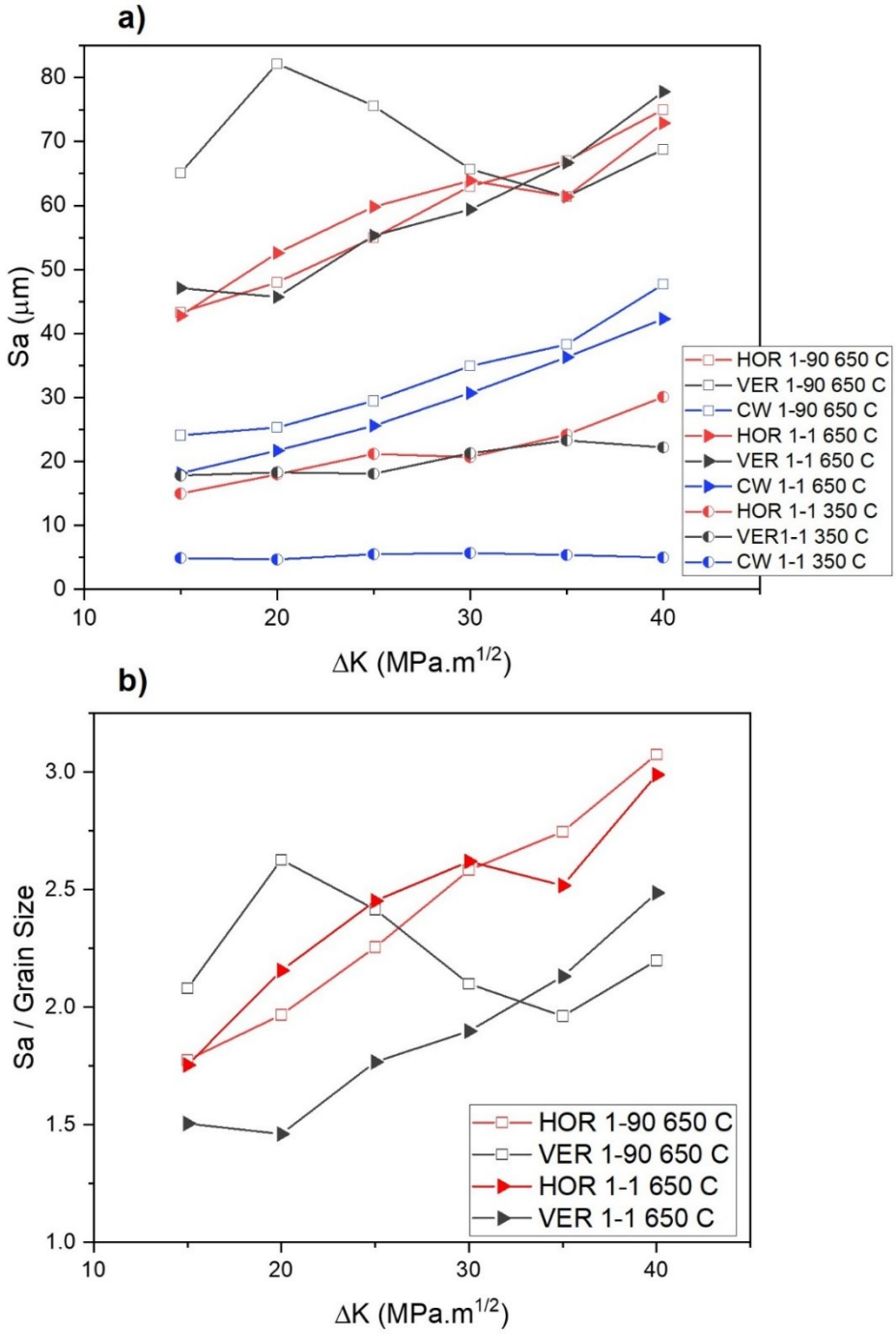

Figure 5.9 Surface area roughness vs ΔK for all testing conditions: a) raw data for all material conditions, b) roughness normalised with grain size for both L-PBF orientations. The filter cut-off (λc) value was set to 8 mm for all specimens except 1-1-1-1 tests at 350 ºC on CW specimens where the recorded roughness was lower, thus the cut-off filter was set to 2.5 mm following BS EN ISO 4288:1998.

Figure 5.10-a and b show Sa values against crack length with the monotonic and cyclic plastic zone size (calculated using Irwin's approach [128]) superimposed for horizontal and vertical specimens respectively. Figure 5.10-a helps explain the results where surface roughness increases with ΔK. Even though the failure mode is intergranular and

grain size does not change across the sample width, the plastic zone size ahead of the crack tip increases with increasing ΔK. As a result, surface roughness values follow the trend set by the cyclic plastic zone size. This does not apply for vertical samples with 90 s dwells however, where the increased tortuosity at low ΔK levels (regions of crack arrest) has a bigger effect on surface roughness. The jumps in plastic zone size seen in Figure 5.10-b are the result of crack arresting and the subsequent increase in load required to increase the applied ΔK and continue the test.

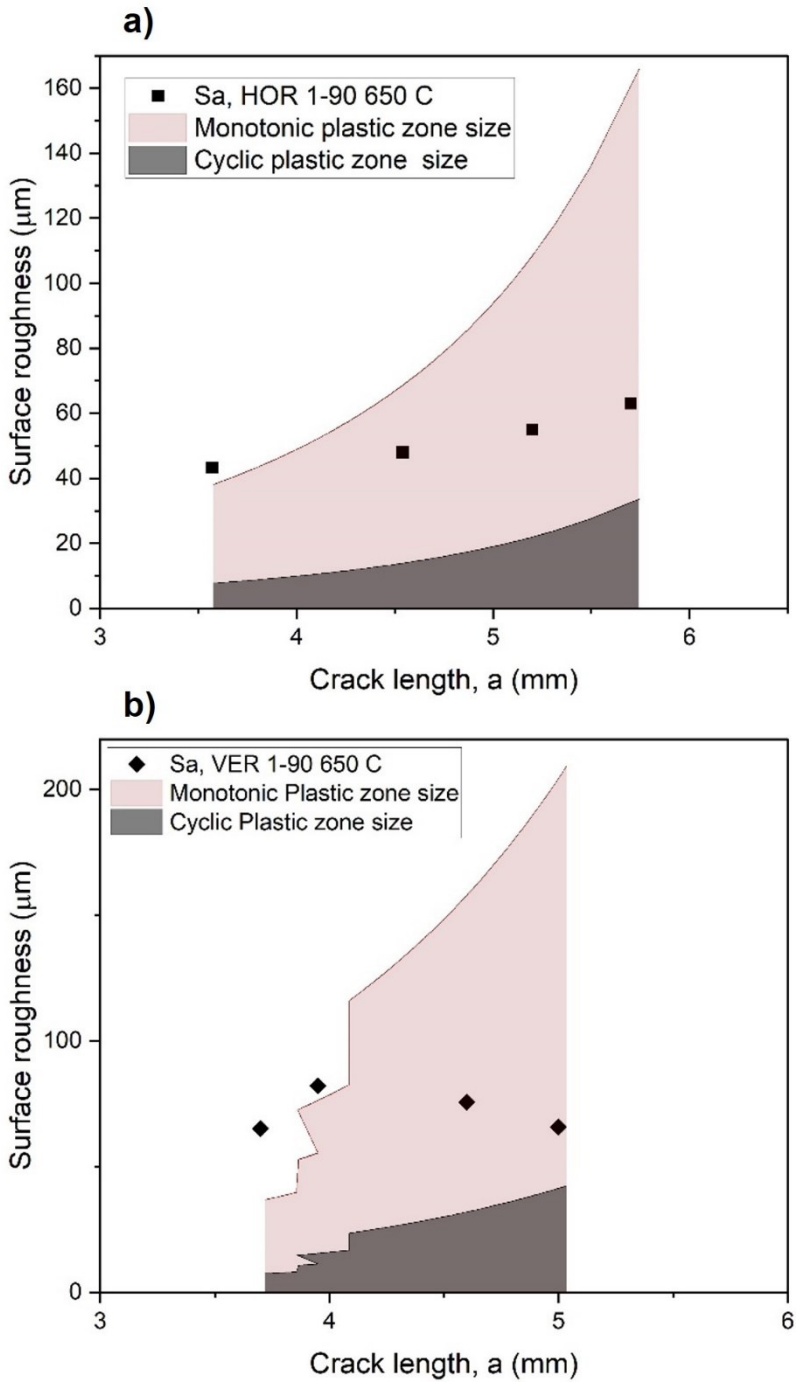

Figure 5.10 Comparison of plastic zone size (monotonic and cyclic) and surface area roughness vs crack length for testing at 650 ºC and 1-90-1-1 testing frequency for: a) horizontal, b) vertical.

5.2.3 Secondary cracks and crack deflection measurements

As shown in the fractography, secondary cracks are present in the fracture surfaces for all tests performed at 650 ºC (time-dependent regime). The amount of secondary cracking can be used to semi-quantitatively analyse the degree of intergranularity for a specific ΔK. A small amount of secondary cracking is usually understood to represent regions of slower crack growth, and the opposite (high number of secondary cracks) would be representative of higher crack growth rates [137]. To support this hypothesis and correlate the FCG rates from L-PBF specimens to fractography, the amount of secondary cracking was measured for testing performed at 650 ºC for both specimen orientations. The analysis was performed by evaluating SEM images at three different ΔK levels (20, 30, and 40 MPa$\sqrt{m}$). Four SEM (secondary electron imaging mode) images were taken at the same magnification (x150) and were subsequently analysed using the ImageJ software. To evaluate secondary cracks, images were segmented using the thresholding technique, to discriminate between cracked and uncracked regions. The critical threshold was determined as the point at which isolated bright pixels increased abruptly. Some additional filtering of the images was performed to remove non-cracked features, an example of such a reconstruction can be seen in Figure 5.11-a and b. The percentage area of secondary cracking was determined by summing the area of all cracked regions and dividing by the total examined fracture surface area. The percentage area of secondary cracking against ΔK is plotted in Figure 5.11-c. The results show an increase in the number of secondary cracks with increasing ΔK, except again at low ΔK for vertical samples tested with 90 s dwells. Furthermore, at a given ΔK there is an increase in secondary cracking comparing 1 s and 90 s dwells for both orientations, showing that even though roughness was comparable, there is a higher degree of intergranular failure for longer dwells (more oxidation damage). When comparing between orientations, horizontal samples show generally a higher number of secondary cracks, which correlates with the higher crack growth rates presented earlier. Finally, at low ΔK = 20 MPa$\sqrt{m}$, vertical samples show the highest percentage area of secondary cracking for any of the analysed samples (consistent with surface roughness measurements and fracture surface images) and will be discussed later in this chapter.

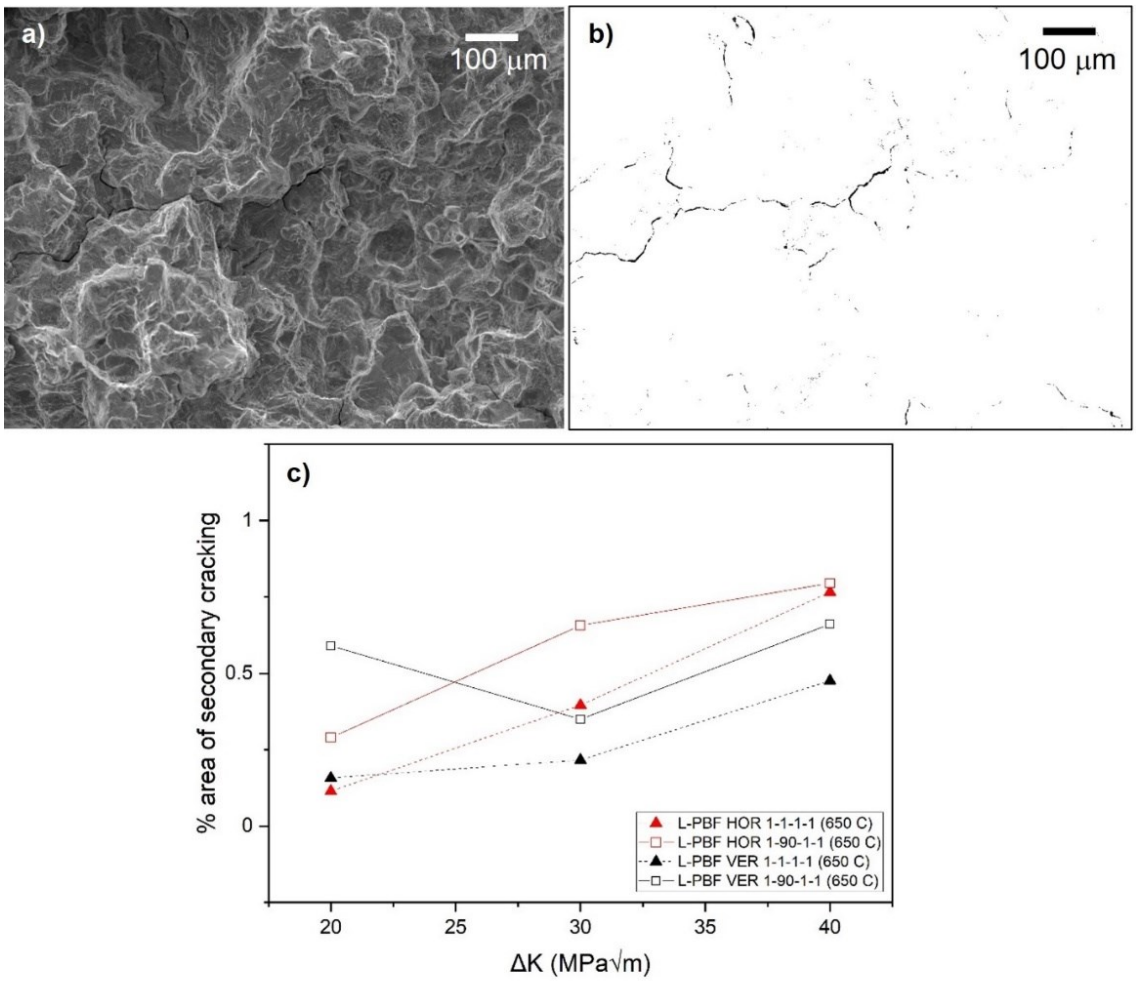

Figure 5.11 a) Original SEM image used to calculate amount secondary cracking, b) reconstructed image after thresholding was applied to isolate secondary cracks, c) percentage area of secondary cracking as a function of applied ⊿K.

To better understand crack growth behaviour at low ΔK values (crack arrest regions) for tests with 90 s dwells at 650 ºC, an assessment of the crack morphology was carried out, as the influence of crack deflection on FCG driving force at low ΔK (close to threshold) could be significant [138]. Specimens were nickel-plated prior to sectioning to preserve fracture surface integrity, and profiles of the crack path at low ΔK were obtained using an optical microscope. Figure 5.12-a presents the crack profiles for horizontal and vertical specimens respectively, showing the region where crack arrest was taking place for vertical samples. The crack deflection angle and ratio of deflected crack path length to projected crack length were measured. Figure 5.12-b presents the ratio of actual to projected crack length across the length of the crack. Scatter in the data can be seen for both specimens, yet horizontal specimens appear to consistently show ratios closer to 1 (straight crack). Vertical specimens exhibit several points with large

ratios of actual to projected crack length, as shown in the sectioned images. The effect of these deflections on the crack tip driving force (k) can be estimated using the equations provided by Suresh et al. [139]. The values of the local stress intensities k_1, and k_2 (see Figure 5.12-c for reference diagram) can be related to the applied K_1 and deflection angle θ by equations (5-1), and (5-2). The effective ΔK resultant from crack deflection can then be calculated by equation (5-3).

$$k_1 = \frac{1}{4}\left(3\cos\frac{\theta}{2} + \cos\frac{3\theta}{2}\right)K_1 \quad (5\text{-}1)$$

$$k_2 = \frac{1}{4}\left(\sin\frac{\theta}{2} + \sin\frac{3\theta}{2}\right)K_1 \quad (5\text{-}2)$$

$$K_{eff} = \sqrt{k_1^2 + k_2^2} \quad (5\text{-}3)$$

These simplified effects of crack deflection on ΔK, across the length of the crack, are plotted in Figure 5.12-d and e for horizontal and vertical specimens respectively. The graphs show the applied ΔK (calculated from the DCPD trace) for each micrograph and effective ΔK. Furthermore, a box is included in the graph to represent a range of IN718 threshold values reported in the literature for testing at 650 ºC and R=0.1 [123], [134]. Horizontal specimens show some scatter in the data, however, effective ΔK values generally match with applied ΔK across the length of the investigated crack. For vertical specimens, the response is very different exhibiting higher reductions in effective ΔK, in some cases even reaching threshold. The marked shifts in applied ΔK data are a result of the crack arrest periods and subsequent increments in load. It can be seen that at the beginning of each block there is a large reduction for effective ΔK, lowering the FCG crack driving force and resulting in crack arrest. Furthermore, this analysis only considers deflections in the profile of the main crack, not considering any effect of secondary crack branching. Figure 5.12-a correlates with the results presented in Figure 5.11-c considering the amount of secondary cracking for vertical specimens at $\Delta K = 20$ MPa$\sqrt{m}$. Where well developed, tortuous secondary cracks can be seen, which will potentially reduce the effective ΔK even more than just the effects of deflection in the main crack.

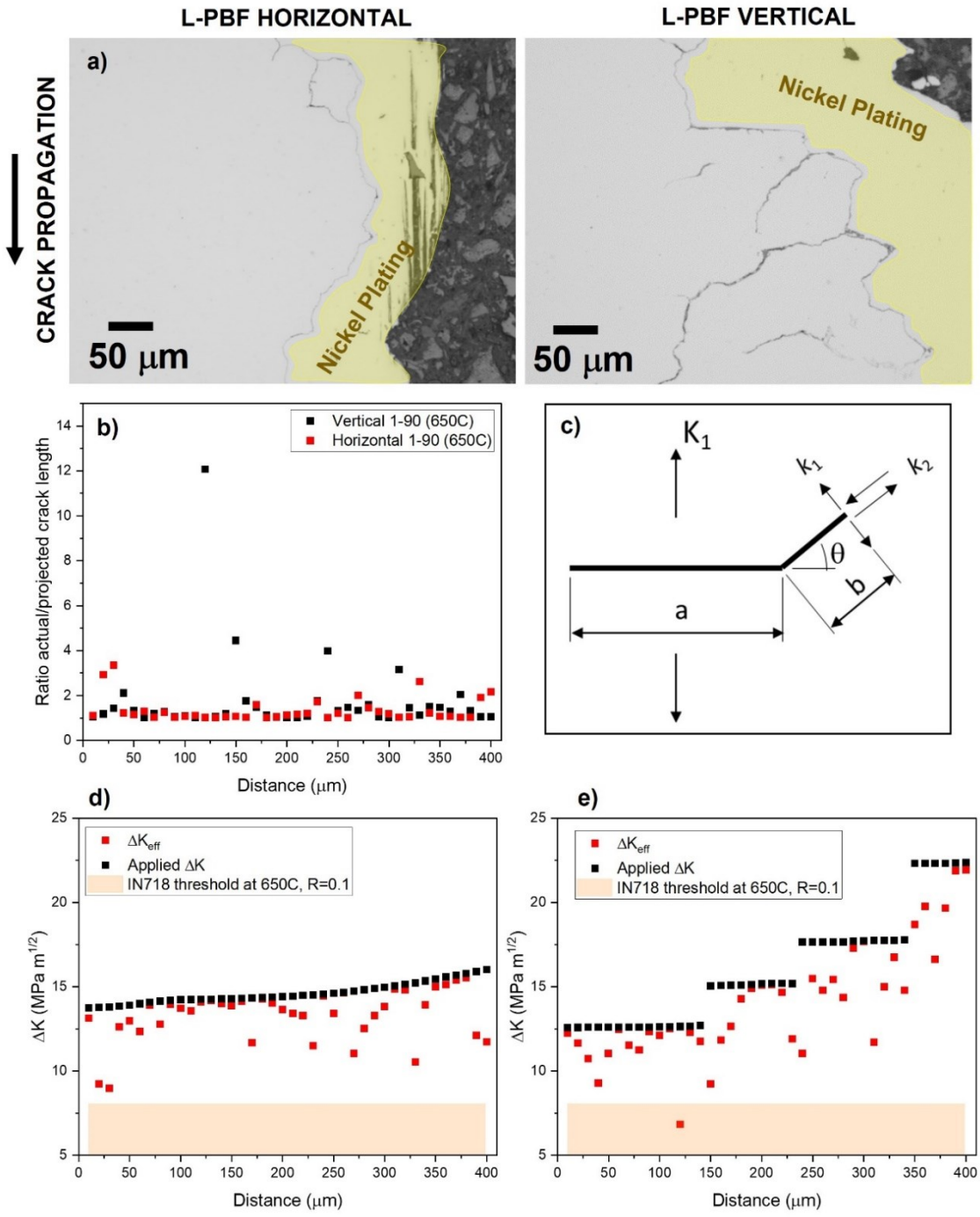

Figure 5.12 Crack deflection measurements: a) Sections of the fracture surface used to calculate ΔK_{eff} from deflected cracks for vertical and horizontal specimens (Nickel plated area is highlighted in yellow) b) ratio of actual/projected crack length vs. distance c) schematic representing a kinked crack and the nomenclature used to describe stress intensity factors d, e) ratio of ΔK_{eff} / ΔK vs. distance for horizontal (d) and vertical (e) specimens, with shaded range for IN718 threshold values reported in the literature [123], [134].

5.3 Discussion

5.3.1 Build orientation, microstructural effects, and comparison with cast and wrought specimens

The results presented in chapter 4, showed that the L-PBF microstructure post heat treatment for both orientations was similar and relatively isotropic from a crystallographic point of view, having eliminated the strong texture characteristic of as-built AM components. There are however marked differences with regards to grain size, distribution, shape, and number of twins. As shown, vertical samples have a larger average grain size (≈ 30 %), and for both orientations the majority of grains range in size between 10-70 μm. However, the area fraction occupied by larger grains (70-250 μm) is 10 % greater for vertical samples. Differences in grain size have been found to have a large influence on the fatigue performance of Ni-based superalloys at high temperature [38–40]. It is well documented that grain boundaries act as preferential diffusion paths for oxidising species due to their relatively high defect density. As such, finer grained structures present a larger number of grain boundaries subject to oxidation, resulting in accelerated fatigue crack growth under time-dependent conditions. In addition to improved oxidation resistance, the larger grains promote more tortuous crack paths, deflecting the crack as it propagates and reducing FCG rates. The orientation of anisotropic grain shapes found in this study, combined with the differences in grain size, would both have contributed to increased crack path deflection in vertical L-PBF samples.

As presented in Figure 4.10, the microstructures for both orientations are not equiaxed with grains having a defined aspect ratio. To correlate grain shape to crack deflection, and roughness studies, an analysis of the orientation of the grains' long axes around the crack path was performed. The long axes' orientations of grains surrounding the crack were recorded at three different ΔK levels (15, 20, and 30 MPa$\sqrt{m}$), and plotted in a histogram with respect to the direction of crack propagation, as shown in Figure 5.13-a. Horizontal samples don't present a preferential long axis orientation, with well distributed grains. However, for vertical samples the majority of grains are oriented perpendicular to the direction of crack propagation. The resultant grain shape distribution is not as extreme as for as-built, or sub-solvus heat treated components [8, 41, 42]. However, it is still present and will have had an effect on FCG rates by reducing the stress intensity at the crack tip by deflecting the crack, as shown in Figure 5.12. To further understand microstructural effects on crack deflection, the grain size distribution for grains surrounding the main fatigue crack was studied. Average grain size was 56 and 42 μm

for vertical and horizontal specimens respectively, and their distribution is shown in Figure 5.13-b. As shown, horizontal specimens have a 25 % higher fraction of small grains (smaller than 25 μm) surrounding the crack. In addition, 15 % of the grains counted in the vertical samples ranged in sizes between 130-220 μm, with none being this large in the horizontal samples. This difference further affected crack deflection which can be linked to these quite subtle microstructural differences between samples. Example EBSD diagrams used to extract the data to characterise the orientation of the grains' long axes and grain size around the crack path are presented for reference in Figure 5.13 for horizontal (Figure 5.13-c) and vertical (Figure 5.13-d) specimens.

Grain boundary character can also have an effect on the crack path chosen affecting FCG rates. There is some evidence in the literature that for IN718 oxygen diffusivity along grain boundaries is slower for special CSL grain boundaries [43, 44]. With Σ3-type grain boundaries showing the highest resistance against oxygen diffusion, and cracking [105]. Therefore, random high angle grain boundaries will be preferentially attacked/embrittled at high temperatures where intergranular cracking is dominant. Investigations of the fatigue crack path, and secondary cracks from tested specimens showed that Σ3 (twin) boundaries were not susceptible to cracking. As explained in chapter 4, the percentage area fraction of Σ3 twin boundaries for vertical samples is larger (≈ 4% higher) when compared to horizontal samples. Thus, this relatively higher fraction of Σ3 twin boundaries can have a beneficial impact by increasing crack front tortuosity, and by increasing the resistance of vertical specimens to dynamic embrittlement. This idea is also supported by the results presented in Figure 5.11-c, which shows that horizontal specimens have on average a higher degree of intergranular failure. Their smaller grain size, and lower area fraction of twins resulting in a higher number of grains being susceptible to embrittlement.

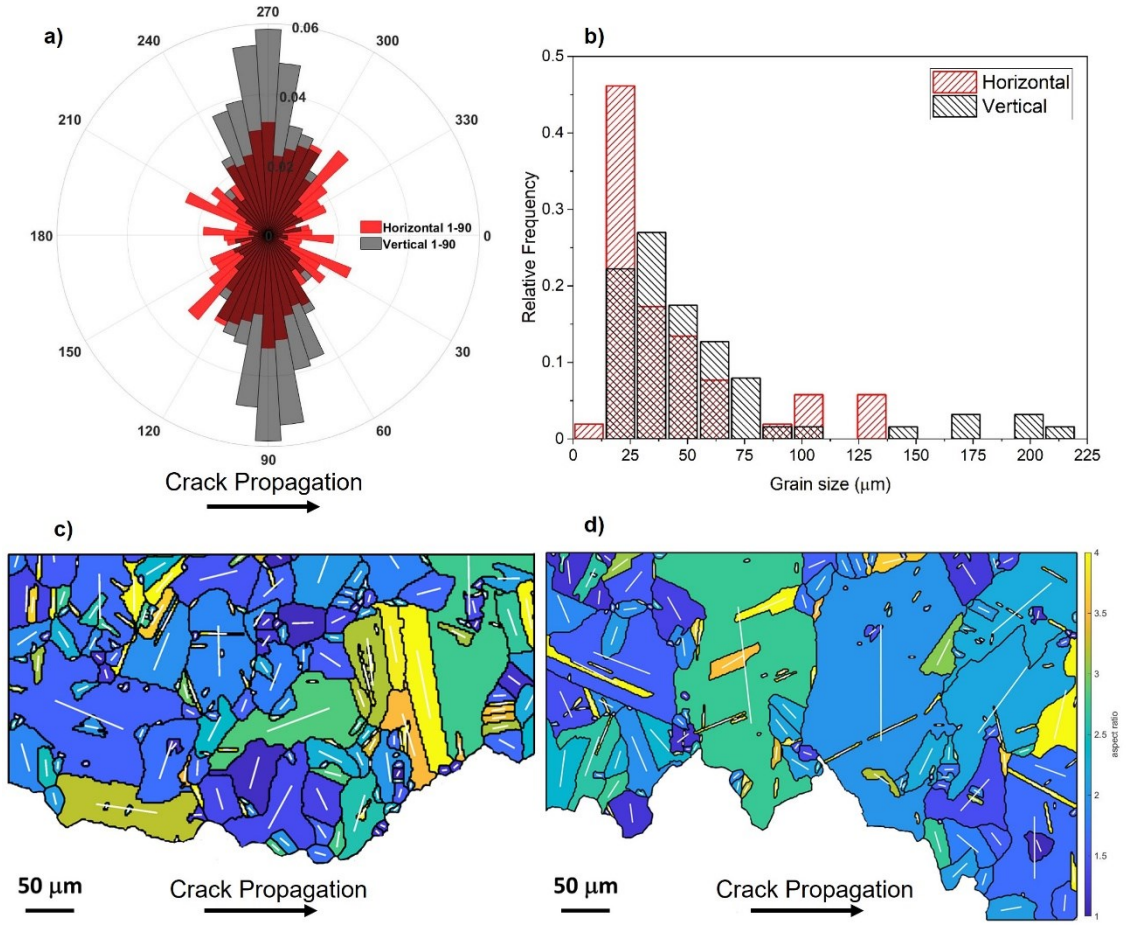

Figure 5.13 Grain shape and size distribution for grains surrounding the main fatigue crack (testing at 650 ºC, and 1-90-1-1 frequency): a) weighted area histogram of grains' long axes distribution (relative frequency) with respect to direction of crack propagation, b) grain size distribution and example EBSD diagrams used to calculate graphs a, b for c) horizontal and d) vertical specimens showing the aspect ratio and orientation of the grains' long axes.

No appreciable differences in FCG rates were found at 350 ºC (transgranular crack propagation) between CW, and L-PBF specimens. However, at 650 ºC (intergranular crack propagation) large differences in both FCG rates and fracture surface appearance (failure mechanisms) were observed between CW and L-PBF specimens. The main differences between material conditions were linked to grain size, grain shape, and percentage area fraction of twins. Although differences in primary carbide dimensions, and precipitation of δ-phase in grain boundaries and intergranular regions also exist. The CW material has a finer grain size distribution with average grain size 16.83 μm, which is 45% and 86% smaller when compared to horizontal and vertical samples. In addition, the percentage area fraction of twin grain boundaries is smaller (≈ 30% lower) compared to L-PBF heat treated specimens. As previously explained, the smaller the grain size, and the lower the percentage of twin grain boundaries, the larger the amount of grain boundaries susceptible to embrittlement and cracking (faster FCG rates). Furthermore, the CW material presents a fairly equiaxed grain structure, compared to the less uniform

shape of the grains in both L-PBF orientations. As a consequence, the effect of crack deflection slowing crack propagation will not be as significant in CW when compared to even the L-PBF horizontal specimens. Slight differences in the precipitation of the δ-phase in grain boundaries between cast and wrought and L-PBF specimens were shown in chapter 4. It is generally understood that the precipitation of δ-phase at grain boundaries is beneficial for high temperature properties of IN718. Its precipitation leads to a γ' and γ'' depleted region around the grain boundaries that has a higher ductility which can relax stress concentration around the crack tip, improving resistance against crack growth [62], [145]. However, it has been reported that, if aligned with the propagating crack, it can also act as a preferential cracking site, accelerating FCG rates [136], [146]. For CW specimens, δ-phase mostly precipitates as almost continuous films aligned with grain boundaries (parallel to crack propagation under intergranular failure). L-PBF specimens, however, have a more discontinuous precipitation of δ-phase along grain boundaries, and no preferred alignment was observed for both orientations (precipitates randomly either appeared parallel or perpendicular to grain boundaries) resulting in a higher resistance to intergranular crack propagation compared to CW specimens. Hence, the combination of differences in grain size, grain shape, number of twins and precipitation of δ-phase can be used to explain the large differences seen on the fracture surface, and higher FCG rates for cast and wrought specimens.

5.3.2 Temperature and dwell time effects on FCG rates for L-PBF specimens

The effect of temperature, and dwell time on FCG rates for AM IN718 have been assessed in this study. The crack growth rates significantly increased when temperatures were increased to 650 ºC, compared to 350 ºC at the same testing frequency (more notably for horizontal samples). The increase in da/dN was not as evident with the introduction of 90 s dwells (compared to 1 s dwells), however, it led to crack arrest at low ΔK values for vertical samples. This dramatic change in FCG rates caused by an increase in temperature, and/or introduction of longer dwells can be primarily associated with oxidation of grain boundaries ahead of the crack tip (manifested by intergranular fracture modes), although creep processes can also have a negative impact on the high temperature fatigue properties of nickel based superalloys [46, 47]. It has been reported that for cast and wrought IN718 the main time-dependent cracking mechanism controlling fatigue is environmentally assisted grain boundary attack, with IN718 showing high resistance against creep for the testing temperatures used in this study. However, recent high temperature studies performed on AM IN718 have shown that creep was

active even at 550 ºC [43, 48]. They found that the dislocation cell substructure present in some AM components was susceptible to creep damage, since this dislocation substructure was similar to that found in the tertiary creep regime, even though the material did not creep during manufacture. However, the HIPing temperature used in this study is higher than the homogenisation temperature used in other studies, and the structure is more recrystallised with no cellular substructure discernible. Furthermore, creep is a thermally activated process (oxygen not necessary) and as such, secondary cracks don't necessarily have to initiate from the main crack. However, all the secondary cracks observed in this study (see Figure 5.12-a for reference) originated from the main crack, suggesting oxygen assisted grain boundary attack as the main cracking mechanism.

The underlying mechanism controlling the interaction between oxygen and the crack tip is, however, not fully understood and there is still debate in the literature. There are two dominating theories: dynamic embrittlement and stress assisted grain boundary oxidation (SAGBO). Dynamic embrittlement proposes an embrittlement of grain boundaries by oxygen diffusion over very short distances, leading to grain boundary cracking when stress is applied. For SAGBO, the diffusing oxygen reacts with Niobium (in the case of IN718) present at grain boundaries (primarily large NbC, or γ'') forming a brittle oxide (Nb_2O_5) ahead of the crack tip. This oxide then cracks under stress leading to accelerated FCG rates and intergranular failure. However, primary carbides formed in AM IN718 are smaller (so expected to have a reduced effect) and the oxidation rate of IN718 at this temperature is relatively slow compared to the observed FCG rates [96], [97], [150]. Therefore, considering the very fast crack propagation rates observed at 650 ºC, it is more likely that the grain boundary attack is caused by dynamic embrittlement.

The effect of dynamic embrittlement on FCG will be highly dependent on the availability of oxidising species at the crack tip, which in turn is related to available diffusion paths, oxygen diffusivity, and diffusion time. The higher diffusivity of oxygen as temperature increases, and longer diffusion time per loading cycle (introduction of 90 s dwell at peak load) will lead to higher FCG rates. Hence the highest FCG rate occurred for 90 s dwells, and 650 ºC for horizontal samples. It is important to note however, that the introduction of 90 s dwells only marginally increased FCG rates for horizontal specimens. Indicating an effective saturation of the FCG rate, and oxidation damage with dynamic embrittlement occurring easily at both frequencies for testing at 650 ºC. For vertical samples, however, the introduction of 90 s dwells led to crack arrest instead of accelerating FCG. Their improved resistance against crack growth can be explained in terms of a coarser grained structure, a higher area fraction of twin boundaries, and grain

boundaries preferentially aligned against the direction of crack propagation. However, the mechanistic reason for significant crack deflection (crack arresting) to be activated with 90 s dwells at 650 ºC cannot be fully explained with the testing presented in this chapter. Chapter 6 will aim to answer this question, and help elucidate the interaction between the crack tip, microstructure, and environment for additively manufactured IN718.

5.3.3 Fracture mechanism assessment on L-PBF specimens: fractography, surface roughness, and secondary cracks

Different types of fracture modes (transgranular or intergranular) have been observed in the fractography presented in this study. At intermediate temperatures (350 ºC), and 1 s dwells (0.25 Hz) the fracture mode was transgranular (cycle-dependent crack growth), whereas at higher temperatures (650 ºC) intergranular fractures were dominant at both tested frequencies and for both orientations. This transition to fully intergranular failure at 650 ºC with 1 s dwells (0.25 Hz) is expected, and consistent with data for cast and wrought IN718 [30, 46, 47]. To better understand the relationship between deformation behaviour and FCG rates, the roughness of the fracture surfaces and degree of secondary cracking was systematically analysed. Normally, roughness will be expected to be of the order of grain size for intergranular failure, and smaller for transgranular crack growth [152], [153]. As shown in Figure 5.9, the roughness of the fracture surface does correlate with fracture modes, with tests at 650 ºC having higher roughness. It is also found that for testing at 650 ºC most roughness values (except vertical 1-90-1-1 tests) lie approximately within a ±10 μm range across all ΔK values. This range is close to the average grain size, indicating a saturation of the surface roughness value. As ΔK increases, the surface roughness increases accordingly for all intergranular fracture surfaces (less significantly so for testing at 350 ºC). This can be linked to two factors: increase in plastic zone size, and a higher amount of secondary cracking. As shown, in Figure 5.10, as surface roughness increases with ΔK, the size of the cyclic and monotonic plastic zone increases accordingly. This will effectively influence the crack wake as it propagates, increasing the measured surface roughness. In addition, a higher amount of secondary cracking (Figure 5.11-b shows that the quantity of secondary cracks increases with ΔK) can lead to the formation of clusters of grains separating from the fracture surface, increasing the surface roughness to higher values than the average grain size. There is, however, one outlier with the results from vertical specimens and 90 s dwells, where the measured surface roughness and number of secondary cracks are significantly higher than for any other case. This, however, can be explained through

crack deflection and microstructural considerations as discussed previously, showing good correlation between crack path, surface roughness, secondary cracking, and FCG rates.

The effect of grain size on fracture surface roughness was further studied by normalising the data to the average grain size for each orientation. The grain size normalised roughness is, on average, 50 % higher for horizontal compared to vertical specimens for all tests at 650 ºC (excepting low ΔK values for vertical 90 s dwell tests). This indicates more severe intergranular failure for the horizontal specimens, and as a consequence higher FCG rates. From these results, it appears that the degree of secondary cracking has a correlation with surface area roughness (normalised with grain size), with both parameters showing the same behaviour across all ΔK values. Therefore, it can be inferred that the surface area roughness of the fracture surface is controlled to some extent by the development of secondary cracks for intergranular failure modes. For transgranular fracture mode, however, the roughness seems to be controlled by the number of facets present in the fracture surface, with no significant difference seen between build orientations.

5.4 Summary

The influence of build orientation on FCG mechanisms with varying temperature and frequency for IN718 fabricated by laser-powder bed fusion were investigated in this chapter and the main conclusions were:

1. At 350 ºC, and 1-1-1-1 frequency there were no differences on FCG rates between cast and wrought, horizontally, and vertically built specimens with the failure mode being primarily transgranular crack growth.

2. The crack growth rate increased with increasing temperature and dwell time for all material conditions, with a transition from transgranular to intergranular crack growth.

3. Build orientation had a significant effect on FCG rates at high temperature under time-dependent crack propagation conditions. This was primarily related to microstructural differences in grain size distribution, grain shape and grain boundary character.

4. Vertical specimens (crack propagating perpendicular to build direction) displayed slower FCG rates at 650 ºC when compared to horizontal specimens. This is linked to more tortuous crack paths, and typically less secondary cracking

due to a coarser grained structure, a higher area fraction of twin boundaries, and grain boundaries preferentially aligned against the direction of crack propagation.

5. Crack arrest occurred only for vertical specimens with the introduction of 90 s dwells at 650 ºC. A combination of grain size distribution, and grain shape for vertical specimens heavily deflected the crack, resulting in a lower effective ΔK arresting the crack.

6. At 650 ºC, large differences in both FCG rates and failure mechanisms were observed between CW, and L-PBF specimens. The CW material has a smaller grain size, and a lower area fraction of twin grain boundaries, which results in a much larger number of grain boundaries susceptible to embrittlement. Plus, the equiaxed grain structure is not as effective at deflecting cracks as the irregularly shaped grain boundaries found in L-PBF materials. This, coupled with preferentially aligned δ-phase at grain boundaries, explains the differences seen in FCG rates, and grain boundary failure mechanisms.

6 Oxidation effects on fatigue crack propagation

6.1 Introduction

Chapter 5 focussed on the effect of temperature and dwell time on FCG rates, and crack propagation mechanisms for L-PBF Inconel 718. It was seen that horizontal specimens have on average a higher degree of intergranular failure, and faster FCG rates. Their smaller grain size, and lower area fraction of twins resulted in a higher number of grains susceptible to embrittlement. With longer dwell times, vertical samples again showed greater crack growth resistance, with crack arrest occurring at low ΔK values due to observable crack deflections reducing the effective stress intensity at the crack tip. In this chapter oxidation-fatigue mechanisms will be further investigated to characterise differences between cast and wrought, and L-PBF specimens as well as differences between sample orientations. Fatigue tests were performed alternating between high and low frequency regimes at 650 ºC (referred to as “block testing”). These assessed the extent of oxidation related damage ahead of the crack tip by analysing the transition region between the two frequencies. Interrupted tests (1-90-1-1 testing frequency) were also performed to further understand the differences in oxidation mechanisms ahead of the crack tip between both sample orientations.

6.2 Results

6.2.1 Block tests

6.2.1.1 Fatigue crack growth behaviour

FCG rates over a range of ΔK values from the alternating frequency testing (block tests) are presented in Figure 6.1 for all material conditions (cast and wrought, and L-PBF vertical and horizontal). The transitions in frequency occurred for all specimens around the same ΔK levels of 18, 22, and 35 MPa$\sqrt{m}$ as shown in Figure 6.1. During the first 5 Hz loading block, FCG rates were similar for all conditions, with cast and wrought exhibiting worse resistance to crack propagation. No difference in FCG rates between L-

PBF orientations can be seen at 5 Hz indicating that at 650 ºC, differences in FCG rates between orientations manifest only at lower testing frequencies. After the first transition, FCG rates during the 90s dwell segment differed significantly. Cast and wrought specimens displayed faster FCG rates when compared to L-PBF. Plus, crack arrest occurred for vertical specimens after a brief period of crack growth post transition from 5 Hz to 90s dwells. This is consistent with the results presented previously in chapter 5 for 1-90-1-1 tests on vertical samples, where crack arrest occurred until ΔK 25 MPa$\sqrt{m}$. In the second transition (from 1-90-1-1 to 5 Hz) the FCG rates for cast and wrought and horizontal specimens were higher than vertical immediately after switching the frequency, and then decreased. This transient behaviour between time to cycle dependent behaviour can be interpreted as the manifestation of an oxidation damaged region. Once the crack had propagated through this region, FCG rates returned to the expected cycle dependent conditions. This behaviour was different for vertical specimens, where FCG rates immediately after the transition were lowest, and then increased to stable crack propagation with similar FCG rates to horizontal specimens (as also seen for the first 5 Hz loading block). After the last transition, very fast crack propagation can be seen for both horizontal and cast and wrought specimens, with no difference in FCG rates between them. This, however, represents very few loading cycles ($\approx$ 10 loading cycles) and isn't very representative of true fatigue, with the samples accumulating progressive gross plastic collapse damage. No second transition from 5 Hz to 90s dwells was obtained for vertical specimens.

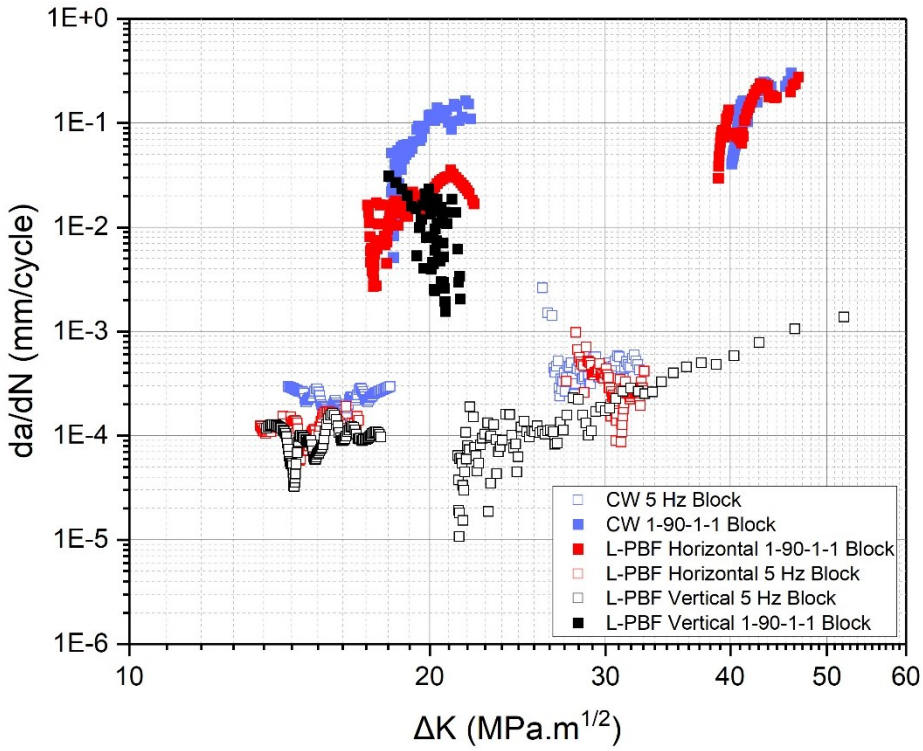

Figure 6.1 FCG rates vs ΔK resultant from the block test for all material conditions (cast and wrought, and L-PBF horizontal and vertical specimens).

A comparison between results obtained for block tests and fully 1-90-1-1 tests is presented in Figure 6.2. Crack arrest occurred at the lower frequency for vertical specimens between ΔK 12-25 MPa√m, with results consistent for 1-90-1-1 and block tests. For horizontal specimens, FCG rates for loading with 90s dwells with block tests were higher when compared to purely 1-90-1-1 testing. This difference can be related to the previous block of testing at 5 Hz leading to a sharpening of the crack tip before starting the 90s dwell regime and increasing FCG rates.

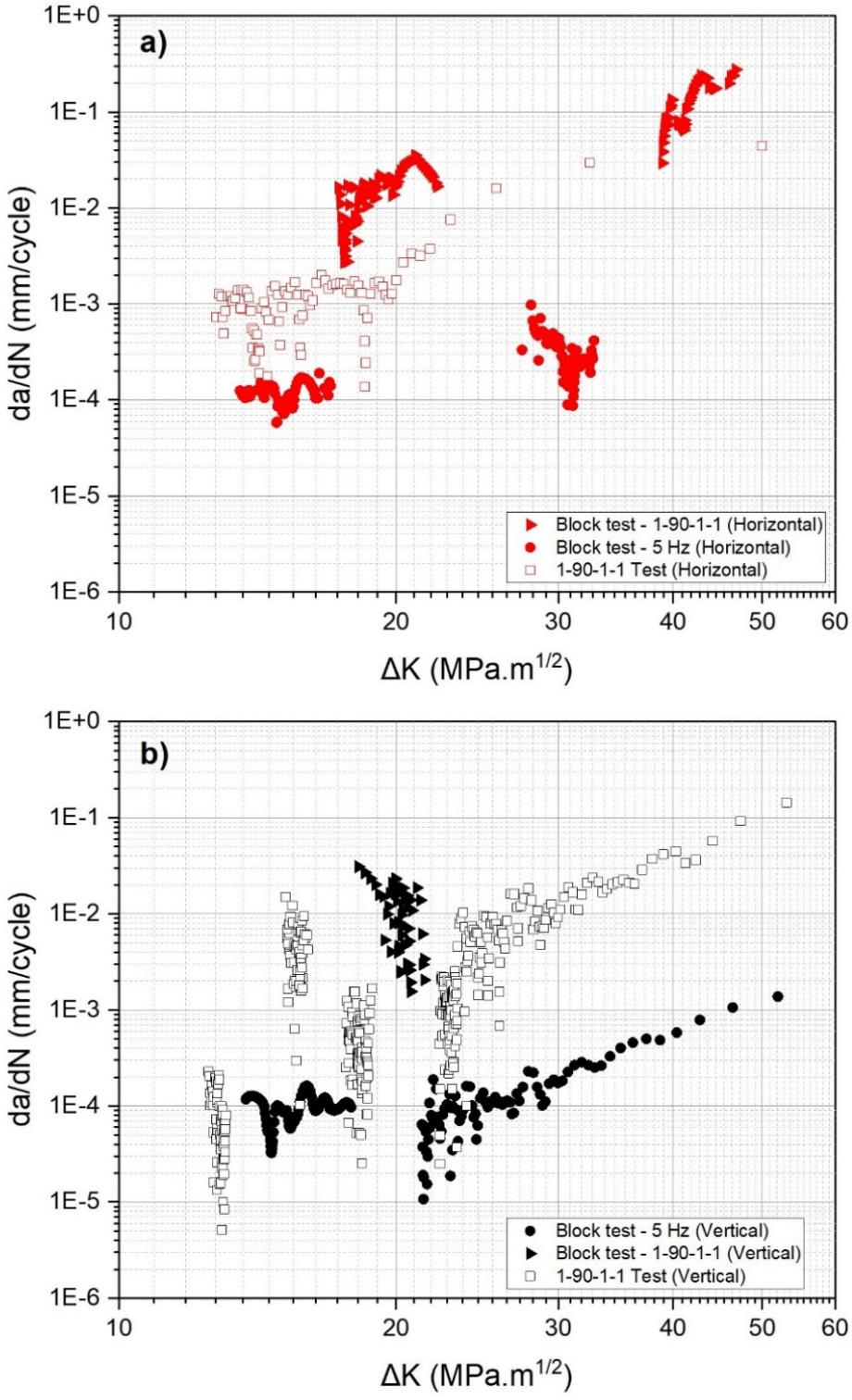

Figure 6.2 Block test comparison between a) horizontal and b) vertical samples.

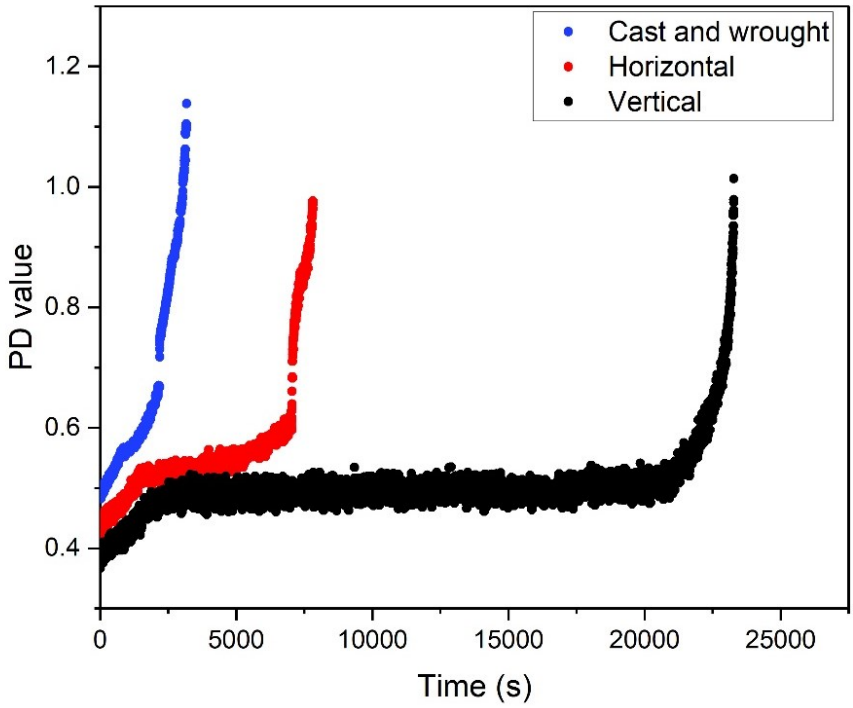

Figure 6.3 Raw PD trace vs time for block tests on all material conditions.

Figure 6.3 shows raw PD traces (a measure of the crack length) across time for all the block tests, where the changes in slope correlate with different loading blocks, either 5 Hz (steeper parts), or 90s dwells (flatter parts). Crack arresting becomes evident when analysing the PD trace for vertical samples. The duration of the 90s dwell block is significantly longer (note that frequencies where only changed when at least 0.5 mm of crack growth was recorded), yet no change in the PD trace can be seen. Figure 6.4, shows the PD traces for each condition individually, along with a more detailed plot of the transition between 90s dwells to 5 Hz. A marked shift in PD values can be seen at the transition between frequency regimes for cast and wrought and horizontal specimens, with no apparent change for vertical samples (as shown in Figure 6.4 e, and f). The more detailed plots in Figure 6.4 b, d show a detailed view of this transient in FCG rates when going from 90s dwells to 5 Hz. The length of this transient behaviour where the crack is rapidly growing before reaching a steady state under cycle dependent crack growth can be linked to the size of the damaged zone formed during time dependent fatigue. The estimated lengths (based on the height of the PD jump) are presented in Table 6-1, with horizontal specimens presenting the larger damaged zone. The size of the monotonic and plastic zone size (calculated using Irwin's approach [128]), and grain size for each material condition is added for reference.

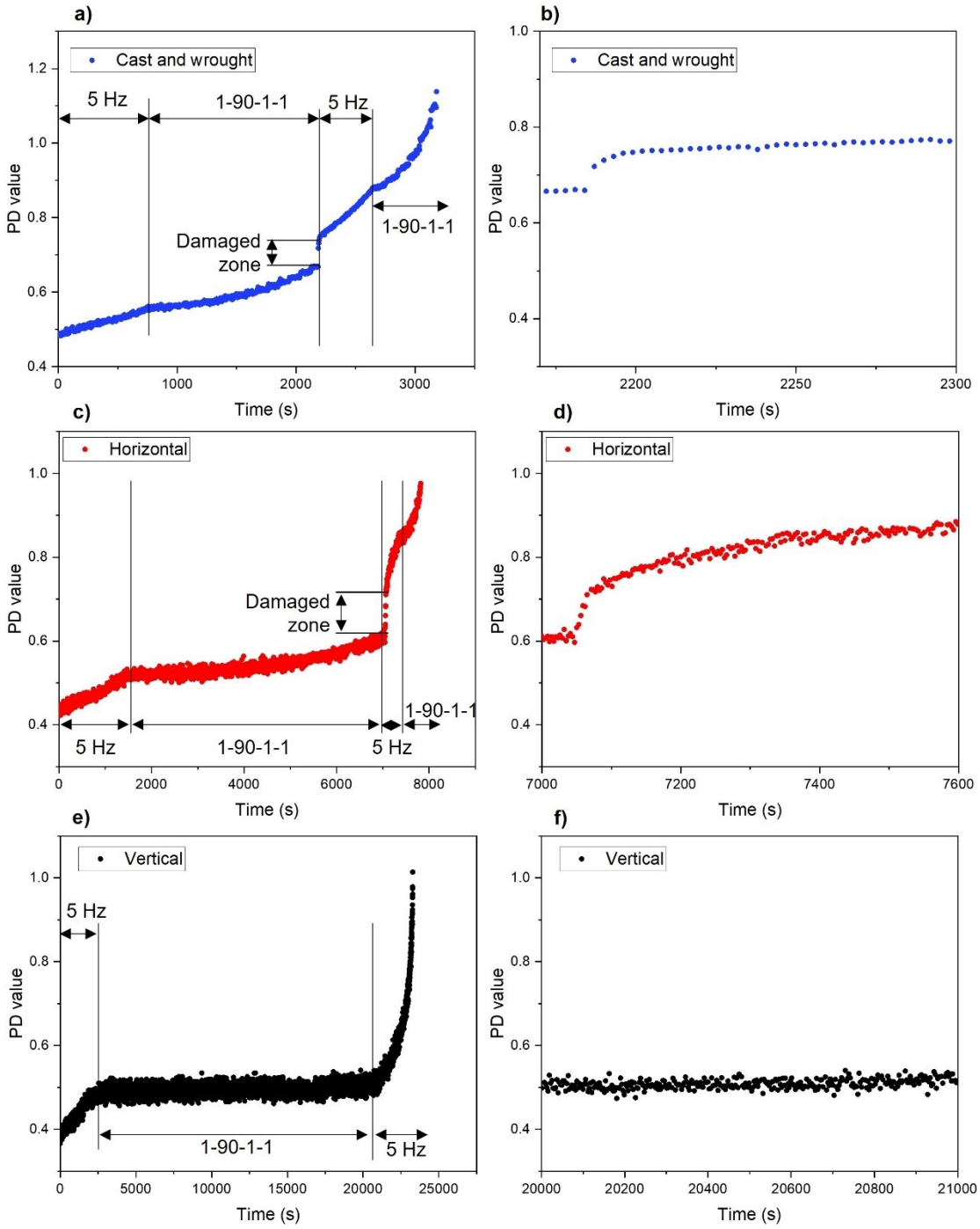

Figure 6.4 Block test raw data with specific changes in frequency superimposed in the graphs for: a, b) horizontal, c, d) cast and wrought, and e, f) vertical specimens.

Table 6-1 Length of damaged zone from block tests for all specimens. The differences in plastic zone sizes between material conditions are related to different yield strength, and K_{max}, ΔK values for the end of each 90 s dwell loading block.

Specimen	Length of damaged zone (μm)	Monotonic plastic zone size (μm)	Cyclic plastic zone size (μm)	Grain size (μm)
Cast and wrought	364	90	18	16.8 ± 13.7
L-PBF horizontal	617	114	23	24.4 ± 27
L-PBF vertical	n/a	105	21	31.3 ± 31.1

To further understand the degree of embrittlement caused by the 90s dwells, the amount of crack propagation during the unloading-reloading, and dwell periods was studied. Figure 6.5 shows the PD traces for each of the individual 1-90-1-1 loading segments for the block tests. It can be seen that for cast and wrought specimens, at lower ΔK levels Figure 6.5 a), crack growth stays constant throughout the dwell with the majority of crack growth occurring during the unloading-reloading part (≈ 62 μm). This marked shift in crack growth, can be related to fracturing through an embrittled zone caused by the dwell period, similar to the transition between frequencies for the block tests. At higher ΔK levels for cast and wrought specimens (see Figure 6.5 b) similar crack growth occurs overall during the unloading-reloading and dwell periods (≈ 91 μm) with no apparent differences between them, which is consistent with data published in the literature for high temperature testing of Inconel 718 [24], [25]. For L-PBF horizontal specimens, however, the crack growth is continuous, and no crack growth can be attributed to a specific part of the loading cycle. Only at the very last few cycles of the test, a higher amount of crack growth can be seen during the unloading-reloading period (see Figure 6.5 d). Finally, no graph for vertical specimens is presented in Figure 6.5, as no crack growth was observed during the 1-90-1-1 loading period as explained previously.

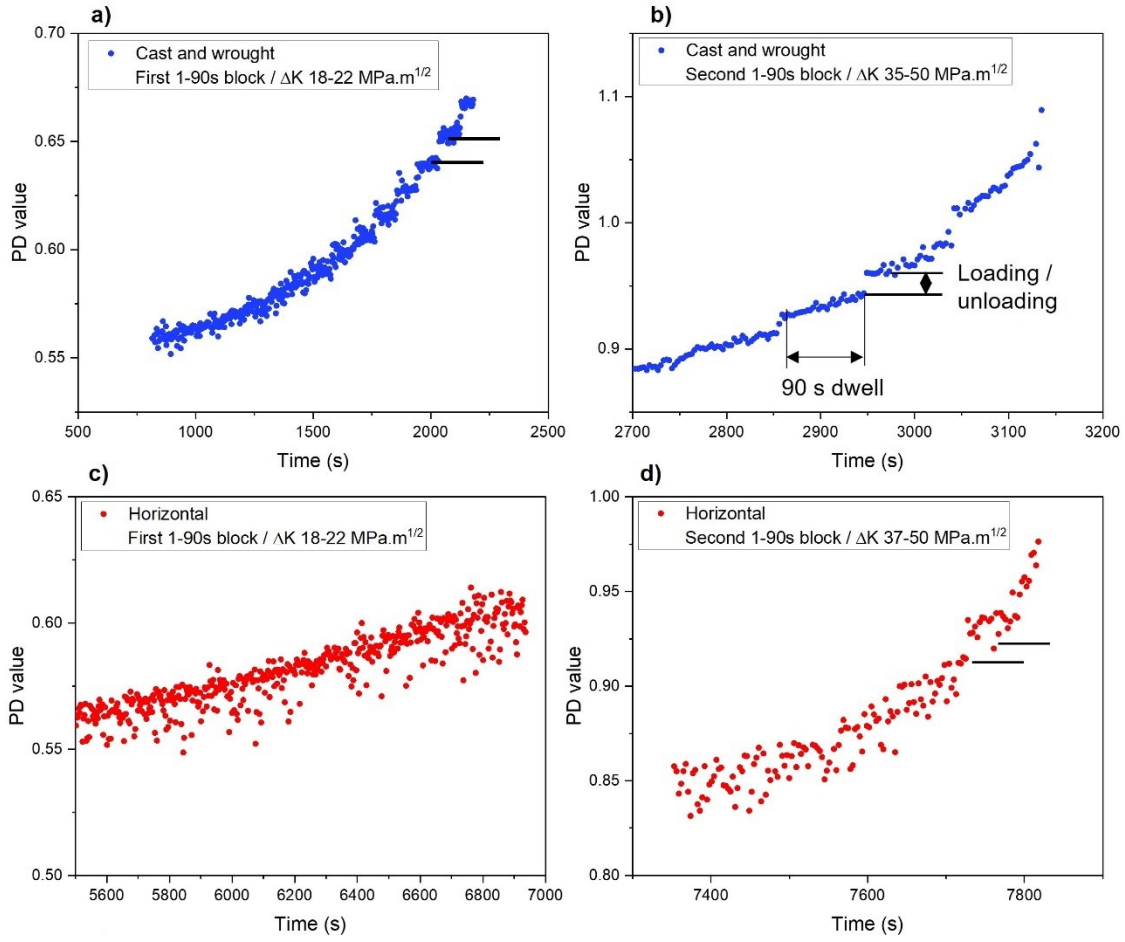

Figure 6.5 PD trace against time for 1-90-1-1 segments of the block tests, a) first 90s dwell block for CW, b) second 90 s dwell block for CW, c) first 90s dwell block for horizontal, d) second 90s dwell block for horizontal specimens.

6.2.1.2 Fractography

The fracture surfaces for all specimens were analysed by optical and SEM microscopy, and the results are presented in Figure 6.6, Figure 6.7 and Figure 6.8. The macroscopic images are labelled showing the different frequency loading blocks, along with higher magnification SEM images of the transitions between frequencies. Intergranular failure modes developed for cast and wrought and horizontal specimens once the frequency is switched to 1-90-1-1 and can be clearly identified by the formation of well-developed secondary cracks (Figure 6.6-a, Figure 6.7-a). At the second transition, the presence of the oxidation damaged zone is apparent for both horizontal and cast and wrought specimens (Figure 6.6-b, Figure 6.7-b). The fracture surfaces exhibit a mixed transgranular/intergranular mode (more evident for cast and wrought specimens) with the presence of secondary cracks. This mixed mode remains active until the last transition to 1-90-1-1 (Figure 6.6-c, Figure 6.7-c) where intergranular failure becomes evident with very tortuous fracture surfaces like those presented in chapter 5 for 1-90-1-

1 tests. Vertical samples show a very different response, mainly related to crack arresting occurring during the 1-90-1-1 loading block. Transgranular fracture modes are evident throughout the 5 Hz loading periods (Figure 6.8-a, c). When the frequency was changed to 1-90-1-1, secondary cracks develop, and the tortuosity of the fracture surface increases (Figure 6.8-b). However, the degree of intergranular failure is not as substantial as that presented for the 1-90-1-1 tests. Furthermore, when the frequency is changed back to 5 Hz (Figure 6.8-b, c), transgranular fracture modes quickly become evident again, not showing the mixed mode seen for horizontal and cast and wrought specimens.

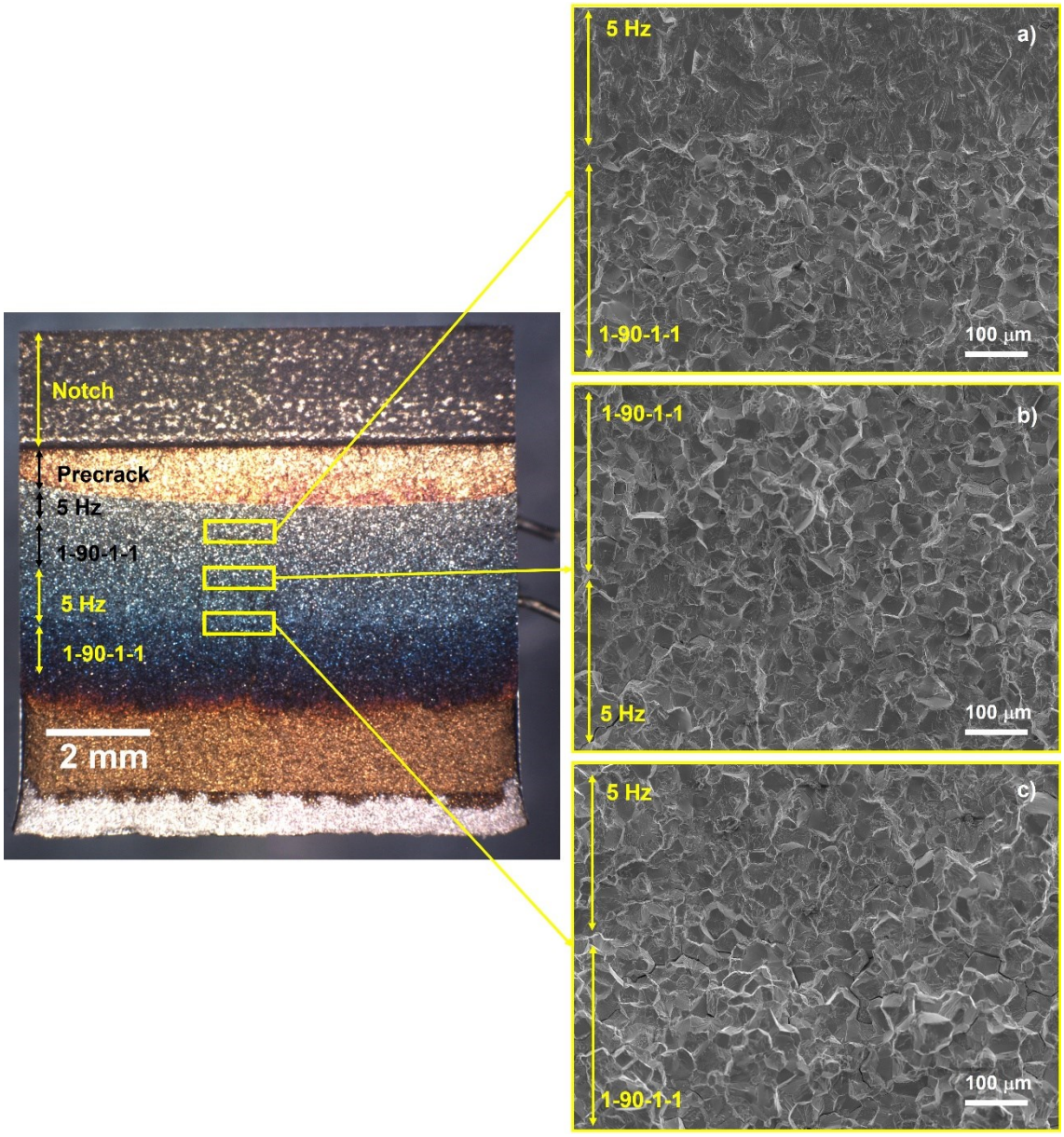

Figure 6.6 Macroscopic overview of the fracture surface resultant from block tests for cast and wrought specimens, and associated images of the transitions between a) 5 Hz to 1-90-1-1, b) 1-90-1-1 to 5 Hz, and c) 5 Hz to 1-90-1-1.

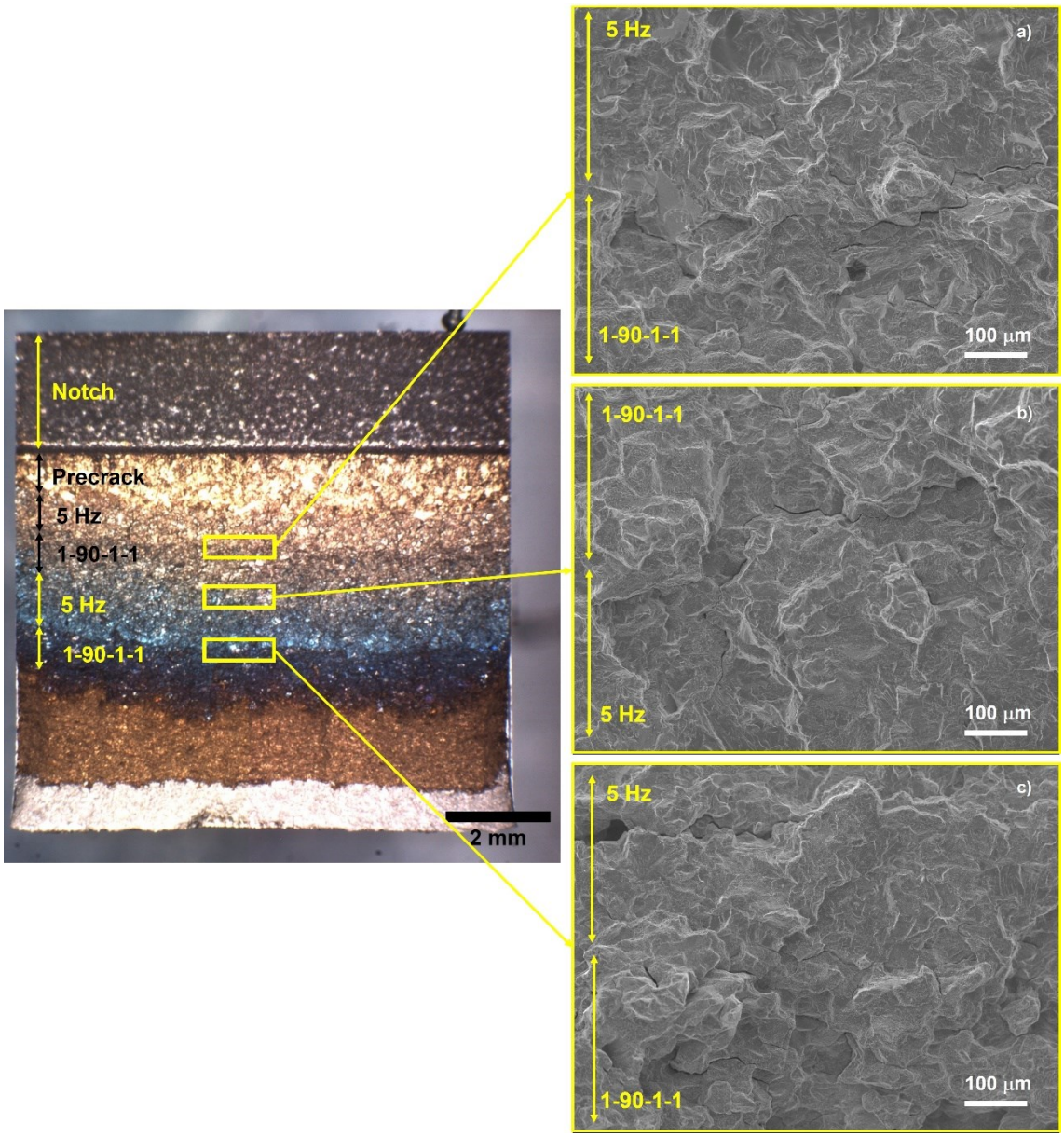

Figure 6.7 Macroscopic overview of the fracture surface resultant from block tests for L-PBF horizontal, and associated images of the transitions between a) 5 Hz to 1-90-1-1, b) 1-90-1-1 to 5 Hz, and c) 5 Hz to 1-90-1-1.

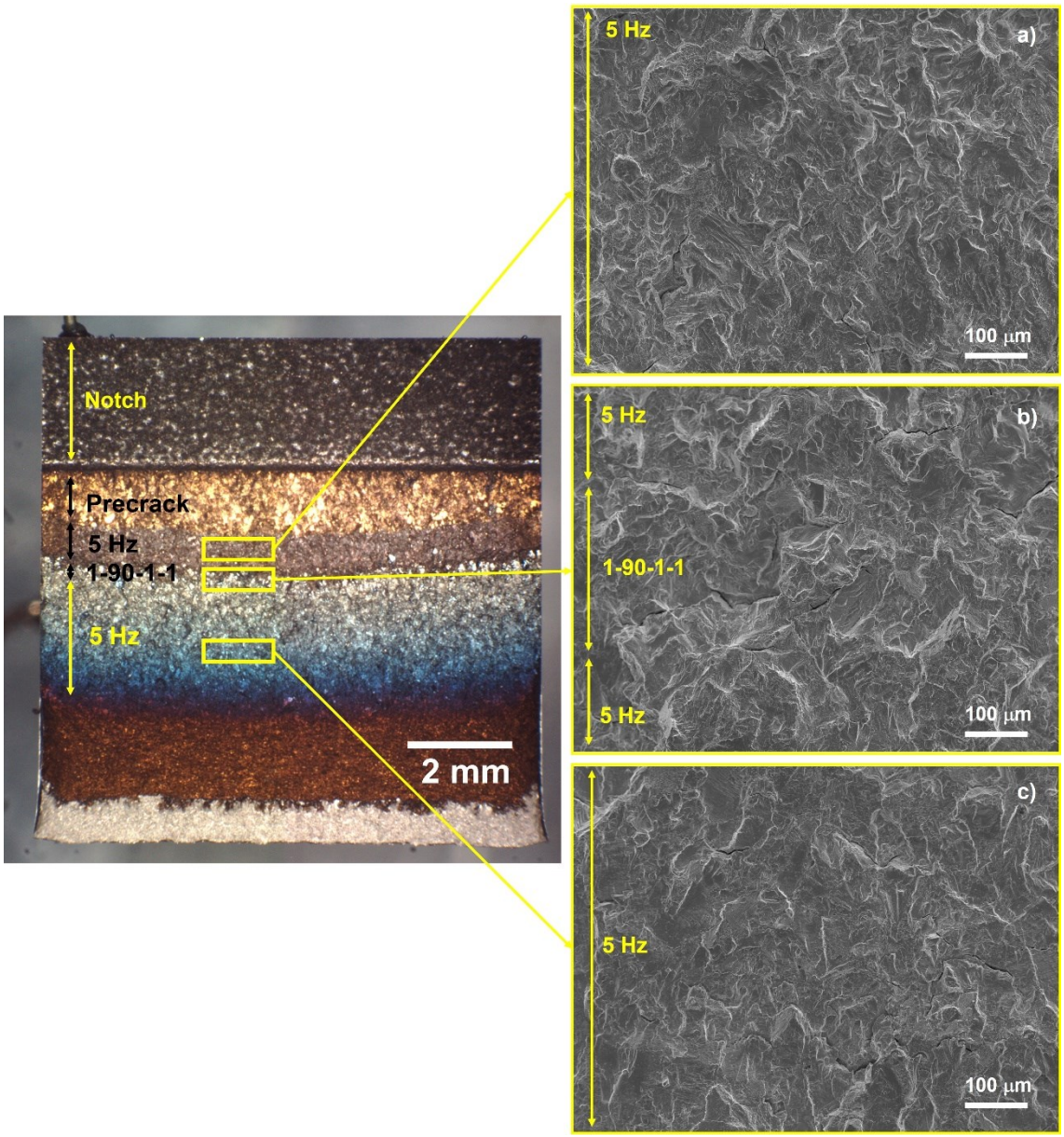

Figure 6.8 Macroscopic overview of the fracture surface resultant from block tests L-PBF vertical, and associated images of a) 5 Hz, b) transition between 5 Hz to 1-90-1-1 to 5 Hz again, and c) 5 Hz.

6.2.1.3 Crack path assessment and secondary cracks

To better understand the transient behaviour between frequencies, profiles of the crack path were studied on sectioned specimens. Figure 6.9 a-c shows the crack path morphology, indicating the different regions: pre-crack, fatigue crack propagation for each frequency, and oxidation damaged zone. More tortuous crack paths can be seen during the time dependent crack growth period (90s dwells) for both L-PBF specimens, which is not as significant for cast and wrought specimens (note the difference in grain size). When the frequency was changed to 5 Hz, flatter crack paths can be seen once passed the oxidation damaged zone, similar to the fracture surface images presented previously. Looking at the crack path during the 90s dwell block for vertical specimens (see Figure 6.9 a) large crack deflections are evident with the crack propagating perpendicular to the expected crack propagation direction, similar to the results presented for the 1-90-1-1 tests where crack arresting occurred. To further understand the effect of crack deflection during the 90s dwell loading block on crack growth behaviour and links to the oxidation damage zone, an assessment of the crack morphology was carried out on both horizontal and vertical L-PBF specimens. This followed the procedure explained in section 5.2.3, and the results are presented in Figure 6.9-d, and e, where the applied ΔK (calculated from PD trace), and resultant effective ΔK are plotted against crack length. The measured crack length varies between specimens, as the crack was arrested for vertical specimens during the 90 s dwell block. Horizontal specimens show more scatter in the data compared to the previously presented crack deflection measurements for 1-90-1-1 tests, with large reductions on effective ΔK as the applied ΔK increases. However, values are generally closer to the applied ΔK across the crack length of the investigated crack. For vertical specimens the applied ΔK changes little across crack length (crack is arrested), and the calculated reduction in effective ΔK is larger. These large deflections on crack path, and subsequent crack arresting could potentially be linked to the different behaviour seen for vertical specimens during the 1-90-1-1 to 5 Hz transition, where no damaged zone was apparent on the PD traces.

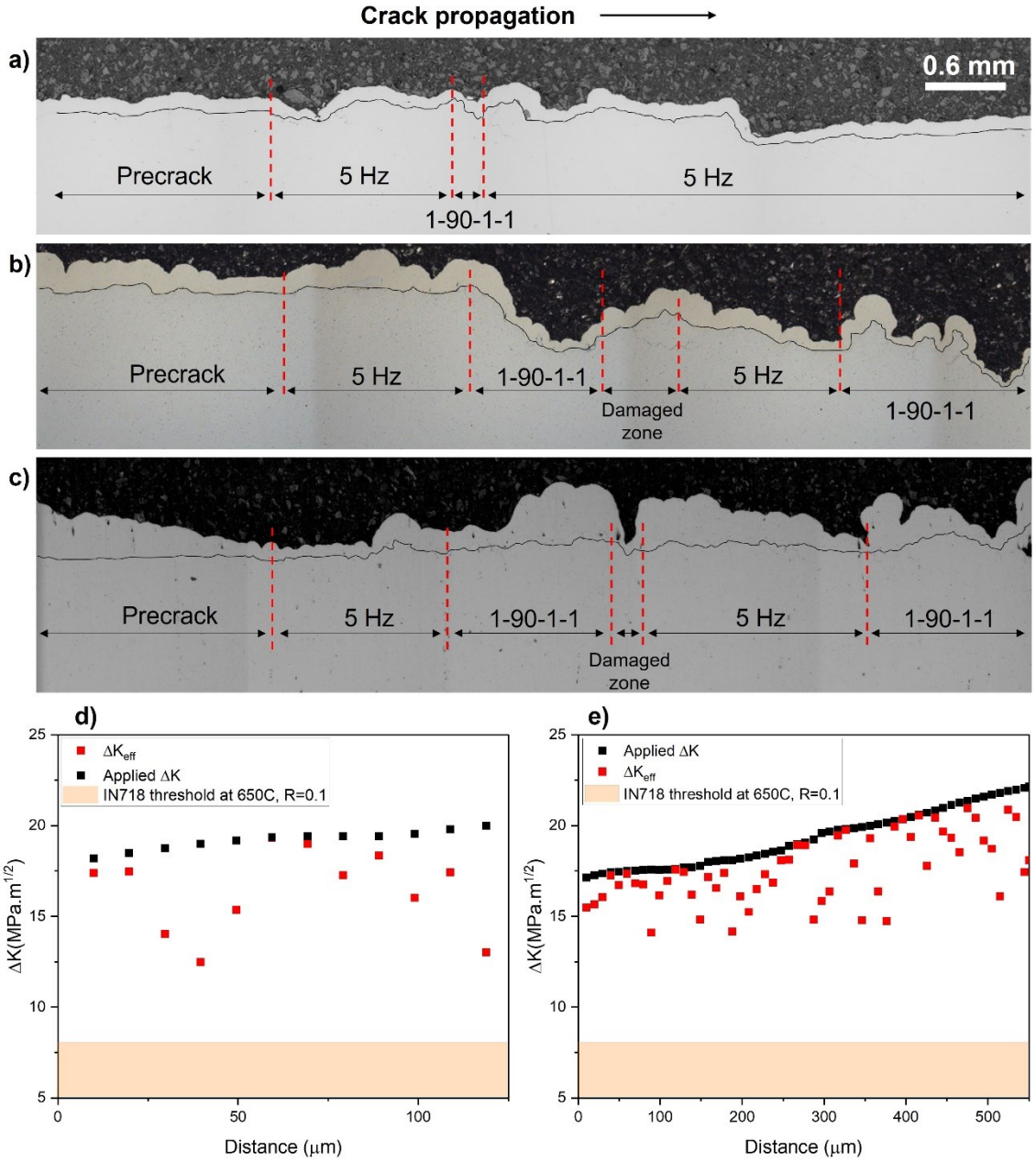

Figure 6.9 Optical micrographs of the crack path morphology on sectioned surfaces showing time dependent, cycle dependent regimes and the oxidation damage zone for: a) L-PBF vertical, b) L-PBF horizontal, and c) cast and wrought IN718 (crack path is outlined in black to aid visualisation, and the same scale applies to all images). Crack deflection measurements extracted from the first 1-90-1-1 loading block for d) vertical, and e) horizontal.

6.2.2 Interrupted tests, crack tip characterisation

6.2.2.1 Crack propagation rates

To further understand the crack growth process during dwell periods and oxidation ahead of the crack tip, interrupted 1-90-1-1 tests were carried out. Cracks were allowed to grow under a 1-90-1-1 loading frequency for approximately the same amount of time (1500

cycles) from ΔK 12 MPa√m at 650 ºC. Samples were then held for 16 hours at 650 ºC at K_{max} 14.21 MPa√m, and 16.67 MPa√m for vertical and horizontal specimens respectively. These K_{max} values were chosen as they capture early stages of crack growth for horizontal specimens (before the marked shift in FCG rates seen for 1-90-1-1 tests, see Figure 5.1 for reference), and they are within the region of crack arresting for vertical specimens. The raw PD traces for both the cyclic and holding part of the tests can be seen in Figure 6.10. The data is somewhat noisy, however, it can be seen that no crack growth was captured by DCPD for vertical specimens during the 1-90-1-1 cyclic part of the tests (Figure 6.10-a), showing again an arrested crack for this material condition at values below ΔK 25 MPa√m. Crack growth was recorded for the horizontal specimen with ΔK increasing from 12.5 to 15 MPa√m, equivalent to approximately 0.7 mm of crack propagation. During the 16 hours holding period PD values remained mostly unchanged for both specimens (see Figure 6.10-b). For horizontal specimens, there is a slight shift in the PD reading, equivalent to approximately 0.12 mm of crack growth after holding for 3000 seconds. However, there is no appreciable difference in average PD values from before and after this slight jump, and no changes in loads/overloads were recorded throughout the 16 hours hold period. For vertical specimens, PD values remain steady through the tests, only showing a slight decrease in the PD trace at the end of the 16 hour hold. This could be related to some degree of crack closure caused by oxidation over time, or stress relaxation occurring at the crack tip towards the end of the test.

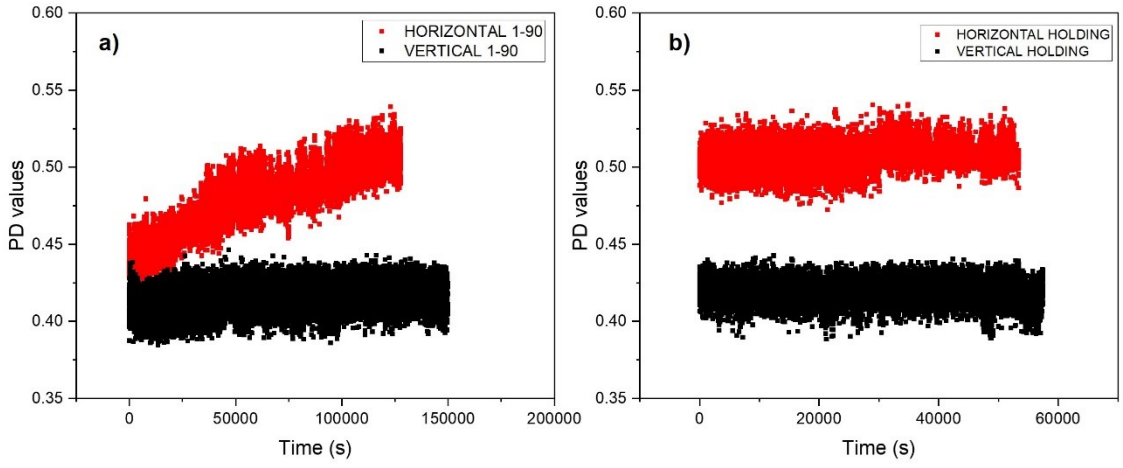

Figure 6.10 PD traces vs time for interrupted tests on vertical and horizontal samples: a) cyclic part of test at 1-90-1-1 frequency, and b) holding at K_{max} 16 MPa√m for horizontal samples, and 13 MPa√m for vertical samples.

6.2.2.2 Interrupted tests, fractography

Oxidation processes at the crack tip on both the side surface, and inside the specimen were characterised by optical microscopy and SEM. Figure 6.11, presents the crack morphology on the side surface for horizontal specimens, where the grain boundaries are clearly visible due to a thermal etching effect. It was found that for horizontal samples only, asymmetric crack growth had occurred during the high temperature 1-90-1-1 part of the test, with the crack not propagating uniformly across the breadth of the sample (≈ 0.4 mm difference in crack length between sides). Post-testing, no uneven loading could be identified, and it is possible that during high temperature crack propagation one side of the sample became more compliant, linked to crack coalescence events or differences in crack front tortuosity at either side of the fracture surface.

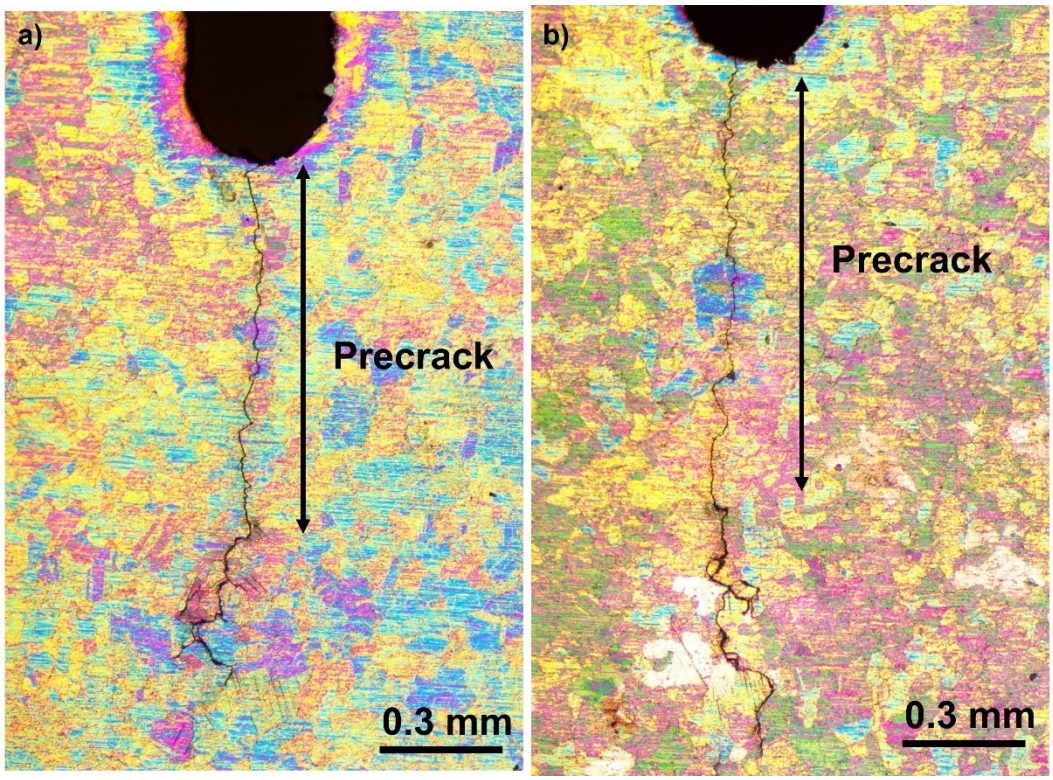

Figure 6.11 Optical micrographs from both side surfaces (a, b) after interrupted tests for L-PBF horizontal.

Low magnification SEM micrographs of the crack path at the side surface resulting from interrupted tests for both specimens are presented in Figure 6.12. A large number of secondary cracks starting from the main fatigue crack can be seen for horizontal specimens (Figure 6.12-a), as well as the formation of oxidised slip bands along the entire length of the fatigue crack. Furthermore, oxidised slip bands can be discerned near the crack tip and in the surrounding grains, representing an oxidation damage region. For vertical specimens, the FCG region is very small and more severe oxidation around the crack tip can be seen. Furthermore, there is a higher concentration of slip

bands around the crack tip, although, they don't extend as far into surrounding grains compared to horizontal specimens. The measured oxidation damaged zone at the crack tips caused during the interrupted tests can be found in Table 6-2 (indicated for reference in Figure 6.12-b), and the values are compared to the monotonic and plastic zone sizes (calculated using Irwins [128] approach for plane stress conditions). The measured oxidation damaged zone on the side surface is close to the calculated monotonic plastic zone size, indicating some effect of plastic deformation on oxide formation (note that differences in plastic zone size are related to a different K_{max}, and ΔK for each crack tip). This is, however, relatively larger for horizontal specimens indicating more localised damage for the vertical specimens. However, it should be noted that the exact position of the crack tip cannot be accurately identified from 2D images given the complex 3D morphology of the crack front, so the extent of the oxidation damaged zone may be overestimated.

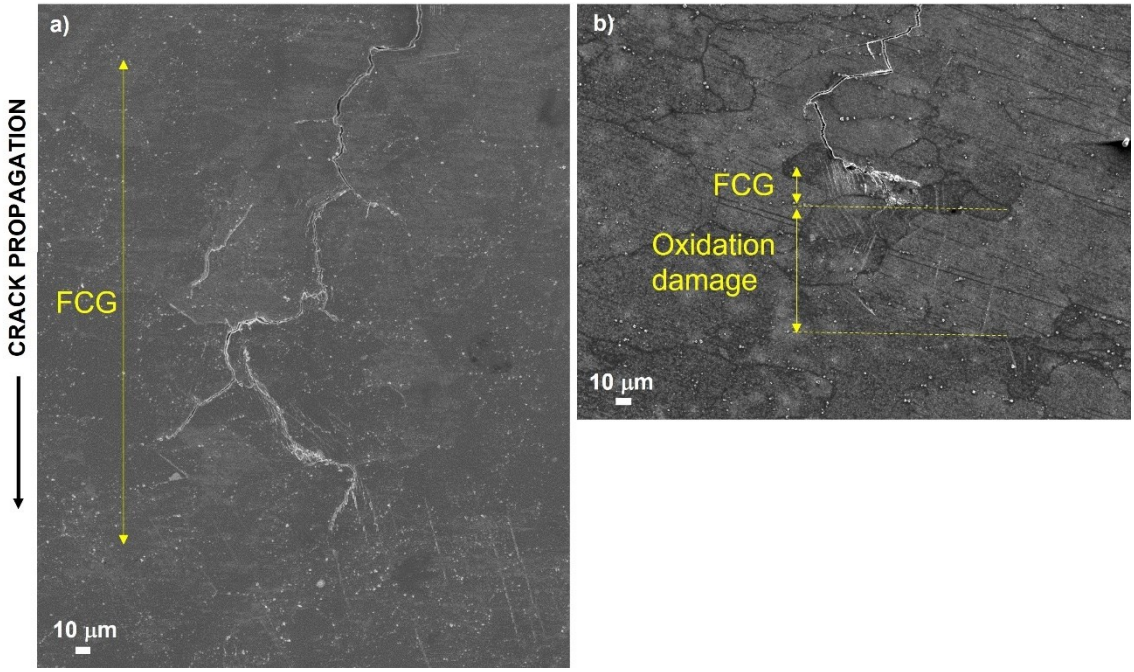

Figure 6.12 Low magnification SEM micrographs showing the fatigue crack path for interrupted tests: a) L-PBF horizontal, b) L-PBF vertical.

Table 6-2 Interrupted tests, measured oxidation damage zone, and monotonic and cyclic plastic zone size for vertical and horizontal specimens.

Specimen	Measured oxidation damaged zone (μm)	Monotonic plastic zone size (μm)	Cyclic plastic zone size (μm)
Horizontal	170	157	32
Vertical	79	114	23

Higher magnification SEM images of the oxidation around the crack path and crack tip on the side surface for horizontal specimens are presented in Figure 6.13, and Figure 6.14. Oxidation is evident around the crack path, and around the crack tip with a large concentration of oxidised slip lines around the crack (see Figure 6.13-b, and d). EDX analysis indicates that the oxides formed around the crack tip and slip lines are Cr and Fe-rich oxides. However, higher resolution EDX would be necessary for a better understanding of the oxidation process. Higher magnification SEM images of the oxides formed around the slip lines are presented in Figure 6.13-g. A lamellar structure can be discerned, with some small globular particles in between. Furthermore, by analysing different positions along the crack wake it appears that the lamellar structure forms first, followed by the formation of globular particles with longer exposure times. Oxidation of slip lines is also visible in the grains ahead of the crack (oxidation damaged zone), as shown in Figure 6.14. They also have a lamellar structure (similar to that seen around the crack path/tip), and some of them appear to be cracked (see Figure 6.14 c for reference). However, the sequence of whether it is an oxidised crack, or an oxidised slip band that has cracked is unknown.

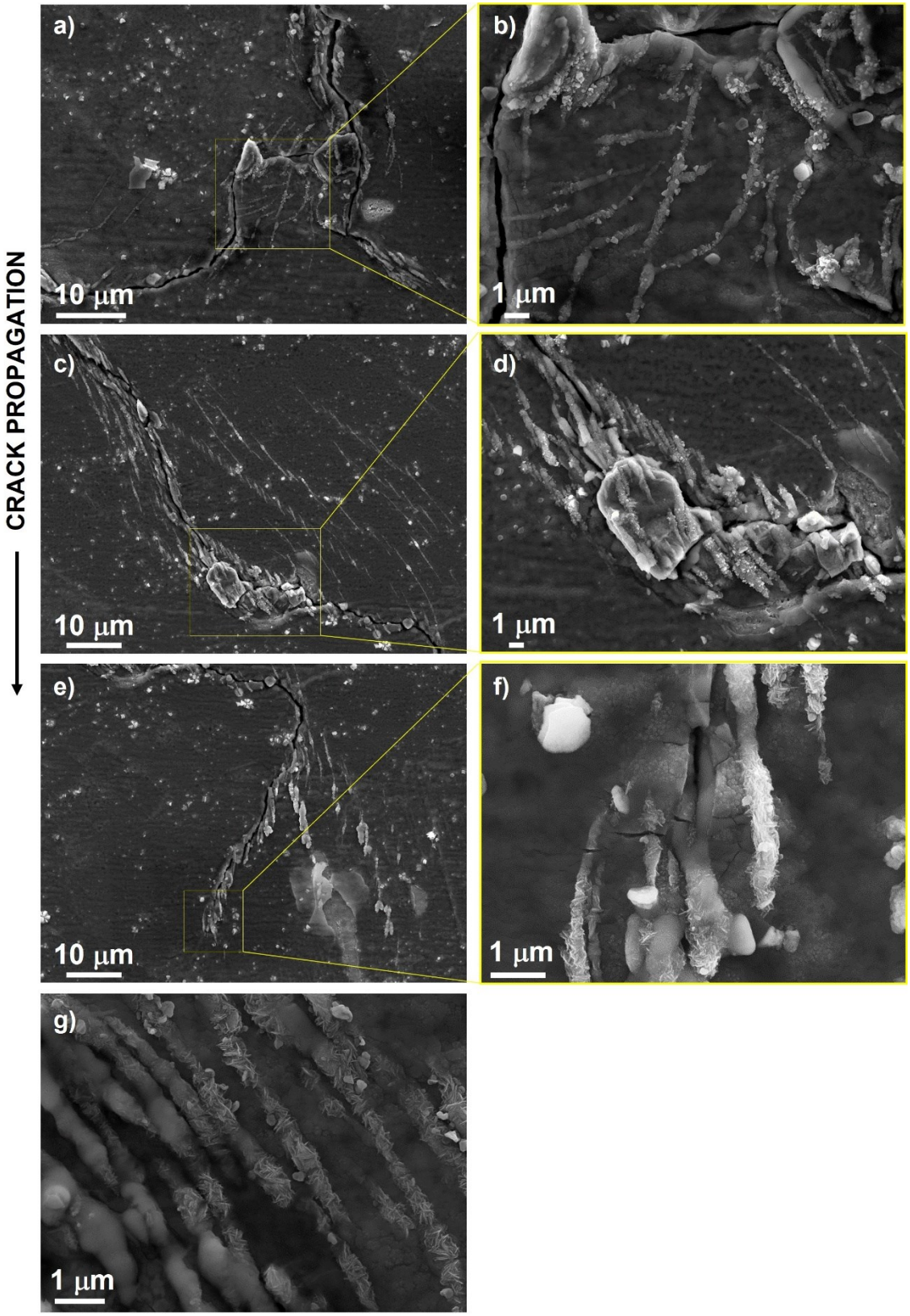

Figure 6.13 High magnification SEM micrographs from L-PBF horizontal specimens showing oxidation processes on the side surface along different positions of the fatigue crack (a-d) crack path, (e-f) crack tip, and g) oxidation of slip bands surrounding the crack path.

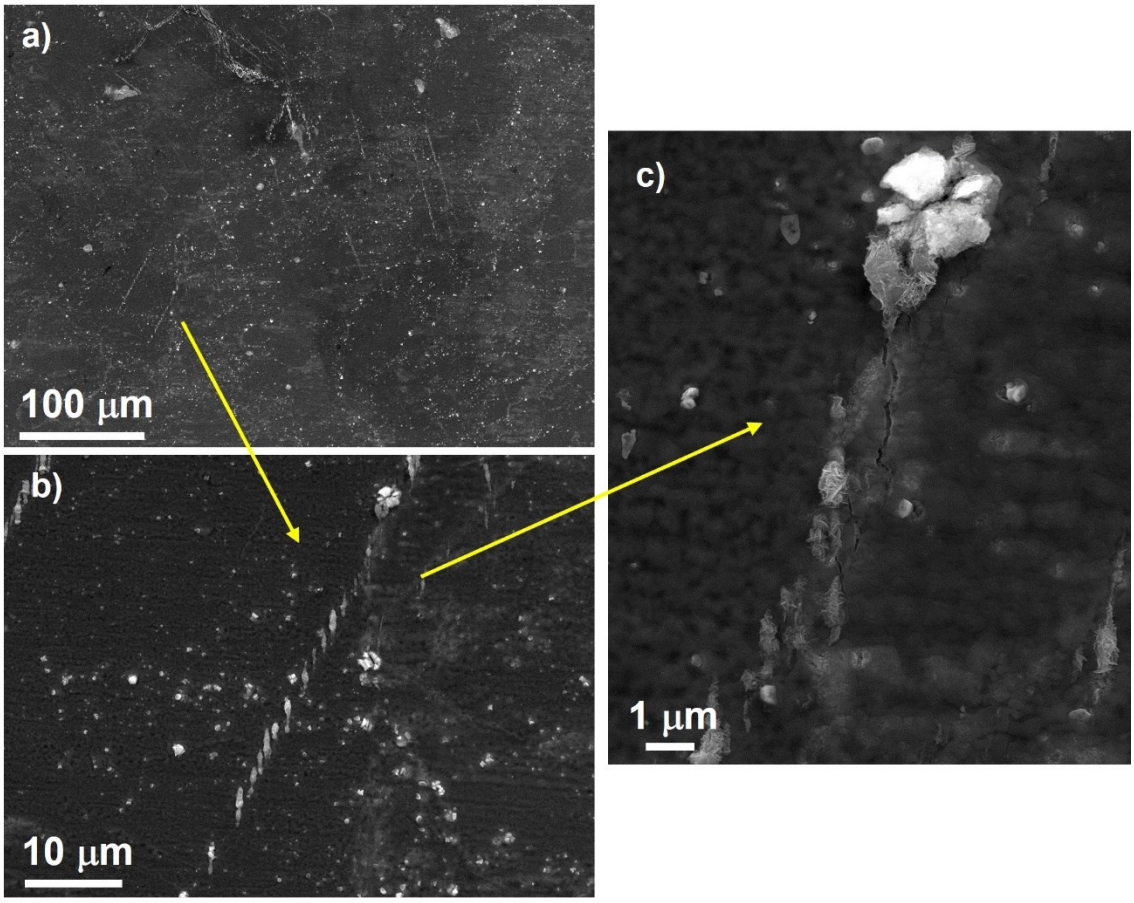

Figure 6.14 High and low magnification SEM micrographs of oxidised slips bands ahead of the crack tip for L-PBF horizontal specimens.

Figure 6.15, shows higher magnification SEM images of the side surface oxidation around the fatigue crack for vertical specimens. As shown, there is a shorter FCG region, and more severe oxidation around the crack path, and crack tip. The crack does not appear to be bifurcated; however, two large, oxidised regions can be distinguished. One at the start of the FCG region following a grain boundary (indicated by the red arrow in Figure 6.15-a), and at the crack tip. Both have the same appearance with globular oxide particles forming, and the lamellar structure seen for horizontal specimens is not present around the crack tip. Preferential oxidation of slip bands in the grains adjacent and ahead of the crack tip has also occurred (see Figure 6.15-e-f), however, none of them appear to be cracked unlike horizontal specimens. Given the larger size of the oxidised region ahead of the crack tip, representative EDX measurements could be obtained (see Figure 6.16) unlike for horizontal specimens. These show O-rich regions ahead of the crack tip and grain boundaries, as well as Ni-depleted regions ahead of the crack tip. Furthermore, internal Cr-rich and external Fe-rich oxide regions can be discerned, which correlates with previous results published in the literature for CW IN718 [100]. Some Nb-rich particles can also be seen at grain boundaries, probably linked to oxidised δ-phase precipitates.

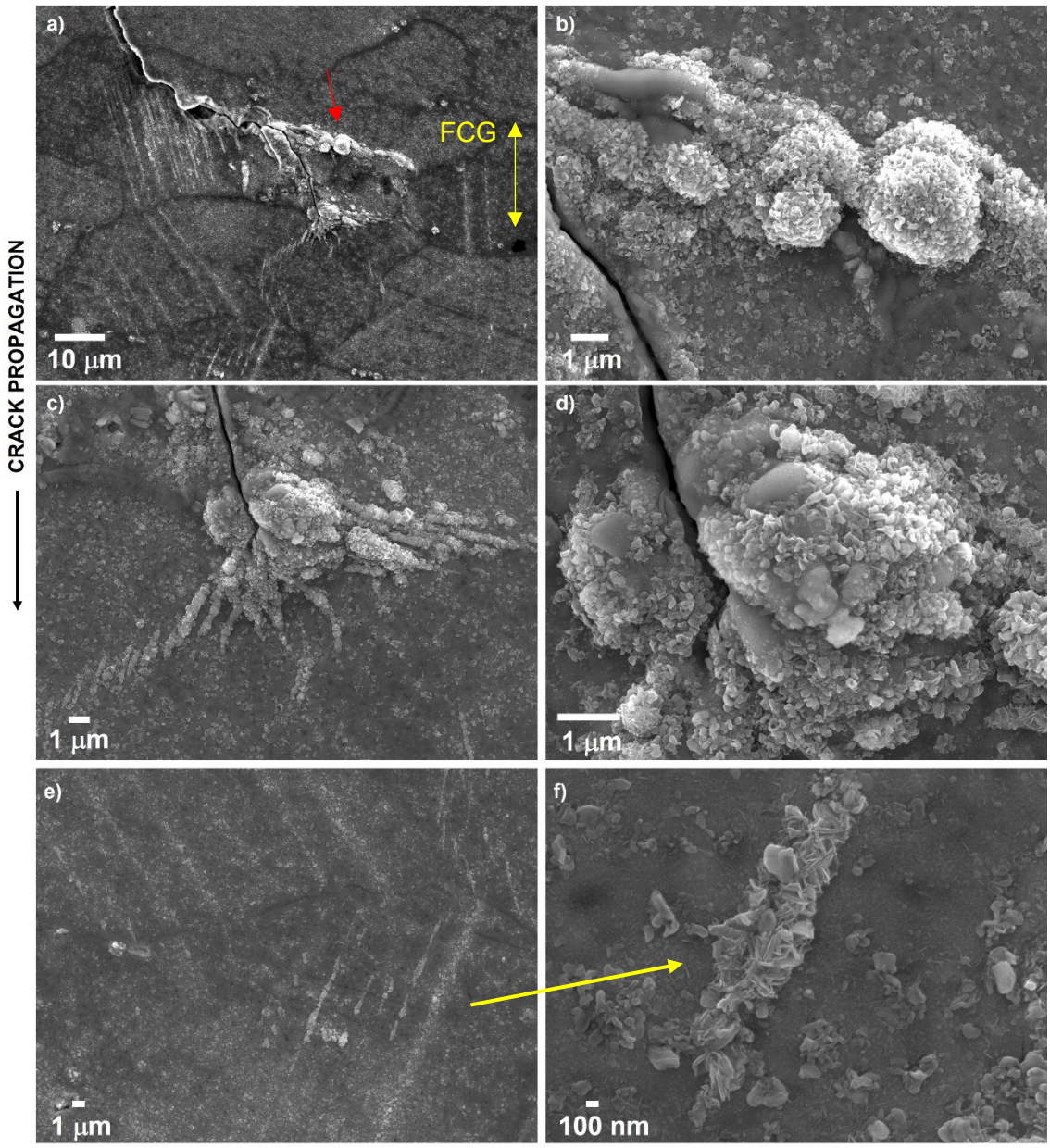

Figure 6.15 High magnification SEM micrographs from L-PBF vertical specimens showing oxidation processes on the side surface along different positions of the fatigue crack (a-d) crack tip, and (e-f) oxidation of slip bands surrounding the fatigue crack.

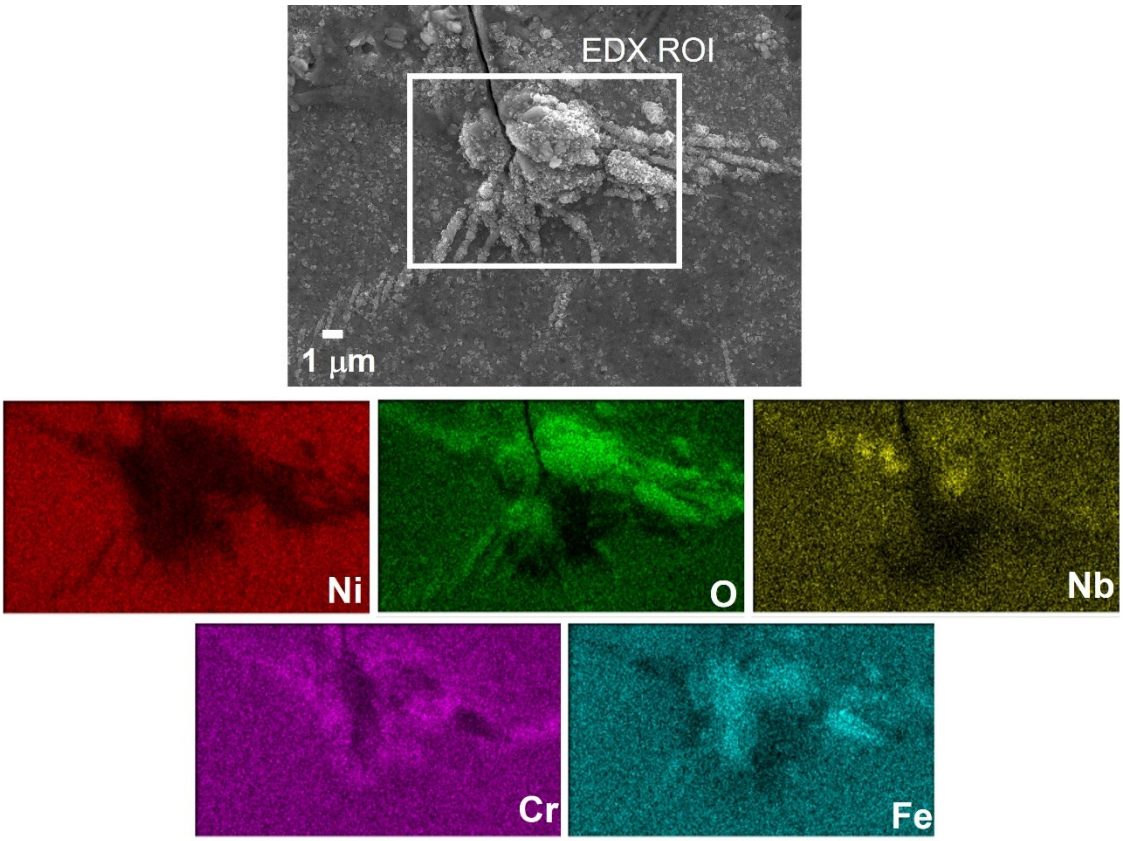

Figure 6.16 EDX mapping of the crack tip (side surface) resultant from interrupted tests on L-PBF vertical specimens.

Figure 6.17 shows the crack path, and crack tip in the bulk material (centre of the sample) after sectioning for horizontal L-PBF specimens. As shown, the geometry and oxidation around the crack tip is simpler when compared to the side surface with no apparent oxidation of slip bands. This is because oxygen availability is higher on the side surface, whereas on the bulk material oxidation around the crack tip is more constrained (only approaching down the crack faces, rather than any side ingress being possible). It should also be noted that differences observed in crack tip geometry might depend on the sectioning plane chosen, which might not fully capture the true 3D geometry of the crack. From Figure 6.17-a, a branched crack path can be distinguished with two separate cracks, which can be linked to the differences in crack length observed in the side surface (see Figure 6.11 for reference). When focussing on the crack tip (Figure 6.17-b), a large, oxidised region can be discerned ahead of the crack tip, as well as the formation of some discontinuous cracks (indicated by the red arrows) along embrittled grain boundaries ahead of the crack tip. EDX mapping has been carried out on the oxidised region ahead of the crack tip, and the results are presented in Figure 6.17-c. These correlate with oxidation observed on the side surface with the formation of a Cr-rich oxide internal layer,

and Fe-rich oxide outer layer. Furthermore, a region with a Nb-rich oxide can also be distinguished, which again can be related to oxidation of a δ-phase particle. To further understand the formation of the discontinuous cracking presented in Figure 6.17-b, EBSD maps were performed on the fatigue cracks. The EBSD results are presented in Figure 6.17-d, e showing the SEM image and KAM map extracted from that region. KAM maps are a measure of local grain misorientation between a point, and its neighbour and can be qualitatively used to analyse the extent of plastic deformation around the crack tip/path in this case. As shown in the KAM maps and as expected, there is generally a higher degree of plastic damage around the crack path/tip when compared to the rest of the material. Furthermore, there is a measurable degree of misorientation ahead of the oxidised crack tip (as indicated by the red arrow) linked to the region where discontinuous cracks were forming along the embrittled grain boundaries. The length of this oxidation damaged zone ahead of the crack tip was measured as 41 μm, which is close to the monotonic plastic zone size for horizontal specimens (52 μm under plane strain conditions), again suggesting that there could be effects of plastic deformation on oxide formation.

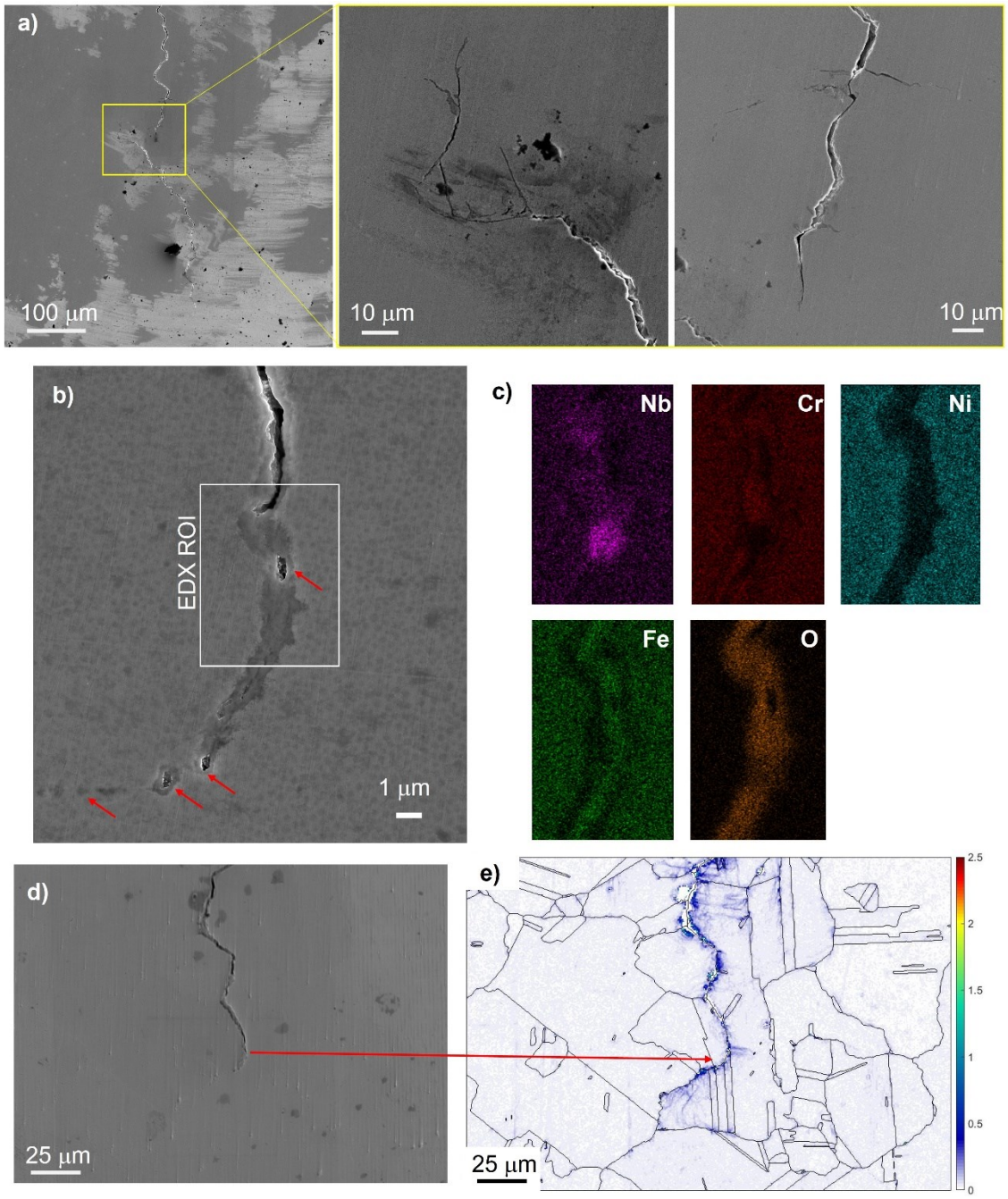

Figure 6.17 Fatigue crack path in the bulk material resultant from interrupted tests on L-PBF horizontal specimes: a) low and high SEM micrographs of the crack mophology, b) oxidation ahead of the crack tip with red arrows representing areas of discontinuous cracking, c) EDX mapping of the oxidised reginon ahead of the crack tip, and d) SEM image of the crack path from which the KAM map in (e) was extracted, red arrow across images represents the location of the crack tip on the KAM map.

Given the complex 3D geometry of the crack, and the analysis through 2D sections, it is difficult to accurately identify the exact location of the crack tip. Furthermore, there is the possibility that some of the discontinuous cracks seen ahead of the crack tip are in fact part of the main crack path (the crack might be longer behind this specific plane), and they don´t appear as a continuous crack in this specific section. Therefore, this same specimen was again ground and polished ($\approx$ 10 μm of material was removed) to systematically characterise crack tip oxidation at a different position, and the results are presented in Figure 6.18. The fatigue crack path shows a similar morphology, although it is now a fully continuous crack, and not two separate cracks as shown in Figure 6.17. The crack is slightly longer in this region, and part of what was identified as damaged, but uncracked by the KAM map is now fully cracked. Focussing on the crack tip (Figure 6.18-d), an elongated oxidised region can be again discerned ahead of it with the same composition previously shown. Discontinuous cracks ahead of the crack tip/path appear again and are indicated in Figure 6.18-c, d with red arrows. Additionally, δ-phase particles are slightly visible in these images, and it can be seen how these cracks occur in between precipitates.

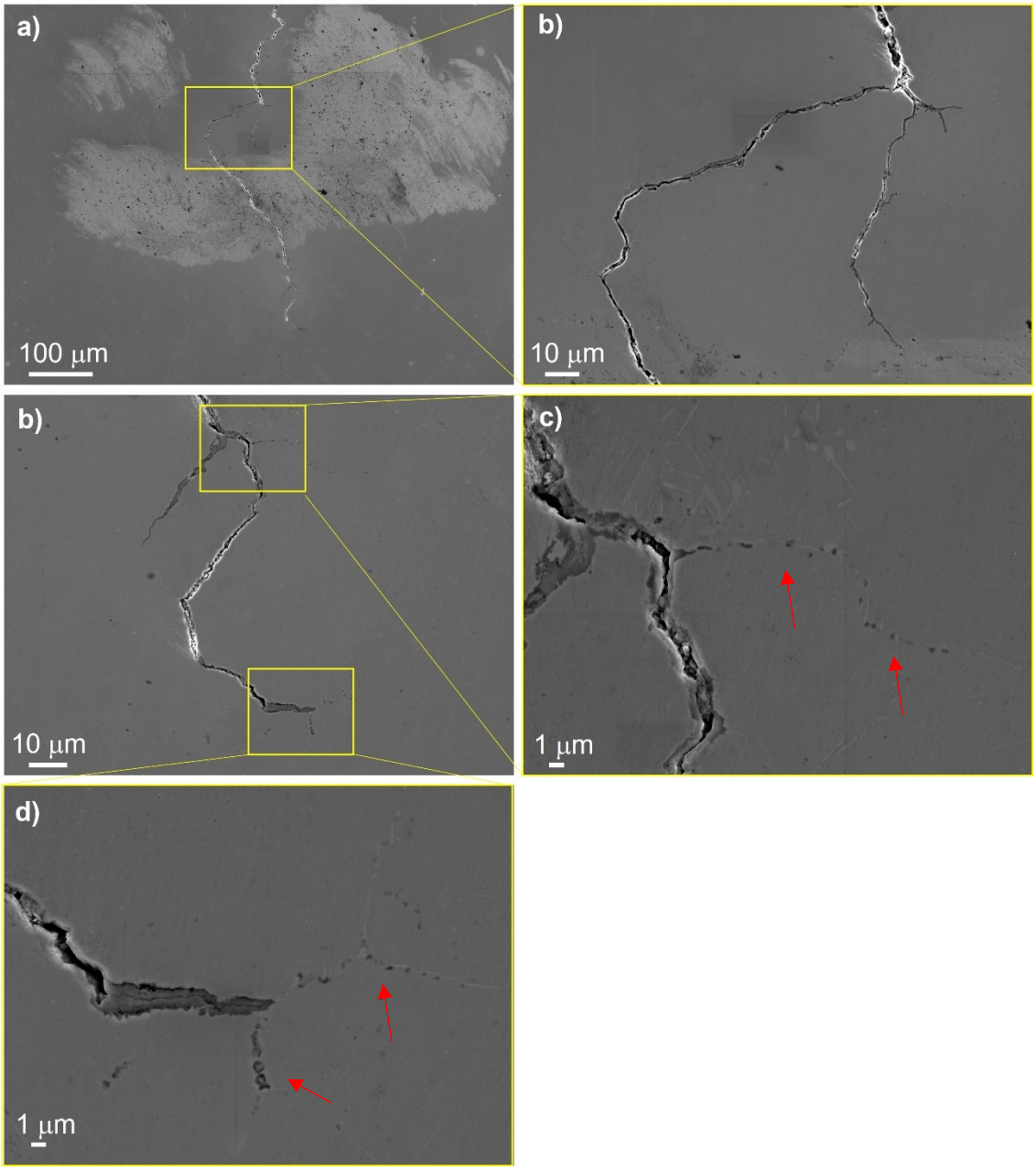

Figure 6.18 Low and high magnification SEM micrographs showing crack morphology and oxidation ahead of the crack tip in the bulk material for L-PBF horizontal specimens. Red arrows (c,d) represent areas of discontinuous craking along grain boundaries.

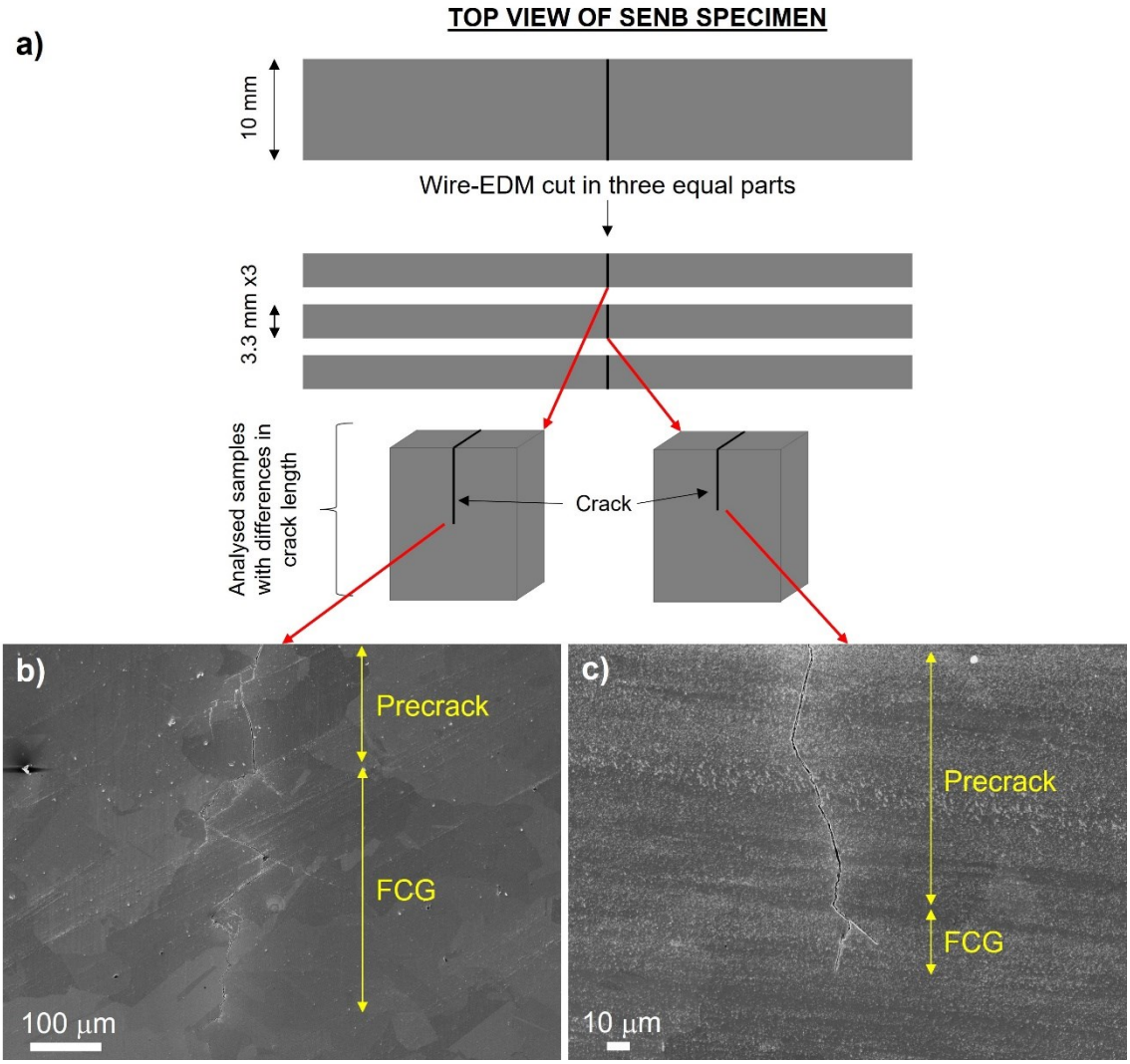

Figure 6.19 a) Schematic illustration of the sectioning strategy for analysis of interrupted tests on L-PBF vertical specimens, b) low magnification SEM images showing large differences in crack length across the breadth of the sample.

The crack morphology in the bulk material was found to be very different for vertical specimens compared to horizontal samples, with a highly tortuous crack path leading to asymmetric crack growth within the bulk material (see Figure 6.19-b, c for reference). It is worth noting that no differences in crack length were observed on the side surfaces, and that no crack growth was recorded by the DCPD system. Figure 6.19-b shows the crack morphology in one section, with approximately 0.3 mm of FCG occurring during cycling at high temperature. Given the contradiction with the DCPD readings (see Figure 6.10 for reference), the specimen was also sectioned in a different position following the procedure detailed in Figure 6.19-a. The resultant crack path is shown in Figure 6.19-c, where approximately 25 μm of crack growth occurred during high temperature loading, which correlates more closely with the DCPD readings and the FCG data presented for

vertical specimens where crack arrest was occurring for testing with 90s dwells. The DCPD method provides an average of the crack growth across the breadth of the sample and does not capture local differences in crack length. This shows that the vertical specimens have a very tortuous, and complex crack front with local differences in crack growth. However, on average across the breadth of the sample no considerable crack growth occurred leading to an overall arrested crack.

EBSD scans were performed on the sectioned specimens to further understand the differences in crack morphology. The results are presented in Figure 6.20, showing both the SEM images and the KAM maps extracted from those regions. The KAM maps show again a higher degree of misorientation around the crack tip/path indicating more plastic damage around that region. Additionally, some vertical lines can be seen across the KAM maps and are linked to marks caused by mechanical polishing. Figure 6.20-a shows the KAM results for the shorter crack. In this case, the crack does not appear to propagate through grain boundaries and, unlike for horizontal samples, plastic damage does not extend much further away from the crack tip. For the other section (see Figure 6.20 c-f), the images show a branched crack with multiple secondary cracks linked to the main crack, and a similar degree of misorientation when compared to horizontal specimens. Focussing on the crack tip (Figure 6.20-f), the highest degree of misorientation is linked to a secondary crack ahead of the apparent crack tip, which could be related to differences in crack morphology behind the analysed plane. Interestingly, there is again no measurable plastic damage on the grain boundaries ahead of the crack tip, opposite to the KAM results from horizontal specimens. This also correlates with the crack growth data presented for the block tests, and the apparent absence of a damaged zone for vertical specimens.

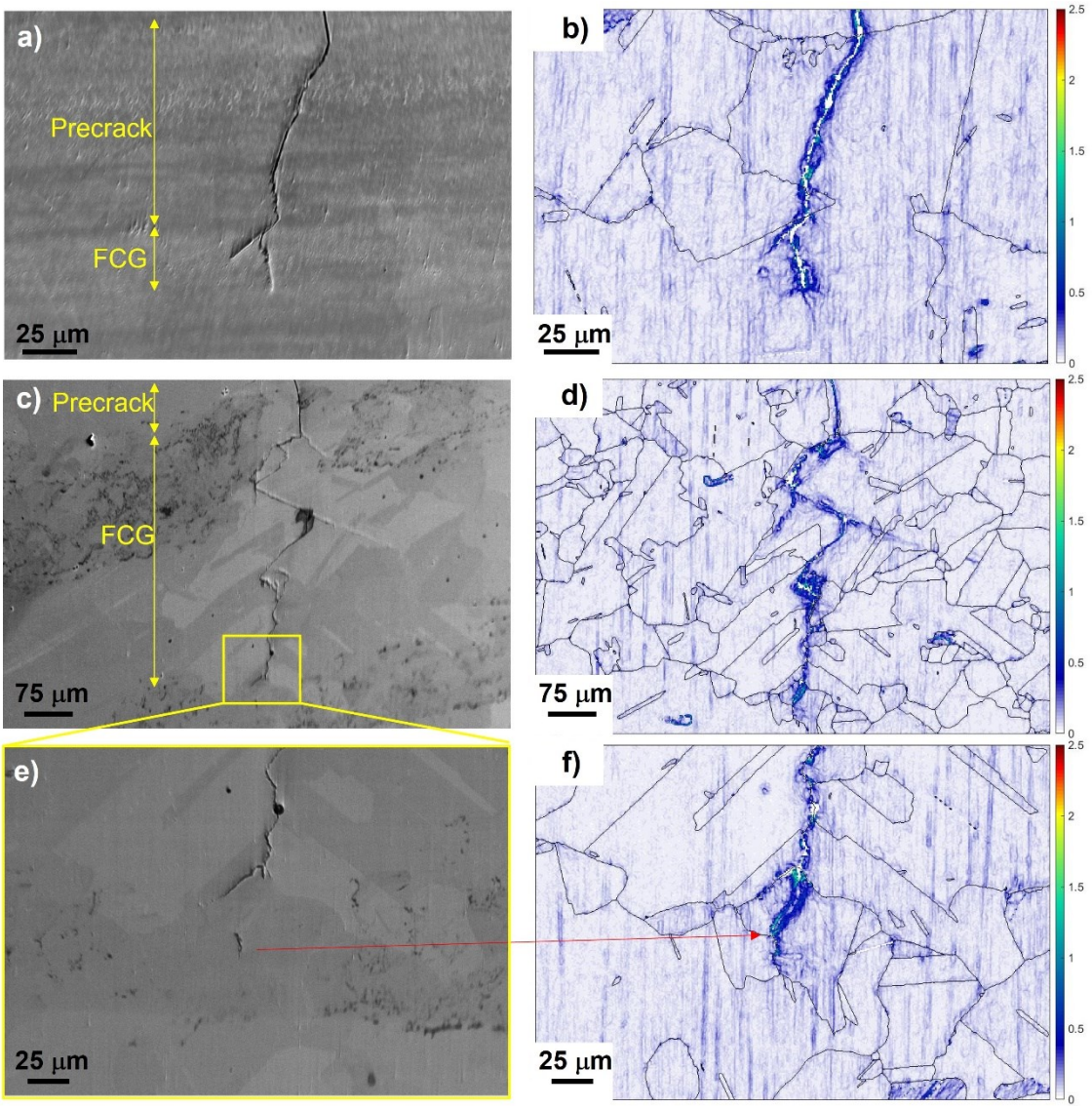

Figure 6.20 SEM micrographs of the crack tip at different locations in the bulk material and their corresponding KAM map showing local misorentation around the fatigue crack.

The section extracted from the vertical specimen with the longer crack (Figure 6.19-b) was reground and polished (≈ 10 μm of material was removed) to further characterise the crack morphology, and oxidation around the crack tip. Figure 6.21 presents an overview of before and after repolishing, where the FCG region has slightly increased in length. The repolished sample (Figure 6.21-b) presents an even more tortuous crack path with a branched crack tip, and a high number of secondary cracks. Furthermore, the new crack morphology around the crack tip follows the misorientation results from the KAM map in Figure 6.20-f. Higher magnification SEM images around the crack path/tip, as well as EDX maps showing the oxide composition at the crack tip are presented in Figure 6.22. As shown, there are oxide filled regions around both the crack path (Figure 6.22-b), and crack tip (Figure 6.22-d, e). EDX measurements show again a Cr and Fe-rich oxide with some points presenting Nb-rich oxides. However, no significant differences could be identified between outer or inner oxide layers, which would require higher resolution EDX to accurately characterise. There are, however, marked differences in the location of the oxidised region between sample orientations. Horizontal specimens exhibit an elongated oxidised region ahead of the crack tip, as well as the formation of what appear as discontinuous cracks along embrittled grain boundaries ahead of the crack tip. This was further corroborated by the KAM maps showing increased plastic damage in the grain boundaries ahead of the crack tip. For vertical specimens, however, oxide filled crack tips are evident with no apparent formation of an oxide layer on the grain boundaries ahead of the crack tip. This difference is also present in the KAM maps, where no difference in local misorientation is evident between the bulk material and grain boundaries ahead of the crack tip.

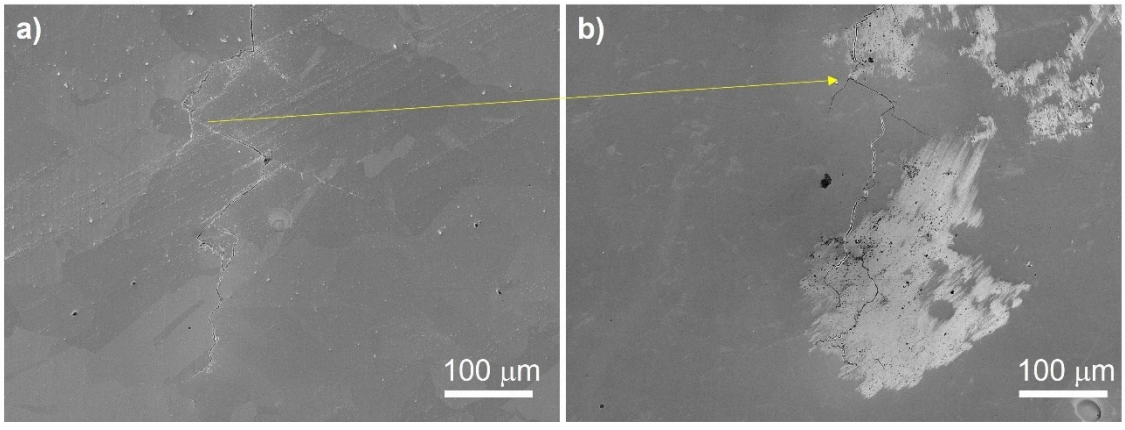

Figure 6.21 low magnification SEM micrographs showing the crack morphology in the bulk material for interrupted tests on vertical specimens before (a), and after (b) repolishing.

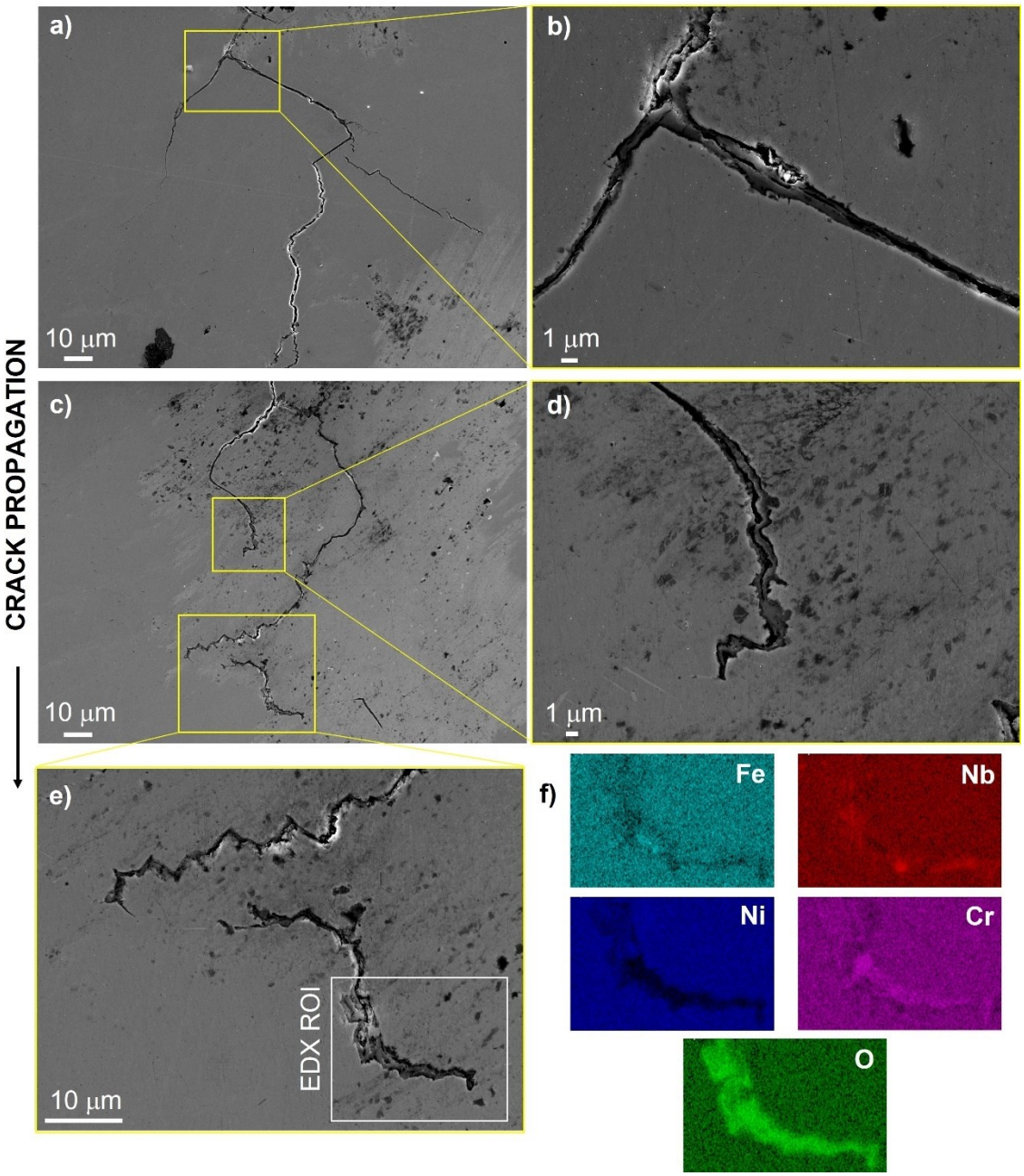

Figure 6.22 Fatigue crack morphology in the bulk material resultant from interrupted tests on L-PBF vertical specimes: a-b) low and high magnificantion SEM micrographs of the crack path, c-d) low and high magnification SEM images of the crack tip, f) EDX mapping of the oxidised crack tip.

6.3 Discussion

6.3.1 Investigation of the oxidation damaged zone

The extent of oxidation related damage formed ahead of the crack tip during dwell fatigue testing was investigated in this chapter through the use of block tests. As explained previously, during dwell fatigue loading conditions, oxygen assisted grain boundary attack will occur leading to enhanced FCG rates and intergranular failure modes for polycrystalline Ni-based superalloys. Where dynamic embrittlement is the favoured theory used to explain the embrittlement of L-PBF IN718 under the studied loading conditions. This, however, will only affect a limited amount of material around the crack tip (damaged zone), and by switching between low and high frequency regimes the size and mechanical effect of this oxidation damaged zone on the different material conditions can be investigated.

The results show large differences in behaviour between L-PBF vertical and the rest of the tested specimens. CW and L-PBF horizontal specimens behave in a similar fashion, even though FCG rates, and the size of the damaged zone are different. In both cases, a transient behaviour in FCG rates can be seen when switching frequency, with higher FCG rates before crack growth stabilises to mixed transgranular/intergranular crack propagation (as shown by the fracture surfaces) during the 5 Hz loading block. When plotting this transition in crack growth against time (see Figure 6.4 for reference) a parabolic time-dependent shape can be identified, characteristic of diffusion controlled processes (dynamic embrittlement) for both horizontal and CW specimens [99]. This behaviour correlates with data from the literature for similar testing on CW IN718 [25], [99], showing that the mechanisms controlling oxidation damage ahead of the crack tip are somewhat similar for both horizontal and CW specimens. There are, however, differences in the overall length of the damaged zone even though ΔK levels, and plastic zone sizes are comparable between specimens. As presented in chapter 5, horizontal specimens exhibit higher resistance to crack propagation compared to CW under time dependent conditions. As a result, the overall time spent under 1-90-1-1 loading for the same increase in crack length is longer for horizontal specimens. Since dynamic embrittlement is a diffusion controlled process, this would allow for a longer time for oxygen to diffuse along the grain boundaries possibly resulting a larger damaged zone. Alternatively, when comparing the size of the damaged zone with grain size we can find that approximately the same number of grains are being damaged (embrittled) ahead of the crack tip. This suggests that, relatively speaking, the same number of grain boundary paths (albeit of different lengths) are being embrittled for both material conditions.

Studies have shown that grain boundary embrittlement rates will widely vary depending on the relative misorientation between two neighbouring grains[154]–[156]. This, linked with the relative difference in damaged zone size, may imply a threshold process to switch between grain boundaries in terms of embrittlement rates, whilst dynamic embrittlement along a grain is relatively fast. The overall rate determining step would then be accessing the grain boundary rather than embrittling it. Nonetheless, it may be concluded that there is an oxidation damaged area ahead of the crack for CW, and horizontal specimens; with the of extent of damage ahead of the crack tip being highly dependent on the testing conditions (dwell time, environment, etc.) as well as the microstructural variables (grain shape/size, grain character, precipitates, etc.) controlling fatigue crack propagation. The more detailed characterisation of the interaction between this embrittled zone, and the crack tip with longer dwells will be discussed in the next sections.

Vertical specimens showed a very different response. No FCG was recorded during the 1-90-1-1 loading block with an arrested crack, and there was no apparent oxidation damaged zone identified by the PD system. In contrast, FCG rates decreased after the transition to 5 Hz, and then increased to stable crack propagation during the 5 Hz loading block. This is manifested in the fracture surfaces of vertical specimens (see Figure 6.8) where only a thin strip of material displays some intergranular failure with well-developed secondary cracks, yet transgranular failure is predominant across the majority of the fracture surface. The response can again be linked to the shape of the grains and preferential orientation of the grain boundaries against the direction of crack propagation for vertical specimens, as presented in Figure 5.13. As the frequency is lowered and intergranular failure becomes dominant, significant crack deflection occurs due to the shape of the grains, reducing the effective ΔK at the crack tip and crack propagation is stopped. Although measurable, the extent of crack deflection seen on the sectioned vertical specimens (see Figure 6.9) extracted from the block tests is not as severe as for the 1-90-1-1 tests. However, these are shorter tests with no changes in the applied load, and the sectioning plane might not be fully representative of the complex 3D geometry of the crack front. Nonetheless, the end result is a local plastically damaged region through the repeated fatigue cycling of an arrested crack, which could ultimately influence the diffusion of oxygen ahead of the crack tip (as will be discussed in more detail for the interrupted tests) [157]. Thus, there will be two competing mechanisms active when changing the frequency back to 5 Hz. The crack will have to first get through this tortuous and plastically damaged region, momentarily slowing FCG rates (as shown

in Figure 6.1), and ultimately outweighing the effect of an embrittled oxidation damaged zone ahead of the crack.

6.3.2 Fatigue crack growth during dwell time

Figure 6.5 showed PD traces (crack length) against time for the 90s dwell loading blocks in the CW and horizontal specimens. This analysis aimed to extend the concept of the damaged zone and its relationship with each loading cycle, as well as investigate during which part of the fatigue cycle (dwell or unloading-reloading) the crack is growing. The corresponding ΔK at the beginning of each 1-90-1-1 loading block was comparable for both specimens, yet slight differences in behaviour could be identified.

The results presented for CW specimens, as expected, closely align with data published in the literature for testing on similar conditions for IN718 [24], [158], [159], and other polycrystalline Ni-superalloys [129], [160]. In this case it is understood that crack propagation across time can be subdivided into three separate regimes. These are represented in Figure 6.23 for tests on CW IN718 at 650 ºC with longer dwells (296 seconds) performed by Christ *et al.* [158]. The specific ΔK values at which these transitions occur will be highly dependent on the temperature and testing parameters. Nevertheless, we can see a similar trend for the testing performed in this thesis for CW specimens where at low ΔK (< 20 MPa$\sqrt{m}$) crack growth is continuous, with no differences between specific parts of the loading cycle. At intermediate ΔK values (20-30 MPa$\sqrt{m}$), crack length is constant during the 90s dwell, with most of the crack growth per cycle occurring during the unloading and reloading process with a stepwise crack propagation. This indicates that a small, embrittled area forms ahead of the crack during a dwell and breaks when unloading and reloading takes place accelerating FCG rates. At higher ΔK values (>30 MPa$\sqrt{m}$ until failure), some crack growth can be identified during dwell time in addition to crack growth occurring during the unloading/reloading phase, however, crack growth at the beginning of the dwell is slower when compared to the end of the previous cycle. Suggesting that there is a period of incubation time for FCG to occur after the embrittled material ahead of the crack fails during unloading/reloading, and this time period reduces as ΔK (crack length) increases.

Interestingly, for L-PBF specimens (tested under the same conditions, see Figure 6.5 for reference) only two regimes can be identified (part I, and II, from Figure 6.23), and the transition occurs at a higher ΔK value (>45 MPa$\sqrt{m}$), almost upon final failure. As a result, for the majority of the test, crack growth is continuous with no apparent differences in the PD data between dwell and unloading/reloading phases. Which could be directly linked

to the improved resistance against crack propagation seen for L-PBF specimens compared to CW. Furthermore, this same behaviour was also observed on the 1-90-1-1 tests presented in chapter 5 for both vertical and horizontal specimens, where difference in crack growth during the unloading/reloading cycles could only be identified in the last loading cycles (>45 MPa√m). This difference in FCG during dwell time can again be linked to microstructural differences between the L-PBF and CW specimens. The coarser grain size, irregular grain shape, and higher percentage of Σ3-twin grain boundaries found in L-PBF specimens compared to CW result in a more complex crack path, and slower FCG rates. This also affects oxygen diffusion along grain boundaries ahead of the crack tip during dwell time reducing the effect of dynamic embrittlement [161]. Thus, the oxidation damage formed ahead of the crack tip with 90 s dwells is not sufficient (until ΔK>45 MPa√m) to be broken during the unloading/reloading phase. Therefore, it is probable that for L-PBF specimens, longer dwells (increase degree of dynamic embrittlement) would be required to promote the stepwise crack propagation seen for CW specimens.

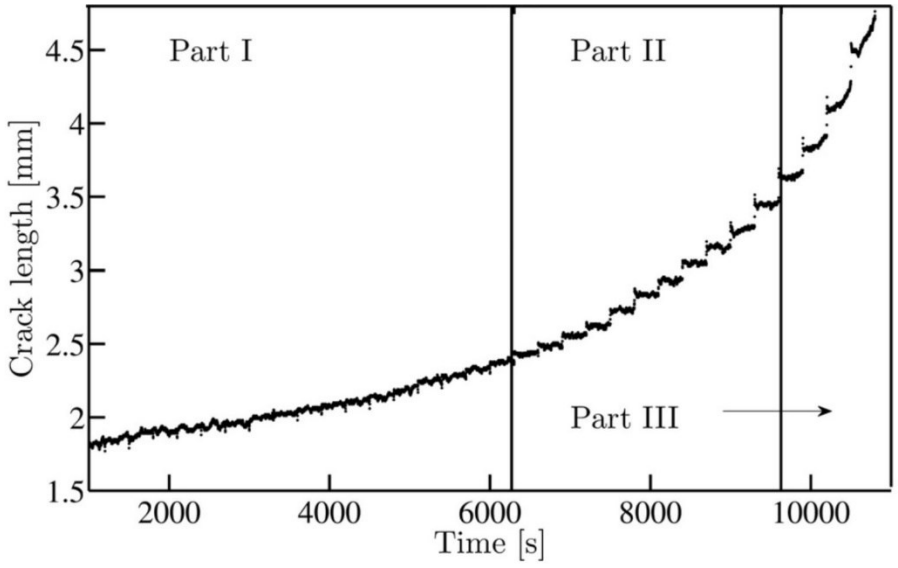

Figure 6.23 Crack length as a function of time for dwell fatigue testing on CW IN718 in air at 650 ºC, R=0.1, and triangular loading waveform (2s-Xs-2s) with a 296 s dwell at peak load, performed by Christ et al. [158].

6.3.3 Deformation ahead of a fatigue crack tip during dwell fatigue for L-PBF specimens

The effect of longer dwells and oxidation (at 650 ºC) on deformation ahead of the fatigue crack tip on horizontal and vertical L-PBF specimens was assessed by holding pre-cracked specimens at a sustained load for 16 hours. On the side surfaces, extensive

oxidation could be observed around the crack path/tip for both specimens. Furthermore, preferential oxidation of slip bands ahead of the crack tip were observed indicating the effects of plastic deformation on oxidation damage. This, however, was more localised for vertical specimens (where the crack is arrested according to DCPD) with a thicker oxide forming ahead of the crack tip. In the bulk material where oxygen transport to the crack tip is more limited, the extent of oxidation damage was less evident with no apparent oxidation of slip bands. The oxides that formed in the bulk material (for both orientations) at the crack tip had a layered structure with an external Fe-rich oxide layer, and an inner Cr-rich layer at the oxide/metal interface, which is consistent with oxidation studies on CW, and L-PBF IN718 [103], [151], [162]. However, the location of this oxide layer (in the bulk material) relative to the crack tip was different for vertical (oxide filling the crack tip) and horizontal (oxide ahead of the crack tip) specimens (see Figure 6.18, and 6.22), possibly resulting in two different cracking mechanisms.

As previously explained, the fatigue cracking process at high temperatures for IN718 under dwell-fatigue conditions is closely related to oxidation related damage along grain boundaries caused by dynamic embrittlement. This mechanism is primarily linked to stress-induced oxygen diffusion along grain boundaries ahead of the crack tip in the nano-metre scale [163]. As such, the effect of dynamic embrittlement on FCG will be closely related to the availability of oxygen and local stress/strain state at the crack tip. Thus, if the applied stress/strain increases (i.e., crack propagates, ΔK increases), the contribution of dynamic embrittlement to fatigue cracking will be expected to increase [164]. The specific microstructure of vertical specimens will, however, promote very complex crack paths under time-dependent fatigue propagation conditions, as shown by the 2D metallographic sections presented in Figure 6.19 with a highly uneven crack front across the breath of the specimen. The complexity of the crack front will hinder, to some extent, the transport of oxygen to the crack tip, plus the reduction in effective ΔK associated with the deflected crack will reduce the local stress/strain acting on the grain boundaries, both reducing the effect of dynamic embrittlement [165]. Hence, it can be deduced that for vertical specimens at low ΔK levels (<25 MPa$\sqrt{m}$) the combination of available oxygen and local stress/strain at the crack tip are not enough to promote grain boundary failure by dynamic embrittlement. Instead, if dwell time is long enough (90 s dwells) oxidation will form inside the crack, arresting the fatigue crack and preventing further oxidation ahead of the crack tip. As ΔK increases (>25 MPa$\sqrt{m}$) the relatively higher stress/strain acting on the grain boundaries will be sufficient to overcome the effects of crack deflection and intergranular crack propagation will occur by dynamic embrittlement as presented in chapter 5 for constant load 1-90-1-1 tests.

Furthermore, the limitations of the DCPD system for capturing high temperature FCG were evident by comparing the sectioned vertical specimens with the PD traces, where no crack growth was captured. DCPD systems provide a measurement of the overall averaged crack length, not being able to capture local differences in crack growth and thus underestimating crack length for complex crack fronts. To fully characterise the extent of crack deflection on the local stress/strain state a more accurate assessment of the crack morphology, and crack propagation rates is necessary. X-ray or diffraction computed tomography (CT) techniques could be used to obtain three dimensional information of the crack morphology and grain orientations around the crack tip [94]. This information could then be integrated into crystal plasticity models to assess strain accumulation at grain boundaries, and its effect on dynamic embrittlement for vertical specimens.

For horizontal specimens, the extent of crack deflection promoted by their microstructure is not as significant. Transport of oxygen and local stress/strain at the crack tip are, therefore, not as affected and the fatigue cracking process by dynamic embrittlement is comparable to that described in the literature for CW IN718. During dwell times stress-induced diffusion of oxygen will occur along grain boundaries, forming an embrittled/damaged zone ahead of the crack tip. The formation of this damaged zone was discussed for cyclic loading with the block tests, and for longer dwells (interrupted tests) it was characterised with KAM maps (see Figure 6.17). Here, increased local misorientation was captured in the grain boundaries ahead of the crack tip over a distance of the order of the monotonic plastic zone size. Furthermore, discontinuously cracked regions were observed ahead of the crack tip within the oxidation damaged zone. This phenomenon has been previously reported for CW IN718 and other alloys subject to dynamic embrittlement [96], [97], [150], [165]–[167]. Because of differences in grain boundary structure, and thus oxygen diffusivity, fatigue cracking rates will vary from boundary to boundary [96], [168]. This can result in intergranular cracking along selective patches of grain boundaries within the damaged region, and the discontinuously cracked regions seen in Figure 6.17, and 6.18 [96]. This phenomenon can be exacerbated in L-PBF specimens where the number of twin grain boundaries is higher compared to CW specimens possibly increasing scatter in crack propagation rates. It should be noted that the uncracked ligaments are still electrically conductive, therefore this cracking process cannot be captured by DCPD systems. More complex CT techniques would be required to fully understand the relationship between damage ahead of the crack tip and these uncracked ligaments.

6.4 Summary

The role of oxidation during dwell fatigue on FCG mechanisms for cast and wrought, and L-PBF IN718 (manufactured in two different orientations) at 650 ºC was studied in this chapter. The main conclusions were:

1. The extent of oxidation-related damage formed ahead of the crack tip during dwell fatigue was assessed with the block tests for both L-PBF orientations, and CW specimens. Similar mechanisms were found for CW and horizontal specimens, with the formation of a large damaged zone during dwell fatigue promoted by dynamic embrittlement. This was linked to a short surge on FCG rates when switching to cycle-dependent loading conditions. Furthermore, build orientation had a significant influence on FCG mechanisms during the block tests. Vertical specimens had again an arrested crack, and no damaged zone could be identified by the DCPD system.

2. The extent of crack propagation occurring per loading cycle during dwell-fatigue was assessed and found to be different for L-PBF and CW specimens:
   2.1. For CW specimens, the majority of crack propagation occurs during the unloading-reloading stage across the majority of the ΔK range. Suggesting that significant embrittlement of the grain boundaries occurs during the 90 s dwell, which then breaks when unloading-reloading the crack. At high ΔK, crack growth can occur during dwell time, although its magnitude is heavily retarded when compared to the end of the previous cycle, indicating a period of incubation time for FCG to occur during dwell time. This time period decreases as crack length increases.
   2.2. For L-PBF specimens, crack propagation was found to be continuous, with no differences between crack growth during dwell time or unloading-reloading captured by the DCPD system until the very last loading cycles. This indicates that, for L-PBF specimens, the degree of embrittlement of the grain boundaries caused by 90 s dwells is not as significant as for CW.

3. Oxides formed after a sustained load at 650 ºC for 16 hours had a layered structure, which consisted of an outermost Fe-rich oxide layer, and an inner Cr-rich oxide layer at the metal/oxide interface for both L-PBF orientations. The extent of oxidation was severe at the side surface, with vertical specimens showing more localised damage and a thicker oxide layer around the crack tip. In the bulk material, where oxygen availability is more localised, the location of the oxide layer relative to the crack tip

was different for horizontal (ahead of the crack), and vertical (filling the crack) specimens.

4. Oxygen diffusion by dynamic embrittlement is highly related to the availability of oxygen, stress state at the crack tip, and their interaction with the local microstructure. The subtle microstructural differences between horizontal and vertical specimens (differences in grain size distribution, grain boundary character, and grain shape) have resulted in two distinct fatigue cracking mechanisms at low ΔK and 650 ºC:
   4.1. The microstructure of vertical specimens will promote a very complex crack path. The complexity of the crack front will compromise oxygen transport to the crack tip, and the reduction in effective ΔK associated with crack deflection will lower the local stress state at the crack tip. With long dwells (90 s), and at low ΔK levels (<25 MPa$\sqrt{m}$) the combination of available oxygen, and local stress will not be sufficient to promote stress-induced oxygen diffusion ahead of the crack tip. Instead, oxidation will form inside the crack, contributing to crack arrest.
   4.2. Horizontal specimens display a more conventional (comparable to CW) failure process by dynamic embrittlement. During dwell time oxygen will diffuse along grain boundaries ahead of the crack tip forming a damaged zone. This area will have a lower resistance against crack propagation, and FCG rates will increase. It should be noted that a discontinuous crack path can be discerned ahead of the crack tip within the damaged region, which can be linked to intergranular failure along selective patches of grain boundaries with lower resistance to oxygen diffusion and cracking.

7 Summary and conclusions

The research developed in this thesis aimed to gain an understanding of the fatigue crack propagation mechanisms controlling the high temperature performance of additively manufactured IN718. Such understanding is expected to inform improved/optimised manufacturing of L-PBF IN718 with a mechanistic understanding of grain boundary failure processes at high temperature. To achieve this, the studied samples consisted of two L-PBF sample orientations (where cracks propagated either parallel [horizontal specimens] or perpendicular [vertical specimens] to build direction). Plus, comparable cast and wrought IN718 was studied to benchmark L-PBF against established manufacturing techniques.

The L-PBF as-built material presented a fine dendritic microstructure preferentially aligned parallel to the build direction. No significant differences were found in precipitation between specimens with Laves and MC-type primary carbides precipitated in interdendritic areas, without precipitation of IN718 common strengthening precipitates (δ-phase, γ', γ''). EBSD scans revealed a strongly textured structure with elongated grains parallel to the build direction and a finer grain size perpendicular to the build direction. Vertical specimens had an overall a coarser grain structure. Post heat treatment, the grain structure was recrystallised eliminating the anisotropic texture and strictly columnar grains. However, some grain shape was retained with grains having high aspect ratios, and their orientation relative to the direction of crack propagation has proven to have a large influence on time dependent fatigue at high temperature. The HIPing heat treatment was successful in promoting the formation of a large area fraction of twin grain boundaries (> 50%), and vertical specimens had again a coarser grain structure. The brittle Laves phase was dissolved during the heat treatment and precipitation of δ-phase, γ' and γ'' occurred with again no apparent differences in precipitation between specimens. Grain boundaries were highly decorated with the δ-phase, with a large amount of intergranular precipitation of δ-phase occurring as well. The cast and wrought material used for benchmarking L-PBF specimens had a finer grain size, an equiaxed grain structure and a lower area fraction of twin grain boundaries. No intergranular precipitation of δ-phase was observed, with it precipitating mainly as

continuous films along grain boundaries. Furthermore, large blocky carbides (5-12 μm) precipitated at grain boundaries for CW specimens, compared to the smaller (0.4-1.5 μm) finely dispersed carbides across the microstructure for L-PBF specimens.

The influence of temperature (350, and 650 ºC) and dwell time (1, and 90 s dwells) on fatigue crack propagation mechanisms for all material conditions were assessed. At lower testing temperatures, and 1s dwells there were no differences on FCG rates between cast and wrought, horizontally and vertically built L-PBF specimens. All conditions displayed transgranular failure modes, indicating that under cyclic dependent conditions the heat treatment was successful in eliminating any influence from build orientation. Intergranular failure modes became evident when testing at higher temperature (650 ºC) with an associated increase in fatigue crack propagation rates. Under time dependent conditions, build orientation did have a significant effect on both FCG rates and mechanisms, with vertical specimens having greater resistance against crack propagation. This was primarily linked to subtle microstructural differences between L-PBF sample orientations in grain size distribution, grain shape and grain boundary character. The microstructure of vertical specimens promoted a more tortuous crack path, with a lower amount of secondary cracking due to a coarser grain structure, a higher area fraction of twin grain boundaries, and grains preferentially aligned against the direction of crack propagation. Under more time-dependent crack propagation with the introduction of longer dwells, crack arresting occurred for vertical specimens at low ΔK values (<25 MPa$\sqrt{m}$). Roughness measurements and crack profile observations revealed a very tortuous crack path, which resulted in a lower (near-threshold) effective ΔK arresting the crack. Comparatively, for all tests performed at 650 ºC, cast and wrought specimens displayed higher FCG rates and differences in grain boundary failure mechanisms could be observed in the fractographic images. The equiaxed and finer grain structure was not as successful in deflecting the fatigue crack. Plus, a combination of smaller grain size and lower area fraction of twin grain boundaries, yielded a higher number of grain boundaries susceptible to embrittlement. The results indicate that, through a careful control of the L-PBF process and heat treatment it is possible for L-PBF specimens to outperform cast and wrought IN718 under time-dependent fatigue crack propagation conditions.

The effects of oxidation on fatigue crack propagation at 650 ºC were further studied by switching between high and low frequency regimes (aforementioned as block tests). Noticeable oxidation related damage was formed ahead of the crack tip during dwell fatigue promoted by dynamic embrittlement for horizontal and CW specimens. This was

linked to a temporary surge in FCG rates when switching to higher frequency (5 Hz) as the fatigue crack propagated through the embrittled grain boundaries. Although the mechanisms are similar, there were differences in the size of the damaged zone, with horizontal specimens exhibiting a larger damage zone (higher diffusion of oxygen along grain boundaries) compared to CW specimens. This was again linked to grain size differences and explains the higher resistance of horizontal specimens to crack propagation. Build orientation had again a significant influence, with an arrested crack observed during the 90 s dwell loading block, without the formation of an apparent damaged zone ahead of the crack tip. In addition, the extent of crack propagation per loading cycle during dwell fatigue was studied and found to be different between CW and L-PBF specimens. In the case of CW specimens (as reported for other polycrystalline superalloys), the majority of crack propagation occurred during the unloading-reloading part of the cycle across the majority of the ΔK range. Significant embrittlement occurred during the 90s dwell, which then failed rapidly when reloading-unloading the specimen. Interestingly, for L-PBF specimens, crack propagation was continuous throughout the test without differences between dwell time or unloading-reloading. Thus, showing a greater resistance against dynamic embrittlement, which is ultimately reflected in slower FCG rates.

The effect of longer dwells on oxidation related damage ahead of the crack tip was further studied by holding pre-cracked samples under a sustained load for 16 hours at 650 ºC. No differences were found in the composition of the formed oxides, with these having a layered structure which consisted of an outermost Fe-rich layer, and an inner Cr-rich oxide layer. This was as expected and correlated with previous oxidation studies performed on both CW and L-PBF IN718. However, the location of the oxide with respect to the crack tip was different for horizontal and vertical specimens, resulting in two different fatigue cracking mechanisms at low ΔK values (<25 MPa$\sqrt{m}$). Horizontal specimens displayed a more traditional grain boundary failure by dynamic embrittlement. In this case, during dwell time, oxygen will diffuse along the grain boundaries ahead of the crack tip forming a damaged zone (as in the block tests), which then breaks when stress is applied. The degree of dynamic embrittlement is, however, highly dependent on the availability of oxygen, local stress state at the crack tip, and their interaction with the local microstructure. The microstructure of vertical specimens will promote a highly tortuous crack path across the breadth of the specimen. This will both hinder oxygen transfer to the crack tip and reduce the effective ΔK at the crack tip, lowering the local stress state. As a result, if ΔK is low enough, the combination of oxygen availability and local stresses will not be sufficient to promote stress-induced oxygen diffusion along

grain boundaries. Instead, if dwell time is long enough, oxidation will fill the crack tip halting fatigue crack propagation.

Based on these conclusions, it can be said that build direction does have a significant influence on fatigue crack propagation under time-dependent conditions. L-PBF components have generally been heavily heat treated to remove anisotropy in their microstructures, and mechanical performance. However, this was only effective at lower testing temperatures under transgranular crack propagation conditions. It is therefore recommended to carefully consider the orientation of the applied tensile axis with respect to the build orientation of the printed parts if used at high temperatures where time-dependent mechanisms are dominant. This study indicates that components where cracks propagate perpendicular to the build direction will exhibit better high temperature fatigue crack propagation performance. Furthermore, the results have shown that it is possible to use L-PBF to engineer microstructures capable of affecting deformation mechanisms ahead of the crack tip during dwell-fatigue crack propagation. This was achieved by manufacturing specimens in two different orientations; however, it may be possible to achieve similar microstructural effects through careful control of the processing parameters and scanning strategy.

8 Further work

8.1 Additional mechanical testing

Chapters 5 and 6 focussed on characterising the crack propagation behaviour of L-PBF and CW IN718 under different testing temperatures (350, and 650 ºC) and frequencies (1-1-1-1, 1-90-1-1 and block tests). For cycle-dependent conditions no appreciable differences were seen between L-PBF orientations. However, there were significant differences between orientations under time-dependent conditions with horizontal samples showing worse resistance against crack propagation. Furthermore, crack arrest occurred for vertical samples with longer dwells (90 s). To further understand this transition in behaviour, it is recommended to perform additional fatigue crack propagation tests with intermediate dwell times (i.e., trapezoidal waveform 1s – 20s – 1s – 1s), and frequency scans (varying between high and low frequency regimes) at constant ΔK levels (20 MPa$\sqrt{m}$, and 30 MPa$\sqrt{m}$). This would allow to further understand the effect of frequency on crack propagation for additively manufactured IN718. It should be noted, that during this work frequency scans at constant ΔK 20 MPa$\sqrt{m}$ were attempted. The crack was allowed to grow ≈0.5 mm at each frequency and the loading sequence was: 5 Hz, 1-1-1-1, 2 Hz, 1-20-1-1, 0.5 Hz, and 1-90-1-1. However, due to noise in the PD reading associated with high temperature testing, it was not possible to accurately maintain stable constant ΔK across the entire test, and comparison between specimens would have not been possible/accurate.

Oxidation ahead of crack tips was characterised by interrupting tests at ≈ΔK 15 MPa$\sqrt{m}$, as this was the region where the biggest difference between orientations was recorded. It would be interesting to repeat these tests using the same conditions but interrupting them at a higher ΔK value (30-40 MPa$\sqrt{m}$) where the crack is not arrested for vertical specimens. This would allow to get a better understanding of oxidation ahead of the crack tip with increasing ΔK. In addition to more interrupted tests, it would be recommended to perform some crack propagation testing under vacuum or inert environment conditions, where effects of oxidation are absent/reduced. This would allow to get a better understanding of the effects of an oxidising environment and allow to

disentangle the roles of oxidation and mechanical damage in fatigue mechanisms and crack propagation rates.

The effects of cyclic loading on oxidation have been presented in chapter 5 and 6. Additional testing to further investigate oxidation and the relationship between loads and exposure are currently ongoing, however, additional experimental and characterisation work is required to provide meaningful results. These involved unloaded (between 1-256 hours) and sustained load (105 % yield strength) oxidation tests at 650 ºC, which will help improve the understanding on the effects of externally applied loads on oxidation for each L-PBF build orientation.

The work presented in this thesis has primarily focused on high temperature crack propagation, as that was identified as the biggest gap in the literature. However, there is still a lack of research regarding high temperature crack initiation and short crack growth behaviour (i.e., temperature and frequency effects) for L-PBF materials. Although not included in this thesis, some room temperature short crack tests on pre-test thermally exposed specimens were performed to compare results with previous work done at Southampton on crack initiation for IN718 [11]. The aim was to complete the test matrix with high temperature short crack tests using the same loading frequencies as for long crack testing and obtain a full picture of crack initiation and propagation mechanism for additively manufactured IN718. However, problems with high temperature testing equipment availability, and COVID meant that this work could not be completed and might now be carried out by future PhD students at university.

8.2 Further characterisation

Build orientation had a significant effect on crack propagation rates under time dependent conditions, where intergranular failure modes are dominant. It was found to be primarily associated with subtle differences in grain size, shape, and grain boundary character leading to a more tortuous crack path and a lower degree of intergranular failure for vertical specimens. These differences were discussed by calculating the reductions in effective ΔK resultant from crack deflections observed on 2D micrographs from sectioned specimens. However, a fatigue crack front is a complex 3D shape, and it is difficult to accurately characterise the crack tip from 2D images. It is recommended to in future perform X-ray computed tomography scans of testing similar to the interrupted tests, or 1-1-1-1, and 1-90-1-1 crack propagation tests, as it would allow to obtain a more complete picture of the differences on crack front tortuosity between orientations. Furthermore, higher resolution TEM-EDX analysis could be performed on TEM foils extracted from the interrupted crack tips using Focussed Ion Beam (FIB). These would

allow to characterise more accurately the influence of build orientation on the deformation structure, and oxidation processes ahead of the crack tip.

Finally, only the microstructures of as-built, and fully heat treated specimens were characterised, and only fully heat treated specimens were fatigue tested. To better understand differences between orientations, and characteristic features of the heat treated microstructure it would be recommended to perform an analysis of the effects of each of the heat treatment steps on the microstructure, as well as trying different temperatures (HIP-no HIP, sub-solvus heat treatment, etc.). This could be followed by long crack testing on some of this new material conditions and would be useful for proposing heat treatments for L-PBF IN718.

9 References

[1] R. C. Reed, *The Superalloys: Fundamentals and Applications*. Cambridge University Press, 2006.

[2] R. C. Reed and C. M. F. Rae, “Physical Metallurgy of the Nickel-Based Superalloys,” in *Physical Metallurgy: Fifth Edition*, vol. 1, Elsevier Inc., 2014, pp. 2215–2290. doi: 10.1016/B978-0-444-53770-6.00022-8.

[3] S. Sanchez *et al.*, “Powder Bed Fusion of nickel-based superalloys: A review,” *Int J Mach Tools Manuf*, vol. 165, p. 103729, 2021, doi: 10.1016/j.ijmachtools.2021.103729.

[4] A. Yadollahi and N. Shamsaei, “Additive manufacturing of fatigue resistant materials: Challenges and opportunities,” *Int J Fatigue*, vol. 98, pp. 14–31, 2017, doi: 10.1016/j.ijfatigue.2017.01.001.

[5] T. DebRoy *et al.*, “Additive manufacturing of metallic components – Process, structure and properties,” *Prog Mater Sci*, vol. 92, pp. 112–224, Mar. 2018, doi: 10.1016/J.PMATSCI.2017.10.001.

[6] W. J. Sames, F. A. List, S. Pannala, R. R. Dehoff, and S. S. Babu, “The metallurgy and processing science of metal additive manufacturing,” *International Materials Reviews*, vol. 61, no. 5, pp. 315–360, 2016, doi: 10.1080/09506608.2015.1116649.

[7] M. P. Haines, V. v. Rielli, S. Primig, and N. Haghdadi, “Powder bed fusion additive manufacturing of Ni-based superalloys: a review of the main microstructural constituents and characterization techniques,” *J Mater Sci*, vol. 57, no. 30, pp. 14135–14187, Aug. 2022, doi: 10.1007/s10853-022-07501-4.

[8] B. Blakey-Milner *et al.*, “Metal additive manufacturing in aerospace: A review,” *Mater Des*, vol. 209, 2021, doi: 10.1016/j.matdes.2021.110008.

[9] Aerospace technology institute, “Insight 08 - Additive manufacturing, applications in aerospace,” 2018.

[10] D. Deng, R. L. Peng, H. Brodin, and J. Moverare, “Microstructure and mechanical properties of Inconel 718 produced by selective laser melting: Sample orientation dependence and effects of post heat treatments,” *Materials Science and Engineering A*, vol. 713, pp. 294–306, 2018, doi: 10.1016/j.msea.2017.12.043.

[11] T. Connolley, P. A. S. Reed, and M. J. Starink, “Short crack initiation and growth at 600 °C in notched specimens of Inconel718,” *Materials Science and Engineering: A*, vol. 340, no. 1–2, pp. 139–154, 2003, doi: 10.1016/S0921-5093(02)00169-7.

[12] E. Hosseini and V. A. Popovich, “A review of mechanical properties of additively manufactured Inconel 718,” *Addit Manuf*, vol. 30, p. 100877, Dec. 2019, doi: 10.1016/J.ADDMA.2019.100877.

[13] D. Deng, J. Moverare, R. L. Peng, and H. Söderberg, “Microstructure and anisotropic mechanical properties of EBM manufactured Inconel 718 and effects of post heat treatments,” *Materials Science and Engineering A*, vol. 693, no. March, pp. 151–163, 2017, doi: 10.1016/j.msea.2017.03.085.

[14] Y. Gao *et al.*, “Effect of δ phase on high temperature mechanical performances of Inconel 718 fabricated with SLM process,” *Materials Science and Engineering: A*, vol. 767, p. 138327, Nov. 2019, doi: 10.1016/J.MSEA.2019.138327.

[15] N. Nadammal *et al.*, “Effect of hatch length on the development of microstructure, texture and residual stresses in selective laser melted superalloy Inconel 718,” *Mater Des*, vol. 134, pp. 139–150, Nov. 2017, doi: 10.1016/J.MATDES.2017.08.049.

[16] Y. Lu *et al.*, “Study on the microstructure, mechanical property and residual stress of SLM Inconel-718 alloy manufactured by differing island scanning strategy,” *Opt Laser Technol*, vol. 75, pp. 197–206, Dec. 2015, doi: 10.1016/J.OPTLASTEC.2015.07.009.

[17] V. A. Popovich, E. V. Borisov, A. A. Popovich, V. Sh. Sufiiarov, D. V. Masaylo, and L. Alzina, “Functionally graded Inconel 718 processed by additive manufacturing: Crystallographic texture, anisotropy of microstructure and mechanical properties,” *Mater Des*, vol. 114, pp. 441–449, Jan. 2017, doi: 10.1016/J.MATDES.2016.10.075.

[18] M. E. Aydinöz *et al.*, “On the microstructural and mechanical properties of post-treated additively manufactured Inconel 718 superalloy under quasi-static and

cyclic loading," *Materials Science and Engineering: A*, vol. 669, pp. 246–258, Jul. 2016, doi: 10.1016/J.MSEA.2016.05.089.

[19] A. Liang, K. S. Pey, T. Polcar, and A. R. Hamilton, "Effects of rescanning parameters on densification and microstructural refinement of 316L stainless steel fabricated by laser powder bed fusion," *J Mater Process Technol*, vol. 302, no. January, p. 117493, 2022, doi: 10.1016/j.jmatprotec.2022.117493.

[20] M. S. Duval-Chaneac *et al.*, "Effect of heat treatment on fatigue crack growth in IN718/316L multiple-materials layered structures fabricated by laser powder bed fusion," *Int J Fatigue*, vol. 160, no. November 2021, p. 106852, 2022, doi: 10.1016/j.ijfatigue.2022.106852.

[21] C. Kantzos, J. Pauza, R. Cunningham, S. P. Narra, J. Beuth, and A. Rollett, "An Investigation of Process Parameter Modifications on Additively Manufactured Inconel 718 Parts," *J Mater Eng Perform*, vol. 28, no. 2, pp. 620–626, 2019, doi: 10.1007/s11665-018-3612-3.

[22] D. Kim, R. Jiang, A. Evangelou, I. Sinclair, and P. A. S. Reed, "Effects of γ' size and carbide distribution on fatigue crack growth mechanisms at 650 °C in an advanced Ni-based superalloy," *Int J Fatigue*, vol. 145, 2021, doi: 10.1016/j.ijfatigue.2020.106086.

[23] A. Pineau and S. D. Antolovich, "High temperature fatigue of nickel-base superalloys - A review with special emphasis on deformation modes and oxidation," *Eng Fail Anal*, vol. 16, no. 8, pp. 2668–2697, 2009, doi: 10.1016/j.engfailanal.2009.01.010.

[24] D. Gustafsson *et al.*, "Influence of high temperature hold times on the fatigue crack propagation in Inconel 718," *Int J Fatigue*, vol. 33, no. 11, pp. 1461–1469, 2011, doi: 10.1016/j.ijfatigue.2011.05.011.

[25] H. J. Christ, K. Wackermann, and U. Krupp, "Effect of dynamic embrittlement on high temperature fatigue crack propagation in IN718 – experimental characterisation and mechanism-based modelling," *Materials at High Temperatures*, vol. 33, no. 4–5, pp. 528–535, 2016, doi: 10.1080/09603409.2016.1187464.

[26] U. Krupp, "Dynamic embrittlement - Time-dependent quasi-brittle intergranular fracture at high temperatures," *International Materials Reviews*, vol. 50, no. 2, pp. 83–97, 2005, doi: 10.1179/174328005X14320.

[27] H. Ghonem, T. Nicholas, and A. Pineau, “Elevated Temperature Fatigue Crack Growth in Alloy 718—Part Ii: Effects of Environmental and Material Variables,” *Fatigue Fract Eng Mater Struct*, vol. 16, no. 6, pp. 577–590, 1993, doi: 10.1111/j.1460-2695.1993.tb00103.x.

[28] M. Clavel and A. Pineau, “Frequency and Wave-Form Effects on the Fatigue Crack Growth Behavior of Alloy 718 At 298 K and 823 K.,” *Metall Trans A*, vol. 9 A, no. 4, pp. 471–480, 1978, doi: 10.1007/BF02646402.

[29] E. Andrieu and A. Pineau, “Study of the coupled phenomena involved in the oxidation assisted intergranular cracking of Ni based superalloys,” *Journal De Physique. IV : JP*, vol. 9, no. 9, 1999, doi: 10.1051/jp4:1999901.

[30] G. E. Korth, “Effects of Various Parameters on the Fatigue Life of Alloy 718,” *Special emphasis symposium on superalloys 718, 625, and various derivatives*, pp. 457–476, 2012, doi: 10.7449/1991/superalloys_1991_457_476.

[31] ASTM International, “ASTM F2792-12a - Standard Terminology for Additive Manufacturing Technologies,” 2012

[32] W. E. Frazier, “Metal additive manufacturing: A review,” *J Mater Eng Perform*, vol. 23, no. 6, pp. 1917–1928, 2014, doi: 10.1007/s11665-014-0958-z.

[33] C. Y. Yap *et al.*, “Review of selective laser melting: Materials and applications,” *Appl Phys Rev*, vol. 2, no. 4, 2015, doi: 10.1063/1.4935926.

[34] W. J. Sames, F. Medina, W. H. Peter, S. S. Babu, and R. R. Dehoff, “Effect of Process Control and Powder Quality on Inconel 718 Produced Using Electron Beam Melting,” in *8th International Symposium on Superalloy 718 and Derivatives*, John Wiley & Sons, Ltd, 2014, pp. 409–423. doi: 10.1002/9781119016854.ch32.

[35] L. N. Carter, M. M. Attallah, and R. C. Reed, “Laser Powder Bed Fabrication of Nickel-Base Superalloys: Influence of Parameters; Characterisation, Quantification and Mitigation of Cracking,” *Superalloys 2012*. 2012. doi: doi:10.1002/9781118516430.ch64.

[36] B. Graybill, M. Li, D. Malawey, C. Ma, J.-M. Alvarado-Orozco, and E. Martinez-Franco, “Additive Manufacturing of Nickel-Based Superalloys,” no. 51357. p. V001T01A015, 2018. [Online]. Available: http://dx.doi.org/10.1115/MSEC2018-6666

[37] S. M. Yusuf and N. Gao, “Influence of energy density on metallurgy and properties in metal additive manufacturing,” *Materials Science and Technology*, vol. 33, no. 11, pp. 1269–1289, 2017, doi: 10.1080/02670836.2017.1289444.

[38] B. Zhang, Y. Li, and Q. Bai, “Defect Formation Mechanisms in Selective Laser Melting: A Review,” *Chinese Journal of Mechanical Engineering*, vol. 30, no. 3, pp. 515–527, 2017, doi: 10.1007/s10033-017-0121-5.

[39] J. L. Bartlett and X. Li, “An overview of residual stresses in metal powder bed fusion,” *Addit Manuf*, vol. 27, pp. 131–149, 2019, doi: 10.1016/J.ADDMA.2019.02.020.

[40] A. Pinkerton and L. Li, “Direct additive laser manufacturing using gas- and water-atomised H13 tool steel powders,” *International Journal of Advanced Manufacturing Technology*, vol. 25, pp. 471–479, 2005, doi: 10.1007/s00170-003-1844-2.

[41] H. Qi, M. Azer, and A. Ritter, “Studies of Standard Heat Treatment Effects on Microstructure and Mechanical Properties of Laser Net Shape Manufactured INCONEL 718,” *Metallurgical and Materials Transactions A*, vol. 40, no. 10, pp. 2410–2422, 2009, doi: 10.1007/s11661-009-9949-3.

[42] Q. Liu, J. Elambasseril, S. Sun, M. Leary, M. Brandt, and P. Khan Sharp, “The Effect of Manufacturing Defects on The Fatigue Behaviour of Ti-6Al-4V Specimens Fabricated Using Selective Laser Melting,” *Adv Mat Res*, vol. 891–892, pp. 1519–1524, 2014, doi: 10.4028/www.scientific.net/AMR.891-892.1519.

[43] W. H. Kan *et al.*, “A critical review on the effects of process-induced porosity on the mechanical properties of alloys fabricated by laser powder bed fusion,” *Journal of Materials Science*, vol. 57, no. 21. pp. 9818–9865, 2022. doi: 10.1007/s10853-022-06990-7.

[44] L. Thijs, F. Verhaeghe, T. Craeghs, J. van Humbeeck, and J.-P. Kruth, “A study of the microstructural evolution during selective laser melting of Ti–6Al–4V,” *Acta Mater*, vol. 58, no. 9, pp. 3303–3312, 2010, doi: 10.1016/J.ACTAMAT.2010.02.004.

[45] Q. C. Liu, J. Elambasseril, S. J. Sun, M. Leary, M. Brandt, and P. K. Sharp, “The effect of manufacturing defects on the fatigue behaviour of Ti-6Al-4V specimens fabricated using selective laser melting,” *Adv Mat Res*, vol. 891–892, no. March, pp. 1519–1524, 2014, doi: 10.4028/www.scientific.net/AMR.891-892.1519.

[46] L. N. Carter, K. Essa, and M. M. Attallah, “Optimisation of selective laser melting for a high temperature Ni-superalloy,” *Rapid Prototyp J*, vol. 21, no. 4, pp. 423–432, 2015, doi: 10.1108/RPJ-06-2013-0063.

[47] A. Bauereiß, T. Scharowsky, and C. Körner, “Defect generation and propagation mechanism during additive manufacturing by selective beam melting,” *J Mater Process Technol*, vol. 214, no. 11, pp. 2522–2528, 2014, doi: 10.1016/J.JMATPROTEC.2014.05.002.

[48] W. Tillmann, C. Schaak, J. Nellesen, M. Schaper, M. E. Aydinöz, and K.-P. Hoyer, “Hot isostatic pressing of IN718 components manufactured by selective laser melting,” *Addit Manuf*, vol. 13, pp. 93–102, 2017, doi: 10.1016/J.ADDMA.2016.11.006.

[49] D. Herzog, V. Seyda, E. Wycisk, and C. Emmelmann, “Additive manufacturing of metals,” *Acta Mater*, 2016, doi: 10.1016/j.actamat.2016.07.019.

[50] M. Ni *et al.*, “Anisotropic tensile behavior of in situ precipitation strengthened Inconel 718 fabricated by additive manufacturing,” *Materials Science and Engineering: A*, vol. 701, pp. 344–351, Jul. 2017, doi: 10.1016/J.MSEA.2017.06.098.

[51] J. Strößner, M. Terock, and U. Glatzel, “Mechanical and Microstructural Investigation of Nickel-Based Superalloy IN718 Manufactured by Selective Laser Melting (SLM),” *Adv Eng Mater*, vol. 17, no. 8, pp. 1099–1105, 2015, doi: 10.1002/adem.201500158.

[52] C. Hammond and J. Nutting, “The physical metallurgy of superalloys and titanium alloys,” *Metal Science*, vol. 11, no. 10, pp. 474–490, 1977, doi: 10.1179/msc.1977.11.10.474.

[53] T. Connolley, “Initiation and growth of short cracks in u-notch bend specimens of superalloy IN718 during high temperature low cycle fatigue.,” Thesis, University of Southampton, 2001.

[54] R. Cozar and A. Pineau, “Morphology of y’ and y” precipitates and thermal stability of inconel 718 type alloys,” *Metallurgical Transactions*, vol. 4, no. 1, pp. 47–59, 1973, doi: 10.1007/BF02649604.

[55] A. Mitchell, A. J Schmalz, C. Schvezov, and S. L Cockcroft, “The Precipitation of Primary Carbides in Alloy 718,” *Superalloys*, vol. 718, pp. 65–78, 1994, doi: 10.7449/1994/Superalloys_1994_65_78.

[56] S. Azadian, “Aspects of Precipitation in Alloy Inconel 718,” Thesis, Malmö university, 2004.

[57] I. Kirman and D. H. Warrington, “The precipitation of Ni3Nb phases in a Ni−Fe−Cr−Nb alloy,” *Metallurgical Transactions*, vol. 1, no. 10, pp. 2667–2675, 1970, doi: 10.1007/BF03037800.

[58] M. Sundararaman, P. Mukhopadhyay, and S. Banerjee, “Some aspects of the precipitation of metastable intermetallic phases in INCONEL 718,” *Metallurgical Transactions A*, vol. 23, no. 7, pp. 2015–2028, 1992, doi: 10.1007/BF02647549.

[59] P. M. Mignanelli *et al.*, “Gamma-gamma prime-gamma double prime dual-superlattice superalloys,” *Scr Mater*, vol. 136, pp. 136–140, 2017, doi: 10.1016/j.scriptamat.2017.04.029.

[60] E. Guo, F. Xu, and E. A. Loria, “Improving Thermal Stability of Alloy 718 via Small Modifications in Composition,” *Superalloys 718*, pp. 567–576, 1989, doi: 10.7449/1989/superalloys_1989_567_576.

[61] E. Guo, F. Xu, and E. A. Loria, “Effect of Heat Treatment and Compositional Modification on Strength and Thermal Stability of Alloy 718,” *Superalloys 718*, pp. 389–396, 1991, doi: 10.7449/1991/superalloys_1991_389_396.

[62] M. Sundararaman, P. Mukhopadhyay, and S. Banerjee, “Precipitation of the δ-Ni3Nb phase in two nickel base superalloys,” *Metallurgical Transactions A*, vol. 19, no. 3, pp. 453–465, 1988, doi: 10.1007/BF02649259.

[63] E. J. Pickering *et al.*, “Grain-boundary precipitation in Allvac 718Plus,” *Acta Mater*, vol. 60, no. 6–7, pp. 2757–2769, 2012, doi: 10.1016/j.actamat.2012.01.042.

[64] G. A. Knorovsky, M. J. Cieslak, T. J. Headley, A. D. Romig, and W. F. Hammetter, “INCONEL 718: A solidification diagram,” *Metallurgical Transactions A*, vol. 20, no. 10, pp. 2149–2158, 1989, doi: 10.1007/BF02650300.

[65] C. Radhakrishna and K. Prasad Rao, “The formation and control of Laves phase in superalloy 718 welds,” *J Mater Sci*, vol. 32, no. 8, pp. 1977–1984, 1997, doi: 10.1023/A:1018541915113.

[66] M. G. Benz, “Preparation of clean superalloys,” in *Impurities in Engineering Materials*, Routledge, 1999, pp. 31–47.

[67] G. E. Maurer, “Primary and Secondary Melt Processing—Superalloys,” in *Superalloys Supercomposites Superceramics*, Academic Press, 1989, pp. 49–97. doi: https://doi.org/10.1016/B978-0-12-690845-9.50009-9.

[68] D. D. Krueger, “The Development of Direct Age 718 for Gas Turbine Engine Disk Applications,” *Superalloys 718 - Metallurgy and applications*, pp. 279–296, 1989, doi: 10.7449/1989/superalloys_1989_279_296.

[69] A. Mostafa, I. Picazo Rubio, V. Brailovski, M. Jahazi, and M. Medraj, “Structure, Texture and Phases in 3D Printed IN718 Alloy Subjected to Homogenization and HIP Treatments.,” *Metals (Basel)*, vol. 7, no. 8, 2017, doi: 10.3390/met7080315.

[70] M. C. Chaturvedi and Y. Han, “Strengthening mechanisms in Inconel 718 superalloy,” *Metal Science*, vol. 17, pp. 145–149, 1983.

[71] D. Fournier and A. Pineau, “Low cycle fatigue behavior of inconel 718 at 298 K and 823 K,” *Metallurgical Transactions A*, vol. 8, no. 7, pp. 1095–1105, 1977, doi: 10.1007/BF02667395.

[72] H. F. Merrick, “Low Cycle Fatigue of Three Wrought Nickel-Base Alloys.,” *Metall Trans*, vol. 5, no. 4, pp. 891–897, 1974, doi: 10.1007/BF02643144.

[73] X. Wang, X. Gong, and K. Chou, “Review on powder-bed laser additive manufacturing of Inconel 718 parts,” *Institution of Mechanical Engineers, Part B: Journal of Engineering Manufacture*, vol. 231, no. 11, pp. 1890–1903, 2017, doi: 10.1177/0954405415619883.

[74] K. N. Amato *et al.*, “Microstructures and mechanical behavior of Inconel 718 fabricated by selective laser melting,” *Acta Mater*, vol. 60, no. 5, pp. 2229–2239, 2012, doi: 10.1016/J.ACTAMAT.2011.12.032.

[75] R. Acharya, J. A. Sharon, and A. Staroselsky, “Prediction of microstructure in laser powder bed fusion process,” *Acta Mater*, vol. 124, pp. 360–371, 2017, doi: 10.1016/J.ACTAMAT.2016.11.018.

[76] P. C. Collins, D. A. Brice, P. Samimi, I. Ghamarian, and H. L. Fraser, “Microstructural Control of Additively Manufactured Metallic Materials,” *Annu Rev Mater Res*, vol. 46, no. 1, pp. 63–91, 2016, doi: 10.1146/annurev-matsci-070115-031816.

[77] R. R. Dehoff *et al.*, “Site specific control of crystallographic grain orientation through electron beam additive manufacturing,” *Materials Science and*

Technology, vol. 31, no. 8, pp. 931–938, 2015, doi: 10.1179/1743284714Y.0000000734.

[78] P. Nie, O. A. Ojo, and Z. Li, “Numerical modeling of microstructure evolution during laser additive manufacturing of a nickel-based superalloy,” *Acta Mater*, vol. 77, pp. 85–95, 2014, doi: 10.1016/J.ACTAMAT.2014.05.039.

[79] Q. Jia and D. Gu, “Selective laser melting additive manufacturing of Inconel 718 superalloy parts: Densification, microstructure and properties,” *J Alloys Compd*, vol. 585, pp. 713–721, 2014, doi: 10.1016/J.JALLCOM.2013.09.171.

[80] Y. M. Arısoy, L. E. Criales, T. Özel, B. Lane, S. Moylan, and A. Donmez, “Influence of scan strategy and process parameters on microstructure and its optimization in additively manufactured nickel alloy 625 via laser powder bed fusion,” *The International Journal of Advanced Manufacturing Technology*, vol. 90, no. 5, pp. 1393–1417, 2017, doi: 10.1007/s00170-016-9429-z.

[81] B. K. Foster, A. M. Beese, J. S. Keist, E. T. McHale, and T. A. Palmer, “Impact of Interlayer Dwell Time on Microstructure and Mechanical Properties of Nickel and Titanium Alloys,” *Metallurgical and Materials Transactions A*, vol. 48, no. 9, pp. 4411–4422, 2017, doi: 10.1007/s11661-017-4164-0.

[82] E. Chlebus, K. Gruber, B. Kuźnicka, J. Kurzac, and T. Kurzynowski, “Effect of heat treatment on the microstructure and mechanical properties of Inconel 718 processed by selective laser melting,” *Materials Science and Engineering A*, vol. 639, pp. 647–655, 2015, doi: 10.1016/j.msea.2015.05.035.

[83] P. Liu, J. Hu, S. Sun, K. Feng, Y. Zhang, and M. Cao, “Microstructural evolution and phase transformation of Inconel 718 alloys fabricated by selective laser melting under different heat treatment,” *J Manuf Process*, vol. 39, pp. 226–232, 2019, doi: 10.1016/J.JMAPRO.2019.02.029.

[84] C. W. Brown, J. E. King, and M. A. Hicks, “Effects of microstructure on long and short crack growth in nickel base superalloys,” *Metal Science*, vol. 18, no. 7, pp. 374–380, 1984, doi: 10.1179/030634584790419881.

[85] A. Pineau and J. P. Pédron, “The effect of microstructure and environment on the crack growth behaviour of Inconel 718 alloy at 650 °C under fatigue, creep and combined loading,” *Materials Science and Engineering*, vol. 56, no. 2, pp. 143–156, 1982.

[86] S. D. Antolovich, “Microstructural aspects of fatigue in Ni-base superalloys,” *Philosophical Transactions of the Royal Society A: Mathematical, Physical and Engineering Sciences*, vol. 373, no. 2038, 2015, doi: 10.1098/rsta.2014.0128.

[87] D. Zheng and H. Ghonem, “Influence of prolonged thermal exposure on intergranular fatigue crack growth behavior in alloy 718 at 650 °C,” *Metallurgical transactions. A, Physical metallurgy and materials science*, vol. 23 A, no. 11, pp. 3169–3171, 1992, doi: 10.1007/BF02646137.

[88] D. Gustafsson *et al.*, “Fatigue crack growth behaviour of Inconel 718 with high temperature hold times,” *Procedia Eng*, vol. 2, no. 1, pp. 1095–1104, 2010, doi: 10.1016/j.proeng.2010.03.118.

[89] M. Khobaib, N. E. Ashbaugh, G. A. Hartman, T. Weerasooriya, D. C. Maxwell, and R. C. Goodman, “Research on mechanical properties for engine life prediction,” Dayton univ OH research institute, 1988.

[90] L. A. James, “Fatigue crack propagation in alloy 718: a review,” *Superalloy 718–Metallurgy and Applications, EA Loria, Ed., MM&MS*, pp. 499–515, 1989.

[91] H. Ghonem, T. Nicholas, and A. Pineau, “Elevated Temperature Fatigue Crack Growth in Alloy 718—Part I: Effects of Mechanical Variables,” *Fatigue Fract Eng Mater Struct*, vol. 16, no. 5, pp. 565–576, 1993, doi: 10.1111/j.1460-2695.1993.tb00767.x.

[92] S. Floreen and R. H. Kane, “An investigation of the creep-fatigue-environment interaction in a Ni-base superalloy,” *Fatigue Fract Eng Mater Struct*, vol. 2, no. 4, pp. 401–412, 1979, doi: 10.1111/j.1460-2695.1979.tb01097.x.

[93] C. Mercer, S. Shademan, and W. O. Soboyejo, “An investigation of the micromechanisms of fatigue crack growth in structural gas turbine engine alloys,” *J Mater Sci*, vol. 38, no. 2, pp. 291–305, 2003, doi: 10.1023/A:1021161532639.

[94] R. Jiang and P. A. S. Reed, “Critical assessment 21: Oxygen-assisted fatigue crack propagation in turbine disc superalloys,” *Materials Science and Technology*, vol. 32, no. 5, pp. 401–406, 2016, doi: 10.1080/02670836.2016.1148227.

[95] U. Krupp, K. Wackermann, H. J. Christ, M. H. Colliander, and K. Stiller, “Intergranular Oxidation Effects During Dwell-Time Fatigue of High-Strength Superalloys,” *Oxidation of Metals*, vol. 88, no. 1–2, pp. 3–14, 2017, doi: 10.1007/s11085-016-9707-z.

[96] J. A. Pfaendtner and C. J. McMahon, “Oxygen-induced intergranular decohesion in IN718,” *Materials Science Forum*, vol. 294–296, pp. 743–746, 1999, doi: 10.4028/www.scientific.net/msf.294-296.743.

[97] U. Krupp, “Dynamic embrittlement - Diffusion-induced intergranular cracking,” *Defect and Diffusion Forum*, vol. 258–260, pp. 192–198, 2006, doi: 10.4028/www.scientific.net/ddf.258-260.192.

[98] W. M. Kane, “Dynamic embrittlement of Nickel-based alloys,” Thesis, University of Pennsylvania, 2005.

[99] D. Gustafsson *et al.*, “Fatigue crack growth behaviour of Inconel 718 - The concept of a damaged zone caused by high temperature hold times,” *Procedia Eng*, vol. 10, pp. 2821–2826, 2011, doi: 10.1016/j.proeng.2011.04.469.

[100] E. Andrieu, R. Molins, H. Ghonem, and A. Pineau, “Intergranular crack tip oxidation mechanism in a nickel-based superalloy,” *Materials science and engineering*, vol. 154, pp. 21–28, 1992.

[101] S. P. Lynch, T. C. Radtke, B. J. Wicks, and R. T. Byrnes, “Fatigue Crack Growth in Nickel-Based Superalloys At 500-700 C. II: Direct-Aged Alloy 718,” *Fatigue Fract Eng Mater Struct*, vol. 17, no. 3, pp. 313–325, 1994, doi: 10.1016/0142-1123(95)99753-W.

[102] A. Diboine and A. Pineau, “Creep crack initiation and growth in Inconel 718 alloy at 650°C,” *Fatigue Fract Eng Mater Struct*, vol. 10, no. 2, pp. 141–151, Feb. 1987, doi: 10.1111/j.1460-2695.1987.tb01156.x.

[103] R. Molins, G. Hochstetter, J. C. Chassaigne, and E. Andrieu, “Oxidation effects on the fatigue crack growth behaviour of alloy 718 at high temperature,” *Acta Mater*, vol. 45, no. 2, pp. 663–674, 1997, doi: 10.1016/S1359-6454(96)00192-9.

[104] J. L. Yuen, C. G. Schmidt, and P. Roy, “Effects of air and inert environments on the near threshold fatigue crack growth behaviour of alloy 718,” *Fatigue Fract Eng Mater Struct*, vol. 8, no. 1, pp. 65–76, 1985, doi: 10.1111/j.1460-2695.1985.tb00420.x.

[105] W. M. Kane and C. J. McMahon, “Part II. Effects of grain-boundary structure on the path of cracking in polycrystals,” *Materials Science and Engineering A*, vol. 507, no. 1–2, pp. 61–65, 2009, doi: 10.1016/j.msea.2008.07.015.

[106] U. Krupp, W. M. Kane, X. Liu, O. Dueber, C. Laird, and C. J. McMahon, “The effect of grain-boundary-engineering-type processing on oxygen-induced cracking of

IN718," *Materials Science and Engineering A*, vol. 349, no. 1–2, pp. 213–217, 2003, doi: 10.1016/S0921-5093(02)00753-0.

[107] A. Yadollahi, M. J. Mahtabi, A. Khalili, H. R. Doude, and J. C. Newman, "Fatigue life prediction of additively manufactured material: Effects of surface roughness, defect size, and shape," *Fatigue Fract Eng Mater Struct*, vol. 41, no. 7, pp. 1602–1614, 2018, doi: 10.1111/ffe.12799.

[108] R. Konečná, G. Nicoletto, L. Kunz, and A. Bača, "Microstructure and directional fatigue behavior of Inconel 718 produced by selective laser melting," *Procedia Structural Integrity*, vol. 2, pp. 2381–2388, Jan. 2016, doi: 10.1016/J.PROSTR.2016.06.298.

[109] H.-Y. Wan, Z.-J. Zhou, C.-P. Li, G.-F. Chen, and G.-P. Zhang, "Enhancing Fatigue Strength of Selective Laser Melting-Fabricated Inconel 718 by Tailoring Heat Treatment Route," *Adv Eng Mater*, vol. 20, no. 10, 2018, doi: 10.1002/adem.201800307.

[110] S. Afkhami, M. Dabiri, S. H. Alavi, T. Björk, and A. Salminen, "Fatigue characteristics of steels manufactured by selective laser melting," *Int J Fatigue*, vol. 122, pp. 72–83, 2019, doi: 10.1016/J.IJFATIGUE.2018.12.029.

[111] P. F. Kelley, A. Saigal, J. K. Vlahakis, and A. Carter, "Tensile and Fatigue Behavior of Direct Metal Laser Sintered (DMLS) Inconel 718," *Volume 2A: Advanced Manufacturing*, 2015, doi: 10.1115/IMECE2015-50937.

[112] A. Riemer, S. Leuders, M. Thöne, H. A. Richard, T. Tröster, and T. Niendorf, "On the fatigue crack growth behavior in 316L stainless steel manufactured by selective laser melting," *Eng Fract Mech*, vol. 120, pp. 15–25, 2014, doi: 10.1016/j.engfracmech.2014.03.008.

[113] K. Morgan and D. Wells, "Overview of fatigue and damage tolerance performance of SLM alloy 718," NASA Marshall Space Flight Centre, 2016.

[114] H. Y. Wan, G. F. Chen, C. P. Li, X. B. Qi, and G. P. Zhang, "Data-driven evaluation of fatigue performance of additive manufactured parts using miniature specimens," *J Mater Sci Technol*, vol. 35, no. 6, pp. 1137–1146, 2019, doi: 10.1016/j.jmst.2018.12.011.

[115] A. R. Balachandramurthi, J. Moverare, N. Dixit, D. Deng, and R. Pederson, "Microstructural influence on fatigue crack propagation during high cycle fatigue

testing of additively manufactured Alloy 718," *Mater Charact*, vol. 149, pp. 82–94, 2019, doi: 10.1016/j.matchar.2019.01.018.

[116] D. B. Witkin, D. Patel, T. v. Albright, G. E. Bean, and T. McLouth, "Influence of surface conditions and specimen orientation on high cycle fatigue properties of Inconel 718 prepared by laser powder bed fusion," *Int J Fatigue*, vol. 132, p. 105392, 2020, doi: 10.1016/j.ijfatigue.2019.105392.

[117] K. Yang, Q. Huang, Q. Wang, and Q. Chen, "Competing crack initiation behaviors of a laser additively manufactured nickel-based superalloy in high and very high cycle fatigue regimes," *Int J Fatigue*, vol. 136, 2020, doi: 10.1016/j.ijfatigue.2020.105580.

[118] D. S. Watring, K. C. Carter, D. Crouse, B. Raeymaekers, and A. D. Spear, "Mechanisms driving high-cycle fatigue life of as-built Inconel 718 processed by laser powder bed fusion," *Materials Science and Engineering A*, vol. 761, 2019, doi: 10.1016/j.msea.2019.06.003.

[119] C. Kantzos, J. Pauza, R. Cunningham, S. P. Narra, J. Beuth, and A. Rollett, "An Investigation of Process Parameter Modifications on Additively Manufactured Inconel 718 Parts," *J Mater Eng Perform*, vol. 28, no. 2, pp. 620–626, 2019, doi: 10.1007/s11665-018-3612-3.

[120] H. Y. Wan, Z. J. Zhou, C. P. Li, G. F. Chen, and G. P. Zhang, "Effect of scanning strategy on mechanical properties of selective laser melted Inconel 718," *Materials Science and Engineering A*, vol. 753, pp. 42–48, 2019, doi: 10.1016/j.msea.2019.03.007.

[121] S. Gribbin, S. Ghorbanpour, N. C. Ferreri, J. Bicknell, I. Tsukrov, and M. Knezevic, "Role of grain structure, grain boundaries, crystallographic texture, precipitates, and porosity on fatigue behavior of Inconel 718 at room and elevated temperatures," *Mater Charact*, vol. 149, pp. 184–197, 2019, doi: 10.1016/J.MATCHAR.2019.01.028.

[122] X. F. Ma *et al.*, "Fatigue short crack propagation behavior of selective laser melted Inconel 718 alloy by in-situ SEM study: Influence of orientation and temperature," *Int J Fatigue*, vol. 139, 2020, doi: 10.1016/j.ijfatigue.2020.105739.

[123] S. Kim, H. Choi, J. Lee, and S. Kim, "Room and elevated temperature fatigue crack propagation behavior of Inconel 718 alloy fabricated by laser powder bed fusion," *Int J Fatigue*, vol. 140, 2020, doi: 10.1016/j.ijfatigue.2020.105802.

[124] D. Deng, R. Eriksson, R. L. Peng, and J. Moverare, “On the Dwell-Fatigue Crack Propagation Behavior of a High-Strength Ni-Base Superalloy Manufactured by Selective Laser Melting,” *Metall Mater Trans A Phys Metall Mater Sci*, vol. 51, no. 2, pp. 962–972, 2020, doi: 10.1007/s11661-019-05548-8.

[125] SAE International (SAE), “AMS5662 Aerospace material specification,” 2009

[126] ASTM International, “ASTM B962-17 Standard Test Methods for Density of Compacted or Sintered Powder Metallurgy (PM) Products Using Archimedes’ Principle,” 2017 doi: 10.1520/B0962-17.

[127] British Standards, “BS ISO 12108 : 2018 BSI Standards Publication Metallic materials - Fatigue testing - Fatigue crack growth method,” 2018

[128] T. L. Anderson, *Fracture mechanics: fundamentals and applications*, 3rd ed. CRC Press, 2005. doi: 10.1007/s42947-020-0181-2.

[129] D. Kim, “Influences of microstructure and oxidation processes on fatigue failure mechanisms in advanced turbine disc Ni-based superalloy,” Thesis, University of Southampton, 2021.

[130] British Standard, “BS EN ISO 4288:1998 - Geometric product specification (GPS). Surface texture. Profile method: Rules and procedures for the assessment of surface texture,” 1998.

[131] P. Tao, H. Li, B. Huang, Q. Hu, S. Gong, and Q. Xu, “The crystal growth, intercellular spacing and microsegregation of selective laser melted Inconel 718 superalloy,” *Vacuum*, vol. 159, pp. 382–390, 2019, doi: 10.1016/J.VACUUM.2018.10.074.

[132] M. Calandri, S. Yin, B. Aldwell, F. Calignano, R. Lupoi, and D. Ugues, “Texture and microstructural features at different length scales in Inconel 718 produced by selective laser melting,” *Materials*, vol. 12, no. 8, 2019, doi: 10.3390/ma12081293.

[133] M. E. Aydinöz *et al.*, “On the microstructural and mechanical properties of post-treated additively manufactured Inconel 718 superalloy under quasi-static and cyclic loading,” *Materials Science and Engineering A*, vol. 669, pp. 246–258, 2016, doi: 10.1016/j.msea.2016.05.089.

[134] D. G. Leo Prakash, M. J. Walsh, D. Maclachlan, and A. M. Korsunsky, “Crack growth micro-mechanisms in the IN718 alloy under the combined influence of fatigue, creep and oxidation,” *Int J Fatigue*, vol. 31, no. 11–12, pp. 1966–1977, 2009, doi: 10.1016/j.ijfatigue.2009.01.023.

[135] T. Weerasooriya, “Effect of Frequency on Fatigue Crack Growth Rate of Inconel 718 at High Temperature,” *Fracture Mechanics: Nineteenth Symposium*, no. June 1987, pp. 907-907–17, 2009, doi: 10.1520/stp33112s.

[136] S. Ponnelle, B. Bréthes, and A. Pineau, “Orientational effects and influence of delta phase on fatigue crack growth rates in a forged disc of Inco718 superalloy,” *Proceedings of the International Symposium on Superalloys and Various Derivatives*, vol. 1, pp. 501–510, 2001, doi: 10.7449/2001/superalloys_2001_501_510.

[137] J. Telesman, T. P. Gabb, A. Garg, P. Bonacuse, and JGayda, “Effect of microstructure on time dependent fatigue crack growth behavior in a P/M turbine disk alloy,” *Proceedings of the International Symposium on Superalloys*, pp. 807–816, 2008, doi: 10.7449/2008/superalloys_2008_807_816.

[138] V. B. Dutta, S. Suresh, and R. O. Ritchie, “Fatigue Crack Propagation in Dual-Phase Steels: Effects of Ferritic-Martensitic Microstructures on Crack Path Morphology.,” *Metallurgical transactions. A, Physical metallurgy and materials science*, vol. 15 A, no. 6, pp. 1193–1207, 1984, doi: 10.1007/bf02644714.

[139] S. Suresh, “Crack deflection: Implications for the growth of long and short fatigue cracks,” *Metallurgical Transactions A*, vol. 14, no. 11, pp. 2375–2385, 1983, doi: 10.1007/BF02663313.

[140] R. Jiang, S. Everitt, M. Lewandowski, N. Gao, and P. A. S. Reed, “Grain size effects in a Ni-based turbine disc alloy in the time and cycle dependent crack growth regimes,” *Int J Fatigue*, vol. 62, pp. 217–227, May 2014, doi: 10.1016/J.IJFATIGUE.2013.07.014.

[141] H. T. Pang and P. A. S. Reed, “Microstructure variation effects on room temperature fatigue threshold and crack propagation in Udimet 720Li Ni-base superalloy,” *Fatigue Fract Eng Mater Struct*, vol. 32, no. 8, pp. 685–701, 2009, doi: 10.1111/j.1460-2695.2009.01366.x.

[142] J. Telesman, P. Kantzos, J. Gayda, P. J. Bonacuse, and A. Prescenzi, “Microstructural variables controlling time-dependent crack growth in A P/M superalloy,” *Proceedings of the International Symposium on Superalloys*, no. January, pp. 215–224, 2004, doi: 10.7449/2004/superalloys_2004_215_224.

[143] A. N. Forsey *et al.*, “Mechanical property heterogeneity in additively manufactured nickel superalloy,” *Materials Science and Engineering A*, vol. 712, pp. 681–684, 2018, doi: 10.1016/j.msea.2017.12.025.

[144] D. Deng, R. L. Peng, and J. Moverare, “A comparison study of the dwell-fatigue behaviours of additive and conventional IN718: The role of dislocation substructure on the cracking behaviour,” *Materials Science and Engineering A*, vol. 797, no. June, p. 140072, 2020, doi: 10.1016/j.msea.2020.140072.

[145] M. Anderson, A. L. Thielin, F. Bridier, P. Bocher, and J. Savoie, “δ Phase precipitation in Inconel 718 and associated mechanical properties,” *Materials Science and Engineering A*, vol. 679, no. August 2016, pp. 48–55, 2017, doi: 10.1016/j.msea.2016.09.114.

[146] J. Saarimäki, M. H. Colliander, and J. Moverare, “Anisotropy effects during dwell-fatigue caused by δ-phase orientation in forged Inconel 718,” *Materials Science and Engineering A*, vol. 692, pp. 174–181, 2017, doi: 10.1016/j.msea.2017.03.063.

[147] D. Deng, R. L. Peng, and J. Moverare, “On the dwell-fatigue crack propagation behavior of a high strength superalloy manufactured by electron beam melting,” *Materials Science and Engineering A*, vol. 760, no. June, pp. 448–457, 2019, doi: 10.1016/j.msea.2019.06.013.

[148] D. Deng, R. L. Peng, and J. Moverare, “A comparison study of the dwell-fatigue behaviours of additive and conventional IN718: The role of dislocation substructure on the cracking behaviour,” *Materials Science and Engineering A*, vol. 797, no. June, p. 140072, 2020, doi: 10.1016/j.msea.2020.140072.

[149] D. Deng, R. L. Peng, and J. Moverare, “High temperature mechanical integrity of selective laser melted alloy 718 evaluated by slow strain rate tests,” *Int J Plast*, vol. 140, no. December 2020, p. 102974, 2021, doi: 10.1016/j.ijplas.2021.102974.

[150] C. J. McMahon, L. Ma, X. Liu, and K. M. Chang, “Comments on ‘identification of SAGBO-induced damage zone ahead of crack tip to characterize sustained loading crack growth in alloy 783,’” *Scr Mater*, vol. 54, no. 2, pp. 305–307, 2006, doi: 10.1016/j.scriptamat.2005.09.030.

[151] H. Ghonem and D. Zheng, “Frequency interactions in high-temperature fatigue crack growth in superalloys,” *Metallurgical transactions. A, Physical metallurgy*

and materials science, vol. 23 A, no. 11, pp. 3067–3072, 1992, doi: 10.1007/BF02646124.

[152] R. Jiang, Y. D. Song, and P. A. Reed, “Fatigue crack growth mechanisms in powder metallurgy Ni-based superalloys—A review,” *Int J Fatigue*, vol. 141, 2020, doi: 10.1016/j.ijfatigue.2020.105887.

[153] F. v. Antunes, A. Ramalho, and J. M. Ferreira, “Identification of fatigue crack propagation modes by means of roughness measurements,” *Int J Fatigue*, vol. 22, no. 9, pp. 781–788, 2000, doi: 10.1016/S0142-1123(00)00048-7.

[154] U. Krupp, “Improving the resistance to intergranular cracking and corrosion at elevated temperatures by grain-boundary-engineering-type processing,” *J Mater Sci*, vol. 43, no. 11, pp. 3908–3916, 2008, doi: 10.1007/s10853-007-2363-6.

[155] H. W. Liu and Y. Oshida, “Grain boundary oxidation and fatigue crack growth at elevated temperatures,” *Theoretical and Applied Fracture Mechanics*, vol. 6, no. 2, pp. 85–94, 1986, doi: 10.1016/0167-8442(86)90028-5.

[156] R. Jiang, N. Gao, and P. A. S. Reed, “Influence of orientation-dependent grain boundary oxidation on fatigue cracking behaviour in an advanced Ni-based superalloy,” *J Mater Sci*, vol. 50, no. 12, pp. 4379–4386, 2015, doi: 10.1007/s10853-015-8992-2.

[157] H. Ghonem and D. Zheng, “Characterization of Environment-Dependent Fatigue Crack Growth in Alloy 718 at 650C,” no. April 2015, pp. 477–490, 2012, doi: 10.7449/1991/superalloys_1991_477_490.

[158] H. J. Christ, K. Wackerman, and U. Krupp, “On the mechanism of dynamic embrittlement and its effect on fatigue crack propagation in IN718 at 650°C,” *Procedia Structural Integrity*, vol. 2, pp. 557–564, 2016, doi: 10.1016/j.prostr.2016.06.072.

[159] L. Ma and K. M. Chang, “Identification of SAGBO-induced damage zone ahead of crack tip to characterize sustained loading crack growth in alloy 783,” *Scr Mater*, vol. 48, no. 9, pp. 1271–1276, 2003, doi: 10.1016/S1359-6462(03)00049-6.

[160] R. Jiang, D. J. Bull, D. Proprentner, B. Shollock, and P. A. S. Reed, “Effects of oxygen-related damage on dwell-fatigue crack propagation in a P/M Ni-based superalloy: From 2D to 3D assessment,” *Int J Fatigue*, vol. 99, pp. 175–186, 2017, doi: 10.1016/J.IJFATIGUE.2017.03.003.

[161] R. Jiang, S. Everitt, N. Gao, K. Soady, J. W. Brooks, and P. A. S. Reed, “Influence of oxidation on fatigue crack initiation and propagation in turbine disc alloy N18,” *Int J Fatigue*, vol. 75, pp. 89–99, 2015, doi: 10.1016/j.ijfatigue.2015.02.007.

[162] L. Li *et al.*, “Influence of Building Direction on the Oxidation Behavior of Inconel 718 Alloy Fabricated by Additive Manufacture of Electron Beam Melting,” *Materials*, vol. 11, no. 12, 2018, doi: 10.3390/ma11120000.

[163] R. Jiang *et al.*, “Role of oxygen in enhanced fatigue cracking in a PM Ni-based superalloy: Stress assisted grain boundary oxidation or dynamic embrittlment?,” *Corros Sci*, vol. 139, pp. 141–154, 2018, doi: 10.1016/J.CORSCI.2018.05.001.

[164] D. Bika and C. J. Memahon Jr, “A model for dynamic embrittlement,” *Acta metall, mater*, vol. 43, no. 5, pp. 1909–1916, 1994.

[165] M. Hörnqvist, L. Viskari, K. L. Moore, and K. Stiller, “High-temperature crack growth in a Ni-base superalloy during sustained load,” *Materials Science and Engineering A*, vol. 609, pp. 131–140, 2014, doi: 10.1016/j.msea.2014.04.102.

[166] D. Bika, J. A. Pfaendtner, and C. J. Mcmahon, “Sulfur-induced dynamic embrittlement in a low-alloy steel,” *Acta metall, mater*, vol. 43, no. 5, pp. 1895–1908, 1995.

[167] L. Viskari, S. Johansson, and K. Stiller, “Oxygen influenced intergranular crack propagation: Analysing microstructure and chemistry in the crack tip region,” *Materials at High Temperatures*, vol. 28, no. 4, pp. 336–341, 2011, doi: 10.3184/096034011X13189599518971.

[168] W. M. Kane, U. Krupp, and C. J. McMahon, “Part I: Anisotropy of cracking from oxygen-induced dynamic embrittlement in bicrystals of IN718,” *Materials Science and Engineering A*, vol. 507, no. 1–2, pp. 58–60, 2009, doi: 10.1016/j.msea.2008.12.002.